



# Università degli Studi di Napoli *Federico II*

DOTTORATO DI RICERCA IN  
**FISICA**

**Ciclo XXXV**

Coordinatore: prof. Vincenzo Canale

## Title: Plasmonic Effect for Nanoparticle Displacement

Settore Scientifico Disciplinare FIS/03

**Dottorando**  
Sergio Balestrieri

**Tutore**  
Ing. Giuseppe Coppola  
Ing. Mario Iodice  
Prof. Enrico Calloni

Anni 2019/2022 (start and end year)



# Contents

|   |           |
|---|-----------|
| <b>Introduction</b>   | <b>5</b>  |
| <b>1 Overview of Propulsion Technologies</b>  | <b>11</b> |
| 1.1 Chemical Thruster . . . . .   | 12        |
| 1.2 Electric Thruster . . . . .   | 15        |
| 1.3 Optical Thruster . . . . .  | 20        |
| <b>2 Principles of Plasmonic Propulsion</b>   | <b>25</b> |
| 2.1 Electromagnetism in dispersive media . . . . .  | 25        |
| 2.2 Optical Response in metals . . . . .  | 27        |
| 2.3 Surface Plasmon Polaritons . . . . .  | 29        |
| 2.4 Excitation of Surface Plasmon Polaritons . . . . .                                    | 34        |
| 2.5 Localized Surface Plasmon . . . . .   | 37        |
| <b>3 Finite Element Method</b>  | <b>45</b> |
| 3.1 Discretization: Linear Triangular Element . . . . .                                   | 46        |
| 3.2 Assembly . . . . .  | 48        |
| 3.3 Convergence in $\mathbb{P}_1$ and Grid Refinement . . . . .                           | 49        |
| 3.4 Quadrilater division of domain . . . . .  | 51        |
| 3.5 Isoparametric Element . . . . .   | 53        |
| 3.6 Matrix Solvers . . . . .  | 54        |
| 3.6.1 Direct Solvers . . . . .  | 54        |
| 3.6.2 Iterative Solvers . . . . .   | 55        |
| <b>4 Plasmonic Device for Nanoparticle Manipulation</b>                                   | <b>59</b> |
| 4.1 Force in Confined Field . . . . .   | 59        |
| 4.2 Plasmon Force Confinement . . . . .   | 61        |
| 4.3 Plasmonic Optical Thruster . . . . .  | 66        |
| 4.4 Plasmonic Device with gap variation: Alternating constant gap<br>trapezoids . . . . . | 74        |
| 4.5 Plasmon Device with a linear variation of gap . . . . .                               | 81        |
| 4.5.1 Elementary cell of the nanostructure . . . . .                                      | 81        |
| 4.5.2 Array Configuration . . . . .   | 85        |
| 4.5.3 Analysis of the influence of geometric parameters . . . . .                         | 88        |

|          |  |            |
|----------|--|------------|
| 4.5.4    | Kinetic of nanoparticles . . . . .   | 95         |
| 4.5.5    | Circular Array . . . . .   | 101        |
| <b>5</b> | <b>Spin-Orbit Coupling Effect</b>  | <b>105</b> |
| 5.1      | Spin-orbit in optics phenomena . . . . .   | 105        |
| 5.2      | Spin momentum in evanescent wave . . . . .   | 108        |
| 5.3      | Polarization-Addressable Optical Force on Plasmonic Nanoparticles and Hot-Spot Spin Vortices . . . . . | 110        |
| 5.3.1    | Spin Momentum in Plasmonic Dimer . . . . .   | 114        |
| <b>6</b> | <b>Fabrication and Characterization</b>  | <b>119</b> |
| 6.1      | Techonogical process for device fabrication . . . . .  | 119        |
| 6.2      | Fabrication Result . . . . .   | 127        |
| 6.2.1    | Scanning Electron Microscope (SEM) . . . . .   | 130        |
| 6.3      | Characterization of the sample . . . . .   | 132        |
|          | <b>Appendix</b>  | <b>146</b> |
| <b>A</b> | <b>Electromagnetism in vacuum</b>  | <b>147</b> |
| A.1      | Vacuum Relation of $E$ and $B$ . . . . .   | 147        |
| A.2      | Electromagnetic wave and optical phenomena . . . . .   | 151        |
| <b>B</b> | <b>Mathematical Tools of Finite Element Method</b>   | <b>155</b> |
| B.1      | Linear Triangular Discretization . . . . .   | 155        |
| B.2      | Assembly . . . . .   | 158        |
| B.3      | Isoparametric Element . . . . .  | 162        |
|          | <b>Bibliography</b>  | <b>164</b> |

# Introduction

In the 1970s humankind was able to perform the first space explorations; the first satellites were launched along the Earth's orbit (Sputnik 1957), then they reached the moon's surface (Apollo 11 1969). The event signified a fundamental historical turning point as space became a territory of conquest by mankind and scientists have the opportunity to acquire new data and images. The need to open new exploratory frontiers in the cosmos made the study and development of space launchers and satellites important to the aerospace industry. Indeed, the first satellites were heavy and bulky and without autonomous propulsion systems; when technology improved, satellites became lighter and resistant, and they also became equipped with propulsion systems that improved their orbital correction capability and stability. As a result of these improvements, it has been possible to build a large number of satellites for various applications. In particular, many of the objects in use in the modern era rely upon satellites in orbit: GPS, television, and telecommunications. In addition, scientists use satellites to monitor the environment and weather and predict disasters in certain areas. The increasing use of low-cost satellites for ordinary activities has stimulated the development of satellites characterized by their small size; for this reason, new frontiers in aerospace have led to the design and development of nanosatellites. Nanosatellites, also known as CubeSats, were initially conceived as theoretical models for academic studies; however, in recent times the idea has arisen that they can be employed for missions both in Earth orbit and for extra orbital travel. In general, CubeSats have a volume of about  $1dm^3$  and a mass on the order of a kilogram, and they have properties that promote their development to other satellites:

- 1) their small size and low cost, which make them a platform for space activities usable by a larger number of players (universities, research centers, private companies);
- 2) the ease in their construction and development.

Due to their size, CubeSats present a challenge, i.e., they have a small payload; for this reason, we have to identify a propulsion system that can be implemented in the nanosatellite without limiting the payload. In general, common thruster systems can be electric or nonelectric, depending on the availability of power within the satellite:

- 1) nonelectrical systems, such as chemical systems, generate propulsion through a combustion reaction with a propellant (solid, liquid, or gaseous). The release of material caused by the resulting chemical reaction generates a force in the opposite direction of the propellant, due to Newton's third law of motion.
- 2) electrical systems exploit physical phenomena to induce propulsion, for example, ion's expulsion induced by a strong electromagnetic potential.

These systems have good parameters of propulsion (i.e., the force induced on the satellite) and specific impulse (the ratio between the force and the mass ejected from the system); however, although the propulsion device's load can be reduced, the injector, combustion chamber, and propellant combination equally occupy a large part of the CubeSat payload. The search for a solution to this problem is one of the motivations behind the PM3 (Modular Multi-Mission Platform) project. Various partners participate in this project, including the National Research Council (CNR), the Campania Aerospace District (DAC), and other national universities and industries. The project aims to develop a CubeSat capable to perform a mission along the Earth's orbit.

My Ph.D. work, in collaboration with CNR, involved the study and development of a secondary propulsion system that could be used in a CubeSat. Given the nanosatellite's small payload capacity, we assumed that we can not equip it with a conventional propulsion system but we can induce propulsion remotely, using a nearby orbiting mother satellite as a control platform. For this reason, it is necessary to study and apply a type of propulsion that allows remote control; the propulsion systems that can ensure these peculiarities are optical-type systems. In general, optical propulsion systems use the interaction between photons and satellite structure either directly, or through the activation of propellant to induce propulsion. Optical thrusters usually have low force and specific impulse parameters compared to other systems since the momentum associated with the photon is very low; however, the phenomena underlying the propulsion can be induced directly by laser or solar radiation, thus making remote activation possible. In general, optical thrusters exploit some phenomena typical of electromagnetic waves to induce forces:

- 1) momentum exchange between a photon and a rigid body, a phenomenon typical of solar sails, which has low propulsion and high specific impulse, but requires a large footprint;
- 2) ablation that is a phenomenon that uses the power of a laser to induce vaporization on a propellant that is ejected due to the pressure induced by the laser itself. Laser ablation thrusters have good values of thrust and specific impulse and also dimensions suitable for loading a CubeSat; however, they have low long-term stability that is likely to impair the ability to maneuver a CubeSat in the long term;
- 3) the gradient force, a phenomenon that exploits a spatially variable electromagnetic field distribution to induce a force capable of ejecting

nanoparticles acting as propellant. This phenomenon requires amplification of the EM field to have effects for propulsion; for this reason, the optical force is combined with a radiation-matter interaction effect to amplify the distribution and obtain thrust and specific impulse values that can be used for practical applications. Such systems have reduced performance compared with other optical systems, but they have small dimensions and excellent precision, and characteristics that make them extremely interesting as secondary propulsion systems in nanosatellites.

In analyzing the various optical propulsion systems found in the literature, our focus is on the gradient force phenomenon. In particular, we analyzed propulsion systems that exploit plasmonic phenomena to generate EM field distributions for inducing sufficiently intense and extremely concentrated forces. The phenomenon that gives rise to the generation of surface plasmonics is based on the radiation-matter interaction between an electromagnetic wave which invests an interface between a metallic medium and a dielectric medium. The plasmonic interaction results in a strongly localized amplification of the electric field that, when properly controlled, implies a very intense and localized optical force near the interface. Plasmonic phenomena are of two types: surface plasmon polaritons (SPPs) and localized surface plasmon (LSPs). SPPs are waves that propagate along the dielectric-metal interface, while LSPs are localized phenomena that occur in the near-field region of a metal nanostructure immersed in a dielectric medium. These phenomena have different modes of excitation and several characteristics that can be coupled to generate an asymmetric field distribution inducing propulsion on nanoparticles. In particular, it is possible to generate an LSP from a plasmonic dimer and make this as a near-field source for the excitation of a set of SPPs. Constructive interference between SPPs leads to the formation of a spatially asymmetric field distribution and thus potentially inducing an optical force on an external body. With this premise, we designed a device capable to induce an optical force useful for the displacement of a macroscopic object. We, therefore, began the study of two nanostructures presented in the literature:

- 1) The "optical nanocannon," [1] which is a V-shaped structure carved out of a gold film laid on a dielectric substrate capable of inducing a strongly asymmetric electric field along its height, generated by coupling the LSP formed at the bottom of the structure with the SPPs formed on its edges. The nanocannon generates an optical force capable of ejecting small nanoparticles at high speed; however, the size and the shape of the device do not allow to reach thrust values sufficient to induce macroscopic displacements and aren't thus useful for application to a nanosatellite.
- 2) trapezoidal constant-gap planar nanostructures [2], which are devices consisting of two gold-based trapezoidal prisms deposited on a glass substrate that generates an asymmetric EM field distribution by coupling the LSP formed in the gap between the structures with the SPPs that are triggered on the edges of the trapezoids. The optical force generated by the

device is not high, but the geometrical configuration is such that a large number of elementary structures can be coupled in an array configuration amplifying the force effects and the exit velocity of the ejected nanoparticles. This configuration has limitations related to the particular spatial distribution of the force field that generates potential barriers limiting the motion of the nanoparticles.

The Ph.D. thesis work was focused on the design of an original structure that is a synthesis of the two solutions found in the literature. It consists of an elementary cell composed of two trapezoidal gold structures deposited on a dielectric substrate and defined in such a way to form a v-shaped gap. The elementary cell, so defined, can be replicated in an array configuration to amplify the nanoparticle's exit velocity, and hence the thrust. In this way, a periodic force distribution is generated that leads to the amplification of the final nanoparticle velocity and, in addition, the shape of the gap of the elementary cell, which has a variable width, results in a strong reduction of the potential barrier that opposes the ejection of the nanoparticles. In this way, the nanoparticles can be ejected at high speed generating a significant boost for our application. The analysis of the new device and verification of its performances conducted using simulations based on the finite element method (FEM), implemented using COMSOL Multiphysics software. Thus, we were able to evaluate the characteristics of the EM field distribution generated by the designed device, and how this field distribution varies as the geometry of the device changes. The proposed device changes its characteristics and performances as a function of variation in the geometrical parameters of the structure (major base, height, angle, gap, thickness of the gold film), modifying the distribution of the generated electric field and resonance wavelength. Once the optimization step was completed, we studied the induced dynamics on different types of nanoparticles to assess whether the estimated velocity is comparable to typical values for a secondary propulsion system. In addition, we analyzed and studied other forms of array configuration, evaluating the hypothesis of a circular array. For such a configuration, we observed that due to the properties of the induced motion, higher velocity values can be obtained with a significant decrease in the size of the whole system. Finally, based on the positive results obtained from the simulations, we moved, in collaboration with the Dutch foundry Nanophab (<https://www.nanophab.com>), to the fabrication of the first set of prototype devices. The technology process used exploits the electron beam lithography step and lift-off. The research activity is continuing with the characterization of the fabricated devices and experimental verification of the plasmonic resonance characteristics.

## Summary of the thesis

The objective of this thesis work is to design, simulate, fabricate, and characterize a family of plasmonic devices capable of inducing propulsion on a population of nanoparticles.

In Chapter 1, the main propulsion methods used for satellite movements are presented in detail, focalizing chemical and electrical propulsion, and specifying the reasons why they cannot be used within a CubeSat. In addition, the main characteristics of optical thrusters are discussed, especially their ability to be remotely controlled, and the reasons why we selected plasmonic thrusters as suitable devices for use in secondary propulsion systems for the CubeSat.

In Chapter 2, the basic concepts of the phenomenon behind plasmonic propulsion, namely surface plasmons, are presented. We analyze how the electromagnetic field acts within metals and at the interface between metallic and dielectric materials, and we discuss in detail the formation and characteristics of surface plasmons.

In Chapter 3, we present the numerical tool at the basis of the study of plasmonic optical thrusters analyzed, namely the finite element method. We show how COMSOL Multiphysics software is able, mediated by FEM techniques, to compute an approximate solution of a differential problem describing one or more physical phenomena at the origin of the operation of plasmonic devices. In particular, we have addressed the different stages of constructing a FEM model, starting with the definition of the mesh, i.e., the subdivision of the physical domain of the definition of the differential problem, which is fundamental for the development of the solution of the problem itself. The basic types of mesh are discussed and also some methods for refining and modeling the mesh depending on the physical problem are presented. Finally, we analyze the solvers present in COMSOL, with special attention to their main characteristics and adaptability according to the physical problem considered.

In Chapter 4, we present some applications of plasmonics, including optical tweezers that exploit optical forces to constrain in a static or dynamic equilibrium a nanoparticle, and other devices that can induce propulsion by optical forces, such as the aforementioned optical nanocannon and constant gap trapezoidal systems. Once we have discussed their main characteristics and application limitations, highlighted by the analysis of their operation, we study original solutions to produce a suitable performance for the secondary propulsion of a nanosatellite. A new prototype device is designed and analyzed using FEM simulations, and an in-depth study of its performance is made as the geometrical parameters of the elementary cell change. Next, we show the dynamic characteristics of the system in a linear array configuration and present a new circular array configuration, which allows further increases in the final velocity of the ejected nanoparticles.

In Chapter 5, we present a method to control the dynamics of nanoparticle output. In particular, we observe that starting from the coupling of the photon helicity (spin) with the angular momentum of the evanescent wave, a transverse, incident-polarization-dependent momentum is generated that will change the nanoparticle exit trajectories making the process fully controllable.

Finally, in Chapter 6, we present the technological process for the fabrication of the demonstrator prototype, analyzing in detail all its subsequent steps. In addition, morphological characterizations of the fabricated prototype, carried out using an atomic force microscope (AFM) and a scanning electron microscope

(SEM), are illustrated and discussed. Afterward, some results from the optical characterization of the sample obtained with coherent light illumination are also presented to evaluate the field re-emitted by the plasmonic structure and the resonance wavelength obtained, verifying the agreement with the simulations carried out.

# Chapter 1

## Overview of Propulsion Technologies

A propulsion system is the primary mobility system of a spacecraft and helps with various maneuvering operations like orbit changing and station keeping. A key parameter that differentiates a propulsion system is its dependence on onboard power. Accordingly, propulsion systems can be classified into non-electric and electric systems[3, 4, 5, 6, 7]. The non-electric propulsion system can be classified into cold gas, liquid, and solid rocket system and require on-board power only to regulate (initiate and terminate) the propulsion process, while the electric propulsion systems are mainly classified into resistojet, electrospray, ion, Hall, and pulsed plasma systems and they actively require on-board power for their operation. Some important performance factors for any propulsion system are outlined[8][3]: thrust ( $\tau$ ), specific impulse ( $I_{sp}$ ), effective exit velocity ( $v_e$ ), and delta-v ( $\Delta v$ ).

The thrust generated is a combination of momentum thrust and pressure thrust as shown:

$$\tau = \dot{m}v_e + (P_e + P_a)A_e \quad (1.1)$$

Momentum thrust depends on the mass flow rate  $\dot{m}$  of propellant and the exit velocity  $v_e$  while pressure thrust, on the other hand, is a function of exit area ( $A_e$ ), exit pressure ( $P_e$ ) and ambient pressure ( $P_a$ ). The ambient pressure for the case of a spacecraft propulsion system is approximated to zero due to vacuum conditions in space. Specific impulse is the impulse generated per unit weight (at sea level) of propellant as shown:

$$I_{sp} = \frac{\tau}{\dot{m}g_0} \quad (1.2)$$

this is dependent on the thrust generated and mass flow rate of the propellant ( $\dot{m}$ ). Exit velocity is the velocity of the propellant at the exit region of the nozzle as shown:

$$v_e = g_0 I_{sp} \quad (1.3)$$

this depends on the specific impulse and the acceleration due to gravity at sea level ( $g_0$ ).

The delta-v is obtained from the Tsiolkovsky Rocket Equation that relates the exit velocity of a spacecraft to its initial ( $m_i$ ) and final ( $m_f$ ) masses, as shown:

$$\Delta v = v_e \ln \frac{m_i}{m_f} \quad (1.4)$$

we can use this basic concept for the description of the fundamental properties of some type of propulsion mechanism.

## 1.1 Chemical Thruster

### Cold Gas Propulsion (CGP) System

A cold gas propulsion system [3][9][10] relies on the process of controlled ejection of compressed liquid or gaseous propellants to generate thrust. Due to the absence of a combustion process, a CGP system requires only one propellant (without an oxidizer), and hence can be designed with minimum complexity. The schematic of a typical CGP system is shown in fig.1.1 and the main components include propellant storage and a nozzle. The simpler design of a CGP system leads to a smaller system mass and lower power requirement for regulation purposes. However, these advantages come at the cost of a monotonically decreasing thrust profile over a time frame. The thrust produced is directly proportional to the pressure of the propellant inside the tank and throughout the mission, tank pressure decreased resulting in a decrease in the maximum thrust that is generated by the system [3]:

$$I_{sp} = \frac{\gamma C^*}{g_0} \sqrt{\frac{2}{\gamma-1} \left(\frac{2}{\gamma-1}\right)^{\frac{\gamma+1}{\gamma-1}} \left(1 - \frac{P_e}{P_c}\right)} \quad (1.5)$$

The specific impulse of a CGP system mainly depends on the exit-to-chamber pressure ( $P_e/P_c$ ) and characteristic velocity  $C^*$ . The exit-to-chamber pressure is related to the expansion of the propellant, while at Poisson constant ( $\gamma$ ) is the ratio of specific heats at constant pressure and constant volume. Exit velocity is another important performance factor that not only depends on the exit-to-chamber-pressure but also the chamber temperature ( $T_c$ ) as shown[3]:

$$v_e = \sqrt{\frac{2\gamma T_c}{\gamma-1} \left(1 - \frac{P_e}{P_c}\right)} \quad (1.6)$$

A cold gas propulsion system use can either liquid or gaseous propellant; however, using a liquid propellant will lead to a reduction in the storage volume. The propellant selected should have high-density  $I_{sp}$  to increase the longevity of the onboard propellant.

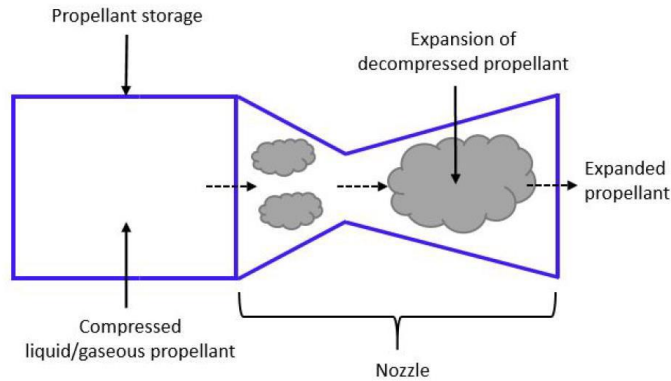


Figure 1.1: Sketch of a Cold Gas Propulsion System. Image reproduced by [3]

## Liquid Propulsion (LP) System

In a liquid propulsion system[3][11][12], thrust is generated by ejecting the gases formed during the process of combustion of liquid propellant. Depending on the mission requirements, a spacecraft can have an LP system with one (mono) or two (bi) propellants. Mono-propellant LP system makes use of a catalyst to decompose the propellant and generate thrust. The decomposition process takes place when the propellant is injected into the combustion chamber through the catalyst bed[13][8]. A bi-propellant LP system, on the other hand, comprises

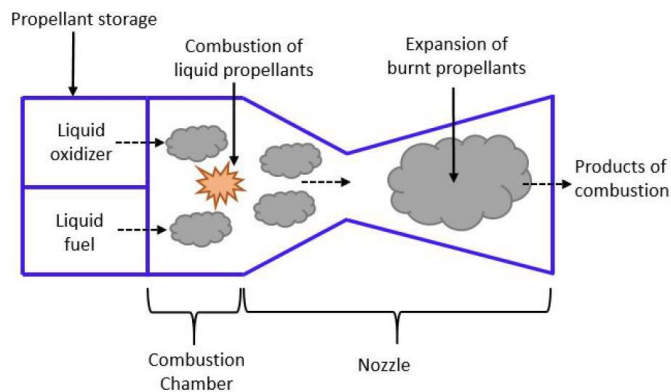


Figure 1.2: Sketch of a Liquid Gas Propulsion System. Image reproduced by [3]

both an oxidizer and fuel. Either LP system has primarily been used on larger satellites for high  $\Delta v$  operation and a single propellant is typically used for

low  $\Delta v$  operations. The schematic of a bi-propellant LP system is shown in fig.1.2 and it primarily consists of a combustion chamber, nozzle, and propellant storage for both oxidizer and fuel. The thrust and the specific impulse of an LP system can be obtained from the eq.1.1 and eq.1.2 respectively. The exit velocity of an LP system, like a CGP system, is dependent on the exit-to-chamber-pressure-ratio ( $P_e/P_c$ ) and combustion chamber temperature  $T_c$ [8][3]:

$$v_e = \text{sqr}t \frac{2\gamma}{\gamma - 1} RT_c [1 - (\frac{P_e}{P_c})^{\frac{\gamma-1}{\gamma}}] \quad (1.7)$$

where  $\gamma$  is the Poisson constant and  $R$  is the universal gas constant.

### Solid Rocket Propulsion (SRP) System

A solid rocket propulsion system [14][15][16] works on the principle of burning solid propellants and generating thrust by ejecting the gases formed during combustion. Similar to an LP bi-propellant system, an oxidizer is used in the SRP system. However, it differs from an LP system in a couple of ways: first, the solid propellant is stored within the combustion chamber itself; second, the sloshing effect seen in the LP system is absent because both fuel and oxidizer are solid. Although SRP systems do not experience sloshing, the lack of control over propellant burn rate creates difficulty for thrust regulation. The schematic of the SRP system is shown in fig.1.3 and comprises a combustion chamber that holds the solid propellant, an igniter that initiates the combustion process, and a nozzle[8][3]. Considering that thrust regulation is difficult in the SRP system,

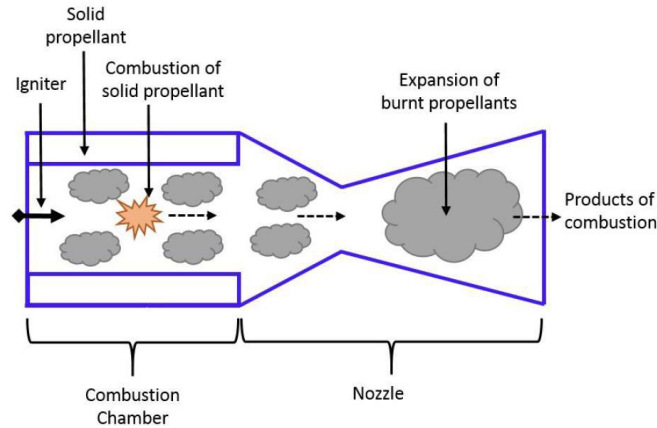


Figure 1.3: Sketch of a Solid Rocket Propulsion System. Image reproduced by [3]

burn rate can be used in the initial phase of the system design. The burn rate allows us to understand the combustion process because it governs the mass

flow rate of hot gases generated during the combustion. The burn rate ( $r$ ) can be expressed by the equation:

$$r = aP_c^n \quad (1.8)$$

is dependent on the chamber pressure ( $P_c$ ), temperature coefficient ( $a$ ) and combustion index ( $n$ ). The temperature coefficient is a non-dimensional empirical constant, while the combustion index describes the influence of chamber pressure on the burn rate.

## 1.2 Electric Thruster

### Resistojet

In a resistojets[17][18][19][3], the propellant is passed through a heat exchanger (or heating element) where it is super-heated and ejected through an expansion nozzle. The heating process reduces the gas (propellant) flow rate from a given upstream pressure through a given nozzle area, thus leading to the increase in the specific impulse that is proportional to the square root of temperature. The working principle of a resistojets is similar to that of a CGP system except that the propellant is heated before the expansion process. Because of the propellant's high energy (gained by heating), an exhaust velocity much greater than the CGP velocity is achieved in the resistojets. The exit velocity of the micro

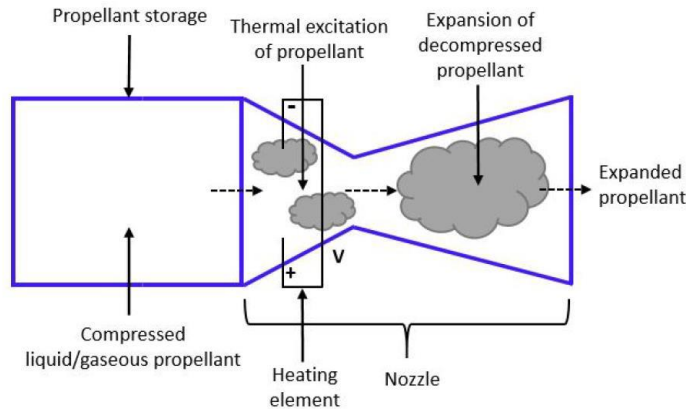


Figure 1.4: Sketch of a Resistojet Propulsion System. Image reproduced by [3]

CGP system ranges between approximately 300 – 700 m/s [20], while those of micro resistojets are approximately 2.2 km/s [21]. A major drawback of resistojets is that their performance ( $\tau, I_{sp}$ ) is limited by the melting temperature of the heating element used. In addition, power and thermal losses during the heating of the elements contribute to the inefficiency of the resistojets. The schematic of a resistojets propulsion is shown in Fig.1.4, and the main component includes

propellant storage, heating element, and nozzle[22]. The thrust produced by the propellant is shown in the equation:

$$\tau = A_0 \left( \frac{n_0 k_B T_0}{2} \right) \chi \quad (1.9)$$

depends on stagnation number density of propellant  $n_0$  in  $\text{m}^{-3}$ , stagnation temperature  $T_0$  and the probability ( $\chi$ ) of molecule exiting the expansion slot area ( $A_0$ ). Specific impulse is shown in the equation:

$$I_{sp} = \sqrt{\frac{\pi k_B T_0}{2m}} \frac{1}{g_0} \quad (1.10)$$

where  $k_B$  is the Boltzmann constant and  $g_0$  is the acceleration due to gravity at sea level.

### Radio-Frequency Ion Thruster (RIT)

Radio Frequency Ion thrusters[23][24][25] belong to a subset of gridded ion thrusters that generate thrust by accelerating the ionized propellant (plasma) through an electrostatic grid. In RITs, the stored propellant is let into the discharge chamber where it is ionized and becomes plasma through Radio Frequency (RF) power (from RF coils). The ionized propellant is then extracted from the discharge chamber and accelerated by a series of grids (ion optics) called screen and accelerator grids[26]. The screen grid extracts propellant

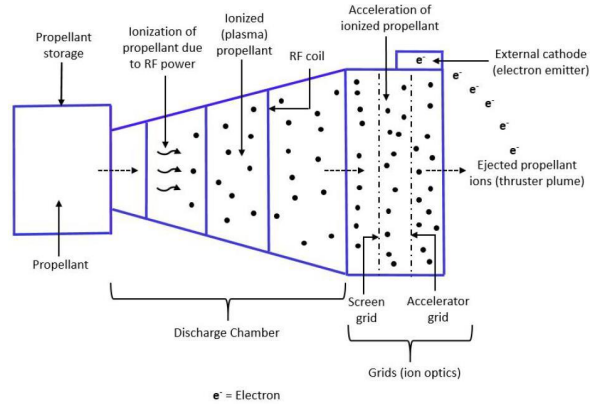


Figure 1.5: Sketch of a Radio-Frequency Ion Propulsion System. Image reproduced by [3]

cations from the ionized plasma and directs them to the exterior of the thruster in all ion engines, providing electrons to neutralize the ionized propellant that is emitted from the thruster. The specific impulse of a gridded thruster can

be varied by changing the voltage that is applied to the accelerating grid. The schematic of an RF ion propulsion system is shown in fig.1.5 which includes the propellant storage, RF coil, discharge chamber, and neutralizing cathode. Ion thrusters are characterized by high thruster efficiency resulting in high specific impulse (from 2000 s to 10000 s)[26]; however, they have been plagued with issues that are caused by cathode wear and contamination over prolonged usage. The performance factor of ion engines are[26][3]:

$$\tau = \sqrt{\frac{2m_{ion}V_i}{q}} I_i \quad I_{sp} = 1.417 \times 10^3 \gamma_c \eta_m \sqrt{\frac{V_i}{m_{ion}}} \quad (1.11)$$

where  $\eta_m$  is the thruster mass utilization efficiency and  $\gamma_c$  is the total thrust correction factor. The thrust is a function of the charge of the propellant ion, mass propellant ion  $m_{ion}$ , and ion accelerating voltage  $V_i$ . Ion engines use heavier elements (elements with higher atomic mass) as propellants because the thrust generated is proportional to the ion beam current ( $I_i$ ). Specific impulse is a function of ion accelerating voltage and mass of the ion.

## Hall thruster

Hall thrusters[26][27][28] are electrostatic devices that generated thrust by first ionizing and then accelerating the propellant in a mutually perpendicular electric and magnetic field. These thrusters work on the principle of the Hall effect that states the following[29]: when the electric current is applied to a conductive material (propellant) placed in a mutually perpendicular electric and magnetic field and formed a potential difference from the field that accelerated the propellant. The schematic of a Hall thruster is shown in fig.1.6 which includes

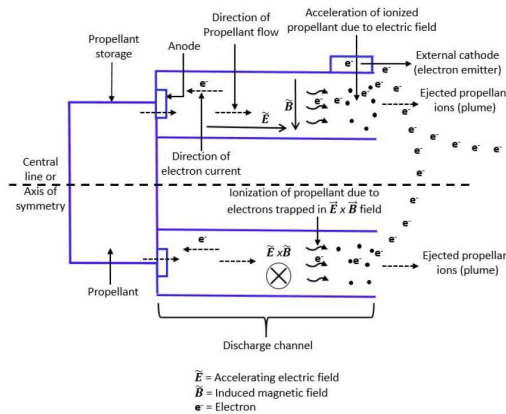


Figure 1.6: Sketch of a Hall Propulsion System. Image reproduced by [3]

propellant storage, discharge channel, external cathode, anodes, and the magnetic field generator. The applied magnetic field is radial, while the accelerating

electric field (acting from the anode towards the cathode) is axial. Note that the Hall thruster, unlike the gridded ion thruster, does not have a grid system, instead the grids are replaced by a strong magnetic field perpendicular to the flow of ions. The magnetic fields reduce the mobility of electrons coming from the external cathode, thereby restraining many advantageous features like a high specific impulse, higher thrust density, and simplicity in design[30]. However, they also face some challenges with the erosion of magnetic circuitry due to discharge plasma and lower efficiency[31]. The performance factor for Hall thrusters like thrust and specific impulse is the same as the RIT's parameters.

## Electrospray thruster

An Electrospray thruster[32] is a plasma-free electric propulsion system that works on the principle of electrostatic extraction and acceleration of charged particles (ions) from liquid (propellant) surfaces to produce thrust. Their fundamental working mechanism is based on a process by which the conductive liquid surface of the propellant is deformed into a sharp cone-shaped meniscus called a Taylor cone[33][34][35]; when a certain threshold of the electric potential is surpassed, ions are extracted from the cone's apex. Electrospray thrusters accelerate positive or negative ions, respectively generating either positive or negative ion beams, thereby eliminating the need for an external cathode to neutralize the ejected ions, unlike in plasma propulsion devices where an external cathode is essential[32]. The propellant used for electrospray thrusters is usually ionic liquid, and their negligible vapor pressure serves as an advantage by resolving the need for propellant pressurization and helps with system miniaturization. The schematic of an electrospray propulsion system is shown in fig.1.7, and the major components comprise propellant storage, emitter, and extractor electrode. The performance of an electrospray thruster can be varied by changing the voltage passed through the emitter and the extractor electrodes. In an electrospray thruster, the mass-to-charge ratio plays an important role in determining the exit velocity and thrust. The underlying mathematical relations summarizing the relationship are given below[36][3]:

$$\left\langle \frac{q}{m_{ion}} \right\rangle = \frac{1}{\rho Q} \quad (1.12)$$

$$v_{ie} = \sqrt{2V_i I_i \left\langle \frac{q}{m_{ion}} \right\rangle} \quad (1.13)$$

$$\tau = \dot{m}_{ion} v_{ei} \quad (1.14)$$

The average mass-to-charge ratio  $\left\langle \frac{q}{m_{ion}} \right\rangle$  is inversely proportional to the density  $\rho$  of the propellant ion/droplet and the volume flow rate (Q) of ion/droplet. The exit velocity is a function of the square root of ion accelerating voltage ( $V_i$ ), ion beam current ( $I_i$ ), and average mass-to-charge-ratio. The thrust is a function of ion accelerating voltage, ion beam current, and mass flow rate of ions ( $\dot{m}_{ion}$ ).

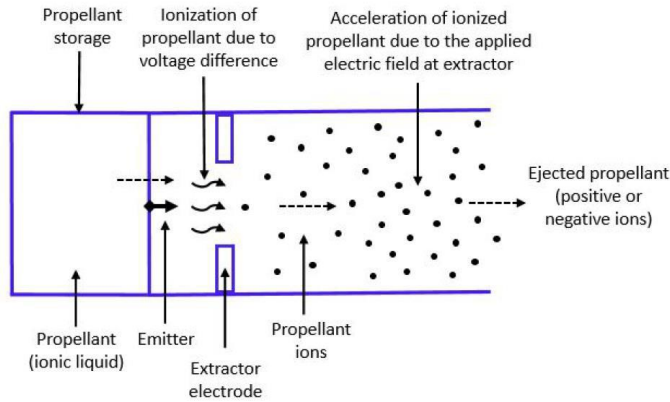


Figure 1.7: Sketch of a Electro Spray Propulsion System. Image reproduced by [3]

## Pulsed Plasma Thruster

Pulsed Plasma Thrusters (PPT)[37][38][39] operate by creating a pulsed, high-current discharge across the exposed surface of a solid insulator that serves as a propellant. The arc discharge ablates the propellant material from its surface, thereby ionizing and accelerating the propellant at high speeds. A current pulse lasting a few microseconds is generally driven by a capacitor that is charged and discharged approximately once every second[40]. The schematic of PPT is shown in fig.1.8 containing a spring-loaded mechanism, propellant, capacitor, anode, cathode, and acceleration chamber. During the process of propulsion, the spring feeds the propellant (usually solid) between two electrodes, and the spark plug is simultaneously fired to raise the electrical conductivity of the acceleration chamber. The electric current from the Power Processing Unit (PPU) flows to the electrodes through the capacitor and then into the arc, thereby completing a current loop and simultaneously generating a magnetic field. The electric arc generated ablates the propellant and ionized plasma is created. The plasma is then accelerated due to Lorentz force generated by the electric arc and the induced magnetic field. The advantages of a PPT are its ability to provide small impulse bits for precision maneuvering, robustness by programming impulse bits to cater to mission needs, design simplicity owing to its ability to use a large variety of propellants, and its ability to maintain constant specific impulse and efficiency over a wide range of input power levels. However, these advantages come at the cost of issues that result due to electron erosion, the presence of macro-particle in plumes due to non-uniform ablation, and very low thruster efficiency[37][38]. The exit velocity and the thruster of a PPT can be obtained

from this equation[41]:

$$\tau = m_{ion} \frac{dv_i}{dt} = q(\mathbf{E} + \mathbf{v}_i \times \mathbf{B}) + \sum (P_i)_k \quad (1.15)$$

$$v_e = \frac{\tau}{\eta 4\pi} = \frac{\mu_0}{\eta 4\pi} \ln\left(\frac{R_a}{R_c}\right) \quad (1.16)$$

The thrust produced is calculated from the law of conservation of momentum. For any electric thruster, Lorentz force describes the relationship between the force (thrust) produced due to charged particles moving through a self-induced magnetic field. Thrust production also depends on the charge of ions ( $q$ ), the sum of all collision forces per particle (propellant) over all particles, and the particle velocity. The effective exit velocity of the ionized propellant is a function of the thrust generated and the mass flow rate of propellant efficiency. Effective exit velocity can also be calculated in terms of the radius of the anode and the radius of the cathode. The specific impulse of a PPT can be obtained from the equation eq.1.2.

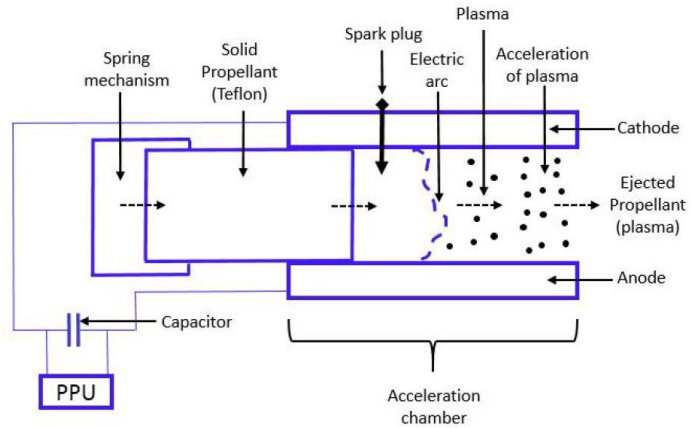


Figure 1.8: Sketch of a Pulsed Plasma Propulsion System. Image reproduced by [3]

### 1.3 Optical Thruster

The propulsion systems analyzed (electric thrusters and chemical thrusters) are suitable for moving large objects. Satellites can accommodate the propellants and the power required to activate these systems. However, this work aims to implement a propulsion system on a nanosatellite known as CubeSat[5][42][43]. CubeSat is a very small satellite in which 1U of CubeSat has 10 cm<sup>3</sup> of volume and reaches 1 kg of mass. Since its early development and use as a university training tool, CubeSat has been increasingly developed for commercial and military purposes and NASA science missions. The decreasing size of technology,

combined with increased capabilities of components used, and the low cost of developing, building, and launching, has led to a proposal for more demanding CubeSat missions. Proposed missions include low-cost technology demonstration missions, formation flying missions that consist of swarms of CubeSat, and inspection satellites that can approach larger satellites already in orbit. Given the small size required for a propulsion system to fit inside a CubeSat, it is assumed that a remotely induced propulsion system (and thus without onboard power) is suitable for moving the nanosatellite. Therefore, our research has shifted to the study of optical propulsion systems. The optical thruster[44] is different from the chemical and electric propulsion system because the thrust is induced by the direct action of light and can not require any onboard power system. In this section, we will review some optical propulsion systems already in use and their characteristics.

## Solar Sail

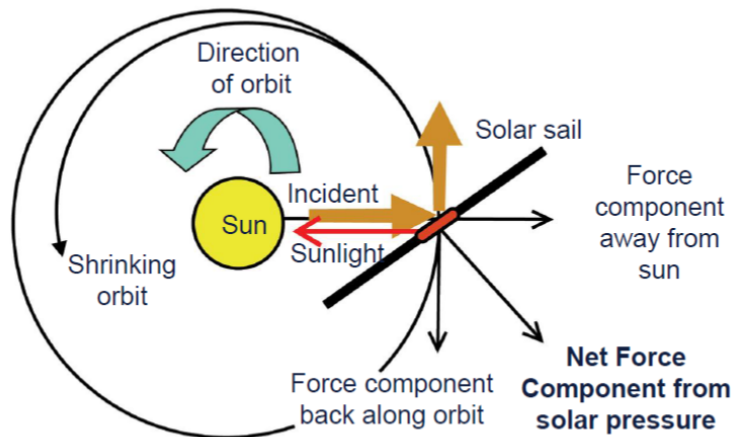


Figure 1.9: Sketch of a Solar Sail Propulsion System

A solar sail is a form of propellant-less spacecraft system that generates thrust through momentum change due to the incoming solar radiation. Solar sails ( sketch in fig.1.9)[45][46][47] have a flat surface and are usually made of thin reflective material supported by a lightweight deployable structure[48]. As they do not use a propellant, solar sails by definition possess infinite specific impulse. However, the main drawback of a solar sail is its very low thrust levels, resulting in a long time to gain appreciable momentum change. A generated force vector ( $\mathbf{f}_{srp}$ ) on a solar sail is a function of the solar radiation pressure ( $P$ ), the surface area of the sail ( $A$ ), and angle of attack ( $\alpha$ ). Accordingly, the

acceleration is obtained from Newton's Second Law as described below[3][49]:

$$a_{srp} = \frac{f_{srp}}{m} = \frac{2PA \cos^2(\alpha) \mathbf{n}}{m_s} \quad (1.17)$$

where  $\mathbf{n}$  is the sail normal vector and  $m_s$  is the mass of spacecraft.

## Laser Ablation Thruster

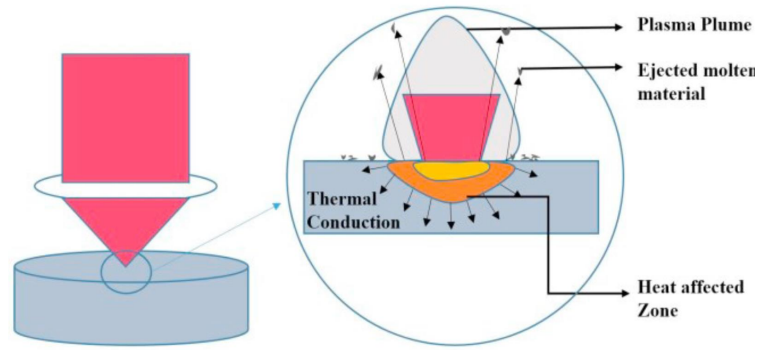


Figure 1.10: Sketch of a Laser Ablation Propulsion System. Image adapted from [50]

A laser ablation thruster[51][52] is an optical propulsion system in which the thrust is induced by vaporizing a solid propellant and ejecting the gaseous propellant with the high pressure generated by the laser beam incidence. The general mechanism of the laser ablation is shown in fig.1.10[50]. When a focused laser beam strikes a surface, the electrons present in the substrate are excited by the laser photons. This excitation results in the generation of heat due to the absorption of photon energy, which is consistent with Beer Lambert's law. Beer Lambert's law states that the amount of light absorbed is dependent on the thickness of the material and intensity of the light source in this manner:

$$A = \epsilon l c \quad (1.18)$$

where  $A$  is the optical absorbance,  $\epsilon$  is the molar attenuator coefficient,  $l$  is the optical path length and  $c$  is the molar concentration. The heating effect causes melting or vaporization of the material, thus resulting in the removal of macroscopic material from the substrate. The transition from solid to gas results in the formation of a plasma plume. The temperature further increases due to incoming pulses and the melt pool reach the vaporization state. High pressure is created during vaporization, which is also called recoil pressure,

which pushes molten materials from the pool where it is ejected. Based on the properties of the laser and of the material such as fluence, absorption coefficient, reflectivity, wavelength, and pulse duration, the ablation mechanism can be purely chemical, thermal, or a combination of both. The typical  $I_{sp}$  of laser ablation propulsion is in the range of 200 – 3000 s [53]. The thrust density is on the order of  $8 \times 10^5$  N/m<sup>2</sup> because the thrust arises on a spot with an area equal to a focused laser beam. Remote thrust generation is a unique and clear advantage of this technique. It has the potential to achieve significant mass reduction and improved payload capability. The use of solid propellant alleviates problems in propellant storage. The thrust is roughly proportional to laser power. Therefore the system size can be scalable to a required thrust. Despite these advantages, laser ablation propulsion systems have some challenges. In particular, the stability of the lasers is easily compromised in long-term travel, and the system requires large amounts of propellant and onboard power. For this reason, the laser ablation propulsion system is not yet used for practical applications.

## Plasmonic Propulsion System

In addition to ablation and the direct incidence with photons (a solar sail), there is another way to use optical forces to induce propulsion. Specifically, it is possible to design a propulsion system that uses the gradient generated by an electromagnetic field to induce an optical force and achieve propulsion. Plasmonic propulsion[2] (an example in fig.1.11) uses the interaction between an electromagnetic wave and the metal-dielectric interface to generate strongly amplified electric fields that can be tuned to have asymmetric spatial distributions. The asymmetry of the field distribution leads to high gradients and thus optical forces which can induce propulsion on a nanoparticle. Given Newton's third law of motion, the ejection of large numbers of nanoparticles implies the displacement of a macroscopic object (e.g., a CubeSat). Plasmonic propulsion has characteristics useful for nanosatellite applications:

- 1) Like solar sails, plasmonic propulsion can not require onboard power, because we can generate the optical force with a remote laser on a mother satellite.
- 2) It does not have a large propellant usage (as in the case of laser ablation) because the nanoparticles used for displacement occupy a small space inside a nanosatellite's payload.
- 3) Compared to solar sails, it has a much smaller size and light intensities are highly concentrated favoring higher force values
- 4) Compared to other propulsion systems, it does not have large values of trust and specific impulse but is highly accurate and therefore useful for orbit corrections and small changes in trajectory

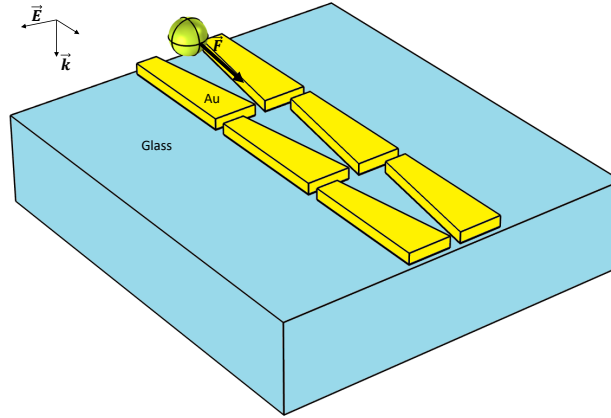


Figure 1.11: Sketch of a Plasmonic Propulsion System

Since the CubeSat dimension, we require a propulsion system remotely driven with a small size. In addition, we need that the propulsion induced has performance useful for trajectory correction and orbit displacement. For this reason, we need small power and good precision. Analyzing all the micro-propulsion systems and focalizing in the optical thrusters, because it is the only propulsion system where we can induce the force at distance, we consider the plasmonic thruster as a system suitable for a CubeSat propulsion system. In the next chapter, we discuss some of the basic principles of the surface plasmon phenomenon, necessary to design a plasmon device.

## Chapter 2

# Principles of Plasmonic Propulsion

The small size and lack of onboard power make some optical thrusters suitable for application in a CubeSat. Thus, the work aims to design an optical thruster that displaces nanoparticles through the space variation of the electric field distribution, i.e., a plasmonic thruster.

However, to build this device, it is necessary to analyze how the electromagnetic field induces a dynamic force and which optical phenomena can improve it. From the study of the electromagnetic field in vacuum and continuous media (Appendix A), the optical forces obtained do not have suitable values for particle displacement. However, the interaction between the electromagnetic field and a dispersive medium presents effects that have a great incidence in the induction of dynamic phenomena. In this chapter, we introduce the electromagnetic field in dispersive media to understand the basic principles of a plasmonic device.

### 2.1 Electromagnetism in dispersive media

In appendix A, we present the basic aspects of electromagnetism with special attention to some features of the induction of mechanical quantity by electromagnetic waves. To design an optical propulsion device, it is not possible to use electromagnetism in a vacuum because the force and energy parameters obtained turn out to have low-level performance. Therefore, it is necessary to study the radiation-matter interactions that allow the formation of phenomena that accumulate and amplify the electromagnetic field.

In this section, we analyze some electromagnetic behaviors in materials, with special emphasis on the case of metals, which will be the argument of the following paragraphs. Dielectric media exhibit behavior that is approximately independent of the wavelength of the incident beam. This is described by equations A.2a-A.2d and constitutive relations eq.A.4a-eq.A.4c considering dielectric permittivity as a constant[54].

Metals, on the other hand, exhibit characteristics that change depending on the frequency (or wavelength) of the incident beam. Three different behaviors of metals can be defined: for microwave and far-infrared, the metal behaves as a perfect conductor, that is, only an extremely small part of the electromagnetic field penetrates the material[55][56]. For near-infrared and visible spectrum the metal has dissipative behavior since the penetration of the electromagnetic field increases considerably. Finally, in ultraviolet, the electromagnetic field exhibits the same behavior as analyzed for dielectric media. To obtain dispersive properties we use the relationship between  $\mathbf{J}$  and  $\mathbf{E}$  (eq.A.4a). We can demonstrate that in metals it is possible to define a similar local relationship between  $\epsilon$  and  $\sigma$ . It is important to note, however, that eqs.A.4a and eq.A.4b have to be generalized for the metals; in particular, given their dispersive nature, the metal optical response depends on the light frequency. For this reason, the constitutive relation is rewritten in the following form[56]:

$$\mathbf{D}(\mathbf{r}, t) = \epsilon_0 \int dt' d\mathbf{r}' \epsilon(\mathbf{r} - \mathbf{r}', t - t') \mathbf{E}(\mathbf{r}', t') \quad (2.1a)$$

$$\mathbf{J}(\mathbf{r}, t) = \int dt' d\mathbf{r}' \sigma(\mathbf{r} - \mathbf{r}', t - t') \mathbf{E}(\mathbf{r}', t') \quad (2.1b)$$

We assume that all length scales are significantly larger concerning the lattice spacing of the material; this ensures homogeneity, i.e., the impulse response functions do not depend on absolute spatial and temporal coordinates, but only their differences. The homogeneity simplifies the eq.2.1a and eq.2.1b by taking the Fourier transform for  $\mathbf{k}$  and  $\omega$  and the convolution becomes a multiplication. This led to the constitutive relations in the Fourier domain

$$\mathbf{D}(\mathbf{k}, \omega) = \epsilon_0 \epsilon(\mathbf{k}, \omega) \mathbf{E}(\mathbf{k}, \omega) \quad (2.2a)$$

$$\mathbf{J}(\mathbf{k}, \omega) = \sigma(\mathbf{k}, \omega) \mathbf{E}(\mathbf{k}, \omega) \quad (2.2b)$$

Consider that in dielectric media exist a relation between  $\mathbf{D}$ ,  $\mathbf{J}$  and the polarization  $\mathbf{P}$ [56]:

$$\mathbf{D} = \epsilon_0 \mathbf{E} + \mathbf{P} \quad \mathbf{J} = \frac{d\mathbf{P}}{dt} \quad (2.3)$$

using this relation we define:

$$\epsilon(\mathbf{k}, \omega) = 1 + \frac{i\sigma(\mathbf{k}, \omega)}{\epsilon_0 \omega} \quad (2.4)$$

The general form of the dielectric response can be simplified to the limit of the local space, i.e.,  $\epsilon(\mathbf{k} = 0, \omega) = \epsilon(\omega)$ . This approximation is valid as long as the wavelength  $\lambda$  in the material is significantly greater than all characteristic dimensions, such as the size of the unit cell or the mean free path of the electrons[57][58]. In general  $\epsilon(\omega)$  and  $\sigma(\omega)$  are complex quantities in function of the angular frequency  $\omega$ .

The characteristics of dispersive media are also reflected in the analysis of the wave solutions obtained through Maxwell's equations[56]. Using eq.A.22 and leading the Fourier domain we obtain:

$$\mathbf{k}(\mathbf{k} \cdot \mathbf{E}) - k^2 \mathbf{E} = -\epsilon(\mathbf{k}, \omega) \frac{\omega^2}{c^2} \mathbf{E} \quad (2.5)$$

Two cases can be distinguished, depending on the polarization direction of the electric field vector. For transverse waves  $\mathbf{k} \cdot \mathbf{E} = 0$  yielding the generic dispersion relation

$$k^2 = \epsilon(\mathbf{k}, \omega) \frac{\omega^2}{c^2} \mathbf{E} \quad (2.6)$$

for longitudinal waves we obtain:

$$\epsilon(\mathbf{k}, \omega) = 0 \quad (2.7)$$

This implies that the longitudinal collective oscillation can only occur at frequencies corresponding to zeros of  $\epsilon(\omega)$ , this can be defined as a bulk plasmon.

## 2.2 Optical Response in metals

The optical properties of metals, over a wide frequency range, can be explained by a plasma model, where a gas of free electrons of number density  $n$  moves against a fixed background of positive ion cores[55][56]. In the plasma model, details of the lattice potential and electron-electron interactions are not taken into account; for this reason in alkali metal, this is a good approximation for the optical properties until the ultraviolet range while in the noble metals, this approach is limited by an interband transition in visible frequency. For the plasma model, the electrons oscillate in response to the applied electromagnetic field, and their motion is damped via collision occurring with a characteristic frequency  $\gamma = 1/\tau$ .  $\tau$  is known as the relaxation time of the free electron gas. We can write a simple equation of motion for an electron of the plasma sea subjected to an external field  $\mathbf{E}$ [57]:

$$m\ddot{\mathbf{x}} + m\gamma\dot{\mathbf{x}} = -e\mathbf{E} \quad (2.8)$$

If we assume a harmonic time dependence  $\mathbf{E}(t) = \mathbf{E}_0 e^{i\omega t}$  of the driving field, a particular solution of this equation describing the oscillation of the electron is  $\mathbf{x}(t) = \mathbf{x}_0 e^{-i\omega t}$ . The complex amplitude  $\mathbf{x}_0$  incorporates any phase shift between the driving field and response:

$$\mathbf{x}(t) = \frac{e}{m(\omega^2 + i\gamma\omega)} \mathbf{E}(t) \quad (2.9)$$

The displaced electrons contribute to the macroscopic polarization  $\mathbf{P} = -nex$  and in the constitutive relations  $\mathbf{D} = \epsilon_0 \mathbf{E} + \mathbf{P}$  obtaining:

$$\mathbf{D} = \epsilon_0 \left(1 - \frac{\omega_p^2}{\omega^2 + i\gamma\omega}\right) \mathbf{E} \quad (2.10)$$

where  $\omega_p = \frac{ne^2}{\epsilon_0 m}$  is the plasma frequency of the free electron gas. Therefore, we arrive at the dielectric function of the free electron gas:

$$\epsilon(\omega) = 1 - \frac{\omega_p^2}{\omega^2 + i\gamma\omega} \quad (2.11)$$

the real and imaginary components of this complex dielectric function are given by:

$$\epsilon_1(\omega) = 1 - \frac{\omega_p^2 \tau^2}{1 + \omega^2 \tau^2} \quad (2.12a)$$

$$\epsilon_2(\omega) = \frac{\omega_p^2 \tau}{\omega(1 + \omega^2 \tau^2)} \quad (2.12b)$$

It is useful to study the eq.2.12a-2.12b to observe the different regimes to the collision frequency  $\gamma$ . We limit only for  $\omega < \omega_p$ , where metals retain their metallic character. For large frequencies close to  $\omega_p$ , the product  $\omega\tau \gg 1$  leads to negligible damping. Here,  $\epsilon(\omega)$  is predominantly real, and:

$$\epsilon(\omega) = 1 - \frac{\omega_p^2}{\omega^2} \quad (2.13)$$

can be taken as the dielectric function of the undamped free electron plasma. However, the behavior of the noble metals [59] in this frequency region is completely altered by interband transitions, where electrons from the filled band below the Fermi surface are excited to a higher band. For low frequencies, i.e.,  $\omega \ll \tau^{-1}$ , hence  $\epsilon_2 \gg \epsilon_1$ , in this region, metals are mainly absorbing and we have a good conductor approximation. Finally the eq.2.13 related the optics response (see eq.2.4) with the metal conductivity in the Drude model[60]:

$$\sigma(\omega) = \frac{\sigma_0}{1 - i\omega\tau} \quad (2.14)$$

where  $\sigma_0 = \frac{ne^2}{m}$ .

In the previous paragraph, we observed that the energy induced by the electromagnetic field in continuous media is defined in the eq.A.12. However, in dispersive media  $\epsilon$  is complex and frequency-dependent and the eq.A.12 is not suitable.

For a monochromatic field, Landau and Lifshitz[61] have shown that the conservation law is valid also in dispersive media if  $u_E$  is replaced by an  $u_{eff}$  defined:

$$u_{eff} = \frac{1}{2} Re \left[ \frac{d(\omega\epsilon)}{d\omega} \right]_{\omega_0} \langle \mathbf{E}(\mathbf{r}, t) \cdot \mathbf{E}(\mathbf{r}, t) \rangle \quad (2.15)$$

where  $\langle \mathbf{E}(\mathbf{r}, t) \cdot \mathbf{E}(\mathbf{r}, t) \rangle$  is the field averaging over one optical cycle, and  $\omega_0$  is the frequency of interest. This expression is valid if  $\mathbf{E}$  is only appreciable in a narrow frequency range around  $\omega_0$  and the fields are slowly varying compared to a timescale  $1/\omega_0$ . In addition, it is assumed that  $|\epsilon_2| \ll |\epsilon_1|$  so that the absorption is small. In metal, the requirement of low absorption limits the validity for visible and near-infrared frequencies. Using the expression of the free

electron type dielectric function eq. 2.13 the typical form of the electromagnetic energy in metals is obtained:

$$u_{eff} = \frac{\epsilon_0}{4} \left( \epsilon_1 + \frac{2\omega\epsilon_2}{\gamma} \right) |\mathbf{E}|^2 \quad (2.16)$$

respect to the eq.2.15 an additional factor  $\frac{1}{2}$  is included due to an implicit assumption of harmonic time.

## 2.3 Surface Plasmon Polaritons

In the eq.2.7, we obtain a solution defined as "plasmon" from the optical properties of dispersive media. The plasmon solution represents the collective oscillations of the electrons of a metal at a certain frequency. The same phenomena can also occur in an interface between a metal surface and a dielectric; in this case, it is called a surface plasmon. Surface Plasmon Polaritons (SPPs) are the propagative surface plasmons. In this section we discuss the characteristics of SPPs; however, to define the properties of SPPs, we need to know how electromagnetic waves propagate within an interface.

As we have seen, Maxwell's equations lead to the wave equation defined to eq.A.22. If we assume a harmonic time dependence of  $\mathbf{E}(\mathbf{r}, t) = \mathbf{E}(\mathbf{r})e^{-i\omega t}$  of the electric field we obtain that the wave equation become[55][56]:

$$\nabla^2 \mathbf{E} + k_0^2 \epsilon \mathbf{E} = 0 \quad (2.17)$$

where  $k_0 = \frac{\omega}{c}$  is the wave vector of the propagation wave in a vacuum. This equation is known as the Helmholtz equation. For an interface solution, it

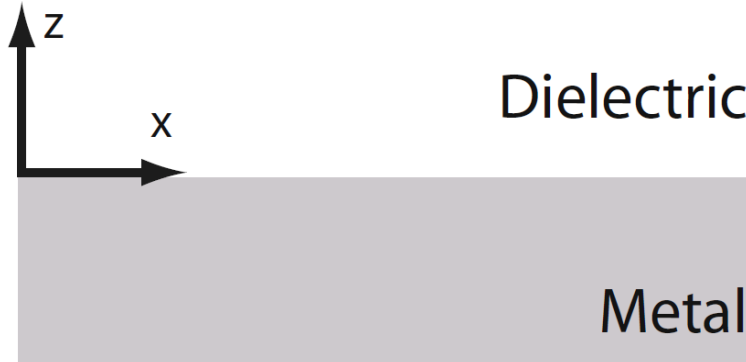


Figure 2.1: Geometry for SPP propagation at a single interface between a metal and a dielectric. Image reproduced by [55]

is necessary to define the wave propagation geometry[62]. In particular, we

consider a surface parallel to the  $xz$  plane (as in fig.2.1). We can assume for simplicity a case of a one-dimensional problem, i.e.,  $\epsilon$  depends only on one spatial coordinate. Specifically, if the waves propagate along the  $x$  direction of a Cartesian coordinate system, and show no spatial variation in the perpendicular ( $y$ -plane) direction therefore  $\epsilon = \epsilon(z)$ .

Applied to electromagnetic surface problems, the plane  $z = 0$  coincides with the interface sustaining the propagating waves, and the electric can be described as  $\mathbf{E}(x, y, z) = \mathbf{E}(z)e^{i\beta x}$ . The complex parameter  $\beta = k_x$  is called the propagation constant of the traveling waves and corresponds to the component of the wave vector in the direction of propagation. Inserting this expression into eq. 2.17 yields the following form of the wave equation[62]:

$$\frac{\partial^2 \mathbf{E}(z)}{\partial z^2} + (k_0^2 \epsilon - \beta^2) \mathbf{E} \quad (2.18)$$

A similar equation exists for the magnetic field  $\mathbf{H}$ . In order to use the wave equation to obtain the spatial field profile and dispersion of propagating waves, we need the explicit expression for different field components of  $\mathbf{E}$  and  $\mathbf{H}$  using the curl equation. However, we can use some approximation if considering a propagation along the  $x$ -direction  $\frac{\partial}{\partial x} = i\beta$  and homogeneity in the  $y$ -direction. It can be shown that the system allows two sets of self-consistent solutions with different polarization properties. The first set is the transverse magnetic (TM or p) modes, where only the field component  $E_x, E_z$  and  $H_y$  are non-zero, and the second set is the transverse electric (TE or s) modes, with  $H_x, H_z$  and  $E_y$  being nonzero. For TM modes, the system of governing equations reduces to:

$$\begin{aligned} E_x &= -i \frac{1}{\omega \epsilon_0 \epsilon} \frac{\partial H_y}{\partial z} \\ E_z &= -\frac{\beta}{\omega \epsilon_0 \epsilon} H_y \end{aligned} \quad (2.19)$$

and the wave equation for TM modes is:

$$\frac{\partial^2 H_y}{\partial z^2} + (k_0^2 \epsilon - \beta^2) H_y = 0 \quad (2.20)$$

For TE modes the analogous set is:

$$\begin{aligned} H_x &= i \frac{1}{\omega \mu_0} \frac{\partial E_y}{\partial z} \\ H_z &= \frac{\beta}{\omega \mu_0} E_y \end{aligned} \quad (2.21)$$

with TE wave equation:

$$\frac{\partial^2 E_y}{\partial z^2} + (k_0^2 \epsilon - \beta^2) E_y = 0 \quad (2.22)$$

Once we have determined the action of propagating waves in space, we can study the behavior of Surface Plasmon Polaritons[55]. The most simple geometry sustaining SPPs is a single flat interface between a dielectric, non-absorbing

half-space ( $z > 0$ ) with positive real dielectric constant  $\epsilon_2$  and an adjacent conducting half-space ( $z < 0$ ) described by a dielectric function  $\epsilon_1(\omega)$  (fig.2.1). The requirement of metallic character implies that  $Re[\epsilon_1(\omega)] < 0$ . The metals fulfilled this condition only frequencies below  $\omega_p$ . We want to observe the propagating wave solution confined to the interface.

Starting with the TM solutions. Using the equation set (2.19-2.20) in both half spaces yields:

$$\begin{aligned} H_y(z) &= A_2 e^{i\beta x} e^{-k_2 z} \\ E_x(z) &= iA_2 \frac{1}{\omega \epsilon_0 \epsilon_2} k_2 e^{i\beta x} e^{-k_2 z} \\ E_z(z) &= -A_2 \frac{\beta}{\omega \epsilon_0 \epsilon_2} e^{i\beta x} e^{-k_2 z} \end{aligned} \quad (2.23)$$

for  $z > 0$  and:

$$\begin{aligned} H_y(z) &= A_1 e^{i\beta x} e^{k_1 z} \\ E_x(z) &= -iA_1 \frac{1}{\omega \epsilon_0 \epsilon_1} k_1 e^{i\beta x} e^{k_1 z} \\ E_z(z) &= -A_1 \frac{\beta}{\omega \epsilon_0 \epsilon_1} e^{i\beta x} e^{k_1 z} \end{aligned} \quad (2.24)$$

for  $z < 0$ .  $k_i (i = 1, 2)$  is the component of the wave vector perpendicular to the interface in the two media. The reciprocal value,  $\hat{z} = 1/|k_z|$  defines the evanescent decay length of the field perpendicular to the interface, which quantifies the confinement of the wave. Continuity of  $H_y$  and  $\epsilon_i E_z$  at the interface requires that  $A_1 = A_2$  and:

$$\frac{k_2}{k_1} = -\frac{\epsilon_2}{\epsilon_1} \quad (2.25)$$

If we consider the previous convention in the exponent, the confinement to the surface demands  $Re[\epsilon_1] > 0$  if  $\epsilon_2 > 0$ , i.e., the surface waves exist only at the interface between materials with opposite sign in the real part of dielectric permittivity; in particular, between conductor and an insulator. The expression for  $H_y$  further has to fulfill the wave eq.2.20 yielding:

$$\begin{aligned} k_1^2 &= \beta^2 - k_0^2 \epsilon_1 \\ k_2^2 &= \beta^2 - k_0^2 \epsilon_2 \end{aligned} \quad (2.26)$$

Combining the eq. 2.25 and eq.2.26 we obtain the dispersion relation of SPPs propagating at the interface between the half-spaces:

$$\beta = k_0 \sqrt{\frac{\epsilon_1 \epsilon_2}{\epsilon_1 + \epsilon_2}} \quad (2.27)$$

This expression is valid for both real and complex  $\epsilon_1$ , i.e., for conductors without and with attenuation. Now, we analyze the situation for TE surface modes.

Using the eq.2.21, the respective expression for the field component is:

$$\begin{aligned}
E_y(z) &= A_2 e^{i\beta x} e^{-k_2 z} \\
H_x(z) &= -iA_2 \frac{1}{\omega\mu_0} k_2 e^{i\beta x} e^{-k_2 z} \\
H_z(z) &= A_2 \frac{\beta}{\omega\mu_0} e^{i\beta x} e^{-k_2 z}
\end{aligned} \tag{2.28}$$

for  $z > 0$  and:

$$\begin{aligned}
E_y(z) &= A_1 e^{i\beta x} e^{k_1 z} \\
H_x(z) &= iA_1 \frac{1}{\omega\mu_0} k_1 e^{i\beta x} e^{k_1 z} \\
H_z(z) &= A_1 \frac{\beta}{\omega\mu_0} e^{i\beta x} e^{k_1 z}
\end{aligned} \tag{2.29}$$

for  $z < 0$ . Continuity of  $E_y$  and  $H_x$  at the interface leads to the condition:

$$A_1(k_1 + k_2) = 0 \tag{2.30}$$

since confinement to the surface requires  $Re[k_1] > 0$  and  $Re[k_2] > 0$ , this condition is only fulfilled if  $A_1 = 0$ , so that also  $A_2 = A_1 = 0$ . Thus no surface modes exist for TE polarization. Surface Plasmon Polaritons exist only for TM polarization.

After the definition of the dispersion relation, we can examine the properties of the SPPs[55]. In fig.2.2 shown a plot of eq. 2.27 for a metal with negligible

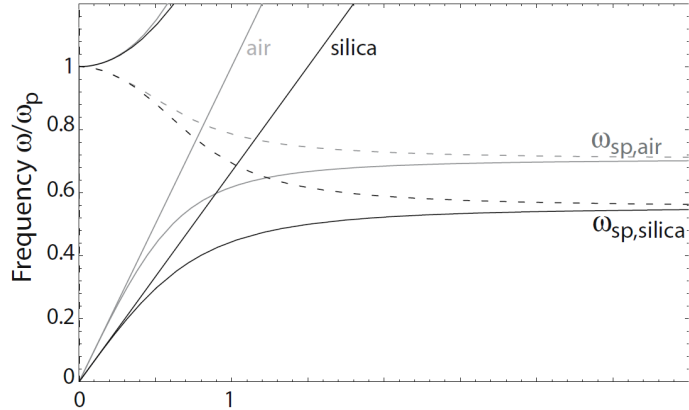


Figure 2.2: Dispersion Relation at the interface between a Drude metal and silica (black curves) and air (gray curves). Image adapted from [55].

damping described by a real Drude dielectric function for air ( $\epsilon_2 = 1$ ) and a fused silica interface ( $\epsilon_2 = 2.25$ ). In this plot, the frequency is normalized to the plasma frequency  $\omega_p$ , and both the real (continuous curve) and the imaginary

part (dashed curve) of the wave vector  $\beta$  are shown. Due to their bound nature, the SPP excitation corresponds to the part of the dispersion curve lying to the right of the respective light lines of air and silica. Radiation into the metals occurs in the transparency regime  $\omega > \omega_p$ . Between the regime of the bound and radiative modes, a frequency gap region with purely imaginary  $\beta$  prohibiting propagation exists. For small wave vector constant is close to  $k_0$  at the light line, and the waves extend over many wavelengths into the dielectric space. In this regime, SPPs acquire the nature of the grazing-incidence light field and are also known as Sommerfeld-Zenneck waves[63]. In the opposite regime of large

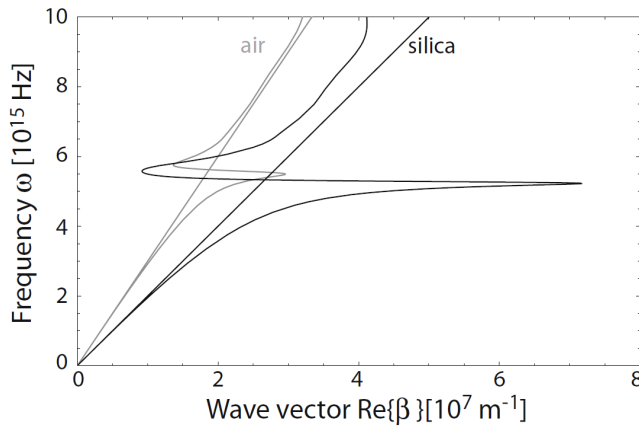


Figure 2.3: Dispersion relation between silver/air (gray curves) and silver/silica (black curves). Image adapted by [55]

wave vectors, the frequency of the SPPs approaches the characteristic surface plasmonic frequency

$$\omega_{sp} = \frac{\omega_p}{\sqrt{1 + \epsilon_2}} \quad (2.31)$$

In the limit of negligible damping of the conduction electron oscillation  $Im[\epsilon_1] = 0$ , the wave vector  $\beta$  goes to infinity as the frequency approaches  $\omega_{sp}$  and the group velocity  $v_g \rightarrow 0$ . The mode thus acquired an electrostatic character, and it is known as surface plasmon. The above discussion of fig.2.2 has assumed an ideal conductor with  $Im[\epsilon_1] = 0$ . Excitation of the conduction electrons of real metals however suffers both from free-electrons and interband damping. Therefore  $\epsilon_1(\omega)$  is complex, and also the SPPs propagation constant  $\beta$ . The traveling SPPs are damped with an energy attenuation length (also called propagation length)  $L = (2Im[\beta])^{-1}$ , typically between  $10\mu m$  and  $100\mu m$  in the visible regime, depending upon the metal/dielectric configuration. Compared with the dispersion relation of completely undamped SPPs depicted in fig.2.3, it can be seen that the bound SPPs induced by a silver/air and a silver/silica interface[55] have a maximum wave vector at the surface plasmon frequency  $\omega_{sp}$  of the system.

## 2.4 Excitation of Surface Plasmon Polaritons

In the previous section, we analyzed the fundamental physics of the Surface Plasmon Polaritons. However, the generation of SPPs on a dielectric metal interface is not easy. Thus, this section reviews the most common techniques of plasmonic generation phase matching, such as prism coupling, grating coupling, as well as excitation using a highly focused beam[55].

First of all, given  $\beta > k$  (eq.2.27) where  $k$  is the wave vector of light on the dielectric interface, the SPPs cannot be excited directly by the light beam. In particular, if we consider the projection along the interface of the photon momentum impinging under an angle  $\theta$  normal to the surface ( $k_x = k \sin(\theta)$ ) is always smaller than the SPP propagation constant  $\beta$  even at grazing incidence, prohibiting phase-matching. This assertion is confirmed in fig.2.2, where the SPP dispersion curve lies outside the light cone of the dielectric. The relation between  $\beta$  and  $k$  implies the use of various optical techniques for the SPP excitation.

### Prism Coupling

The phase-matching to SPPs can be achieved in a three-layer system consisting of a thin metal film sandwiched between two insulators of different dielectric constants. For simplicity[55], we consider one of the insulators to be air ( $\epsilon = 1$ ). A beam reflected at the interface between the insulator of higher dielectric constant  $\epsilon$ , usually in a prism shape, and the metal will have an in-plane momentum  $k_x = k\sqrt{\epsilon} \sin(\theta)$ , which is sufficient to excite SPPs at the interface between the metal and the lower-index dielectric, i.e., in this case at the metal/air interface. As can be seen in fig.2.4, the range of frequency in which the propagation

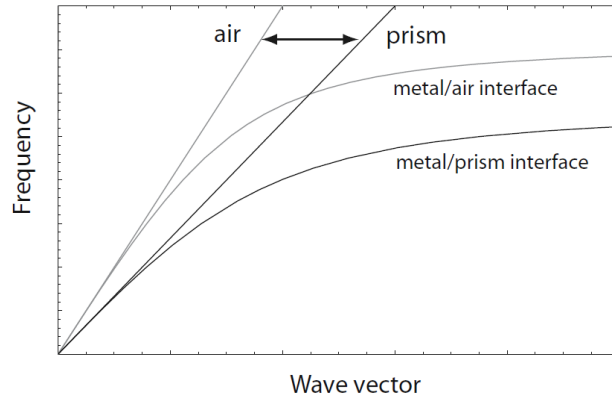


Figure 2.4: Prism coupling and SPP formation: the metal-air SPPs lie between the light line of the air and the prism so we obtain  $k = \beta$  that induce an SPPs. Image reproduced by [55]

constant  $\beta$  excites the SPP lies from the light lines of the air and the light lines of the prism. For the prism coupling, we can design two different geometries, sketched in fig.2.5. The most common configuration is the Kretschmann method[64], in which a thin metal film is placed above a glass prism. The light beam illuminates the prism at an angle greater than the critical angle of total internal reflection through the metal film and excites SPPs at the metal/air interface.

Another geometry is the Otto configuration[65], in which the prism is separated from the metal film by a thin air gap. Total internal reflection takes place at the prism/air interface, exciting SPPs via tunneling to the metal/air interface.

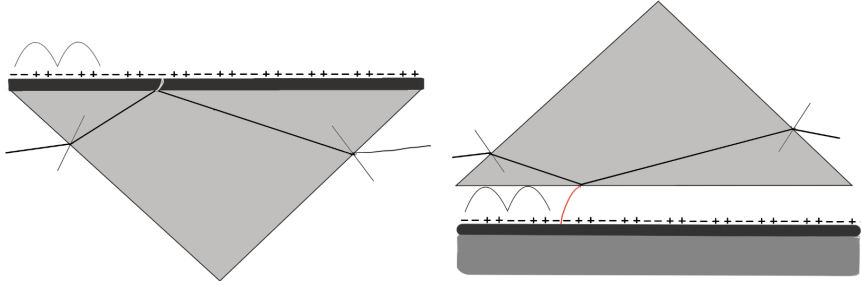


Figure 2.5: Prism coupling configuration: in the left part of the figure Kretschmann configuration, in the right part of the figure Otto configuration. Image adapted by [55]

## Grating Excitation

The mismatch in wave vector between the in-plane momentum  $k_x = k \sin(\theta)$  of incident photons and  $\beta$  can also be overcome by patterning the metal surface with a shallow grating of grooves or holes with a lattice constant  $a$ . For a one-dimensional sample of grooves in fig.2.6, phase matching takes place when the following condition[55]:

$$\beta = k \sin(\theta) \pm \nu g \quad (2.32)$$

is fulfilled, where  $g = 2\pi/a$  is the reciprocal vector of the grating, and  $\nu = 1, 2, 3, \dots$ . As the prism coupling, excitation of SPPs is detected as a minimum of reflected light.

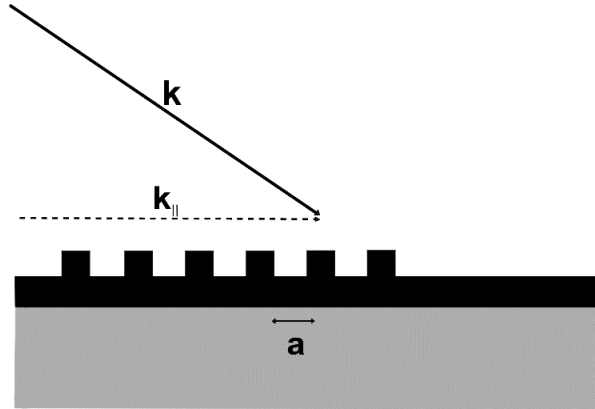


Figure 2.6: Phase-matching of light to SPPs using a grating coupling. Image adapted by [55]

The reverse process can also take place: SPPs propagating along a surface modulated with a grating of grooves or holes radiate an electromagnetic wave in which the direction has an angle  $\theta$  with the grating surface. In addition, given the eq.2.32 the exit angle ( $\theta$ ) of the electromagnetic field depends on the grating parameter  $a$ .

The gratings do not need to be milled directly into the metal surface, but the surface can also consist of dielectric material. Thus we can generalize the grating incidence[66]: SPPs can also be excited on films in areas with random surface roughness or manufactured localized scatters. Momentum components  $\Delta k_x$  are provided via scattering so that the phase matching condition is:

$$\beta = k \sin(\theta) \pm \Delta k_x \quad (2.33)$$

## Near Field Excitation

In excitation schemes such as a prism or grating coupling, we obtain SPPs over a macroscopic area defined by the dimensions of the spot of the coupling beam at wavelength  $\lambda_0$ [55]. In contrast, near-field optical microscopy techniques allow for the local excitation of SPPs[67] over an area  $a \ll \lambda_0$ , and can thus act as a point source for SPPs. Fig.2.7 sketches the typical geometry: a small probe tip of aperture size  $a \leq \lambda_{SPP} \leq \lambda_0$  illuminates the surface of a metal film in the near field. Due to the small aperture size, the light ensuing from the tip will consist of wave vector component  $k \leq \beta \leq k_0$ , thus allowing phase-matched excitation of SPPs with propagation constant  $\beta$ . Due to the ease of lateral positioning of such probes in scanning near-field optical microscopes, SPP at a different location on the metal surface can be excited[55].

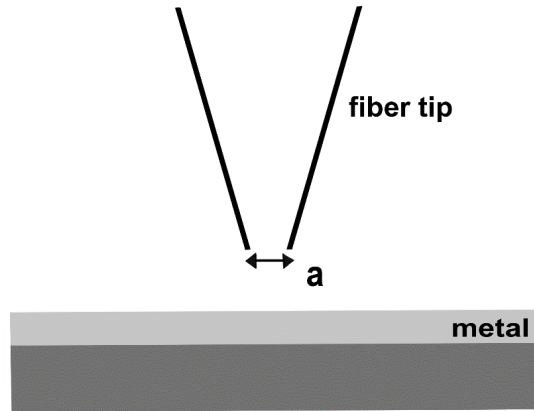


Figure 2.7: Local excitation of SPPs using near-field illumination. Image adapted by [55]

## 2.5 Localized Surface Plasmon

In the previous section, we explored the physics of propagating surface plasmons (SPPs). However, there is another phenomenon that is generated at a metal-dielectric interface known as Localized Surface Plasmon (LSP), which will be discussed in detail in this section. LSPs, as well as SPPs, have interesting energy localization properties in areas smaller than the diffractive limit ensuring interesting applications in nanotechnology. First of all, consider the interaction

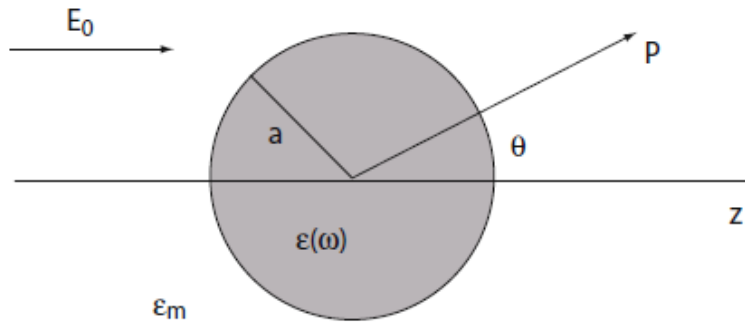


Figure 2.8: Sketch of a homogeneous sphere placed into an electrostatic field. Image reproduced by [55]

of a particle of size  $d$  with the electromagnetic field. If  $d \ll \lambda$ , i.e. the particle is much smaller than the wavelength of light in the surrounding medium, the electric field can be analyzed using the quasi-static approximation. In this case,

the phase of the harmonically oscillating electromagnetic field is practically constant over the particle volume, so we can calculate the spatial field distribution assuming the simplified problem of a particle in an electrostatic field. We start with the most convenient geometry for an analytical treatment (as can be seen in fig.2.8): a homogeneous, isotropic sphere of radius  $a$  located at the origin in a uniform static electric field  $\mathbf{E} = E_0 \hat{z}$ . The surrounding medium is isotropic and non-absorbing with dielectric constant  $\epsilon_m$ , and the field lines are parallel to the  $z$ -direction at a sufficient distance from the sphere. The dielectric response of the sphere is further described by the dielectric function  $\epsilon(\omega)$ , which we take as a simple complex number  $\epsilon$ . In the electrostatic approach[56], we are interested in a solution of the Laplace equation for the potential  $\mathbf{E} = -\nabla\phi$ . Due to the azimuth symmetry of the problem, the general solution is of the form

$$\Phi(\mathbf{r}, t) = \sum_{l=0}^{\infty} [A_l r^l + B_l r^{-(l+1)}] P_l(\cos(\theta)) \quad (2.34)$$

where  $P_l(\cos(\theta))$  are the Legendre Polynomials of order  $l$ , and  $\theta$  the angle between the position vector  $\mathbf{r}$  of the point P and the  $z$ -axis (see fig.2.8). Due to the requirement that the potentials remain finite at the origin, the solution for  $\Phi_{in}$  inside and  $\Phi_{out}$  outside the sphere can be written as:

$$\begin{aligned} \Phi_{in}(\mathbf{r}, \theta) &= \sum_{l=0}^{\infty} A_l r^l P_l(\cos \theta) \\ \Phi_{out}(\mathbf{r}, \theta) &= \sum_{l=0}^{\infty} [B_l r^l + C_l r^{-(l+1)}] P_l(\cos(\theta)) \end{aligned} \quad (2.35)$$

The coefficient  $A_l, B_l$  and  $C_l$  can now be determined from the boundary conditions at  $r \rightarrow \infty$  and at the sphere surface  $r = a$ . The requirement that  $\Phi_{out} \rightarrow -E_0 z = E_0 r \cos(\theta)$  as  $r \rightarrow \infty$  demands that  $B_1 = -E_0$  and  $B_l = 0$  for  $l \neq 1$ . The remaining coefficient  $A_l$  and  $C_l$  are defined by the boundary condition at  $r = a$ .

Equality of the tangential component of the electric field demands that:

$$-\frac{1}{a} \frac{\partial \Phi_{in}}{\partial \theta} \Big|_{r=a} = -\frac{1}{a} \frac{\partial \Phi_{out}}{\partial \theta} \Big|_{r=a} \quad (2.36)$$

and the equality of the normal components of the displacement field:

$$-\epsilon_0 \epsilon \frac{\partial \Phi_{in}}{\partial r} \Big|_{r=a} = -\epsilon_0 \epsilon_m \frac{\partial \Phi_{out}}{\partial r} \Big|_{r=a} \quad (2.37)$$

Application of these boundary conditions leads to  $A_l = C_l = 0$  for  $l \neq 1$ , and the calculation of the remaining coefficient  $A_1$  and  $C_1$  leads the potential evaluation[56] to:

$$\begin{aligned} \Phi_{in} &= -\frac{3\epsilon_m}{\epsilon + 2\epsilon_m} E_0 r \cos(\theta) \\ \Phi_{out} &= -E_0 r \cos(\theta) + \frac{\epsilon - \epsilon_m}{\epsilon + 2\epsilon_m} E_0 a^3 \frac{\cos(\theta)}{r^2} \end{aligned} \quad (2.38)$$

It is interesting to physically interpret the equation:  $\Phi_{out}$  describes the sphere of magnitude proportional to  $|E_0|$ . If we introduce the polarizability  $\alpha$ , defined via  $\mathbf{p} = \epsilon_0 \epsilon_m \alpha \mathbf{E}_0$ , we obtain that:

$$\alpha = 4\pi a^3 \frac{\epsilon - \epsilon_m}{\epsilon + 2\epsilon_m} \quad (2.39)$$

Eq.2.39 represents the complex polarization of a small sphere of sub-wavelength diameter in the electrostatic approximation. Fig.2.9 shows the absolute value and phase of  $\alpha$  for frequency of a dielectric constant  $\epsilon(\omega)$  of the Drude form. The polarizability shows a resonant enhancement under the condition that  $|\epsilon + 2\epsilon_m|$  is a minimum and for the case of small or slowly-varying  $Im[\epsilon]$  the resonance simplifies to:

$$Re[\epsilon(\omega)] = -2\epsilon_m \quad (2.40)$$

This relationship is called the Froelich condition and the associated mode is the dipole surface plasmon of the metal nanoparticle. We note that the magnitude of  $\alpha$  at resonance is limited by the incomplete vanishing of its denominator, due to  $Im[\epsilon(\omega)] \neq 0$ . The distribution of electric field  $\mathbf{E} = -\nabla\Phi$  can be evaluated from the potentials:

$$\begin{aligned} \mathbf{E}_{in} &= \frac{3\epsilon_m}{\epsilon + 2\epsilon_m} \mathbf{E}_0 \\ \mathbf{E}_{out} &= \mathbf{E}_0 + \frac{3\mathbf{n}(\mathbf{n} \cdot \mathbf{p} - \mathbf{p})}{4\pi\epsilon_0\epsilon_m} \frac{1}{r^3} \end{aligned} \quad (2.41)$$

As expected, the resonance in  $\alpha$  also implies a resonant enhancement of both internal and dipolar fields.

From the viewpoint of optics, it is much more interesting to note that another consequence of the resonantly enhanced polarization  $\alpha$  is the efficiency that a metal nanoparticle scatters and absorbs light. The corresponding cross section for scattering and absorption  $C_{sca}$  and  $C_{abs}$  can be calculated via the Pointing vector[68]:

$$C_{sca} = \frac{k^4}{6\pi} |\alpha|^2 = \frac{8\pi}{3} k^4 a^6 \left| \frac{\epsilon - \epsilon_m}{\epsilon + 2\epsilon_m} \right|^2 \quad (2.42a)$$

$$C_{abs} = k Im[\alpha] = 4\pi k a^3 Im\left[ \frac{\epsilon - \epsilon_m}{\epsilon + 2\epsilon_m} \right] \quad (2.42b)$$

For small particles with  $a \ll \lambda$ , the efficiency of absorption, scaling with  $a^3$ , dominates over the scattering efficiency, which scales with  $a^6$ . The expression for the cross sections is valid both for metallic scatterers and dielectric scatterers. The eqs.2.42a-2.42b also shows that for metal nanoparticles both absorption and scattering are resonantly enhanced at the dipole particle plasmon resonance, i.e. when the Froelich condition (eq.2.40) is met. For this reason, in a sphere of volume  $V$  and a dielectric function  $\epsilon = \epsilon_1 + i\epsilon_2$  in the quasi-static limit, we can define the extinction cross section  $C_{ext} = C_{sca} + C_{abs}$  that has the following expression[69]:

$$C_{ext} = 9 \frac{\omega}{c} \epsilon_m^{3/2} V \frac{\epsilon_2}{[\epsilon_1 + 2\epsilon_m]^2 + \epsilon_2^2} \quad (2.43)$$

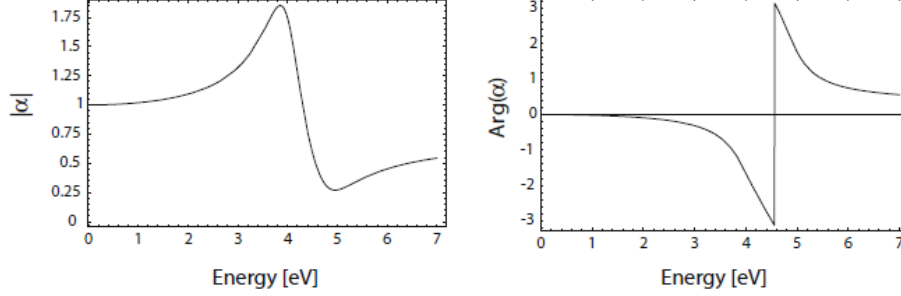


Figure 2.9: amplitude and argument of the polarizability in terms of the frequency in quasi-static approximation. Image reproduced by [55]

We can relax the assumption of a spherical nanoparticle shape. Even if the physics is well defined of the sphere, we can define a more general geometry in which we can use the analytical treatment in the electrostatic approximation. The geometry is an ellipsoid with semiaxes  $a_1 \leq a_2 \leq a_3$ , specified by  $\frac{x^2}{a_1^2} + \frac{y^2}{a_2^2} + \frac{z^2}{a_3^2} = 1$ . A treatment of the scattering problem in the ellipsoidal coordinate lead to the following expression for the polarizabilities  $\alpha_i$ , along the principal axes ( $i = 1, 2, 3$ )[69]:

$$\alpha_i = 4\pi a_1 a_2 a_3 \frac{\epsilon - \epsilon_m}{3\epsilon_m + 3L_i(\epsilon - \epsilon_m)} \quad (2.44)$$

$L_i$  is a geometrical factor given by:

$$L_i = \frac{a_1 a_2 a_3}{2} \int_0^\infty dq (a_i + q) f(q) \quad (2.45)$$

where  $f(q) = \sqrt{(q + a_1^2) + (q + a_2^2) + (q + a_3^2)}$ . The geometrical factor satisfy  $\sum L_i = 1$  and for a sphere  $L_1 = L_2 = L_3 = \frac{1}{3}$ . An important special class of ellipsoids is spheroids, in which two of the three axes are equal, (for example  $a_1 = a_2$ ). Using the eq.2.44, we reveal that a spheroids metal nanoparticle exhibits two spectrally separated plasmon resonances, corresponding to the oscillation of its conduction electrons along the major or minor axis respectively.

The resonance due to oscillation along the major axis can show a significant spectral red-shift compared to the plasmon resonance of a sphere of the same volume. Thus, plasmon resonance can be lowered in frequency into the near-field region of the spectrum using metallic particles with a large aspect ratio. It is observed that considering a quasi-static approximation, the metallic sphere acts like an electric dipole and obtains a resonance behavior controlled by the value of polarizability  $\alpha$ [69][55].

However, the theory of the dipole particle plasmon is strictly valid only for a vanishing small particle; in practice, the calculation outlined provide a reasonably good approximation for spherical and ellipsoidal particles with dimension

below  $100nm$  illuminated with visible or near-infrared radiation. In fact, for the particle of larger dimensions, where the quasi-static approximation is not justified due to the significant phase change of the driving field over the particle volume, a rigorous electrodynamics approach is required. Mie[70] developed a complete theory of the scattering and absorption of electromagnetic radiation by a sphere. The approach that is known as Mie Theory is to expand the internal and scattered fields into a set of normal modes described by harmonic vectors. The quasi-static results valid for sub-wavelength spheres are then recovered by a power series expansion of the absorption and scattering coefficient and retaining only the first term. Under this consideration, we will now analyze changes to the spectral position and width of the plasmon resonance with particle size not captured by the quasi-static approximation. Two regimes will be considered: First, a larger particle where the quasi-static approximation breaks down due to the retardation effect, and second the regime of a very small metal particle of a radius  $a < 10nm$ , where the particle dimensions are appreciably smaller than the mean free path of its oscillating electrons. Starting with larger particles, a straight-forward expansion of the first TM mode of Mie-Theory yield for the polarizability of a sphere of volume  $V$  the expression[70]:

$$\alpha_{sph} = \frac{1 - (\frac{1}{10})(\epsilon + \epsilon_m)x^2 + O(x^4)}{\frac{1}{3} + \frac{\epsilon_m}{\epsilon - \epsilon_m} - \frac{1}{30}(\epsilon + 10\epsilon_m)x^2 - i\frac{4\pi^2\epsilon_m^{3/2}}{3}\frac{v}{\lambda_0^3} + O(x^4)}V \quad (2.46)$$

where  $x = \frac{\pi a}{\lambda_0}$  is the so-called size parameter, relating to the radius of the free-space wavelength. Compared to the simple quasi-static solution eq.2.39, some additional terms appear in the numerator and denominator, each having a physical significance. The term quadratic in  $x$  in the numerator includes the effect of retardation of the exciting field over the volume of the sphere, leading to a shift in the plasmon resonance. The quadratic term in the denominator also causes an energy shift of the resonance, due to retardation of the depolarization field inside the particle[71]. For Drude and the noble metals[59], the overall shift is towards lower energies; the spectral position of the dipole resonance red-shift with increasing particle size. Intuitively, this can be understood by recognizing that the distance between the charges at the opposite interface of the sphere increases with the size, thus leading to a smaller restoring force and therefore a lowering of the resonance frequency. The quadratic term in the denominator also increases the magnitude of polarization, and thus inherently lessens the influence of the absorption due to the imaginary part of  $\epsilon$ . However, this increase in strength is counteracted by the third, completely imaginary term in the denominator, which accounts for radiation damping. Radiation damping is caused by a direct radiative decay route of the coherent electron oscillation into photons and is the main cause of the weakening of the strength of the dipole plasmon resonance as the particle volume increases[72]. We can summarize that the plasmon resonance of particles beyond the quasi-static regime is damped by two competing processes: a radiative decay process into photon, dominating for larger particles, and a non-radiative process due to absorption. To arrive at a quantitative description, these two damping processes can be incorporated into

a simple two-level model of the plasmon resonance. Using it, the homogeneous line-width  $\Gamma$  of the plasmon resonance can be related to the internal damping processes via the introduction of a dephasing time  $T_2$ . In energy unit, the relation between  $\Gamma$  and  $T_2$  is[73]:

$$\Gamma = \frac{2\hbar}{T_2} \quad (2.47)$$

We note that in analogy to dielectric resonators, the strength of a plasmon resonance can also be expressed using the notion of a Quality factor  $Q$ , given by  $Q = E_{res}/\Gamma$ , where  $E_{res}$  is the resonant energy. In this theory, the dephasing of the coherent excitation is either due to energy decay, or scattering events that do not change the electron energy but its momentum. This can be expressed by relating  $T_2$  to a population relaxation or decay time  $T_1$ , describing both radiative and non-radiative energy loss processes, and a pure dephasing time  $T_2^*$  resulting from elastic collisions:

$$\frac{1}{T_2} = \frac{1}{2T_1} + \frac{1}{T_2^*} \quad (2.48)$$

it can be shown that in general  $T_2^* \gg T_1$  so that  $T_2 = 2T_1$ . We can now turn our attention to the regime of very small particles. For gold and silver particles of radius  $a < 10nm$ , an additional damping process, loosely termed chemical interface damping, must be considered. Empirically, the associated broadening of the experimentally observed plasmon line-width  $\Gamma_{obs}$  can be modeled via[72]:

$$\Gamma_{obs}(R) = \Gamma_0 + \frac{Av_F}{R} \quad (2.49)$$

here,  $\Gamma_0$  describes the plasmon line-width of particle that are outside the regimes where interface damping or radiation damping dominate.  $v_F$  is the Fermi velocity of electrons, and  $A \simeq 1$  a factor incorporating details of the scattering processes. Eq.2.46 then allows us to determine how the resonance varies as the size of the sphere increases due to effects outside the limit of the quasi-static approximation[74]. Mie's theory[70] allows us to evaluate analytically the electric field and polarizability of spherical and spheroidal plasmonic structures of any size as seen in eq.2.44. To evaluate plasmonic structures of generic shape, it is necessary to modulate the form of eq.2.46 with terms obtained by numerical simulations, obtaining the following formula[75]:

$$\alpha \simeq \frac{V}{(L + \frac{\epsilon_m}{\epsilon_1 - \epsilon_m}) + A\epsilon_m x^2 + B\epsilon_m^2 x^4 - i \frac{4\pi i^2 \epsilon^{3/2}}{3} \frac{V}{\lambda_0}} \quad (2.50)$$

where  $A$  and  $B$  are the parameters to be determined and depend on the material used and the morphology of the nanostructure. This implies that the resonant condition, in the limit of low radiation loss ( $\epsilon_1 \gg \epsilon_2$ ) is therefore:

$$(L + \frac{\epsilon_m}{\epsilon_1 - \epsilon_m}) + A\epsilon_m x^2 + B\epsilon_m^2 x^4 = 0 \quad (2.51)$$

To determine the parameters the eq.2.50 is compared with a light scattering in Au and Ag spheroid (eq.2.42a-2.42b). Then by analyzing the results for plasmonic structures with different  $L$  and different materials compared with the spheroidal case we obtain a numerical estimate of the values of  $A$  and  $B$ [75]:

$$\begin{aligned} A(L) &= -0.4865L - 1.046L^2 + 0.8481L^3 \\ B(L) &= 0.01909L + 0.1999L^2 + 0.6077L^3 \end{aligned} \quad (2.52)$$

## Coupling Between Localized Plasmons

We have seen that the localized plasmon resonance of a single metallic nanoparticle can be shifted in frequency from the Froelich condition via alterations in particle shape and size. In particle ensembles, additional shifts are expected to occur due to electromagnetic interactions between the localized modes. For small particles, the coupling is essential of a dipolar nature, and the particle ensemble can in a first approximation be treated as an ensemble of interacting dipoles. We will now describe the effects of such interactions in ordered metal nanoparticle arrays. Here, we assume that the particles of size  $a$  are arranged within an ordered one-or-two dimensional array with interparticle spacing  $d$ . We further assume that  $a \ll d$ , so that the dipolar approximation is justified, and the particles can be treated as point dipoles[55]. Two regimes have to be distinguished, depending on the magnitude of the interparticle distance  $d$ . For closely spaced particle  $d \ll \lambda$ , near-field interactions with a distance dependence of a  $d^{-3}$  dominate, and the particle array can be described as an array of point dipoles interacting via their near-field. In this case, strong field localization is due to a suppression of scattering into the far field via the excitation of plasmon modes in particles along the chain axis, mediated by near-field coupling[76]. One can intuitively see that interparticle coupling will lead to shifts in the spectral position of the plasmon resonance compared to the case of an isolated particle. Using the simple approximation of an array of interacting point dipoles, the direction of the resonance shifts for in-phase-illumination can be determined by considering the Coulomb forces associated with the polarization of the particle. The restoring force acting on the oscillating electrons on each particle in the chain is either increased or decreased by the charge distribution of the exciting light, this leads to a blue shift of the plasmon resonance for the excitation of transverse modes, and a redshift for longitudinal modes. For larger particle separation[77], far-field dipolar coupling with a distance dependence of  $d^{-1}$  dominates. The far-field coupling has pronounced influences on the plasmon line shape, both in terms of resonance frequency as well as spectral width. In particular, the quality factor (Q) is subject to the influence of the far-field coupling and decrease in function of  $d$ .

In this chapter, we have set the basis for understanding plasmonic phenomena. In particular, starting with the behavior of dispersive media, we focalize on the analysis of an important radiation-matter phenomenon: Surface Plasmon. The surface plasmon has two different phenomenologies: SPPs are phenomena of propagation of an evanescent wave along a metal-dielectric interface while

LSPs are localized phenomena that generate amplified electric fields. In the next chapters, we will see how the physical properties of surface plasmons are used for practical applications. In particular, modulation of electric fields involves defining forces that can manipulate nanoparticle trajectories for various uses.

## Chapter 3

# Finite Element Method

The analysis and design of a plasmonic device require numerical techniques to analyze the electric field response as a function of various input parameters. We require numerical algorithms that solve differential equations over a 3D domain with varying conditions depending on the type of device considered and the solution obtained has to be consistent with the physics of the problem. For this reason, we choose the software COMSOL Multiphysics. COMSOL is software that exploits the Finite Element Method (FEM) to solve complex systems of differential equations that can be traced back to physical problems applied to 2D or 3D models. In this chapter, we will review the features of the FEM method focusing on the properties useful in constructing the model for a periodic electromagnetic problem.

The finite element method (FEM)[78] is a numerical technique for solving a problem that is described by partial differential equations or can be formulated as functional minimization. The domain of interest is represented as an assembly of finite elements. Approximating functions in finite elements are determined in terms of nodal values of the physical field which is searched. A continuous physical problem is transformed into a discrete finite element problem with unknown nodal values. For a linear problem, a system of linear algebraic equations should be solved. Values inside finite elements can be recovered using nodal values. Two features of the FEM are worth to be mentioned:

- 1) Piece-wise approximation of physical fields on finite elements provides a good precision even with simple approximation functions (increasing the number of the element we can achieve any precision).
- 2) Locality of approximation leads to a sparse equation system for a discretized problem. This helps to solve problems with a very large number of local unknowns.

The FEM can be summarized in a list of steps:

- 1) Discretize the continuum. The first step is to divide a solution region into finite elements. The description of mesh consists of several arrays

main of which are nodal coordinates and element connectivities.

- 2) Select interpolation functions. Interpolation functions are used to interpolate the field variables over the element. Often, polynomials are selected as interpolation functions. The degree of the polynomial depends on the number of nodes assigned to the element.
- 3) Find the element properties. The matrix equation for the finite element should be established which relates the nodal values of the unknown function to other parameters.
- 4) Assemble the element equations. To find the global equation system for the whole solution region we must assemble all the element equations. In other words, we must combine the local element equation for all elements used for discretization. Element connectivities are used for the assembly process. Before the solution, boundary conditions (which are not accounted for in the element equations) should be imposed.
- 5) Solve the global equation system. The finite element global equation system is typically sparse, symmetric, and positive definite. Direct and iterative methods can be used for the solution. The nodal values of the sought function are produced as a result of the solution.
- 6) Compute additional results. In many cases, we need to calculate additional parameters which are obtained after the solution of the global equation system.

In the following sections, all points of the finite element method will be described in detail.

### 3.1 Discretization: Linear Triangular Element

The first step of the finite element method is to discretize the physical domain. The physical domain can be either 2D or 3D. In our specific case, the electromagnetic field is evaluated within a parallelepiped-shaped physical domain. To obtain the best results from the surface plasmon, the software COMSOL generates a subdivision of the domain as efficiently as possible. In this section, we show the mathematical tool for a subdivision in a 2D domain[79]. It's important to know that the 3D subdivision of the domain occurs with the same method but the fundamental element is different. Considering a 2D generic domain  $\Omega$  as in the fig.3.1(a). An elliptical partial differential equation in weak form with boundary condition is defined as:

$$\left\{ \begin{array}{l} \text{find } u \text{ in } H^1(\Omega), \text{ such that} \\ u = g_0 \text{ on } \Gamma_D \\ \int_{\Omega} \nabla u \cdot \nabla v + c \int_{\Omega} uv = \int_{\Omega} fv + \int_{\Gamma_N} g_1 v \quad \forall v \in H_{\Gamma_D}^1(\Omega) \end{array} \right. \quad (3.1)$$

where  $u$  is the unknown function,  $c$  is a non negative constant value,  $f$  is the source term defined in the physical domain.  $g_0$  and  $g_1$  are two functions defined

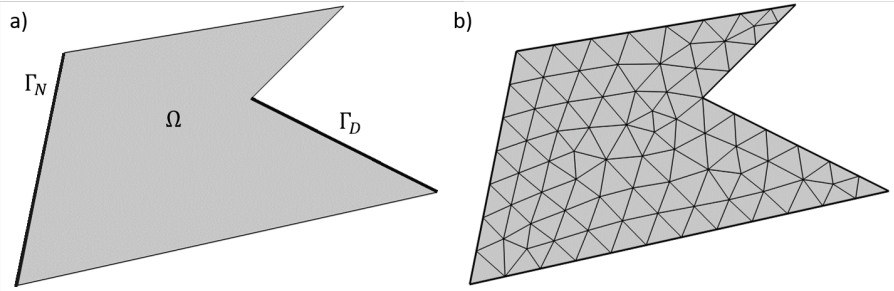


Figure 3.1: a) Generic 2D Domain  $\Omega$ . b) Triangulation of  $\Omega$

in two different parts of the boundary; in particular,  $g_0$  is defined in  $\Gamma_D$  that is the Dirichlet boundary while  $g_1$  is defined in  $\Gamma_N$  that is the Neumann boundary.

$v$  is a test function defined in the physical domain, without losing the generality we can redefine  $v$  such that  $v = 0 \in \Gamma_D$ . The space indicated is the Sobolev space defined as:

$$H^1(\Omega) = \left( u \in L^2(\Omega) \mid \frac{\partial u}{\partial x_1}, \frac{\partial u}{\partial x_2} \in L^2(\Omega) \right) \quad (3.2)$$

where  $L^2(\Omega)$  is the space of the square-integrable functions.

Now, we want to discretize this differential equation and the physical domain for an approximate value of  $u$ . The easiest way to divide a physical domain is a polygonal subdivision. Software that takes advantage of the FEM method (including COMSOL), subdivides the domain in such a way as to have a reasonable number of elements to best approximate  $u$  with the minor use of computational resources. The simplest polygonal to subdivide a 2D physical domain are triangles. When the domain is 3D, as in our case, the triangles become tetrahedrons.

Let us take an arbitrary, non-degenerate triangle  $K$ , a vertices  $p$  is uniquely determined by the value of points  $(x_1, x_2)$  for the following equation:

$$p = a_0 + a_1 x_1 + a_2 x_2 \quad a_0, a_1, a_2 \in \mathbb{R} \quad (3.3)$$

The set of the vertices  $p$  that follows this equation is called  $\mathbb{P}_1$ . In other words, an edge is determined only from the adjacent vertices, this point is called the local grade of freedom.

Starting from the eq.3.3, we can generate the domain partition into a triangle. A triangulation of  $\Omega$  (fig.(3.1(b))) is a subdivision of this domain into triangles that must cover all  $\Omega$  with the followings rules:

- 1) if two triangles have some intersection, it is either on a common vertex or a common full edge and two different triangles do not overlap;
- 2) the triangulation must respect the partition into Dirichlet and Neumann boundaries. This means that an edge of a triangle that lies of  $\Gamma$  cannot be part Dirichlet and part Neumann, there must be a transition from the boundaries.

The set of triangles that the domain has been divided is called  $T_h$  with  $h$  as the length of the longest side among all the triangles. If we consider the functions  $u_h \in \mathbb{P}_1$  for all vertices of all triangles we obtain a function space  $V_h$  defined as:

$$V_h = \left( u_h \in C(\bar{\Omega}) | u_h|_K \in \mathbb{P}_1, \quad \forall K \in T_h \right) \quad (3.4)$$

An element of  $V_h$  is uniquely determined by a set of vertices of the triangulation. The value of the vertices is the degrees of freedom that determine an element of  $V_h$ . In this context, we call nodes the vertices where we take the value. In other words, the triangulation nodes are the mathematical elements where the physical problem is applied. In COMSOL, the memory usage of the software is highly dependent on the number of nodes considered in the approximation of the physical problem. Thus, the construction of an optimal mesh requires control over the number and the placement of the nodes efficiently. Once the nodes within the physical domain are defined, the differential equation described above (eq.3.1) is discretized (all steps are described in appendix B1) and the following result is obtained:

$$\sum_{j \in Ind} (W_{ij} + cM_{ij})u_j = b_i - \sum_{j \in Dir} (W_{ij} + cM_{ij})g_0(p_j) \quad (3.5)$$

where  $Ind$  is the set of independent node,  $Dir$  is the set of Dirichlet node.  $W_{ij}$  and  $M_{ij}$  are called Stiffness and mass matrix respectively (defined in appendix B1). Both matrices are symmetric and the mass matrix is positive definite, instead, the stiffness matrix is semidefinite positive. This is a linear system in which the nodal values of  $u_h$  on the free vertices (non-Dirichlet) of the triangulation are unknown. After solving the linear system, the formula for  $u_h$  (eq.B.11) recovers the function everywhere, not only on the nodes. This represents the fundamental difference between a finite element algorithm respect other types of algorithms (e.g. finite difference). Indeed, a finite difference algorithm applied in a 2D or 3D domain evaluates the function in the domain by interpolating the values obtained in the nodes. A finite-element algorithm (COMSOL) fully recovers the function within each element ensuring greater accuracy in estimating  $u$ . After the discretization step, we transform a differential equation in integral form (eq.3.1) into a finite set of differential equations. We obtain a simplification of the problem but the result is not numerically solvable yet.

## 3.2 Assembly

In the previous paragraph, we discussed the discretization part of the Finite Element Method. In particular, we search the solution of a partial differential equation  $u$  with a discretization of the physical domain  $\Omega$  and transform the continuous system in eq.3.1 in a discretized system in eq.3.5. The next step in which the discretized system becomes an ensemble of the linear systems is called the assembly algorithm and in this section, we will explain it[79].

Assembly algorithms are usually "invisible" to the COMSOL user but fundamental in the development of numerical analysis because we transform a differential equation in data that the computer can calculate. Assembly algorithms have two basic steps: localization of the equation's variables and association with solution easy to evaluate. It is known that eq.3.5 is defined on the nodes of the whole system, i.e., the whole mesh of the domain. In the first step, eq.3.5 is redefined such that the variables are defined in each triangle of the mesh. This is possible through the definitions of particular local functions that "cut" all the domains except a given triangle. (Details are discussed in appendix B2). Once the localization of the equation has been obtained, the second step is to transform the single triangle into a known geometry called the reference triangle[79]. The reference triangle ( $\hat{K}$ ) is usually the triangle that has the following vertices:  $\hat{p}_1 = (0, 0)$ ,  $\hat{p}_2 = (1, 0)$ ,  $\hat{p}_3 = (0, 1)$ . The reference triangle simplifies the solution of eq.3.5 however, moving from the triangular element to the reference triangle involves the definition of a  $B_K$  transformation matrix that contain all the physics and geometrical issue (see appendix for details). Then, once the assembly process is completed, the set of differential equations becomes a system of numerical equations whose only unknown is the coefficients of the transformation matrix  $B_K$ . Once the assembly process is completed, we calculate the matrix coefficient by some matrix algorithms known as solvers.

### 3.3 Convergence in $\mathbb{P}_1$ and Grid Refinement

In the previous section, we have shown a practical application of the Finite Element Technique. the finite element method allows us to obtain an approximate solution  $u_h$  of a system of differential equations with unknown  $u$ . To obtain, the best estimate of  $u$  it is necessary to estimate the difference between the real solution and the approximate solution by estimating the error  $\epsilon$ . To be able to arrive at an analytical formulation of the error, it is necessary to recall some mathematical definitions typical of the finite element method also called Galerkin's method[80]. In general, given a Sobolev space  $H^1(\Omega)$  define a norm  $\|u\|$  such that:

$$\|u\| = \left( \int_{\Omega} |\nabla u|^2 + \int_{\Omega} |u|^2 \right)^{1/2} \quad (3.6)$$

and a closed subspace  $V_0$ , if  $V$  is a Hilbert space, define a bilinear form  $a(u, v)$  in  $V$  that is continuous, i.e. exist a positive constant  $M > 0$  such that:

$$|a(u, v)| \leq M \|u\| \|v\| \quad \forall u, v \in V \quad (3.7)$$

and has a property of ellipticity, i.e. exist  $\alpha > 0$  such that:

$$a(u, v) \geq \alpha \|v\| \quad \forall v \in V_0 \quad (3.8)$$

define a linear form  $l$  continuous, i.e. exist a constant  $C_l > 0$  such that:

$$|l(v)| \leq C_l \|v\| \quad \forall v \in V \quad (3.9)$$

Thus, a general problem has the following form:

$$\begin{aligned} \text{find } u \in V \text{ such that} \\ a(u, v) = l(v) \quad \forall v \in V_0 \end{aligned} \tag{3.10}$$

that has a unique solution and well-posed  $u$ . Galerkin's Method consists of a choice of a finite-dimensional space  $V_h^0 \subset V$  and takes the following discrete problem:

$$\begin{aligned} \text{find } u_h \in V_h^0 \text{ such that} \\ a(u_h, v_h) = l(v_h), \quad \forall v_h \in V_h^0 \end{aligned} \tag{3.11}$$

that have a unique solution  $u_h$ . The solution  $u_h$  differ from the solution of the problem  $u$  for an error  $\epsilon$  defined as follows[80][79]:

$$\epsilon \leq \left(1 + \frac{M}{\alpha}\right) \inf \left( \|u - v_h\| \mid v_h \in V_h, \quad v_h(p) = g_0(p), \quad \forall p \text{ Dirichlet node} \right) \tag{3.12}$$

Then if  $\epsilon$  is small enough, the solution of the discrete space  $u_h \in V_0^h$  accurately approximates the solution of the system  $u \in V$ .

Now, we want to check [81] if the solution of the triangulation of  $\Omega$  ( $u_h \in \mathbb{P}_1$ ) used in the previous paragraph is a good approximation for the value of  $u$ . Let us consider that the error of the finite element method is bounded by the error of interpolation of the exact solution in the finite element space. The interpolation is done triangle by triangle so the global error for interpolation is the sum of the errors element by element. Thus, the error in  $\mathbb{P}_1$  is defined as:

$$\epsilon \leq Ch \left( \int_{\Omega} |\partial_{xx}u|^2 + |\partial_{xy}u|^2 + |\partial_{yy}u|^2 \right)^{1/2} \tag{3.13}$$

where  $C$  is a constant, and  $h$  is the size of the longest edge of the triangulation. The expression on the right side is the Sobolev seminorm. The eq.3.13 involves that the error depends on the coefficient of the problem, the geometry of the physical setting, and the smallest angle of the triangle. The error value defines the mesh quality in a COMSOL model.

In particular, we can see that the geometric characteristics of triangles are crucial in the evaluation of mesh quality. In general, a mesh should be refined if:

- 1) the triangles have large dimensions compared to the physics of the model.
- 2) the angles of the triangles have angles greater than  $90^\circ$ .

The dependence of the error on the edge of the triangle implies that the mesh quality can be improved by reducing the size of the triangles. In addition, the error equation in the  $\mathbb{P}_1$  approximation (eq.3.13) is proportional to  $h$  thus, the approximation method is the order one. In addition, mesh quality in  $\mathbb{P}_1$  approximation has a linear dependence on the size of the triangle edge. However,

the reduction of the triangle sides has negative effects from a computational point of view. A reduction in the sides of the triangles implies an increase in the number of unknowns since the matrices to be computed are equal to the number of triangles obtained by subdividing the domain. Thus, a different method is needed for mesh enhancement in a model. One recommended method is to apply a triangulation of higher order than  $\mathbb{P}_1$ .

Let us consider the space of polynomials in two variables with degree at most two[79]:

$$\mathbb{P}_2 = \left( a_0 + a_1x + a_2y + a_3x^2 + a_4y^2 + a_5xy \mid a_0, \dots, a_5 \in \mathbb{R} \right). \quad (3.14)$$

An element of  $\mathbb{P}_2$  is determined by six independent parameters (the quantities  $a_i$ ), so the space  $\mathbb{P}_2$  has a dimension equal to six. Let us take a triangle  $K$  and the nodes are the three vertices of the triangle and the midpoints of the three edges. In addition, an element of  $\mathbb{P}_2$  is a parabolic function and is determined by three different points. Therefore the value of a function in  $\mathbb{P}_2$  on an edge of the triangle is uniquely determined by its three values on the nodes that lie on that edge (two vertices and one midpoint). Because of these properties, we can link together two  $\mathbb{P}_2$  triangles as in the  $\mathbb{P}_1$  case. The triangulation has the same condition and recovers a similar space  $V_h$  for the triangulation function. If we want to implement  $\mathbb{P}_2$  we need to compute the usual integrals for mass and stiffness matrices. The final matrices for the computation of the discrete system of equations are evaluated with the same procedure as in the  $\mathbb{P}_1$  case. However, given  $\mathbb{P}_2$  has a larger number of vertex respect to  $\mathbb{P}_1$ , the resulting mass and stiffness matrix are 6x6 instead of 3x3 as in the case of  $\mathbb{P}_1$ , related to the increase of the number of nodes. In  $\mathbb{P}_2$  the error is[81]:

$$\epsilon \leq Ch^2 |u|_{3,\Omega} \quad (3.15)$$

where the constant  $C$  depends on the PDE operator, the geometry, and the smallest angle of triangle  $K$  and  $|u|_{3,\Omega}$  is the Sobolev seminorm that uses the third order partial derivative of  $u$ . In the error of order two, reducing the size of the triangle the gain of precision is much faster to the  $\mathbb{P}_1$  case. It is possible to increase the order of  $\mathbb{P}$  (ex.  $\mathbb{P}_3, \mathbb{P}_4 \dots$ ) by increasing the number of nodes present on a single triangle. The procedure for the evaluation of stiffness and mass matrices is the same as in the  $\mathbb{P}_1$  and  $\mathbb{P}_2$  cases. When the order has increased the solution gains an accuracy advantage since ( $\epsilon \leq Ch^n |u|_{n+1,\Omega}$ ) but the stiffness matrix and the mass matrix increase in size gaining a larger number of unknowns.

### 3.4 Quadrilater division of domain

Division of a physical domain is not necessarily carried out using triangulation. Some domains, such as rectangles or a box in 3D, are better subdivided into smaller rectangles. Sometimes the triangulation becomes messy. Because the

triangulation is produced, working from the boundary to the interior and avoiding very acute angles (that increase the error), this implies a very disorganized and non-symmetric pattern. If the problem favors directions, this is not the best way to generate discretization.

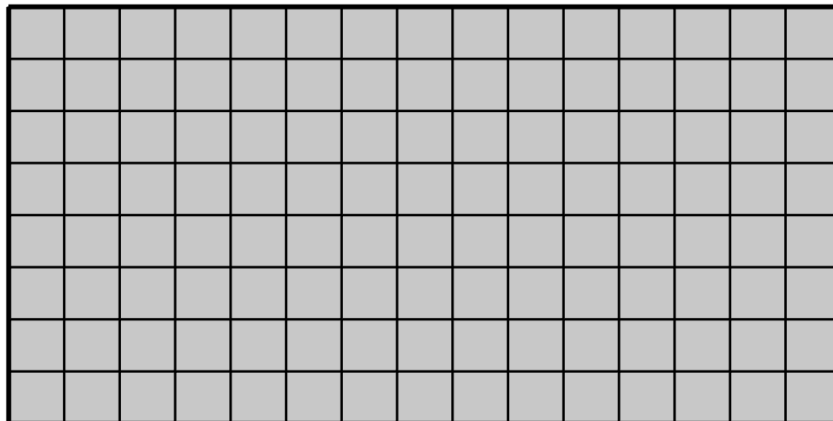


Figure 3.2: Quadrilateral subdivision of a domain

First of all, we define a new polynomial space, introduced in the reference variables[79]:

$$\mathbb{Q}_1 = \left( a_0 + a_1\xi + a_2\eta + a_3\xi\eta \mid a_0, a_1, a_2, a_3 \in \mathbb{R} \right) \quad (3.16)$$

These are polynomials on two variables both of order one in each variable separately. In general, the discretization of a rectangular domain (or similar) into a set of parallelograms is performed with the same rules used for the triangulation described in the previous paragraph, i.e. the edges of the parallelograms cannot be overlapped and the Neumann and Dirichlet edge condition is always satisfied (fig.3.2). Once the domain is discretized, the calculation of the stiffness and mass matrices occurs using the same method as in the triangular case. The obtained solution  $u_h$  differs from the real solution  $u$  of a value  $\epsilon$  given by the eq.3.12[81]. Compared to the  $\mathbb{P}_k$  case,  $h$  indicates the largest edge on the parallelogram. However, there is a difference in FEM calculation between the two types of domain subdivisions. At the time of assembly, transforming the reference rectangle into a parallelogram, which is the fundamental element of a quadrilateral mesh, is very complex compared to the triangular case. In particular, the transformation matrix between the reference element and the mesh element depends on the geometric characteristics of the element under consideration, i.e., quadrilateral angles and quadrilateral side size. Thus, if the

quadrilateral mesh does not perfectly fit the physical domain, the calculation becomes difficult, and mesh error occurs, unlike in the triangular case. It follows that the quadrilateral mesh is optimal only for particular types of domains such as Perfectly matched layer (PML) domains or in computing flows in polygonal domains (given the directionality of the solution).

### 3.5 Isoparametric Element

In the previous sections we have analyzed various types of discretization (Triangles, Parallelograms), and the difference between the real solution and the approximate solution by observing the error and its trend to the geometry of the system. We also showed how to refine the discretization for example, going from a  $\mathbb{P}_1$  space to a  $\mathbb{P}_k$  space. The physical domains used, however, were always suitable for the discretizations employed (e.g., rectangular for parallelograms or polygonal for triangulations). It is necessary to understand what happens when the domain has curvatures and thus how the finite element method "fits" the curvatures of the domain[79]. Let us consider a curve domain  $\Omega$  and let us gen-

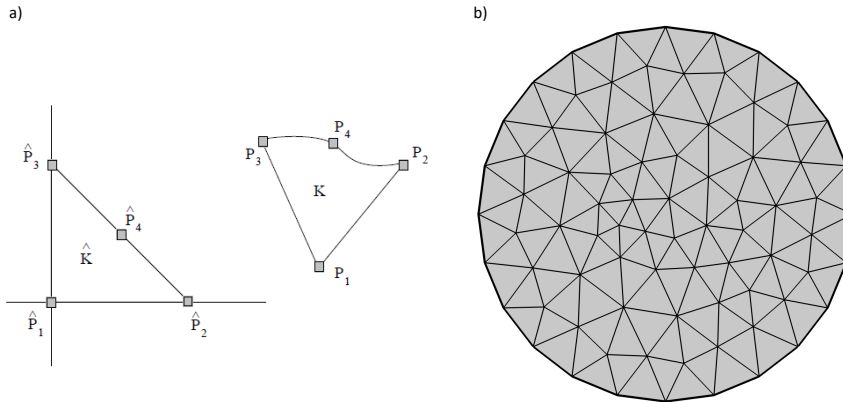


Figure 3.3: a) Triangle and isoparametric triangle. Image adapted by [79] b) Subdivision of a curved domain approximation ( $\Omega_h$ )

erate a triangulation, and substitute the real domain with a polygonal approximation. It is important to note that when the grid is generated all boundary nodes of the triangulation have to be placed on the real boundary. This means that if you need small triangles, you cannot obtain them by simply subdividing your grid but you add new vertices of the triangles on the boundary. Thus, it is deduced that in a curved domain, exist an error produced by the geometrical approximation and not depending on the triangulation method considered.

Thus we can use any high-order method  $\mathbb{P}_k$  of triangulation but the solution does not converge.

Given the condition in which a triangle has vertices on the boundary of  $\Omega$ , the transformation functions  $F(K)$  that relate a reference triangle with an element of the triangular mesh has a non-linear element. This non-linear term is dependent on the distance between the polygonal approximation of  $\Omega$  and the boundary of  $\Omega$  itself. Thus the triangle formed by this transformation (details are shown in the appendix B3) is called isoparametric (see fig.3.3(a)) and has one of the edges that "fit" with the curved boundary.

The triangulation process is a set of triangles and isoparametric triangles that do not overlap each other. When we write the equations of the finite element method using the local space, the union of all triangles (curved and straight) is not the original domain  $\Omega$  but an approximation of it, which we called  $\Omega_h$ . The Diriclet node, however, is in the correct boundary  $\Gamma$ .

The matrices obtained after the assembly process are non-linear, thus the isoparametric element is difficult to evaluate numerically.

The final result shows some difficulty to mesh a curved domain. In particular, the mesh defined in a sphere or cylinder (see fig.3.3(b)) has some error derived from the isoparametric approximation. The mesh refinement of this domain is possible but the number of the element or the approximation level is higher. This impacts the CPU memory and can decrease the mesh quality in a model.

## 3.6 Matrix Solvers

Given a system of differential equations over a physical domain, we have shown that through Galerkin's method, it is possible to transform it into a system of equations over a discrete domain (Chapters 3.1 and 3.2). The assembly algorithms subsequently allow us to reduce the differential equation to the evaluation of a system  $Au = f$ . To solve this linear system, simulation software (including COMSOL) uses computational algorithms called solvers. In this section, we analyze the two most common types of solvers: direct solvers and iterative solvers[82].

### 3.6.1 Direct Solvers

Direct solvers are algorithms that simplify the matrix in such a way as to derive the solution of a linear system analytically. In Direct solvers, the actual approximate solution is obtained with robust and high-precision algorithms. However, the derivation of a solution involves a large allocation of processor memory so it is often recommended not to use these algorithms for problems with a high number of unknowns ( i.e., when we need a large number of nodes to solve the problem). There are many direct solvers, for example in COMSOL Multiphysics there are MUMPS, PARDISO, and SPOOLES. The direct solvers return the same value of the approximate solution and the only difference between them is in the speed of execution and allocation properties: PARDISO is

the fastest followed by MUMPS and finally by SPOOLES, while MUMPS and PARDISO can also generate solutions in out-of-core (i.e. using in the simulation the hard disk in addition to the RAM of the machine used) MUMPS allows the use of eventual multi-core of the machine to speed up the process.

In the numerical evaluation of the solution, all direct solvers use a solving technique known as lower-upper (LU) decomposition[83][84], in which a sparse matrix (such as that obtained by assembly algorithms) is factorized into the product of a low triangular matrix and a high triangular matrix.

$$A = LU \rightarrow \begin{bmatrix} a_{11} & a_{12} & a_{13} \\ a_{21} & a_{22} & a_{23} \\ a_{31} & a_{32} & a_{33} \end{bmatrix} = \begin{bmatrix} l_{11} & 0 & 0 \\ l_{21} & l_{22} & 0 \\ l_{31} & l_{32} & l_{33} \end{bmatrix} \begin{bmatrix} u_{11} & u_{12} & u_{13} \\ 0 & u_{22} & u_{23} \\ 0 & 0 & u_{33} \end{bmatrix}$$

where  $L$  is a lower triangular matrix and  $U$  is an upper triangular matrix. The LU method is a consequence of the Gauss reduction algorithm. Recall that the Gauss reduction algorithm transforms a sparse matrix into an upper triangular matrix. The upper triangulation is achieved after  $n - 1$  steps, where  $n$  is the matrix rank. To have a Gauss reduction algorithm well-defined, the matrix entries  $a'_{11} \dots a'_{n-1, n-1}$  must be nonzero. These quantities are called pivots. If no zero pivots are encountered, then Gauss transformation  $M_1, \dots, M_{n-1}$  are generated such that  $M_{n-1} \dots M_1 A = U$  is upper triangular. It is easy to check that if  $M_k = I_n - \tau^{(k)} e_k^T$ , then its inverse is prescribed by  $M_k^{-1} = I_n + \tau^{(k)} e_k^T$  and so:

$$A = LU \quad L = M_1^{-1} \dots M_{n-1}^{-1}$$

$L$  is a unit lower triangular matrix because each  $M_k^{-1}$  is a unit lower triangular. Once the matrix is divided into two triangles calculating the result of the system becomes very quick and simple. Since the size of the matrix affects the speed of the Gauss reduction algorithm, it is clear that a large number of unknowns implies a longer computation time and for some solvers (such as MUMPS) a huge use of computer memory. Direct solvers are the best method when the mesh is sustainable by the computer although a thoughtful choice of the solver is necessary based on the characteristics of the computational system with which the simulation is carried out.

### 3.6.2 Iterative Solvers

The iterative solvers use an iterative method for the  $Au = f$  problem generating a sequence of approximate solutions  $u^{(k)}$  that converges to  $u = A^{-1}f$ . Typically, the matrix  $A$  is involved only in the context of matrix-vector multiplication and that is what makes this framework attractive when  $A$  is large and sparse. The use of an iterative solver involves less use of machine memory being an approximate computation of the solution and this implies a higher speed of solving the linear system. The use of an approximate solution is very useful for systems with a large number of unknowns and greater versatility since the algorithm does not depend on the properties of matrix  $A$  like the direct case. However,

using a non-direct solution reduces the robustness of the solver because the iterative solution has a difference from the solution obtained[82]. Some iterative solvers exist in COMSOL Multiphysics including CG, BiCG, BCGSTAB, GMRES, and others. Unlike the direct case where the various solvers guarantee the same solution, in the case of iterative solvers the solution can be different from solver to solver since the method of calculating the approximate solution is different. In addition, it is noted that pre-conditioning or matrix transformation is necessary to simplify the numerical calculation in the various iterative solvers. COMSOL Multiphysics software uses some pre-conditionings (SOR, Multigrid, etc.) that combine with the different iterative solvers.

- 1) **Conjugate Gradient method (CG)**[82][85]: The conjugate gradient (CG) method is an iterative algorithm that applies to a symmetric positive definite system. The solver is based on the evaluation of  $\phi(x) = \frac{1}{2}u^T Au - u^T f$ . Thus, the solver applies an iteration that produces a sequence of even-better approximate minimizes for  $\phi$ . The minimization of  $\phi$  produces an approximate solution to  $Au = f$ . The simple example of the minimization of  $\phi$  is the method of steepest descent. In this method, the minimization of  $u_c$  is improved by searching in the direction of the negative gradient, i.e., the direction of the most rapid decrease.
- 2) **Biconjugate Gradient Method (BiCG)**[86]: The biconjugate gradient method is a generalization of the conjugate gradient (CG) algorithm that applies to non-symmetrical systems as well as symmetrical ones. However, the BiCG has a strong numerical instability that can be solved through some numerical stabilization methods.
- 3) **Biconjugate Gradient Method Stabilized (BiCGSTAB)**[87][88]: the biconjugate gradient stabilized method, is an iterative method developed by H. A. van der Vorst for the numerical solution of nonsymmetric linear systems. It is a variant of the biconjugate gradient method (BiCG) and has faster and smoother convergence than the original BiCG as well as other variants such as the conjugate gradient squared method (CGS). To solve the system, the BiCGSTAB exploits a Krylov matrix ( $K = span(r_0, Ar_0, \dots, A^{n+1}r_0)$ ) where  $r_0$  is the starting solution of the iterative method. Unlike the original BiCG method, it doesn't require multiplication by the transpose of the system matrix.
- 4) **General minimal residual method (GMRES)**[89][90]: the generalized minimal residual method (GMRES) is an iterative method for the numerical solution of an indefinite nonsymmetric system of linear equations. The method approximates the solution using the Krylov matrix ( $K$ ) to find a vector and apply the minimization.

### Preconditioning Algorithm

In general, in an iterative method for  $Au = f$ , the matrix  $A$  can be sparse, making solution evaluation very slow and complex. However, if the matrix  $A$

had a particular form, for example, it was positive defined such that  $A = I + \Delta A$  it is observed that an iterative method returns a solution after a limited number of steps  $k$ . In this section, we analyze the principle of preconditioning algorithms that simplify the matrix  $A$  making the iteration process easier. Having a good preconditioner means fewer interactions. However, the cost of an iteration is an issue associated with the construction of the preconditioner matrix.

- 1) **Jacobi Preconditioner**[82][91]: The Jacobi preconditioner is one of the simplest forms of preconditioning, in which the preconditioner is chosen to be the diagonal of the matrix  $P = \text{diag}(A)$  and the matrix is split in  $A = P - N$  and the resolution of the problem becomes  $Px_1 = Nx_0 + b$ . In this manner, the iteration is simplified.
- 2) **Symmetric successive over-relaxation (SSOR)**[92]: The Symmetric successive over-relaxation consists of dividing the matrix into a diagonal an upper triangular and a lower triangular ( $A = D + L + L^T$ ) by defining the preconditioner  $M = (D + L)D^{-1}(D + L)^T$ . Successive over-relaxation (SOR) is derived from SSOR but it is faster.
- 3) **Incomplete LU Factorization**[93]: The incomplete LU Factorization uses the LU method to derive a preconditioner  $M = LU$  and solve the iteration system.

## Brief Conclusion

This chapter reviewed the main features of the finite element method. In our specific case, through the use of COMSOL software, the FEM models will be used for various simulations in the context of optics and therefore the meshes used will be adapted to the characteristics that the physics of the problem requires i.e., triangulation size much smaller than the incident wavelength, mesh refined on metallic objects given the strong variability of the response, use of parallelograms for the PML (Perfectly Matched Layer), and mesh extremely controlled in the case of periodic boundary conditions. it is important to consider that the mesh construction is highly dependent on the physics considered and the demands of the problem. This prevents the definition of a general algorithm for all cases but requires a case-by-case analysis. To obtain an estimate of the physical solution, a solver appropriate for the number of unknowns in the problem and the computational speed of the machine must be used in addition to the mesh. In addition, in some software like COMSOL, we can use post-processing tools for data manipulation. In general, The data can then be put into 2D or 3D graphs or a part of it can be cut obtaining a 1D evaluation. The data can also be manipulated to obtain the evaluation of certain derived variables, for example, the optical force from the electromagnetic field according to eq.A.21 in our specific case. In the next chapters, we will discuss in detail some physical problems in the field of optics by characterizing them from the point of view of numerical analysis by seeing how the analysis carried out for mesh construction applies to a "real" problem.



## Chapter 4

# Plasmonic Device for Nanoparticle Manipulation

In the previous chapter, we showed that the Maxwell tensor  $T$  (see. eq.A.18) indicates the moments and forces induced by the electromagnetic field applied to an object. It is possible to demonstrate that the effect induced by direct light produces low values of forces and momentum. Thus, for practical use of the optical forces, an amplification of the electric field and the force associated is required. The radiation-matter interaction phenomena, for example the surface plasmon discussed in the previous chapter, are necessary for the optical forces amplification. However, the surface plasmons have large concentrations of energy in dimensions that are smaller than the diffraction limit[55], i.e., concentrated in a small area (about  $\simeq 10^{-12}/10^{-13}m^2$ ); for this reason, we can use the optical forces for the manipulation of micro- and nanometric-sized objects.

In this chapter, we present some nanodevices in which the optical forces control the dynamics of nanoparticles. A typical example is the optical tweezer that constrains the nanoparticles in well-defined areas in statical or dynamic equilibrium. In addition, the literature reports some nanodevices that manipulate the optical force to induce a thrust in the nanoparticle. The characteristics of these structures focus on a possible application for propulsion in macroscopic objects. Finally, we discuss the limits of this class of devices.

### 4.1 Force in Confined Field

From the previous chapters, the eq.A.21 recalls the force induced by the electromagnetic field on a body. The formula has general validity and depends on the electromagnetic field along the object's surface. In this chapter, we define a force approximation when the body has a small size[94].

Let us consider a system with a size much smaller than the incident wavelength  $d \ll \lambda_0$ ; we can approximate the system with a dipole, i.e., two oppositely charged particles with masses  $m_1$  and  $m_2$ , separated by a small distance  $|\mathbf{s}|$ , and

illuminated by an arbitrary electromagnetic field  $\mathbf{E}, \mathbf{B}$ . In the non-relativistic limit, the equation of motion for each particle follows from eq.A.13 by setting  $\mathbf{F}$  equal to  $m_1\dot{\mathbf{r}}_1$  and  $m_2\dot{\mathbf{r}}_2$  respectively. The dots denote differentiation to time. Since the bound of the particles, we consider a binding energy  $U$ . the two-particles equations are:

$$\begin{aligned} m_1\ddot{\mathbf{r}}_1 &= q[\mathbf{E}(\mathbf{r}_1, t) + \dot{\mathbf{r}}_1 \times \mathbf{B}(\mathbf{r}_1, t)] - \nabla U(\mathbf{r}_1, t) \\ m_2\ddot{\mathbf{r}}_2 &= -q[\mathbf{E}(\mathbf{r}_2, t) + \dot{\mathbf{r}}_2 \times \mathbf{B}(\mathbf{r}_2, t)] + \nabla U(\mathbf{r}_2, t) \end{aligned} \quad (4.1)$$

The two particles constitute a two-body problem which is solved using the center of mass coordinate  $\mathbf{r} = \frac{m_1}{m_1+m_2}\mathbf{r}_1 + \frac{m_2}{m_1+m_2}\mathbf{r}_2$ . Expressing the problem in terms of  $\mathbf{r}$  allows us to separate the internal motion from the center of mass motion. The electric field at the position of two particles can be represented by a Taylor expansion[94]:

$$\begin{aligned} \mathbf{E}(\mathbf{r}_1) &= \sum_{n=0}^{\infty} \frac{1}{n!} \left[ (\mathbf{r}_1 - \mathbf{r}) \cdot \nabla \right]^n \mathbf{E}(\mathbf{r}) = \mathbf{E}(\mathbf{r}) + [(\mathbf{r}_1 - \mathbf{r}) \cdot \nabla] \mathbf{E}(\mathbf{r}) + \dots \\ \mathbf{E}(\mathbf{r}_2) &= \sum_{n=0}^{\infty} \frac{1}{n!} \left[ (\mathbf{r}_2 - \mathbf{r}) \cdot \nabla \right]^n \mathbf{E}(\mathbf{r}) = \mathbf{E}(\mathbf{r}) + [(\mathbf{r}_2 - \mathbf{r}) \cdot \nabla] \mathbf{E}(\mathbf{r}) + \dots \end{aligned} \quad (4.2)$$

A similar expansion can be found for  $\mathbf{B}(\mathbf{r}_1)$  and  $\mathbf{B}(\mathbf{r}_2)$ . For  $|\mathbf{s}| \ll \lambda$ , we can truncate it after the second term (dipole approximation) and define the dipole moment  $\mathbf{d} = q\mathbf{s}$  with  $\mathbf{s} = \mathbf{r}_1 - \mathbf{r}_2$ ; leading the following formula for the total force acting on the system of particles:

$$\mathbf{F} = (\mathbf{d} \cdot \nabla) \mathbf{E} + \dot{\mathbf{d}} \times \mathbf{B} + \dot{\mathbf{r}} \times (\mathbf{d} \cdot \nabla) \mathbf{B} \quad (4.3)$$

The second term in eq.4.3 can be represented as:

$$\dot{\mathbf{d}} \times \mathbf{B} = -\mathbf{d} \times \frac{d}{dt} \mathbf{B} + \frac{d}{dt} (\mathbf{d} \times \mathbf{B}) = \mathbf{d} \times (\nabla \times \mathbf{E}) + \frac{d}{dt} (\mathbf{d} \times \mathbf{B})$$

We have approximated the  $\frac{d}{dt}$  like  $\frac{\partial}{\partial t}$  because the velocity of the center of mass is small compared to  $c$  and we use the Maxwell eqs.A.1a-A.1d. We obtain that the eq.4.3 become:

$$\mathbf{F} = (\mathbf{d} \cdot \nabla) \mathbf{E} + \mathbf{d} \times (\nabla \times \mathbf{E}) + \frac{d}{dt} (\mathbf{d} \times \mathbf{B}) \quad (4.4)$$

In addition, the last term vanishes, and the force has the following form:

$$\langle \mathbf{F} \rangle = \sum_i \langle d_i \nabla E_i(t) \rangle \quad (4.5)$$

If we consider that the dipolar particle is irradiated by an arbitrary electromagnetic wave with angular frequency  $\omega$ , we obtain the following equation:

$$\begin{aligned} \mathbf{E}(\mathbf{r}, t) &= \text{Re}[\mathbf{E}(\mathbf{r}, t)e^{-i\omega t}] \\ \mathbf{B}(\mathbf{r}, t) &= \text{Re}[\mathbf{B}(\mathbf{r})e^{-\omega t}] \end{aligned}$$

In the Taylor expansion (eq.4.2) we consider a linear relationship between the dipole and fields, so the dipole assumes the same time dependence and becomes:

$$\mathbf{d} = \text{Re}[\mathbf{d}e^{-i\omega t}] \quad (4.6)$$

We assume that the particle has no static dipole moment. The first order of the dipole momentum is proportional to the electric field in the position  $\mathbf{r}$ :

$$\mathbf{d} = \alpha(\omega)\mathbf{E}(\mathbf{r}) \quad (4.7)$$

where  $\alpha$  denotes the polarizability of the particle and generally is a tensor of rank two but for some atoms and particles  $\alpha$  has a scalar representation. The force in eq.4.4 can be represented as:

$$\langle \mathbf{F} \rangle = \sum_i \frac{1}{2} \text{Re} \left[ d_i^* \nabla E_i \right] = \frac{1}{4} \nabla \left( \mathbf{d}^* \cdot \mathbf{E} + \mathbf{d} \cdot \mathbf{E}^* \right)$$

Using the expression of  $\mathbf{d}$  (eq.4.7) and representing the complex amplitude of the electric field in terms of real amplitude  $E_0$  and phase  $\phi$  as:

$$\mathbf{E}(\mathbf{r}) = E_0(\mathbf{r})e^{i\phi(\mathbf{r})} \mathbf{n}_E \quad (4.8)$$

with  $\mathbf{n}_E$  denoting the unit vector of the polarization, allow us to cast the force into the following form:

$$\langle \mathbf{F} \rangle = \frac{\alpha'}{4} \nabla E_0^2 + \frac{\alpha''}{2} E_0^2 \nabla \phi \quad (4.9)$$

where we used  $\alpha = \alpha' + i\alpha''$ . So, the force induced by an electromagnetic field is composed of two terms. The first term, called "gradient force" depends on the variation of the electric field amplitude and the real part of the polarizability; this term is also known as the scattering force since it can be assumed to result directly from the collision of photons with the nanoparticle. The second term, the "radiation pressure", depends on the phase variation of the electric field and the dissipative part of the polarizability; we consider this term as the pressure exerted by the light beam on the nanoparticle surface.

## 4.2 Plasmon Force Confinement

The previous paragraph illustrates the force behavior in the microscopic environment through the eq.4.9. Thus, a nanoparticle immersed in an electromagnetic field suffers two types of force: radiation pressure and gradient force. When we consider the field generated by a surface plasmon, the gradient force tends to dominate over the radiation pressure, thus a nonuniform field distribution induces intense optical forces.

This paragraph presents some plasmonic devices capable to induce the gradient force for nanoparticles[95]. In particular, one of the earliest uses of optical

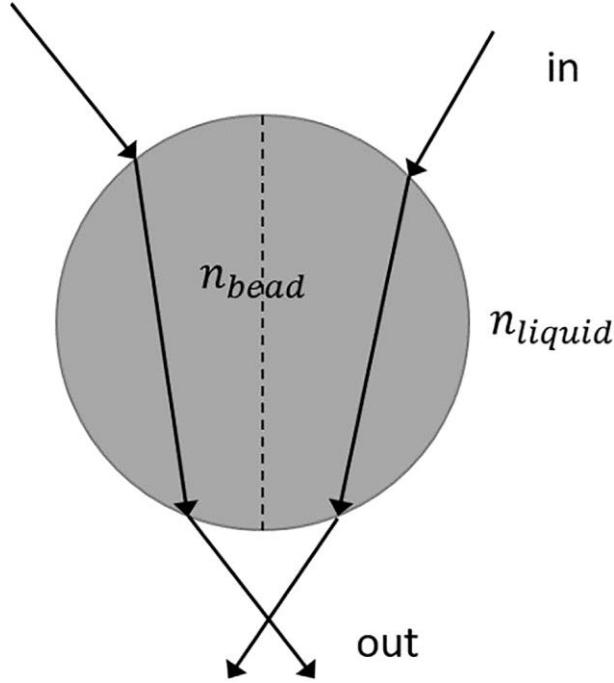


Figure 4.1: Optical trapping method used by Askin. Image reproduced by [95]

forces was to transport and trap static or dynamic equilibrium nanoparticles; in literature, these devices are called optical tweezers.

An optical tweezer is a device proposed for the first time by Askin[96][44] in 1970. Their operation in a macroscopic case is defined as follows: a spherical particle of dielectric material (index of refraction  $n_b$ ) immersed in a liquid (refractive index  $n_l$ ). A laser is focused on the dielectric particle at a point far from the center of the sphere. Due to the transmission effect, the momentum of the incoming beam ( $\mathbf{p}_{in}$ ) has a different direction than the momentum of the outgoing beam ( $\mathbf{p}_{out}$ ). The formation of ( $\Delta\mathbf{p} = \mathbf{p}_{out} - \mathbf{p}_{in}$ ) defines a force that has the same intensity as the force of gravity of the nanoparticle. (see fig.4.1). Moreover, if the particle deflects from the equilibrium point, a pullback force reports the particle to its original position, making the equilibrium stable. If we reduce the particle size to the order of microns or less, Askin's method is unable to maintain the stable equilibrium of the particle due to effects that disturb its effectiveness[97]. In particular:

- 1) The reduction of the pullback force is related to its dependence on the volume of the particle.
- 2) The reduction in viscous fraction due to the dependence on the surface area of the particle.
- 3) The increase of the temperature effect when the particle is microscopic and the consequent generation of chaotic motion around the equilibrium point.

The intensity increase of the incident laser beam mitigates the delocalization effect and other microscopic effects. The main limitation of this technique is related to the size of the particles. When this reaches a value close to half of the wavelength of the incident beam, diffractive effects appear which tend to disperse the beam of light and prevent it from focusing on the particle. To overcome this limitation we can use the surface plasmon phenomena[97][98][99] that generate extremely concentrated fields beyond the diffractive limit, succeeding to trap a nanoparticle with extreme efficiency. When an electromagnetic wave irradiates a plasmon optical tweezer at the resonance frequency, a symmetrical field distribution (hotspot) is generated in a specific area of the structure such that the resulting force tends to trap the nanoparticles in the hotspot center. A

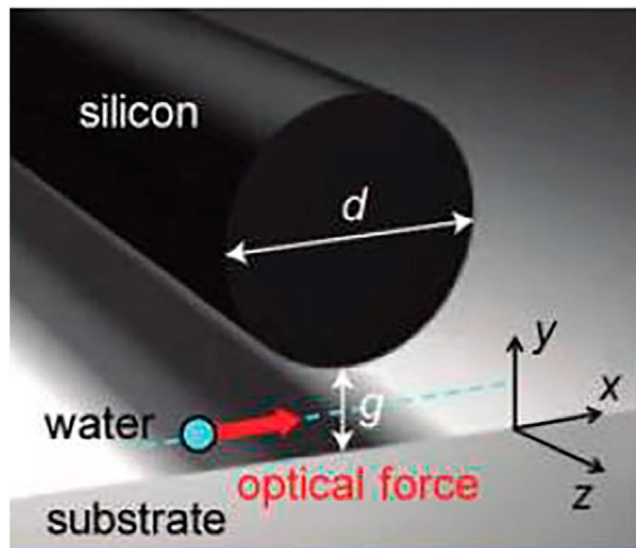


Figure 4.2: Image showing the silicon waveguide separated by a sub-micrometer gap to metal substrate, showing the optical force applied to the nanoparticle. Image reproduced by [100]

typical example of a plasmonic optical tweezer is shown in fig.4.2[100], where a cylindrical silicon waveguide is placed at a distance ( $g$ ) from a metallic substrate.

When the system is illuminated from the  $z$  axis, an electric field hotspot is generated in the space between the guide and the metal substrate, and the associate force is such that the nanoparticle is trapped in this gap. In addition, generating symmetrical field distribution that tends to lock the nanoparticles at a defined point, plasmonic optical tweezers can also be designed to achieve equilibrium dynamically, that is generating a stationary movement around a given point. An example of these types of structures is illustrated in fig.4.3(a)[101], where an optical tweezer is constructed using a plasmonic bull's eye configuration to transform the incident wave into converging plasmonic waves. For the particles to be trapped in the center of the structure, the plasmonic wave has to interfere constructively in the center, and a phase shift of  $\pi$  is required in the generation of various SPPs. It is necessary to modulate the plasmonic wave in such a way that the interference of the various SPPs occurs at different positions from the center of the structure.

Thus, the phase function ( $\phi$ ) of the incident beam must depend on both the polar angle of the bull's eye ( $\theta$ ) and the spatial point where the particle is trapped ( $x, y$ ):

$$\phi(x, y, \theta) = \begin{cases} 2\pi\sqrt{\left(\cos\theta + \frac{x}{a}\right)^2 + \left(\sin\theta + \frac{y}{a}\right)^2} & -\frac{\pi}{2} \leq \theta \leq \frac{\pi}{2} \\ \pi + 2\pi\sqrt{\left(\cos\theta + \frac{x}{a}\right)^2 + \left(\sin\theta + \frac{y}{a}\right)^2} & \frac{\pi}{2} \leq \theta \leq \frac{3\pi}{2} \end{cases} \quad (4.10)$$

where  $a$  is the period of the Bull's eye pattern which is chosen equal to the wavelength of the SPP at the interface between silver and water. To verify this behavior, the authors carried out some simulations using COMSOL in which the plasmonic ring was modeled assuming a set of sources along the ring with a field defined as:

$$E_z^{sp}(\rho, \theta) = \frac{e^{ik_{sp}\rho}}{\sqrt{\rho}} e^{i\phi} \cos(\theta) \quad (4.11)$$

where  $\rho$  is the distance from the source point,  $k_{sp}$  is the wave number of the SPP with  $\theta, \phi$  defined in the eq.4.10. The simulation shows that a hot spot (fig.4.3(b)-(c)) is formed whose position depends on the phase of the incident beam, confirming the assumption defined above. Fig.4.3(d) shows the difference between the x-long component of the resulting force in a Bull's eye device case (orange) compared to a conventional optical tweezer (blue). It can be seen that the force generated by the Bull's Eye is much more intense than in the conventional case; the same result is also obtained if we compare (fig.4.3(e)) the component along  $z$  of the forces of the Bull'eye (orange) for the conventional case (blue). For this reason, the plasmonic Bull's Eye has more effective trapping than the conventional case. Moreover, the result shows that using a beam with a time-varying phase, the trapping site moves, generating a movement of the nanoparticle. The motion obtained is such as generating either linear trajectories along specific directions or circular trajectories (some examples are shown in fig.4.3(a)). Fig.4.4[102] proposed another particular case of a plasmonic op-

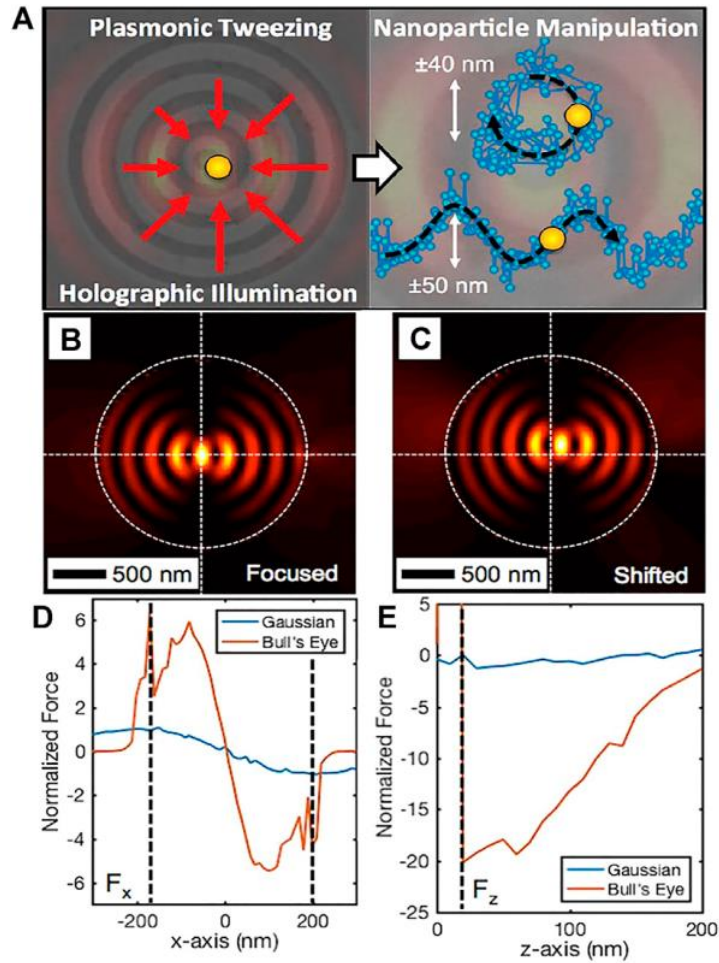


Figure 4.3: a) the plasmonic bull's eye with the direction of the plasmonic waves used to trap the particle in the center and some trajectories that can be generated with time-dependent beam; b) centered hot spot simulated with eq.4.10 c) shifted phase profile hot-spot simulated with eq.4.10;d) Normalized force plot for a Bull's eye device and conventional optical tweezers for x-component force ;(e) Normalized force plot for a Bull's Eye device and a conventional optical tweezers for z-component force. Images reproduced by [101]

tical tweezer with dynamic equilibrium obtained using an array of gold dimers separated by a gap. These are irradiated by a polarized field along x, generating forces and relative moments on polystyrene nanoparticles in the vicinity of the system.

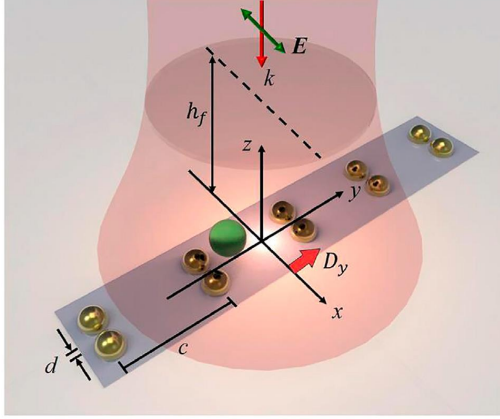


Figure 4.4: Configuration of a 1D gold dimer array trapping a nanoparticle using a normally incident Gaussian beam. The dimer gap, lattice constant, and displacement along  $y$  are denoted respectively by  $d$ ,  $c$ , and  $D_y$ . The Gaussian beam is polarized along  $x$  and has parameters  $h_f$  and  $w_0$ . Image reproduced by [102]

The fig.4.5(a) shows the optical force generated by the system; to achieve the equilibrium this optical force is compensated by the friction force generated by the liquid in which the nanoparticle is immersed. The system generates two types of equilibrium: a contact equilibrium in which the nanoparticle tends to adhere to a gold dimer, and a non-contact equilibrium in which the dimers generate a swirling motion around a point in space, known as the stagnation point. The resulting moment is the combination of the angular momentum generated by the Maxwell Tensor and the momentum generated by friction with the liquid. Fig.4.5(b) illustrates the generation of two nanoparticle spins, the direction of which depends on the vortex's torsion. In particular, if the vortex rotates clockwise (Fig.4.5(a)), there will be an anticlockwise nanoparticle spin (Fig.4.5(b)), whereas if the vortex rotates anti-clockwise (Fig.4.5(a)), there will be a clockwise nanoparticle spin. Moreover, the result shows that if the dimer array is moved away from the focal point of the beam, the nanoparticle initially tends to follow the array. However, there is a threshold length which, if exceeded, generates an additional vortex leading to trapping of the nanoparticle away from the dimeric matrix. Finally, since these structures are plasmonic, the increase in the vortex intensity reduces the distance or gap between the dimers.

### 4.3 Plasmonic Optical Thruster

The previous paragraph explains how plasmonic optical tweezers can keep a nanoparticle in equilibrium using a symmetrical electric field distribution. How-

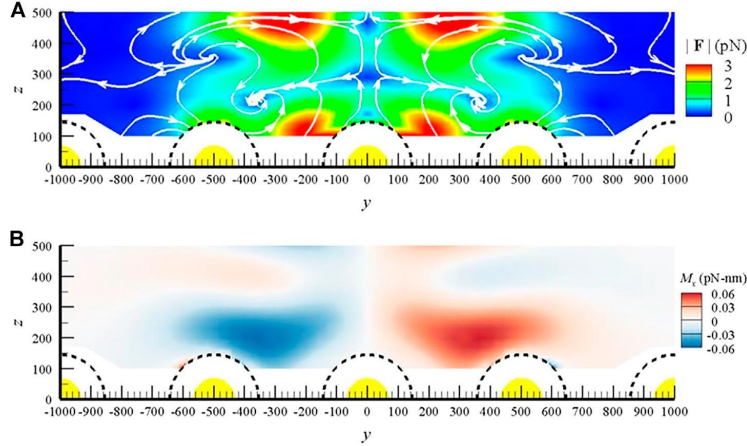


Figure 4.5: a) Optical vortex manifested in a streamlined map of the optical force field. In particular, this streamlined map depicts the field of forces ( $F_y$ ,  $F_z$ ) applied to a polystyrene nanoparticle centered at different places in space ( $y, z$ ) in the  $yz$  plane at  $x = 0$ . The arrows and colors represent the direction and magnitude of the optical force respectively. The dotted lines represent the physical limit of the polystyrene nanoparticle considered here with a radius of 100 nm. The image is evidence of the presence of both contact and non-contact modes for optical trapping. The stagnation points of the non-contact modes are shown at  $x_0 = (0, \pm 361nm, 207nm)$ . b) Map of nanoparticle spin moments. The coloring represents the intensity of the moment. Images reproduced by [102]

ever, it is possible to induce a long-range force in a microscopic object using a gradient force induced by a specific field distribution. This paragraph shows that the surface plasmonic effect achieves the gradient force for nanoparticle displacement.

A simple plasmonic device [103] consisting of a metal layer placed on a base of a prism with the tip pointing downwards (Kreshmann configuration) (see Fig.4.6). A gold nanoparticle is placed in this structure in an aqueous solution. If the particles are free from any constraint they tend to move only for thermal effects. These effects generate a chaotic motion (Brownian motion) in all space directions. When an incident beam illuminates the prism at a certain angle, a nanoparticle tends to acquire a drift velocity in the direction parallel to the air-metal interface ( $x$ -axis) and in the direction orthogonal to it ( $z$ -axis) (we can see in Fig.4.6). However, the drift only occurs if the incident beam has a TM polarization. This suggests that the cause of the drift phenomenon is

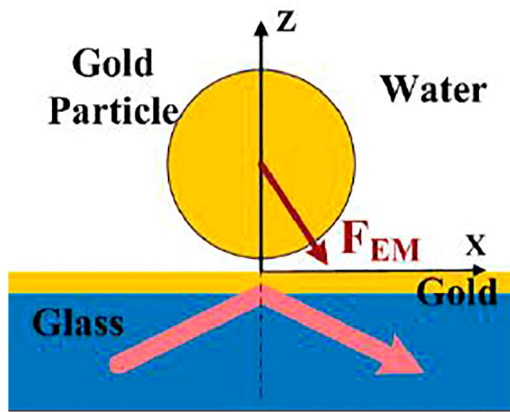


Figure 4.6: Interface of plasmonic coupling with gold nanoparticle ( $xz$  plane). Image reproduced by [103]

attributable to the formation of SPP. The contextual observation of a chaotic motion along the  $y$ -axis confirms the hypothesis. The SPPs are such that they generate field distribution only along the interface and orthogonal to it so this implies that forces are obtained only along the aforesaid directions, leaving the  $y$ -axis free from any constraint. Fig.4.7 presents the results of the analysis of the optical forces (and the induced velocity) acting on the nanoparticles, as a function either of the distance between the metal surface and the aqueous solution and the intensity of the optical beam. In particular, the drift speed tends to increase in function of the incident beam intensity, implying that the optical force also increases as the intensity increase. On the other hand, as the distance between the metal and the nanostructures increase, the force tend to decrease, with different behavior depending on the force component observed. The force along  $z$  tends to decay exponentially as the distance varies, while that along  $x$  decays linearly. Finally, the authors[103] compare the propulsion generation obtained through the formation of an SPP, and the propulsion generation obtained through total internal reflection,i.e., using the same structure but without the metal layer. The results show that the SPPs electric fields are much more intense, although they can only be used if the excitation beam illuminates the structure at the right resonance angle. A more complex configuration capable of generating propulsion with an output speed that can be used for medical-biological applications is the optical nanocannon[104][1]. The structure ( see Fig.4.8) consists of a V-shape cavity made of a gold film deposited on a glass substrate. When a TM-polarized light wave irradiates the structure from above

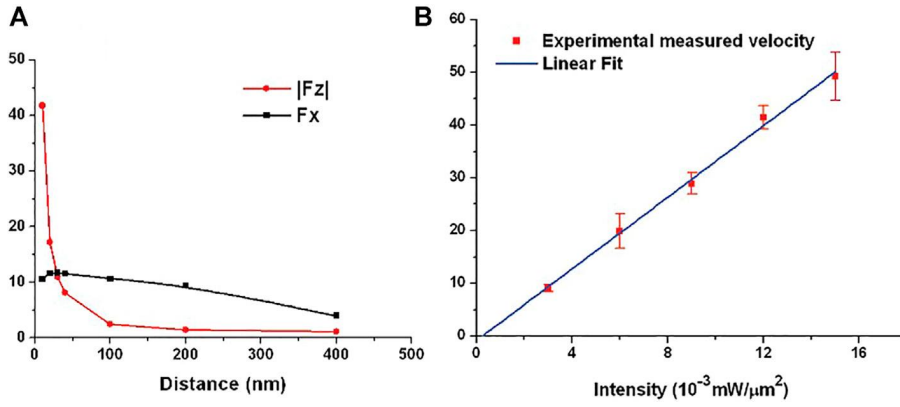


Figure 4.7: a) The components of the optical force applied to the nanoparticle as a function of the distance between the particle and the metal substrate. b) The velocity of the particle is measured as the intensity of the incident beam changes. Images reproduced by [103]

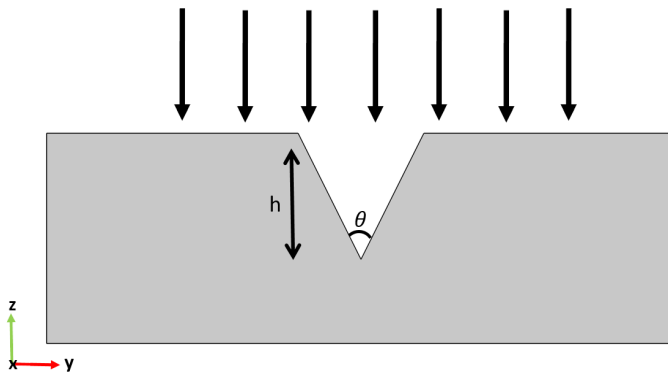


Figure 4.8: Sketch of the V-shape plasmonic structure, illuminated by a TM-polarized light. Image adapted by [104]

(see fig.4.8), generates an intense electric field at the bottom of the trench; this is due to the generation of a resonant LSP. Once the resonance is excited, two SPPs are formed along the edges of the structure by near-field excitation. The coupling of the two Surface Plasmons implies a significant field amplification. The amplification factor is a function of the geometrical parameters and in particular, an increase can be obtained if the angle ( $\theta$ ) of the V-shape is reduced. In particular, when the two edges of the V-shaped trench approach each other,

the interference effects between the two SPPs are amplified. Even the resonance is highly dependent on the depth ( $h$ ) and angle ( $\theta$ ) of the V-shape. In particular, the wavelength of the resonance increases (red-shift) if the trench depth  $h$  increases or its angle  $\theta$  decreases. On the other hand, the amplification factor of the electric field tends to decrease when the resonances are at long wavelengths. This behavior can be explained by considering that gold at long wavelengths tends to behave like an ideal metal, absorbing most of the SPPs that form along the edges. The plasmonic structure generates an electromagnetic field with an asymmetric distribution. The distribution presents a maximum at the bottom of the V-shape and a minimum at the top of the trench, at the surface of the metal layer. This distribution can be explained by taking into account that SPPs tend to reduce their effectiveness as they propagate along the edge of the trench. Starting from the spatial distribution of the electromagnetic field and integrating the Maxwell tensor on the surface of a nanoparticle (eq.A.21), the force acting on the particle and its outward ejection can be determined. The force obtained from the Maxwell tensor (eq.4.9) has a dominant gradient term over the radiation pressure. In particular, the gradient force displaces the nanoparticle along the z-axis (i.e., along the height of the V-shape) with a velocity derived from the formula (eq.A.21) that takes on the following value[1]:

$$\mathbf{v} = \sqrt{\frac{3}{2\rho_{eff}} \tilde{\alpha} \epsilon_0 \mathbf{E}} \quad (4.12)$$

where  $\rho_{eff}$  is the effective density of the nanoparticle, whereas  $\tilde{\alpha}$  represents the polarizability per unit volume that is a function of the dielectric permittivity relative to the substrate and the metal. The eq.4.12 is derived by considering that the force is entirely a gradient force and that the potential generated by it is entirely transformed into kinetic energy. Numerical simulations were carried out on the structure and the velocity of a silver nanoparticle with a radius of 8 nm was estimated. The estimated velocity is  $0.1m/s$ [1] when illuminating the plasmonic structure by a TM-polarized wave having a power density of  $1 - 2 \frac{mW}{\mu m^2}$  and a wavelength in the visible range (required for the SPPs formation). The speeds obtained allow the transport of drugs and genetic material in the cells and are therefore interesting for possible application in the medical-biological sector. However, a single structure does not induce a high velocity in nanoparticles, so the propulsion described above can be used for applications requiring the movement of a small object for extremely small distances.

Rovey's[2][105][106] group has designed a plasmonic structure that allows higher values of thrust and velocity. Rovey's device does not increase the force generated in a single structure; however, the single device can be coupled in a large number of elementary structures defining an array configuration. The resulting force is the sum of elementary contributions related to the single structure. The resultant force is greatly amplified and can be used in numerous applications, including space propulsion. The system (see Fig.4.9) consists of two trapezoidal gold structures separated by a constant gap and deposited on a glass substrate.

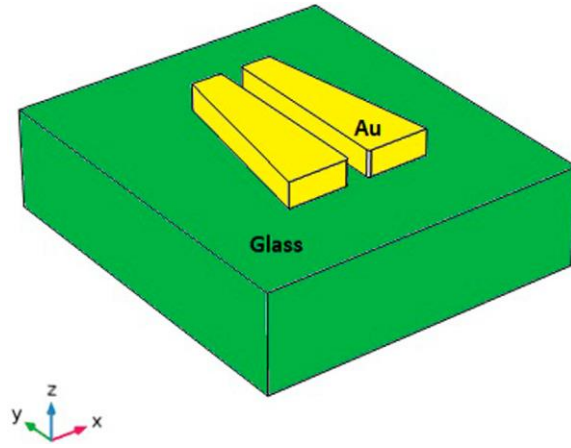


Figure 4.9: Sketch of the asymmetrical trapezoidal plasmonic structure. Image reproduced by [95]

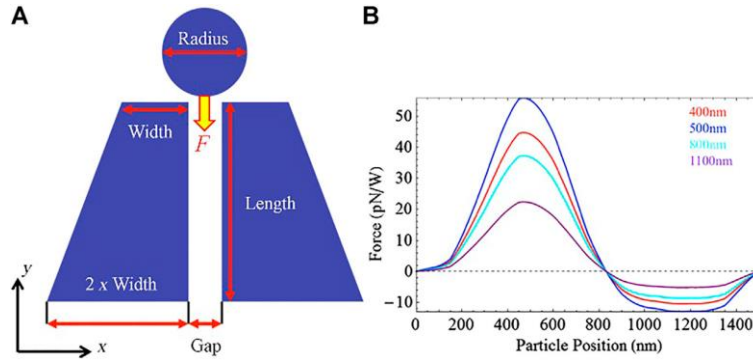


Figure 4.10: a) A cut in the  $xy$  plane of the trapezoidal structure, showing the direction of the ejection force; b) the graph of the force in function of the  $y$ -coordinates for different resonant wavelength. Images reproduced by [2]

When the structures are uniformly illuminated, a resonance, due to the generation of an LSP, is formed in the gap between the two trapezoids. The resonance wavelength depends on the geometrical parameter of the gold structures, i.e., the width of two bases of the trapezium, its length, its thickness, and the gap size. After the formation of an LSP, the near-field excitation forms two SPPs along the edges of the two trapezoids that couple within the gap and, as in the structure discussed in the previous paragraph, generate a strongly amplified and asymmetric field distribution. By calculating the forces through the Maxwell tensor (eq.A.21), we obtain a distribution that depends on the position along  $y$ -coordinate of the system (see Fig.4.10(a)), such that a nanopar-

ticle undergoes a strong initial acceleration followed by a deceleration zone of lesser intensity (see Fig.4.10(b)). Preliminary experimental results for this configuration confirm the functionality expected from theory and simulation[106]. In general, the structures with larger horizontal asymmetries (i.e. along the x-axis) have more amplified electric fields. Therefore to induce further asymmetry, the oblique side of the trapezoid can be modified in a stepwise manner. (Fig.4.11) shows a comparison of the field distribution between a trapezoidal structure with linear and stepper oblique sides[107]. As mentioned above, the

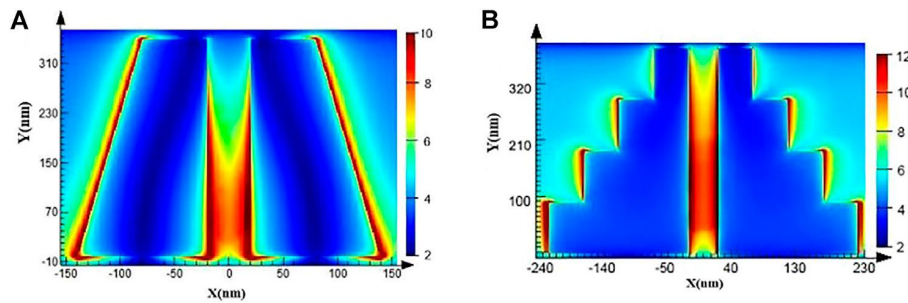


Figure 4.11: a) Electric field distribution in a trapezoidal structure the wave is polarized along x at wavelength 532 nm; b) electric field distribution of a modified oblique-sided trapezoidal structure with the wave polarized along x and at wavelength 580 nm. Image reproduced by [107]

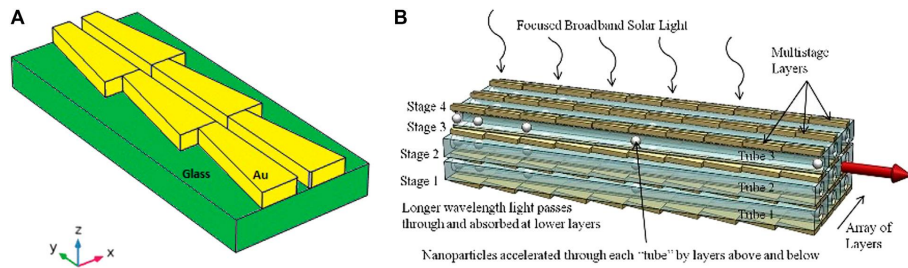


Figure 4.12: a) A sketch of the array configuration in end-to-end mode; b) the thruster hypothesized by Rovey et al. (2015) to make full use of sunlight.[2]. Images reproduced by [95] and [2]

output speed induced by a single plasmonic structure is relatively low. To obtain more efficient performances useful for practical application, an array of the above elementary structure can be constructed by organizing it through a 2D

distribution in a so-called end-to-end configuration (Fig.4.12(a)). In this configuration, the minor base of a trapezoid is adjacent to the major base of the next structure. The array configuration implies a continuous sequence of pushes on the nanoparticle, which implies a considerable increase of the force applied and, consequently, of the output speed. The plasmonic structure [2] was arranged in a multilayer array configuration where each layer has a different resonance wavelength to function properly even with broadband illumination such as solar radiation (see Fig.4.12(b)). In fact, with this approach, each layer of the stack can use a specific part of the solar spectrum, increasing the overall efficiency. The nanoparticles are contained in a nanochannel between the active layers so that the resulting force applied to the nanoparticle will be a combination of the forces obtained from the arrays above and below each channel. Thanks to

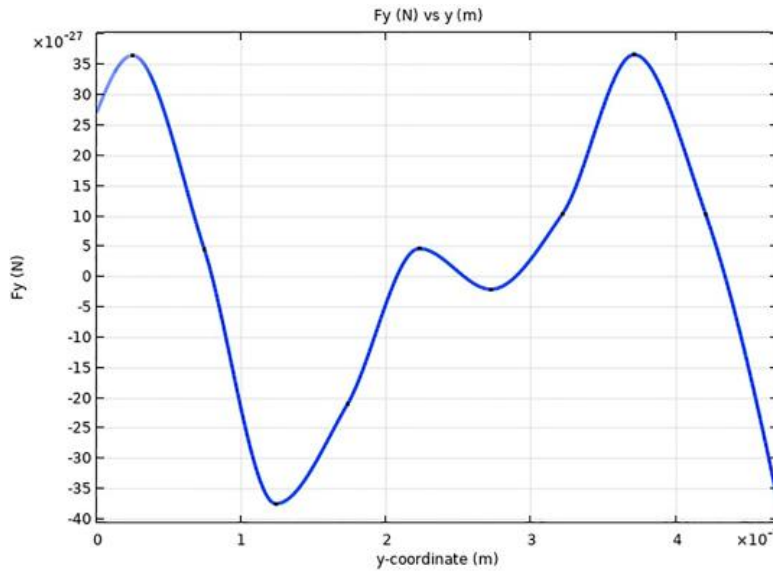


Figure 4.13: Y-component of the force applied to a glass particle of radius 50 nm as a function of the y-coordinate of a set of trapezoidal structures as in Rovey et al. (2015), placed in an end-to-end configuration with the following parameters: height 350 nm, major base 120 nm, minor base 60 nm, gap 40 nm, thickness 50 nm. The light is polarized along x and at wavelength 730 nm and the amplitude of the incident electric field is such that it is normalized. Image reproduced by [95]

its estimated performance, this plasmonic configuration has been proposed as a thruster for space applications. The values of thrust, specific impulse, and ejection velocity of a nanoparticle for the thruster based on the multilayer array

configuration are estimated using the following relationships:

$$\frac{v_i^2}{2} = \int_0^L \frac{F_{above}(y) - F_{below}(y)}{m} dy \quad (4.13)$$

$$\mathbf{T} = \sum m f \mathbf{v}_i \quad I_{sp} = \frac{|\mathbf{T}|}{N m f g_0}$$

where  $m$  is the mass of the nanoparticle,  $N$  is the number of arrays in a single layer (the number of rows in Fig.4.12(b)),  $f$  is the ejection rate of the nanoparticle,  $L$  is the acceleration length, and  $F_{above}, F_{below}$  are the force distribution generated by the arrays located above and below the nanoparticle under consideration, respectively. The result obtained from the simulations shows propulsion values of around  $400 - 600nN$  and specific impulse around  $20s$ , with an exit velocity of  $3 - 4m/s$ . These parameters are highly dependent on the area of the amplification lens, which determines the actual value of the optical power density illuminating the structure.

However, as can be seen in fig.4.13[108], the array presents a potential limitation. When the elementary structures are organized in an array with an end-to-end configuration, the distribution of forces is such that the particle must overcome a potential barrier to pass from one elementary structure to the next. The intensity of this potential barrier is such that the kinetic energy of the particle is not sufficient to allow its overcoming in the short space in which the particle acquires velocity. For this reason, the particle needs an additional initial thrust that is sufficiently high to overcome the potential barrier and continue the motion.

In this chapter, we then presented some applications of optical forces induced by surface plasmons. In particular, we focused on the characteristics and limitations of plasmonic devices that induce a propulsive optical force. The devices just described lay the foundation for the design of a secondary plasmonic propulsion system. As we will discuss in the next chapter, the design, and analysis of new plasmonic structures that induce dynamics in nanoparticles will depend on overcoming the limitations exposed in the literature.

## 4.4 Plasmonic Device with gap variation: Alternating constant gap trapezoids

We introduce some devices capable of inducing propulsion such as the optical nanocannon or trapezoidal structures. In paragraph 4.3 we showed that the devices considered have a limitation that reduces their effectiveness in some specific cases: e.g. the nanocannon has good parameters only for the ejection of small nanoparticles while the trapezoidal structures need an initial boost to induce a good estimate of force. However, for the displacement of a CubeSat, it is necessary to design a plasmonic optical thruster without dynamic restrictions. Let us consider the eq.4.9 and observe a relation between the electric field variation and the optical force applied to a nanoparticle. If we want to

overcome the previous limitations we need a periodic structure ( in order to have a periodic growth of the velocity), with the slope of the electric field amplitude distribution having strong variability, because the associated gradient induces a good estimate of the force according to eq.4.9. Given the propagation equation of SPPs (eq.2.23-2.24), we observe that the wave is evanescent along a transverse direction to the propagation. In the case of a trapezoidal structure, propagation follows the direction of the gap (i.e., the y-axis), and we will observe evanescence along the x- and z-axis. The presence of an evanescent wave along the x-axis implies that the distance between the trapezoid edges reduces the interference effect between the SPPs. Thus, the amplitude of the center gap resonance decrease. Therefore, it is possible to control the electric field strength by varying the gap of the trapezoidal structures. In particular, if we design a periodic nanodevice with a large gap in one part of the structure and a very slow gap on the other side, the electric field distribution will be strongly asymmetric.

The following hypothesis is the design of an alternating system consisting of a pair of rectangular trapezoids with constant gap  $g_1$ , followed by another couple of rectangular trapezoids with constant gap  $g_2$ . When an incident light beam illuminates at the resonance wavelength, the structure forms an LSP along the major bases of the trapezoid. However, due to the evanescent property of SPPs, if  $g_1 > g_2$  we have that  $|E_2| > |E_1|$ . As in the previous case, the LSPs become a near-field source for the SPPs along the edges, and the coupling generates two asymmetric electric field distributions with different intensity values. The different intensity values imply an increase in the electric field gradient and the formation of an optical force without dynamics limitation.

We performed a FEM simulation to verify the optical force in this trapezoidal device using COMSOL Multiphysics software. The model (see fig.4.14) consists

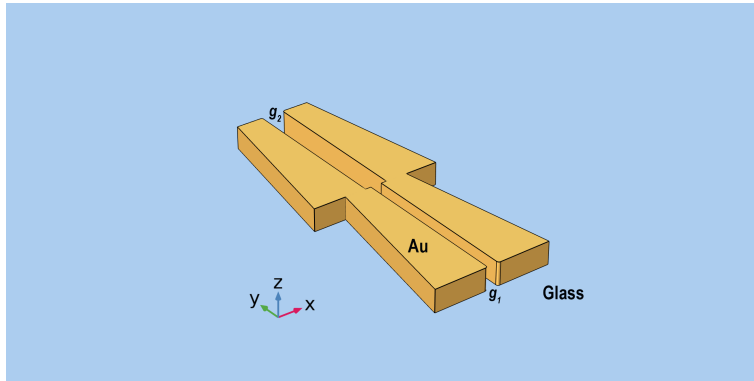


Figure 4.14: Sketch of plasmonic structure with alternating gap

of four trapezoids that have the following dimensions: major base ( $B$ ) =  $120nm$ , minor base ( $b$ ) =  $60nm$ , height ( $h$ ) =  $350nm$ , thickness ( $t$ ) =  $50nm$ ; two trapezoids are placed at distance  $g_1 = 25nm$ , while the other two are placed at distance  $g_2 = 50nm$ . We design a pair of trapezoids with gap  $g_1$  and a pair of

trapezoids with gap  $g_2$  such that the minor base of  $g_1$  trapezoids is adjacent to the major base of  $g_2$  trapezoid. The structure is made of gold, and a block of air, with width ( $w = 600nm$ ) and height ( $h_2 = 1500nm$ ), is defined above the structure, and a block of silica with the same dimension below the structure. Physics is described using the "wave optics" [109] module of COMSOL Multiphysics. In particular, the "wave optics" module defines the incident wave in two different ways. 1) Background wave: the incident wave is defined through a plane wave with electric field  $E = E_0 e^{i\omega t}$  with  $t$  fixed, which represents an approximation of an incident wave in an infinite-size substrate; however, this approximation doesn't consider the optical response of the substrate (reflections, transmissions, diffraction). 2) Port: Simulates the presence of an electromagnetic source that "illuminates" an object placed at a certain distance. Unlike the background wave case, the port does not approximate the incident field, so it simulates the real case of a source impinging on a substrate of the dimensions defined in the geometry.

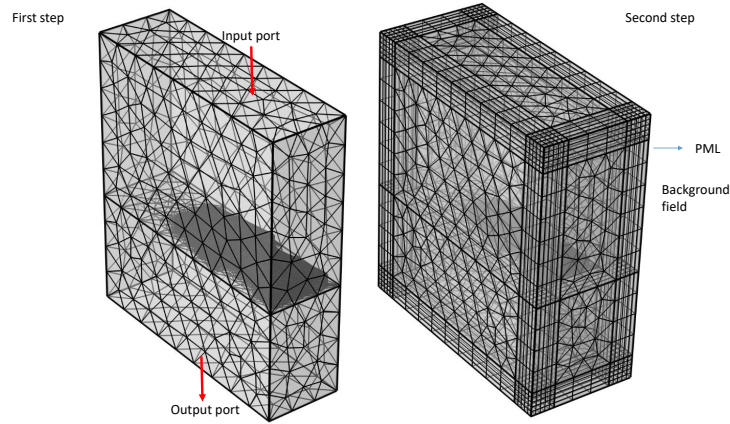


Figure 4.15: Two-step model used for the simulation with and the mesh of the domain

To simulate the case of a wave acting in a plasmonic device placed in an infinite substrate, a background wave is not suitable since the electric field response would not be complete given the plane wave approximation. However, the ports also present some issues because, for a good approximation of the infinite-size substrate, the geometric domain has to be one order of magnitude larger than the structure size. Thus, the number of nodes in the domain subdivision during the FEM calculation will be huge and the available computer is not able to reach to evaluate them. For this reason, a technical artifice observed in the COMSOL application [110] is used (fig.4.15). A double study was considered; the first step use a port with an x-polarized incident field  $E_0 = 1V/m$  and a power given by the formula  $P = \frac{1}{2} \frac{E_0^2 A}{Z}$ , where  $Z_0$  is the vacuum impedance and  $A$  is the illuminated area. The port illuminates an air-substrate system and the result

of the first step becomes the background wave acting on the structure for the second step. PML surrounds the physical domain to avoid backscattering effects and simulate the infinite-size substrate for a single isolated cell. The PML is an artificial absorbing layer for the wave equation, commonly used to truncate computational regions in numerical methods ( FEM methods) to simulate problems with open boundaries. In particular, a PML layer is designed to absorb waves propagating using the following transformation: considering  $z$  the propagation direction and  $\partial/\partial z$  its derivative we apply the following transformation:

$$\frac{\partial}{\partial z} = \frac{1}{1 + \frac{i\sigma(z)}{\omega}} \frac{\partial}{\partial z} \quad (4.14)$$

where  $\omega$  is the angular frequency and  $\sigma$  is some function of  $z$  positive defined. When using this transformation the propagating waves are attenuated because:

$$e^{i(kz-\omega t)} = e^{i(kz-\omega t) - \frac{k}{\omega} \int_z \sigma(z') dz'} \quad (4.15)$$

Given the properties of PML[111],[112], the electric field dampens in the artificial domain,i.e., we are simulating the following property of infinite-length domains:

$$\mathbf{E}(x, y, z) \rightarrow 0 \quad \text{if } x, y, z \rightarrow \infty \quad (4.16)$$

Finally, the result obtained from the second study will be the electric field response from a plasmonic device immersed in a domain of infinite dimension.

Once the physics of the system is defined, we define the subdivision of the geometric domain for the FEM calculation; in COMSOL, this is called "mesh definition." In this specific case, the mesh has two different subdivisions: one for the physical domain and one for the PML (see fig.4.15). For the PML case, we use a parallelepiped subdivision because the directionality of the PML requires a quadrilateral mesh. In the physical domain, on the other hand, we don't need to consider any directionality, therefore, a solid with fewer nodes is preferred to facilitate computation. We use a set of tetrahedrons for the physical domain mesh. The tetrahedrons have different sizes depending on the region of the physical domain we subdivide. In air and silica domain, we will have tetrahedrons of maximum size  $\lambda/5$  and minimum size  $\lambda/90$ . On the other hand, in the gold region, since the evanescent wave has a small spatial range tetrahedrons have maximum size  $\lambda/20$  and minimum size  $\lambda/200$ . Moreover, we chose the tetrahedrons in such a way that they are very dense around the plasmonic device region and with increasing size the further we move away from the plasmonic zone. We use a direct solver (MUMPS) to solve the numerical system, and the study initially evaluates the wavelength range from 600nm to 1000nm for the research of the resonance wavelength. Once we found the resonance wavelength at 730nm, we evaluate the electric field of the structure ( $|E|$ ) observed in fig.4.16(a).

Fig.4.16(b) shows that the electric field induced by the plasmonic device is located within the gap between the trapezoid pairs (along the red dashed line of the fig.4.16(a)). In particular, we observe the presence of two peak maxima:

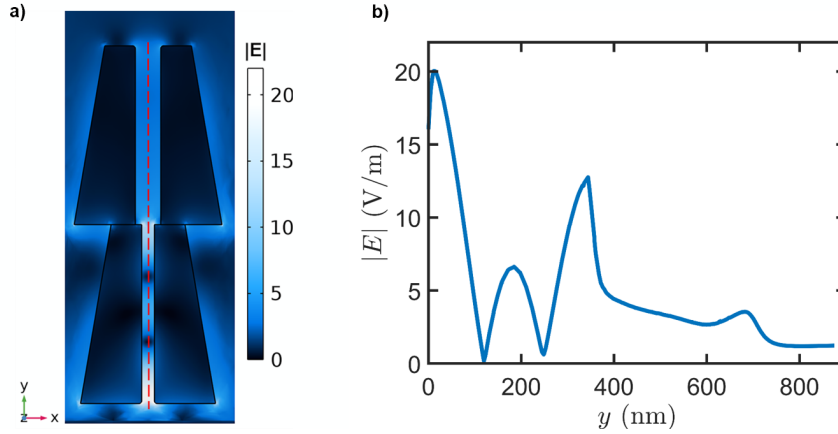


Figure 4.16: a) 2D distribution of the electric field amplitude in the trapezoidal structure with an alternating gap. b) Electric field amplitude in the function of  $y$  coordinate in the trapezoidal structure with an alternating gap along the red line of the fig.4.16(a)

a main maximum located around the major base of the trapezoids with gap  $g_1$  and a secondary maximum located at the major base of the trapezoids with gap  $g_2$ . The resonance wavelength of the LSP depends on the shape of the plasmonic structure (major base, minor base, height, and thickness). Thus, the gap variation doesn't change the resonant wavelength. Instead, the gap variation affects the amplitude of the electric field that depends on the trapezoid's distance. The two peaks obtained (one per pair of structures) have different field values. The result increases the asymmetry of the electric field distribution.

For the evaluation of the dynamic properties of the plasmonic device, we place the elementary cell in an end-to-end linear array configuration. The FEM simulation model for the linear array configuration is different from the isolated cell model. We use the same geometry of the single isolated cell case but the boundary surface of the computational domain coincides with the boundary surface of the plasmonic device. The physics of an array configuration is reproduced using periodic boundary conditions along the surfaces of the computational domain. This physics tool simulated an infinite times reproduction of the elementary cell; for this reason, we did not use the previous double study. The Perfectly Matched Layer is no longer placed all around the structure but only above and below the ports to cancel the backscattering effects of the incident beam.

In mesh construction, periodic boundary conditions require special attention. In particular, the surfaces where the periodicity condition is valid must have the same triangulation. In preserving the equivalence between the periodic boundary condition, dummy surfaces are defined, such that the same triangulation is imposed between the boundary surfaces. In contrast, the model's volume

has the same mesh as the single-structure case. We have for the physical domain a set of tetrahedral with the same dimensions as the previous case and the PML presents a set of parallelepipeds to maintain the directionality typical of this artificial domain.

As in the case of a single structure, a direct solver (MUMPS) is used to resolve the linear system, and the study analyzes the solution for wavelengths ranging from 600nm to 1000nm, evaluating the resonance wavelength. Once the resonance wavelength is found at 780nm we plot of electric field amplitude in Fig.4.17. Fig.4.17 shows that the electric field of the linear array configuration

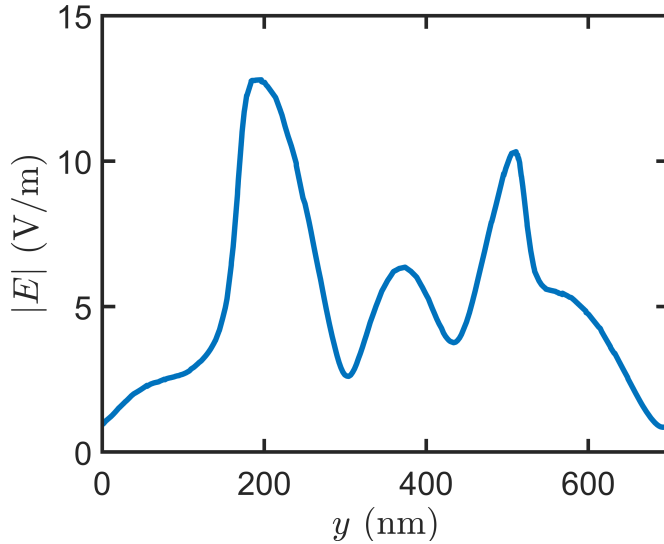


Figure 4.17: Electric field amplitude in the function of  $y$  coordinate in an array configuration of trapezoidal structure with an alternating gap along the red line in the fig.4.16(a)

exhibits the same characteristics as the single-structure case, i.e., the presence of two peaks of maximum: one main peak around the major base of the trapezoid with gap  $g_1$  and the other secondary peak around the major base of the trapezoid with gap  $g_2$ . However, the amplification of the electric field is globally reduced in the array configuration compared with the single-structure case. The coupling of the elementary cells generates destructive interference that dampens the plasmonic amplification. For the force analysis, since the nanoparticle has dimensions smaller than the incident wavelength we can approximate the optical force using the eq.4.9. Since the radiation pressure depends on the incident electric field and it will be negligible compared to the gradient force that depends on the total electric field (more amplified from the plasmon phenomena), the gradient force is the value that determines the cinematic of a nanoparticle.

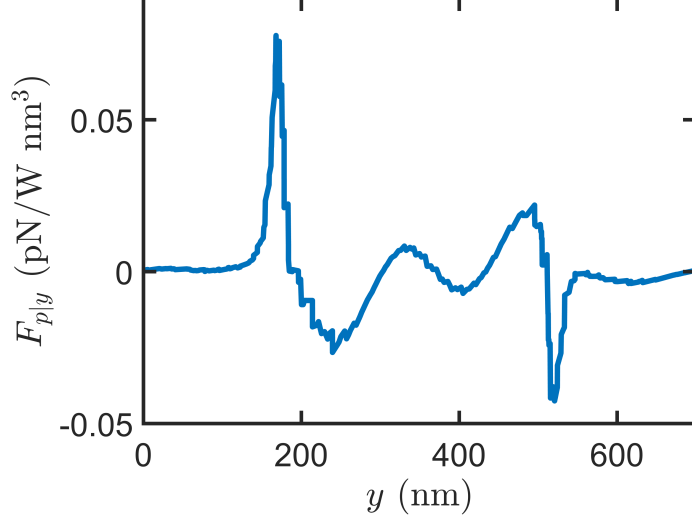


Figure 4.18:  $F_{p|y}$  in the function of  $y$  coordinate in an array configuration of trapezoidal structure with alternating gap along the red-line in fig.4.16(a)

We can define the following quantity:

$$\mathbf{F}_p = \mathbf{F}/(P\alpha') = \frac{\epsilon_0 \nabla |\mathbf{E}|^2}{P} \quad (4.17)$$

where  $\alpha'$  is the real polarizability of the nanoparticle.  $\mathbf{F}_p$  represents the optical force contribution per unit of power produced by the plasmonic device. In fig.4.18 the trend of  $\mathbf{F}_p$  for constant gap trapezoidal structure is shown; we can compare it with the constant trapezoidal force case shown in fig.4.13. In the constant-gap trapezoidal structure, we show that an initial boost is required to obtain good propulsion estimates, since the distribution of  $F_{p|y}$  is different between the two cases we assume that the net dynamic effect is positive without the use of velocity boost. However, the force-induced velocity obtained from the alternating gap case is very low, especially about the distances traveled by the nanoparticle in going from one push to the next (which are twice as long as in the constant gap case). In a real case, it could lead to a net friction effect between the medium and the nanoparticle reducing or eliminating the propulsive effect. For this reason, a different configuration is needed that allows the development of a strongly asymmetric electric field without considerably altering the distances traveled by the nanoparticle between one push and the next. Therefore, in the next section, we will discuss a new type of trapezoidal structure that is designed according to the characteristics just defined.

## 4.5 Plasmon Device with a linear variation of gap

The design of a nanodevice that induces optical thrust implies, as the literature shows, the search for a system that overcomes some dynamic limitations: the small exit velocity and the requirement of an initial boost. The first solution is a periodic trapezoid structure with alternating gap variation. However, the force obtained does not still reach values suitable for the ejection of a nanoparticle.

In this section, we consider the next step of gap variation in the trapezoidal system, i.e., the trapezoid gold couple has a continuous variant gap. Since the gap has a v-shape form, the system is considered a hybridization and optimization of the characteristics of the optical nanocannon[1] and trapezoidal structures[2] observed in the previous chapters. In this chapter, therefore, we will analyze the physical and geometrical characteristics of the structure, also focusing on the numerical model considered. Finally, we will evaluate the improvements obtained with this device compared to previous ones.

### 4.5.1 Elementary cell of the nanostructure

A sketch of the elementary cell of the proposed nanostructures is shown in Fig.4.19. The elementary cell consists of two gold scalene trapezoids fabricated

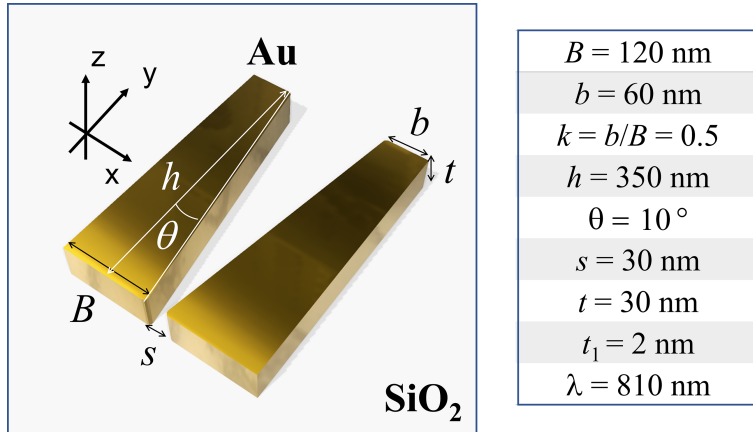


Figure 4.19: Sketch of the proposed gold trapezoids nanostructure with design parameters

on a glass substrate; the oblique sides of the trapezoids are separated by a no-constant gap, forming a V-shaped section.

When light, with appropriate wavelength, illuminates this nanostructure, two resonant LSPs are generated near the major base ( $B$ ) on both sides of the gap. LSPs generate hot spots due to the amplification of the incident electric field amplitude. These LSPs act as near-field excitations that generate SPPs

along the edges of the gap; the coupling between the SPPs produces an asymmetric field distribution along the y-axis, which induces a resultant force on a nanoparticle positioned around the nanostructure gap. The geometry of the nanostructure not only influences the characteristics of the generated force but also determines the wavelength of the LSP resonance. Therefore, the resonance wavelength can be matched to the optical radiation of interest by appropriately designing the geometry of the nanostructure. To evaluate the resonance wavelength, electric field distributions and induced forces produced by plasmonic nanostructures, simulations were carried out with COMSOL Multiphysics. The COMSOL model of the nanostructures consists of a pair of gold trapezoidal prism positioned in such a way that the oblique side forms an angle with the y-axis equal to  $\theta$  so that the dimension of the oblique side is  $h/\sin(\theta)$ . The lower substrate is glass, whereas the vacuum surrounds the entire structure. The thickness of the three-dimensional elementary cell is  $(t + t_1)$ , where  $t$  is the thickness of the gold. Given the low adhesion of gold on the glass substrate, the system needs a thickness  $t_1$  of a material that bonds to the substrate. However, the material and the thickness are determined such that the electric field response of the surface plasmon suffers a minimum variation. Among the various materials, titanium and chromium have a higher absorption coefficient than gold, so the plasmonic system with a gold-titanium hybrid layer exhibits a less amplified electric field than a gold plasmonic system without modifying the electric field distribution. For the material selection, we use a COMSOL simulation on a rectangular trapezoid with constant gaps and analyze the damping difference between the chromium and the titanium. From the simulations, we observe that the device with a chromium layer shows a greater electric field loss for the titanium layer case.

Thus the model has a  $t_1$  titanium buffer layer required in the manufacturing process. However, a thin layer of titanium should be deposited to avoid excessive plasmonic energy losses. The value of  $t_1 = 2nm$  is selected to minimize performance losses of the plasmonic device while ensuring good adhesion of the gold to the substrate.

In addition, considering that technological processes do not allow the fabrication of perfect edges, the model is constructed to have rounded edges and therefore more similar to a real structure. Again, we simulated the physics of the system in the "wave optics" [109] module of COMSOL Multiphysics with the same method used in the single structure of the alternating gap system in the previous paragraph. A double study was considered; the first step use a port with an x-polarized incident field (because the transverse gap polarization generates the maximum amplitude of the electric field)  $E_0 = 1V/m$  and a power given by the formula  $P = \frac{1}{2} \frac{E_0^2 A}{Z}$ , where  $Z_0$  is the vacuum impedance and  $A$  is the illuminated area. The port illuminates an air-substrate system and the result of the first step becomes the background wave acting on the structure for the second step. PML surrounds the physical domain to avoid backscattering effects and simulate the infinite-size substrate for a single isolated cell. The mesh of the system also has the same characteristics as the case in paragraph

4.4, obtaining a good level of accuracy of the result which we evaluate with a direct MUMPS solver. The table in fig.4.19 shows the values of the nanostructure geometry derived from parametric simulations (described in Section 4.5.3 below) and inducing an optimal electric field distribution for incident optical radiation at 810nm. A 2D plot of the induced electrical field strength is illustrated in fig.4.20(a), whereas, its profiles along the three axes (specifically, along the position 1 for the  $x$ -axis, at the center of the gap for the  $z$ -axis and along the dashed line for the  $y$ -axis) are illustrated in Fig. 4.20(b),4.20(c), and 4.20(d), respectively. In particular, the  $x$  profile of the induced electric field amplitude (fig.4.20(b)) has a parabolic shape in which the minimum is at the center of the gap, as a consequence of the symmetry of the structure along the  $y$ -axis. In fact, the evanescent electric field of LSPs [55] generated on each trapezoid has a maximum near the edges of the plasmonic structure and reaches a minimum at the center of the gap. The  $z$ -profile (fig.4.20(c)) is maximum within the structure gap at  $z = (t_1 + t_2)/2$ , while for  $z > t_1 + t_2$  the effect of the evanescent behavior of LSPs and SPPs [55] results in an exponential decay of the electric field amplitude.

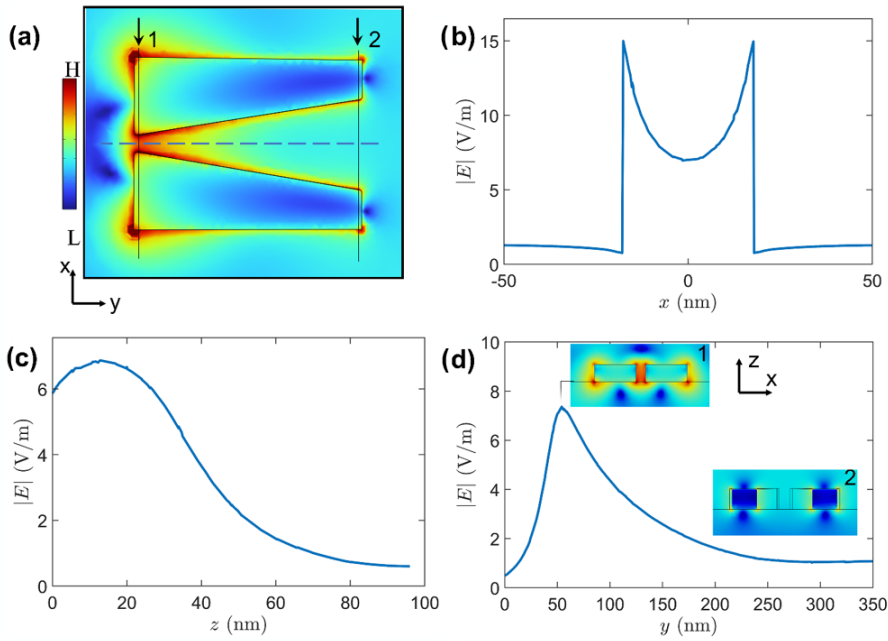


Figure 4.20: (a) Pseudocolor plot of the magnitude of the electric field generated in the trapezoid structure along the  $xy$  plane. Electric field profile: (b) along  $x$ -axis at position 1 (fig.4.20(a)) and  $z = (t_1 + t_2)/2$ ; (c) along  $z$ -axis at position 1 and  $x = 0$ ; (d) along the dashed line of the fig.4.20(a)- the inset 1 and 2 show a pseudocolor plot of the electric field in the  $xz$  plane in the  $y$ -position indicated by fig.4.20(a)

Finally, the  $y$  profile (fig.4.20(d)) is highly concentrated and amplified near the major base ( $B$ ) of the trapezoids (i.e. position 1 in fig.4.20(a)) due to the small gap size, which implies a strong coupling between the SPPs generated on each trapezoid. On the contrary, the amplification of the generated field is reduced near the minor base (i.e. position 2 in fig.4.20(a)) due to the large value of the gap, which implies decoupling between the generated SPPs.

As in the alternating gap case, the spatial distribution of the electric field can be used to evaluate (eq.4.9), the gradient force contribution generated by the proposed plasmonic nanostructure. Therefore, in fig.4.21(a) shows the  $x$  component of the force per unit of incident power and per unit of polarizability (i.e.,  $\mathbf{F}_p$  eq.4.17). We note that the potential well of the electric field results in an oscillating force that at equilibrium traps a particle located in the gap. For the  $z$ -component (fig.4.21(b)) the negative values imply that the force is directed toward the substrate and any particles located above the structure tend to be 'captured' in the direction of the plasmonic nanostructure. However, this is observed only in the area where the electric field is amplified by the LSP. In fact, the force along  $z$  tends to zero at 40/50 nm above the plasmonic nanostructure.

Finally, the force along the  $y$ -component (Fig.4.21(c)) has a positive value up about 50 nm, which moves the nanoparticle from the major base towards the minor base. From 50 nm onwards, the force takes on a negative value, which tends to move the nanoparticle in the opposite direction. The net effect between the two terms is such that the nanoparticle experiences predominantly the effect of the positive term weakly constrained by the negative term and therefore tends to move along the positive direction of the  $y$ -axis. Indeed, the energy density per power unit acting on a nanoparticle can be estimated by evaluating the area under the curve shown in Fig.4.21(c)). The result obtained is  $1.26 \times 10^{-11} \frac{pJ}{W * nm^3}$ , which guarantees positive kinetic energy and thus a propulsive motion of the nanoparticle. Thus, the plasmonic device acts as optical tweezers for the  $x$ - and  $z$ - components of the force and induces propulsion only along the  $y$ -axis. The achieved result allows us to compare the performance of the proposed nanostructure with the structures proposed by Rovey [2] and Shalin[1]. The comparison of the maximum forces obtained is shown in table 4.1.

| Structure | Estimated force                           |
|-----------|---|
| Rovey's   | $\simeq 10^{-5} pN / (W * nm^3)$          |
| Shalin's  | $\simeq 10^{-3} pN / (W * nm^3)$          |
| our       | $\simeq 6 \times 10^{-2} pN / (W * nm^3)$ |

Table 4.1: Performance comparison between the proposed isolated nanostructure and others reported in the literature

As expected, the elementary cell of the proposed structure (i) induces a generated force almost comparable to the V-shaped structure proposed by Shalin; (ii) is characterized by a high asymmetrical field distribution that guarantees

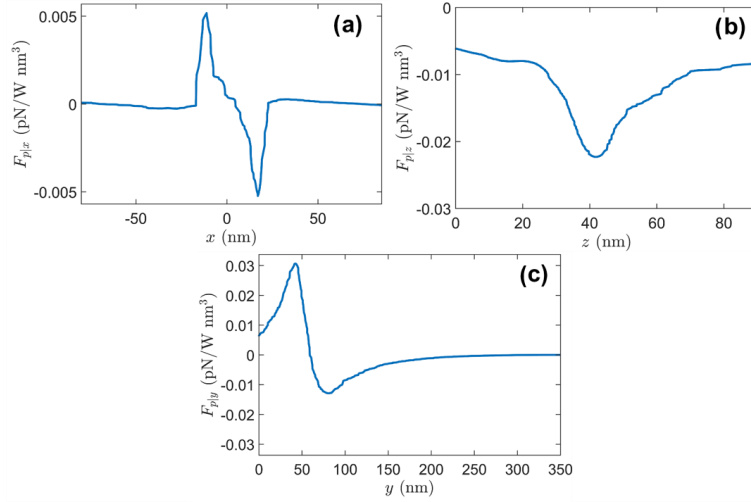


Figure 4.21: Component of  $\mathbf{F}_p$  derived from the electric field illustrated in: (a) fig.4.20(b) for the x component; (b) fig.4.20(c) for the z component, and (c) fig.4.20(d) for the y-component

a positive net energy, ensuring the movement of a nanoparticle, and (iii) can be organized in an array configuration to further increase, as discussed in the following sections, the propulsion force.

## 4.5.2 Array Configuration

The force induced by the V-shaped elementary cell described in the previous paragraphs can be enhanced by creating a sequence of elementary cells in a configuration called end-to-end, i.e., with the minor base of one elementary cell attached to the major base of the adjacent one. A sketch with a sequence of three elementary cells of such a configuration is shown in Fig.4.22. If an optical beam linearly polarized along the x-axis illuminates the entire array of nanostructures, a resonant source is generated at each plasmonic elementary cell in the array, and the resulting force is a sequence of periodic pushes. This produces on a nanoparticle an amplification of its kinetics and a significant spatial displacement. FEM simulations of the array configuration require the addition of appropriate periodic conditions (Floquet periodic boundary) on the boundaries perpendicular to the plane of the structure (see Fig.4.19) to model the periodic distribution of the elementary cells. The mesh considered for this model is similar to the array case considered in section 4.4. However, as observed in Fig.4.23, the periodic conditions have different dummy surfaces due to the asymmetry of the v-shape structure. In addition, to improve the quality of the simulation, we added a dummy volume (as seen in Fig.4.23) that has thickness  $t + t_1$  and whose mesh is dense compared to the rest of the model air volume.

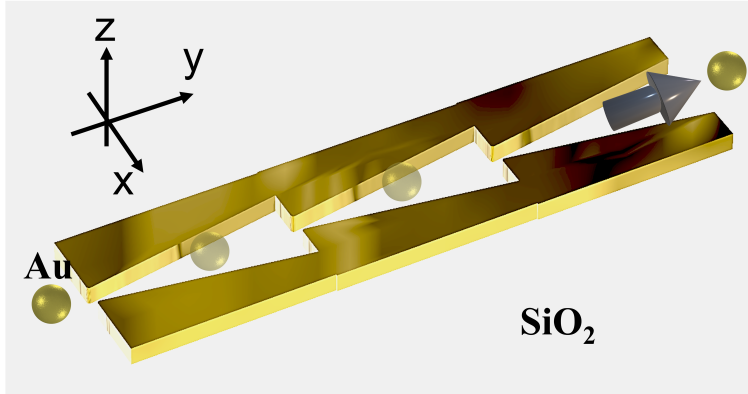


Figure 4.22: sketch of a sequence of three elementary cells of trapezoids structures

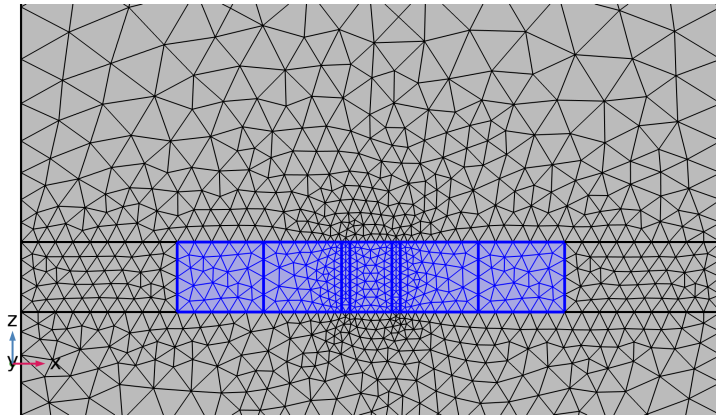


Figure 4.23: Mesh in the boundary surface in array case of the trapezoidal device

The dimensions of the tetrahedron for the dummy volume have  $\lambda/60$  as the maximum and  $\lambda/200$  as the minimum. In addition, we refine the size of the device tetrahedron, so we have a maximum size of  $\lambda/140$  and a minimum  $\lambda/1000$ . The mesh ensures higher accuracy and avoids differences in the various electric field peaks caused by numerical inaccuracies.

The red line of fig.4.24 shows the force distribution ( $F_{p|y}$ ) obtained along the y-axis in the gap and relative to three successive elementary cells for an array designed with the geometrical parameters given in fig.4.19. In particular, the

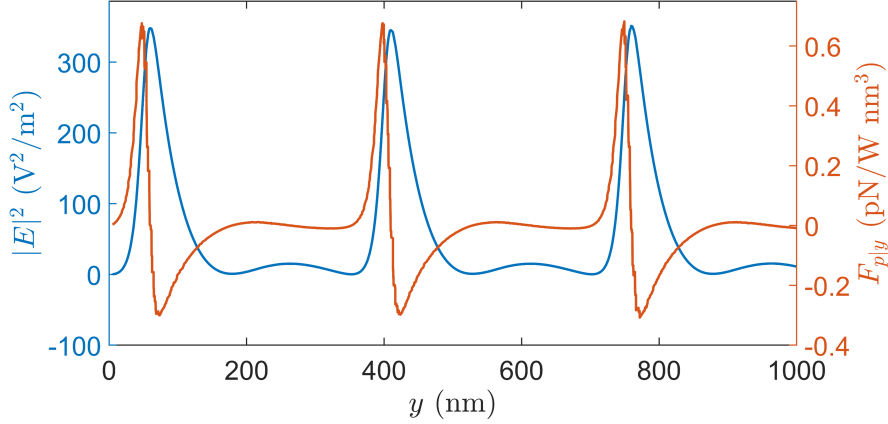


Figure 4.24: Profile along the  $y$ -axis of the contribution of  $F_{p|y}$  (red line) and of the contribution of the electric field intensity (blue line).

profile of the  $F_{p|y}$  magnitude presents a maximum value higher than that of the elementary cell (see fig.4.21(c)). The result can be explained by considering that the SPPs generated around the minor base of an elementary cell can propagate a few microns towards the adjacent elementary cell and thus interfere with the LSPs of the major base of this cell[55]. In addition, the periodic condition also induces a small amplification around the minor base, caused by the interference between the SPPs that propagate towards the adjacent elementary cells. This small amplification induces a second peak of the electric field amplitude that is shown in the blue line of fig.4.24. We can verify that the amplification characteristics are due to the group effect due to the periodicity condition of the array. In particular, if we define spacing along the  $y$ -coordinate in the system (as in Fig.4.25) the electric field and resonance wavelength tend to regain the values of the isolated cell case. Thus, in fig.4.25, we observe the difference between plasmonic devices placed in an end-to-end configuration and a configuration of plasmonic devices in arrays with spacing along  $y$  of  $d = 20$ . The figure shows how the spacing between elementary cells reduces the group effect between the various surface plasmons. The reduction of the coupling effect results in a reduction of the electric field amplification. In addition, the resonance wavelength given the spatial period variation of the system tends to undergo a blue shift in value. The blue shift of the resonance wavelength tends to increase as parameter  $d$  increases until it reaches the value of the isolated cell case. When  $d$  is about 500nm, the SPPs decay in the gap transverse direction. In this case, the array condition is negligible and the system returns in an isolated cell case. This analysis ensures that the end-to-end configuration optimizes the system field. Therefore to obtain the best dynamic conditions the elementary cell will always be placed in an array configuration.

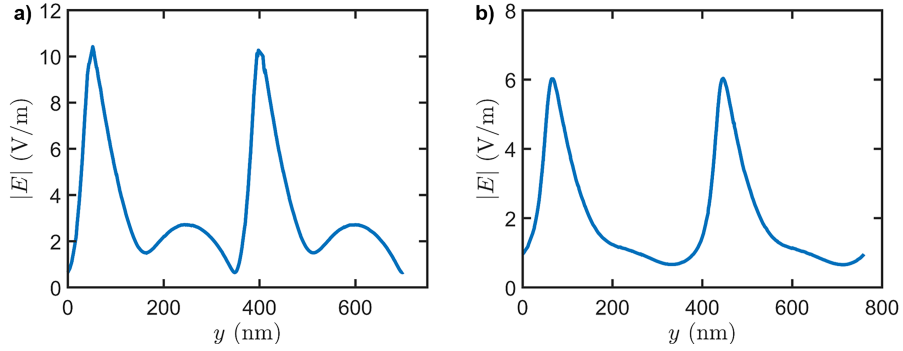


Figure 4.25: a) Electric field profile along the y-axis (dashed line fig.4.20(a)) of an end-to-end array configuration b) Electric field profile along the y-axis (dashed line fig.4.20(a)) for an array configuration with a spacing between the elementary cells  $d = 20nm$

### 4.5.3 Analysis of the influence of geometric parameters

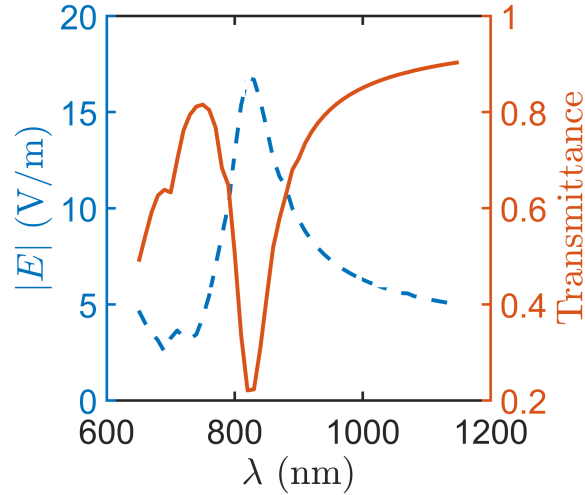


Figure 4.26: Transmission spectrum (solid red line) and maximum field distribution (dashed blue line) as a function of wavelength of the incident field for a nanostructure with geometrical parameter reported in fig.4.19

The geometry of the proposed nanostructure's elementary cell was determined through an interactive simulation process that optimized the optical interaction between the incident radiation and the trapezoidal nanostructure array, in order to maximize the force induced on a nanoparticle. The transmission spectrum of a single elementary cell of the array nanostructure with

geometric dimensions given in fig.4.19 is shown in Fig.4.26.

From this spectrum, it is possible to identify a wavelength at which strong absorption of light occurs. Moreover, at this wavelength, the magnitude of the electric field has its maximum value. This means that if the nanostructure is illuminated with an appropriate wavelength, the absorbed light is strongly confined, allowing a strong induced force to be generated. Therefore, depending on the wavelength of the radiation beam to be used, the geometrical parameters (such as minor base ( $b$ ), major base ( $B$ ), height ( $h$ ), angle ( $\theta$ ), metals thickness ( $t + t_1$ ) and the gap ( $s$ ) of the structures) have to be appropriately defined. COMSOL simulations were performed to assess the influence of the geometric parameters on the electric field distribution and thus on the induced force, which as seen in the previous section occurs within the gap between the two trapezoids. We observe the effect of the gap on the plasmonic device in Fig.4.27. Fig.4.27 shows the trend of maximum  $F_{p|y}$  as the wavelength changes

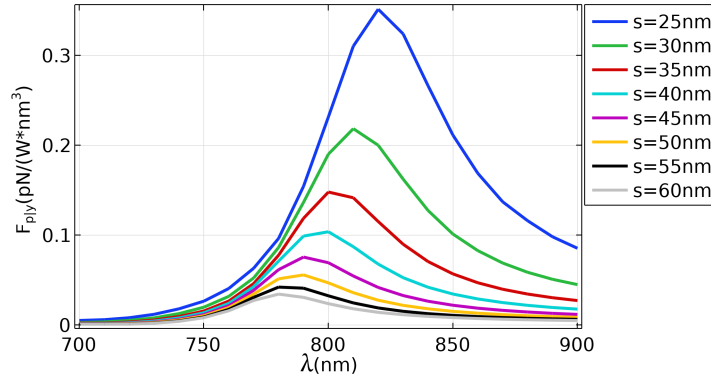


Figure 4.27: Maximum of  $F_{p|y}$  as a function of wavelength for different gap value; the other geometrical parameters are reported in table of fig.4.19

for different values of structure gap. For the amplification value, the analysis of  $F_p$  is useful to evaluate the structure that is performing propulsive rather than the structure with the most intense amplification. It is clear from the figure that the strength tends to decrease as the gap changes. The effect is in agreement with the characteristics of plasmonic dimers. The plasmonic dimer has an inversely proportional response as the gap increases. In addition, the resonance wavelength exhibits a slight blue shift as the gap increases. This is in agreement with the interparticle coupling effect of plasmonic dimers, which exhibit a blue shift in the transverse excitation modes induced in the gap of the dimers when the dimer distance increase. The fig.4.28 shows the effect of the thickness on the plasmonic device on the electric field amplitude and the resonant wavelength. We observe that a larger bulk size tends to decrease the intensity of  $F_{p|y}$ . The damping of  $F_{p|y}$  results from the properties of gold that absorbs part of the incident radiation, reducing the amplification effect of the surface plasmon. In addition, we observe a blue shift of the resonance wavelength. This is in agree-

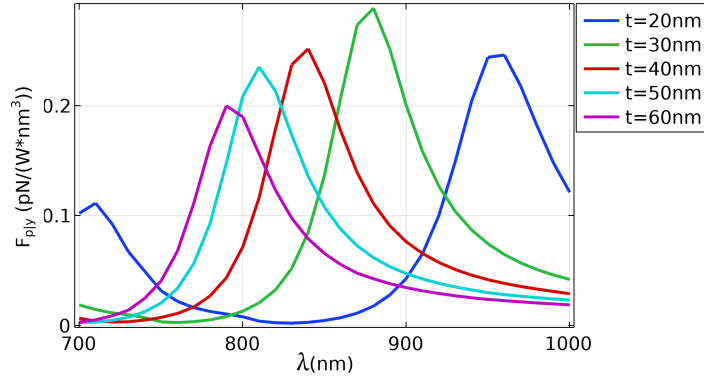


Figure 4.28: Maximum of  $F_{ply}$  as a function of wavelength for different thickness values; the other geometrical parameters are reported in the table in fig.4.19

ment with Froelich's condition (eq.(2.50) when the structure has a non-negligible size. Thus, the resonant wavelength acquires a volume dependence.

We make some consideration about the result of the fig.4.27-4.28 for the definition of the optimal trapezoidal structure:

- 1) Gap variation has negligible wavelength variation to the other geometric parameters but the amplitude variation is significant. Therefore, in the geometrical analysis, we consider the case of the minimum gap allowed by fabrication tools (30nm).
- 2) The thickness variation does not change the amplitude of the electric field. However, a set of plasmonic devices with different thicknesses implies a complication in the fabrication process; thus, we consider only the optimal thickness (30nm) without any variation.

Considering that the structure is composed of two rectangular trapezoids separated by a variable distance, formed by the oblique sides of the two trapezoids (see Fig. 4.19), a geometric relation can be defined that relates the geometrical parameters ( $h, \theta, B, b$ ):

$$\cos(\theta) = \frac{(B - b)}{\sqrt{h^2 + (B - b)^2}} = \frac{1}{\sqrt{1 + \frac{h^2}{B^2(1-k)^2}}} \quad (4.18)$$

where  $k$  is the ratio between minor base ( $b$ ) and major base ( $B$ ). As a result of this dependence, the analysis of the electric field and the electric field gradient was carried out only as a function of  $k, h, \theta$ . Each geometric parameter varies while the other two are kept constant, as illustrated in Fig.4.29. The maximum of both the electric field and gradient electrical field as a function of the incident wavelength for different values of the ratio of the bases  $k$  are shown in Fig.4.30(a) and Fig.4.30(b), respectively. In particular,  $k = 0$  means that a right triangle

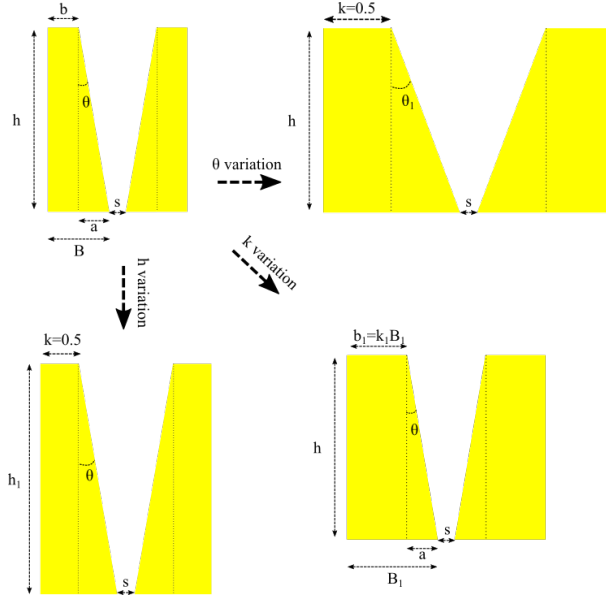


Figure 4.29: Variation of geometric parameters adopted for COMSOL interactive simulations

with base  $a$  is considered, while by increasing  $k$ , a rectangle with base  $b$  is combined with the previous right triangle, to obtain a rectangular trapezoid with minor base  $b$  and major base  $B = b + a$  (see Fig.4.29).

The fig.4.30(a) shows that the electric field amplitude tends to grow when  $k$  lies in the range  $[0.1, 0.4]$ , reaches a maximum in the range  $[0.5, 0.7]$ , and then decreases for  $k > 0.7$ . In addition, there is a plasmon resonance blue shift with increasing  $k$ .

The behavior of the electric field amplitude and plasmonic resonance shift could be explained physically if the trapezoidal device is roughly schematized as a set of  $N$  plasmonic dimers with length ( $w$ ) and gap ( $g$ ) gradually increasing in the interval  $[b, B]$  and  $[s, s + 2(B - b)]$ , respectively, and height  $\delta h = h/N$ .

As the plasmonic dimer gap ( $g$ ) narrows, the enhanced optical fields in the gap increase, and the plasmonic resonance red-shifts[55][113]. On the other hand, as the length ( $w$ ) of the plasmonic dimer increases, radiative contributions to the plasmonic damping have to be taken into account; the loss of plasmon energy due to the emission of electromagnetic radiation implies a weaker enhanced optical field[72].

For small values of  $k$ , the dimensions of the dimers forming the minor base region have small dimensions and are therefore characterized by a large area/volume ratio, resulting in a high non-radiative contribution to plasmonic damping. As  $k$  values increase, this non-radiative contribution decreases, and the amplification of the electric field amplitude increases[72]. However, for high

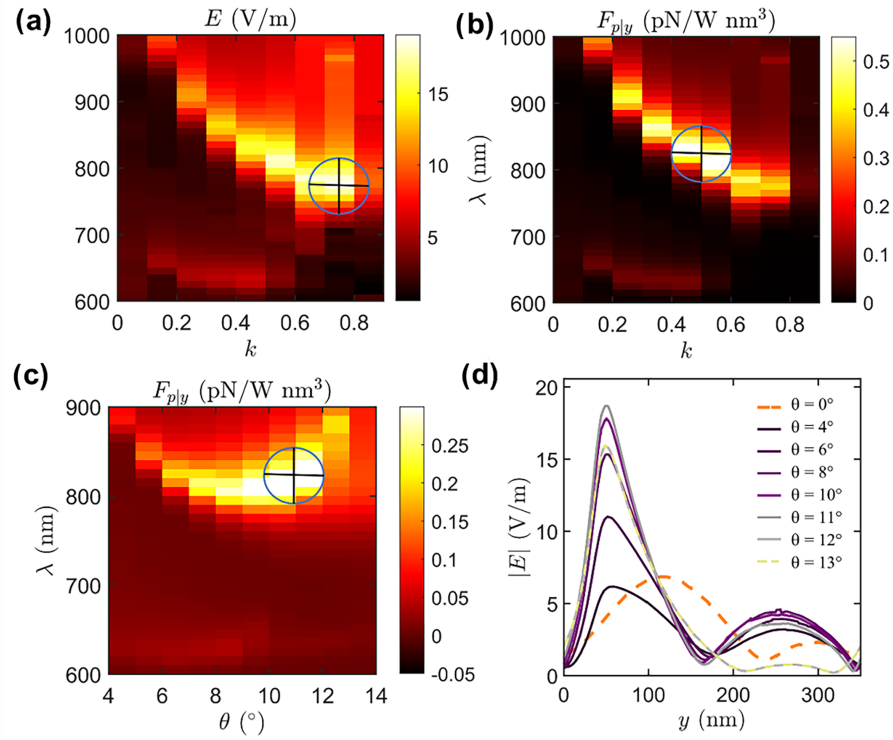


Figure 4.30: (a) Pseudo-colour plot of the variation of the maximum electric field amplitude as a function of incident wavelength and the basic ratio  $k = b/B$  (crosshairs indicate the maximum values reached). (b) Pseudo-colour plot of the variation of  $F_{p|y}$  as a function of incident wavelength and the basic ratio  $k = b/B$  (crosshairs indicate the maximum values reached). (c) Pseudo-colour plot of the variation of the force maximum  $F_{p|y}$  as a function of incident wavelength and angle  $\theta$  (crosshairs indicate maximum values attained). (d) Electric field amplitude along the dashed line shown in fig.4.20(a).

values of  $k$ , the radiative contributions to plasmonic damping increase, causing a weakness in the generated electric field[55][114]. The plasmonic resonance shift is attributable to the dependence of polarizability on the shape and size of the nanostructure (eq.2.50).

Fig.4.30(b) shows the behavior of the maximum of  $F_{p|y}$  as a function of the incident wavelength parameterized to the base ratio  $k$ .  $F_{p|y}$  grows by the trend of the maximum electric field up to  $k = 0.5$ . Then,  $F_p$  tends to decrease for  $k > 0.5$  despite the electric field having a similar maximum amplitude between  $k = 0.5$  and  $k = 0.7$ . To explain this result, the schematization of the structure as composed of dimers can once again be useful. The plasmonic device for

$k > 0.5$  has large dimensions along the x-axis and the dimers will be characterized by  $w \gg g$ , so all the dimers have approximately the same plasmonic behaviour. This implies a symmetric distribution of the electric field along the y-axis and therefore, according to equation eq.4.17, a reduced value of the force. In order to investigate the influence of the angle  $\theta$ , Fig. 4.30(c) shows the maximum of the force  $F_{p|y}$  as a function of the incident wavelength for values of  $\theta$  from  $0^\circ$  (i.e., constant gap) to  $14^\circ$  (see Fig.4.29), while  $h$  and  $k$  are constant and equal to the value in table (fig.4.19). Two interesting behaviors can be observed from the figure: firstly, the amplitude of the force generated increases as the angle increases, reaching a maximum for  $\theta =$  around  $10^\circ$ , then decreasing. Furthermore, the variation of  $\theta$  induces a shift in the resonance wavelength.

As  $\theta$  increases, the distance between the structures increases and this induces a blue-shift of the plasmon resonance. On the other hand, to keep the ratio  $k$  constant, the bases  $B$  and  $b$  have to increase (see Fig.4.29), so the length of the set of dimers increases, causing a red-shift of the resonance. The net effect is the weak blue shift shown in Fig. 4.30(c). These behaviors are typical of V-shaped nanostructures, in fact, similar results were observed for the bulk V-shaped structure proposed by Shalin et al.[1][104], showing that only a specific couple ( $\theta$ ,  $h$ ) allows to optimize the structure performance. The second aspect highlighted is the increase in the quality factor (which is defined as the ratio of the resonance wavelength to the full width at half maximum (FWHM) of the resonance) of the plasmonic device as the angle increases. A high Q-factor corresponds to a stronger and sharper plasmonic resonance. The influence of the angle  $\theta$  on the Q-factor can be justified by considering the variation in size of the dimers mentioned above. Indeed, a plasmonic dimer generates a resonance in the gap if the distance ( $g$ ) between the edges does not exceed 50/60nm and, moreover, an increase in  $g$  induces a blue shift of the resonance[55, 114]. Thus, for low angles, all the dimers have a similar gap implying similar, slightly shifted resonances, so the overall envelope is a diffuse wavelength response. As the angle  $\theta$  increases, the dimers that can resonate (i.e.  $g \leq 50/60\text{nm}$ ) are fewer and fewer, resulting in a narrowing of the envelope and, consequently, an increase in the Q-factor. Furthermore, taking into account the V-shape of the proposed structure, the  $g$  gap of the set of dimers tends to increase moving from the major to the minor base. As a result, the electric field amplification tends to decrease from the major to the minor base, creating a strong asymmetric field distribution. As shown in Fig.4.30(d), this asymmetry becomes more pronounced as the angle  $\theta$  is around  $10^\circ$  and, consequently, the induced force on a nanoparticle is maximized (see equation 4.17). For higher angles, the radiative contributions to plasmonic damping increase, causing a weakening of the induced force. The dependence of the height  $h$  of the trapezoid on the plasmonic performance of the nanostructure is shown in fig.4.31, where the maximum value of  $F_{p|y}$  as the incident wavelength varies and with  $k$  and  $\theta$  having the values indicated in fig.4.19. As the height  $h$  increases, a linear red-shift of the structure's wavelength resonance is observed (larger plasmonic structures tend to have a higher plasmonic resonance than smaller structures[55]). Furthermore, the maximum field amplitude tends to increase linearly up to  $h=550$  nm. This can be explained by considering again

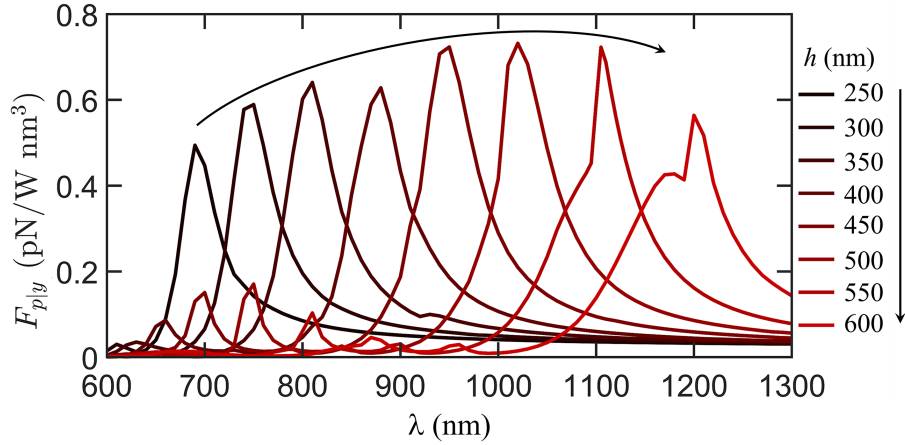


Figure 4.31: Maximum of the force  $F_{p|y}$  in the function of the incident wavelength parameterized respect to the height of trapezium  $h$

the trapezoid as a set of dimers. As  $h$  increases, both the number of plasmonic dimers composing the trapezoidal structure and their length  $w$  increase (see Fig.4.29). Considering the electromagnetic field of the entire nanostructure as a superposition of the fields of the individual dimers, it can be assumed that the increase in the number of large dimers leads to greater amplification of the field and the value of  $F_{p|y}$  grows in virtue of eq.4.17. However, for  $h > 600$  nm, as the resonance wavelength is greater than 1100 nm, gold becomes a perfect conductor[59], and thus its optical absorption coefficient increases[104][56] (i.e., the contribution of the non-radiative term to the plasmonic damping increases). As a result, the electric field is absorbed more and this leads to a decrease in the maximum  $F_{p|y}$ .

The analysis of the influence of geometrical parameters on the performance of the nanostructure presented in this paper can provide a flowchart to be adopted to design the plasmonic structure according to the desired incident wavelength. Starting from the incident wavelength, the first value to be determined is  $h$ , because of its strong wavelength dependence. In particular, with reference to the type of plasmonic structure analyzed in this work, the following fitting equation can be derived from fig.4.31:

$$h = 669.79 \cdot 10^{-2} \lambda - 210.26 \quad (4.19)$$

Then, taking into account the analysis of the variation of  $\theta$ , the structure has to be designed with an angle of about  $10^\circ$ . This allows to determine the base  $a$  ( $a = h/\tan(\theta)$ ) of the rectangle triangle shown in Fig.4.29. Since the ratio,  $k$  that optimizes the performance of the structure must be 0.5, the major base  $B$  of the trapezoidal structure will be equal to  $2a$  and the minor base  $b$  will be equal to  $a$ . Optimizing  $\theta$  and  $k$  generates small resonance displacements, so the

design process requires an interactive approach to be sure that the geometric parameters can maximize the force generated at the desired incident wavelength.

#### 4.5.4 Kinetic of nanoparticles

To evaluate the kinetic performance induced by an array configuration, eq.4.9, which relates the gradient of the electric field strength and the optical force, was used to estimate the dynamics induced by the plasmonic structure on a nanoparticle. In the FEM model, the principal variation is the introduction of a sphere (representing the nanoparticle) placed at a user-controlled position  $(x_0, y_0, z_0)$ . In the physics of the model, we define the force using Maxwell's tensor (eq.A.21) and integrate it on the surfaces of the sphere. Since the optical force depends on the electric field evaluated around the sphere, a very accurate mesh on the sphere surface is required. So we construct a fictitious cubic volume circumscribing the sphere and refine the mesh inside the cube. A free set of tetrahedrons subdivide the cube domain, and their maximum and minimum sizes are the same used for the subdivision of the device volume. (see paragraph 4.4). We analyze the optical force acting on a nanoparticle relative to two

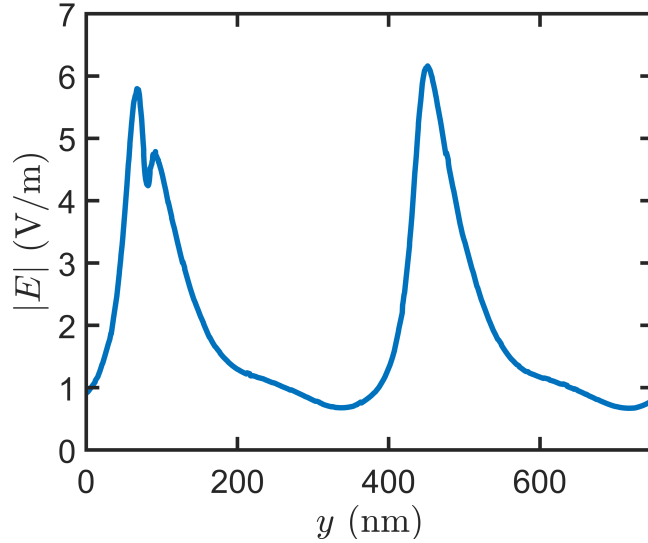


Figure 4.32: Electric field profile along the y-axis (dashed line fig.4.20(a)) of an end-to-end array configuration with a 10nm silica particle placed above it

different nanoparticle materials: glass (dielectric) and gold (metal). In Fig.4.32 we observe the electric field of a plasmon device evaluated along the y-axis in which a glass particle is placed above them[56]. Fig.4.32 shows that when the incident wave interacts with the glass nanoparticle, i.e., a dielectric material, it can pass undisturbed. Consequently, the plasmonic field is weakly affected by

the presence of the nanoparticle. Gold, on the other hand[59], as observed in

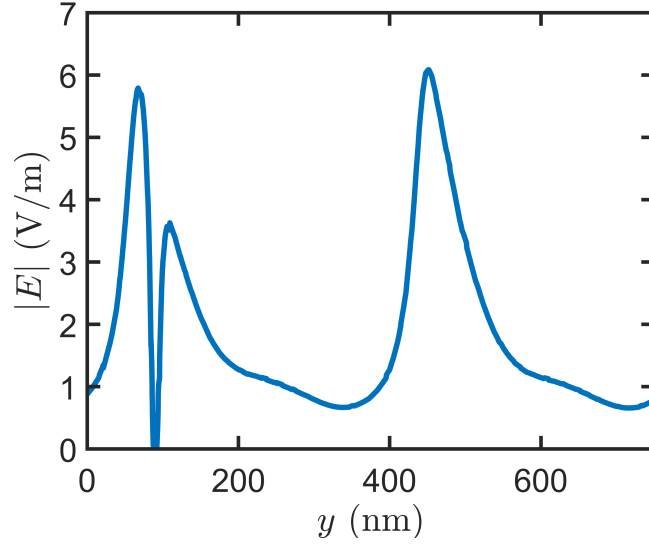


Figure 4.33: Electric field profile along the y-axis (dashed line fig.4.20(a)) of an end-to-end array configuration with a 10nm gold particle placed above it

fig.4.33, being a metal, modify the incident electric field then the field generated by the plasmonic device suffers a variation due to the presence of the gold nanoparticle. We observe the difference between the two effects in fig.4.34, which shows the optical force (normalized with the input power  $\tilde{\mathbf{F}} = \mathbf{F}/P$ ) applied to the nanoparticle for different materials. In particular, the optical force on a glass particle (green solid line) exhibits a similar functional form to that of  $F_p$  in fig.4.24, since the material does not considerably alter the field. In contrast, the optical force on gold has a slightly different functional form where the area with  $F_y < 0$  increases relative to that with  $F_y > 0$ . In addition, an increase in the optical force values on the gold particle compared to the values on the glass particle is observed in Fig.4.34 because the presence of a gold nanoparticle above the plasmonic structure alters the electric field distribution by increasing the gradient of the electric field. Since the response to the plasmonic field provides higher optical forces, we use gold as the material for subsequent analysis. Fig.4.35(a) shows the profile along the y-axis of the generated optical force (normalized to the incident power as the previous case) applied to a gold sphere of radius 10nm. We evaluate the optical force for two different z-positions of the sphere's center: inside the gap (solid blue curve) and just above the gap (dashed red curve), i.e., tangent to the plasmonic structure. As was to be expected, when the nanosphere is inside the gap of the structure, the induced force has an intensity approximately one order of magnitude greater than when the nanosphere is above the structure. The effect is due to the

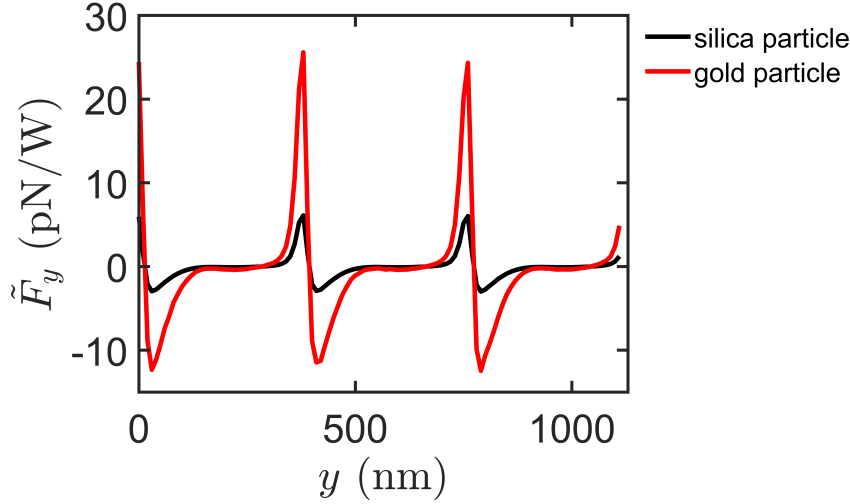


Figure 4.34:  $y$  component of  $\tilde{\mathbf{F}}$  of a 10nm silica particle (solid black line) and a 10nm gold nanoparticle (solid red line)

evanescence of the plasmonic wave along the  $z$ -axis. Indeed, the exponential decay of the plasmonic electric field shown in fig.4.20(c), drastically reduces the optical force applied to the nanoparticle. In figure 4.35(b), the effect of the size of the gold nanoparticle on the induced force distribution along the  $y$ -axis is illustrated. Gold nanoparticles with a radius between 10nm and 50nm were simulated, and each nanoparticle was positioned so as to be tangent to the plasmonic structure. For nanospheres with a radius of 10nm, the force profile has an asymmetric distribution where the area relative to  $\tilde{F}_y < 0$  is greater than that for  $\tilde{F}_y > 0$ . The net effect is the displacement of the nanoparticle along the  $y$ -axis. Increasing the volume of the nanoparticles induces stronger forces, because the force is a function of polarizability (eq.4.9) that is (eq.2.50) proportional to the sphere volume. However, if the nanoparticles have a radius greater than half the gap ( $s/2=15\text{nm}$ ), part of the nanoparticle will extend above the gold trapezoids. Thus, when the incident optical radiation comes from above the structure, part of the nanoparticle obscures the plasmonic structure (and thus absorbs part of the radiation that should excite the plasmonic structure), creating scattering effects. All these effects cause the damping of the force and the kinetic of larger nanoparticles tend to slow down. The effects due to the larger particles can be avoided by changing the direction of the incidence of the light beam. In particular, since the substrate is glass and therefore transparent, the incident optical beam can illuminate the nanostructure through the substrate. Fig.4.35(c) shows the force distribution induced on a large gold

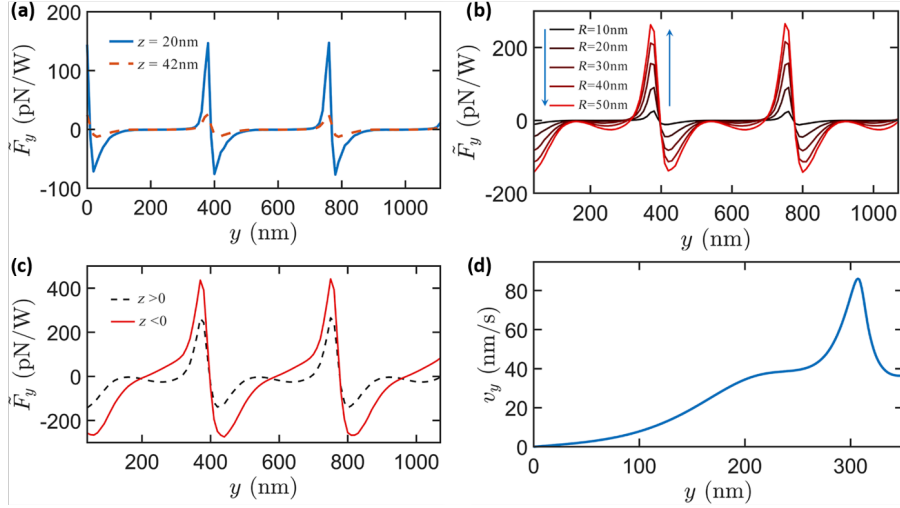


Figure 4.35: (a) Profile along the  $y$ -axis of the force induced on a gold nanosphere with a radius of 10nm and positioned within the gap ( $z=20\text{nm}$  blue solid curve) and above the structure ( $z=42\text{nm}$  red dashed curve). (b) Profile along the  $y$ -axis of the force induced on a nanoparticle positioned above the nanostructure ( $z = t + t_1 + r$ ) and parameterized with respect to the radius of the sphere. (c) Profile along the  $y$ -axis of the force generated with illumination from above the nanostructure (black dashed curve) or from the substrate (red solid curve). (d) Velocity along the  $y$ -axis of a nanoparticle of radius 50nm placed above the nanostructure gap and estimated from the force distribution shown in Fig. 4.35(c).

nanoparticle ( $r=50\text{nm}$ ) for illuminating the nanostructure from both above ( $z > 0$ ) and below ( $z < 0$ ). By illuminating the trapezoidal nanostructure through the substrate, the surface plasmon excitation occurs before the nanoparticle interference and the net effect of the force is improved.

The distribution of force acting on the nanoparticle can be used to estimate the induced kinetics. Since COMSOL does not allow the kinetic of the particle to be coupled with the variation of the electric field by the particle's motion, the induced kinetics was evaluated by combining the functionalities of COMSOL Multiphysics and MATLAB using *LiveLink<sup>TM</sup>* [115]. Specifically, the simulation process involves the following steps:

- 1) Force estimation, through the Maxwell tensor, using the COSMOL simulation of the trapezoidal model with the nanoparticle located at the origin of the array configuration.
- 2) Force field processing using MATLAB code to evaluate (via the equation of motion) the dynamics in terms of velocity and displacement of the nanoparticle.

- 3) The new position of the gold nanoparticle is transferred to the FEM model for a new COMSOL evaluation of the optical force distribution.
- 4) The cycle is repeated.

In fig.4.35(d), the velocity of a gold particle, with a radius of 50 nm and located above the nanostructure gap, is shown as a function of the space. The initial velocity of the nanoparticle is set to zero then, recalling the profile of the force distribution, the velocity initially tends to increase strongly reaching a maximum value of about  $85\text{nm/s}$ , then there is a deceleration due to the positive part of the force distribution ( $\tilde{F}_y > 0$ ) resulting in a final velocity at the end of the first elementary cell of about  $32\text{nm/s}$ . Therefore, the net effect is that the gold nanoparticle acquires kinetic energy from the optical forces even though the initial velocity is zero. If we compared with the literature configuration shown in Section 4.3, we observe that it is not necessary to use a strong initial boost to induce propulsion but the system can eject the nanoparticle autonomously.

Fig.4.36 shows the final nanoparticle velocity at the end of an elementary cell as a function of nanoparticle radius. The velocity initially grows in the range ( $r = 10\text{nm}$ ,  $r = 40\text{nm}$ ) while for  $r = 50\text{nm}$  the velocity of the nanoparticle decreases. Indeed, according to the results shown in fig.4.35(b), the optical force increases with increasing nanoparticle size. However, for  $r = 50\text{nm}$  the value of the nanoparticle mass reduces the effect of the optical force and this leads to a reduction in the final velocity. Furthermore, according to Figs. 4.35(a) and 4.35(c), the cases of particles inside the gap or illumination from below induce an improvement in particle velocity.

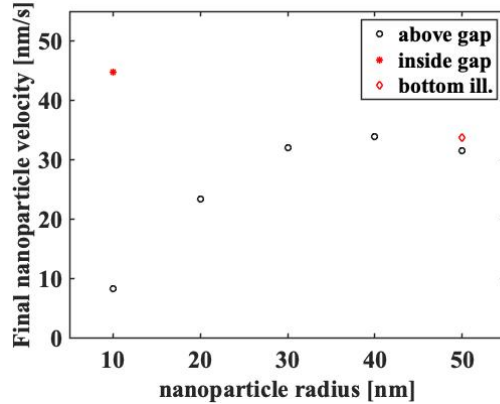


Figure 4.36: Nanoparticle velocity at the end of an elementary cell as a function of nanoparticle radius with incident electric field  $E_0 = 1\text{V/m}$

Taking advantage of the periodicity property of the array structure it is possible to estimate the final velocity achieved when the nanoparticle passes the N elementary cell of the linear array. Specifically, if a conservative system

composed by N elementary cells of the periodic array is considered, the following conservation of energy can be assumed:

$$E_p = \frac{1}{2}mv_f^2 \quad (4.20)$$

where  $E_p$  is the system's potential energy induced by the optical force, and  $v_f$  is the final velocity of the particle at the end of the N-th elementary cell. Considering that the shape of the force distribution for a periodic array can be seen as the repetition of the distribution induced on the single elementary cell, we can assume that:

$$E_p = NE_{pi} \quad (4.21)$$

where  $E_{pi}$  is the potential energy for a single elementary cell, so:

$$v_f = \sqrt{N}v_i \quad (4.22)$$

where  $v_i = \sqrt{2E_{pi}/m}$  is the velocity reached by the particle when crossing an elementary cell of the matrix. Thus, the speed of the nanoparticle increases proportionally to the square root of the number of elementary cells that compose the array. For example, for an array 1 mm long and considering the dimension reported in fig.4.19, the number N of elementary cells of the proposed trapezoidal structure is approximately 2860. So the final speed of a nanoparticle with a radius of 10nm and located above the gap can reach values of about 0.4  $\mu\text{m/s}$ . In order to attempt a comparison with similar structures reported in the

| Structure | Incident Intensity | Estimated velocity  |
|-----------|--------------------|---------------------|
| our       | $1W/m^2$           | $1.88\mu\text{m/s}$ |
| Rovey's   | $1W/m^2$           | $1.16\mu\text{m/s}$ |
| Shalin's  | $10^9W/m^2$        | $0.3m/s$            |

Table 4.2: Comparison between the proposed nanostructure and others reported in the literature for the velocity reached by a 10 nm nanoparticle at the end of an isolated elementary cell

literature, only the isolated elementary cell can be considered. In fact, Shalin's structures [1] do not allow for any periodic configuration, whereas the array configurations shown by Rovey [2][108] require an initial boost on which the final velocity of the nanoparticle depends. A comparison of the speed reached by a nanoparticle with a radius of about 10nm at the end of an isolated elementary cell for the structures mentioned above is given in table 4.1. For our structure, the same incident light intensity as used by Rovey ( $1W/m^2$ ) was considered. The proposed nanostructure allows a velocity almost similar to that obtained by Rovey, but with the advantage that, when considering an array configuration, no initial thrust is required (i.e. the movement of the particle is obtained even without imposing an initial velocity on the nanoparticle). On the other hand, it is worth noting that the high speed reported by Shalin is due to very intense lighting.

### 4.5.5 Circular Array

In addition to the linear end-to-end configuration, the periodicity of the plasmonic nanostructure can also be realized using a circular end-to-end configuration for which the number of elementary cells positioned depends on the radius of the ring (see Fig.4.37(a)). If  $N = L/h$  is the number of plasmonic cells that compose a linear array of length  $L$  (where  $h$  is the height of the individual cell), the same number of cells is present in a circular configuration with a diameter of  $L/\pi$ . Thus, the circular configuration allows for a more compact spatial arrangement. However, due to the presence of surface plasmons, the SPPs/LSP coupling effect is only generated when the polarization of the incident radiation is transverse to the structure gap. Fig.4.37(b) shows the amplitude of the elec-

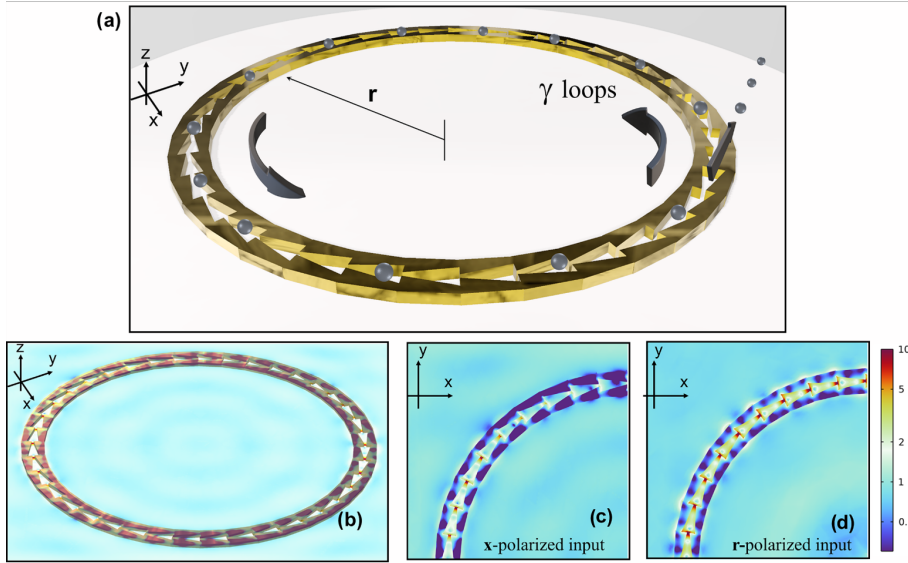


Figure 4.37: (a) Sketch of the circular arrangement of the trapezoidal structure showing the direction of movement of the nanoparticles. (b) Pseudocolor plot of the electric field amplitude in a circular array induced by incident light with linear polarization. Detail of the electric field amplitude induced by (c) linear polarization and (d) radial polarization.

tric field distribution generated on a circular array illuminated with incident radiation linearly polarized along the  $x$ -axis. In particular, the field distribution varies between an induced maximum in the elementary cells with gaps transverse to the  $y$ -axis and a minimum (ideally no excitation) in the elementary cells with a gap transverse to the  $x$ -axis(fig.4.37(c)). In order to generate the same electric field distribution over all elementary cells in the array, incident radiation with radial polarization (i.e., with the electric field always directed parallel to the radius of the ring[116]) was simulated. Indeed, in this case, the polarization is always transverse to the gap of the elementary plasmonic cells,

and so the resulting electric field is adequately excited in any nanostructure (see Fig.4.37(d)). The resulting electric field generates periodic optical forces along the ring and thus the induced velocity is directed tangent to the ring, leading to a circular motion at a nanoparticle placed in the nanostructure. In terms of kinetic, the advantage of the circular configuration is that the final velocity reached by a nanoparticle is not limited by the number  $N$  of elementary cells that composite the ring. Since the circumference is a closed curve, a "final" elementary cell can not be individuated, but the nanoparticle continues to rotate along the ring until it is ejected. Indeed, a circular configuration allows to a nanoparticle to accumulate velocity until the centrifugal force induces a change in trajectory thus ejecting the nanoparticle. In order to estimate the number of rounds performed by a nanoparticle before its ejection, the centrifugal force has to be considered:

$$F_c = \frac{mv^2}{r}$$

where  $m$  is the mass,  $v$  is its velocity, and  $r$  is the radius of the circular array. For an array of nanoplasmonic cells, the nanoparticle velocity depends on the number  $n$  of elementary cells that the particles have crossed (see eq. 4.22), so in a first approximation, the following relationship can be written:

$$F_c \simeq \frac{mnv_i^2}{r} \quad (4.23)$$

if  $N$  is the total number of elementary cells that compose a circular array with radius  $r$ , i.e.,  $r = Nh/2\pi$ , the centrifugal force can be rewritten in the following form:

$$F_c \simeq \frac{2\pi nmv_i^2}{Nh} = \gamma \frac{2\pi mv_i^2}{h} \quad (4.24)$$

where  $\gamma = \frac{n}{N}$  is the number of rounds the nanoparticle performs. The nanoparticle is ejected when the centrifugal force exceeds the trapping force  $F_t$  present in the transverse direction to the gap (see the red line in fig.4.20(b)). Thus, the number of rounds performed by the nanoparticle before ejection is:

$$\gamma \simeq \frac{F_t h}{2\pi mv_i^2} \quad (4.25)$$

Thus,  $\gamma$  doesn't depend on the number of elementary cells composing the circular configuration array. For example, considering a gold nanoparticle of  $10nm$  radius and located above the gap, an incident field of  $E_0 = 1V/m$  induces a trapping force  $F_t$  that requires approximately  $\gamma = 10$  rotations for the ejection of the nanoparticle. The possibility of ejecting the nanoparticle after  $\gamma$  rounds allows the size of the nanostructures to be drastically reduced, particularly compared to the linear configuration. For example, as seen above, using a linear array  $1\text{ mm}$  long, a nanoparticle of radius  $10nm$  reaches a final velocity of approximately  $0.4\ \mu\text{m/s}$  traveling through  $2860$  elementary cells. Similarly, the same number of cells can be traversed with  $10$  rounds of a circular array configuration of about  $286$  elementary cells, which means that it is possible to realize a circular nanostructure with a radius of about  $16\ \mu\text{m}$  can be realized.

In this chapter, we defined a new plasmonic device capable of inducing propulsion by hybridizing the characteristics of plasmonic acceleration systems already found in the literature, namely Shalin's Nanocannon and Rovey's Trapezoidal structures. The device analyzed through a FEM model, exhibits a field response capable of defining an optical force that produces propulsion. In addition, the geometry is such that it produces a periodicity of the force, and thus we can construct array configurations capable of increasing the output velocity of the system. The system has strong versatility since the resonance changes over a wide range (from 700 to 1300nm wavelength) by varying the geometry of the elementary cell, i.e., major base, minor base, height, and angle of the trapezoids. The kinetics associated with the trapezoidal structure present good results, we observed that a circular array configuration would lead to a kinetic energy buildup, given the characteristics of circular system velocity and force performance. Before moving on to the fabrication phase of the system, given the simulative results obtained, we will discuss a phenomenon that through the coupling of spin with angular momentum allows the manipulation of nanoparticle trajectories and thus could be of interest in dealing with the ejection direction of the nanoparticle once accelerated by the plasmonic system.



## Chapter 5

# Spin-Orbit Coupling Effect

In the previous chapter, we designed and evaluated, through FEM analysis, a plasmonic system capable of inducing propulsion. The result allows the ejection of nanoparticles with good velocity parameters using a periodic array configuration. However, in the CubeSat displacement, strong directional control is required. Given the small size of the nanoparticles, we can not achieve directional control through the usual methods. In this chapter, we will observe an interesting phenomenon induced by spin-orbit coupling, i.e., the coupling of the photon spin (helicity) with the orbital angular momentum of the light wave. In particular, evanescent waves and thus surface plasmons generate a transverse momentum, which defines a polarization-dependent displacement of the nanoparticle that allows us to remotely control the position of a nanoparticle. In this chapter, we look at the basic principles of spin-orbit coupling focusing on the effects present in evanescent waves. We will discuss the behavior of the momentum generated by a gold nanoparticle as the incident polarization changes and the trajectory changes induced by the aforementioned spin momentum. Finally, the case of a plasmonic dimer will be evaluated, given the particular electric field configuration, observing a discontinuous spin distribution that will be of interest for numerous practical applications in the field of spin optics[117].

### 5.1 Spin-orbit in optics phenomena

In the previous chapters, we analyzed electromagnetic phenomena from a classical point of view to understand the phenomenology of evanescent waves. The electromagnetic field can also be analyzed from a quantum point of view as a particle (photon). The behavior of the photon generates a set of forces and moments that can lead to macroscopic effects[118][119].

we observed in eq.A.18 that the moment of forces and angular momentum can be carried by electromagnetic waves and plays a crucial role in many radiation-matter interactions. However, electromagnetism being a field theory has quantum effects that can define new dynamic properties[120].

Let us consider a momentum  $\mathbf{p}(\mathbf{r})$  in a quantum or classical field theory, that can be written as a local expectation value of the canonical momentum operator  $\hat{p} = -i\nabla$ , i.e.,  $p = Re(\psi^\dagger \hat{p} \psi)$ , where  $\psi(\mathbf{r})$  is the wave function, and we use units  $\hbar = 1$ . For the field vector, an additional spin momentum density was introduced in 1939 by Belinfante[121] to explain the spin of quantum particles and symmetrize the canonical energy-momentum tensor in field theory. Thus the momentum density in a vector field theory can be written as:

$$\mathbf{p} = Re(\psi^\dagger \hat{p} \psi) + \frac{1}{2} \nabla \times \mathbf{s} = \mathbf{p}^O + \mathbf{p}^s \quad (5.1)$$

where  $s$  is the spin Angular momentum (AM) density defined as the local expectation value of the corresponding matrix spin operator  $\hat{\mathbf{s}}$ , i.e.  $s = \psi^\dagger \hat{\mathbf{s}} \psi$ . This relation is valid for various types of particles. For example in the electrons  $\hat{\mathbf{s}}$  is the spin-1/2 operator and  $\psi(r, t)$  is the Dirac bi-spinor. In the case of the electromagnetic field, the eq.5.1 yields the time-averaged Poynting vector (see appendix A1) when  $\hat{\mathbf{s}}$  is given by the helicity of the photon (left-handed polarization or right-handed polarization). Using the Maxwell equation (eq.A.1a-A.1d) we can define optical momentum and optical spin density with the following formula:

$$\begin{aligned} \mathbf{p}^O &= \frac{1}{16\pi\omega} Im[\mathbf{E}^* \cdot \nabla \mathbf{E} + \mathbf{H}^* \cdot \nabla \mathbf{H}] \\ \mathbf{s} &= \frac{1}{16\pi\omega} Im[\mathbf{E}^* \times \mathbf{E} + \mathbf{H}^* \times \mathbf{H}] \quad \mathbf{p}^S = \frac{1}{2} \nabla \times \mathbf{s} \end{aligned} \quad (5.2)$$

The momentum of the Poynting vector  $\mathbf{p}$  generates, respectively, the orbital and spin parts of the AM density (since the eq.5.1). The orbital AM density  $\mathbf{l} = \mathbf{r} \times \mathbf{p}^O$ , and this is an extrinsic origin-dependent quantity. At the same time, the spin AM density  $\mathbf{s}$ , eq.5.2 is intrinsic (origin-independent). The orbital momentum  $p^O$  is naturally proportional to the local phase gradient (scattering force in eq.4.9) in the field. On the other hand, the spin momentum provides the physical origin of the spin AM of quantum particles; but it is usually considered as an auxiliary quantity, which cannot be observed by itself. Indeed, the spin momentum represents a solenoidal current, which does not contribute to the energy transport and only generates spin AM. The characteristics of the observed moments become clearer by considering the moment and spin measurements for the electromagnetic field. A small absorbing particle immersed in the field can be employed as a natural meter of these quantities. From the particles, it is possible to measure force (eq.4.9) and torque, which has the following formula:

$$\mathbf{T} = \frac{1}{8\pi\omega} Im(\alpha) \mathbf{s} \quad (5.3)$$

The force gives us an estimate of the complex orbital momentum ( $\mathbf{p}^O$ ) while the calculation of the torque allows us an estimate of the spin AM density ( $\mathbf{s}$ ). It follows from the following result that the  $\mathbf{p}^O$  and not the Poynting vector ( $\mathbf{p}$ ) is physically significant because the momentum  $\mathbf{p}^s$  is a "virtual" quantity that is not observable in weak-interactions measurement.

The interplay and mutual conversion between the two types of optical angular momentum (orbital angular momentum and spin angular momentum) produce the optical spin-orbit interaction.

In general, the fundamental mechanism underlying the spin-dependent deformation of optical fields is geometric phases. These can be explained as originating from the coupling between the SAM (Spin angular moment) and rotation of the coordinate frames naturally determined in a particular problem[118].

The first important example of SOI (Spin-Orbit Interaction) occurs in the propagation of paraxial light in an inhomogeneous isotropic medium[122][123]. It is well-known from geometrical optics that light changes its direction of propagation and momentum due to refraction or reflection at medium inhomogeneities. However, the trajectory of an optical beam is independent of the polarization in traditional geometrical optics in the absence of anisotropy. This is because geometrical optics neglect all wavelength-scale phenomena, which become important for nano-optics. Let us consider the propagation of light in a gradient-index medium with refractive index  $n(\mathbf{r})$ . The smooth trajectory of a light beam in a such medium can be described by the mean coordinates  $\mathbf{R}$  and the momentum  $\mathbf{P}$  which vary with the trajectory length  $\tau$ . Considering semi-classical correction to this formalism the trajectory of light in a gradient-index medium is described by the following equation:

$$\dot{\mathbf{P}} = \nabla n(\mathbf{R}) \quad \dot{\mathbf{R}} = \frac{\mathbf{P}}{P} - \frac{\sigma}{k_0} \frac{\mathbf{P} \times \dot{\mathbf{P}}}{P^3} \quad (5.4)$$

Here the overdot stands for the derivative for  $\tau$ ,  $k_0$  is the vacuum wavenumber and we used the dimensionless momentum  $\mathbf{P} = \langle \mathbf{k} \rangle / k_0$ . The last term in eq.5.4 describes the transverse spin-dependent displacement of the trajectory, i.e., the Spin-Hall effect of light[124]. It was shown that the helicity-dependent term in eq.5.4 can be considered as a Lorentz force produced by the geometric phase variation analogous to those for electrons in condensed matter. However, while the electron's momentum is driven by an applied electric field, in optics the refractive-index gradient plays the role of an external driving force.

The Spin-Orbit Interaction manifests itself in free-space nonparaxial fields[124][125][126]. Consider, for example, focused circularly-polarized vortex beams carrying spin and orbital intrinsic AM. The simple association of the SAM and OAM with the polarization and vortex is not valid anymore. For a nonparaxial beam, consisting of circularly-polarized plane waves with the wave vectors forming a cone with an opening angle  $\theta$ , the SAM and OAM become:

$$\mathbf{S} = \sigma \cos \theta \frac{\mathbf{P}}{P} \quad \mathbf{L} = [l + \sigma(1 - \cos \theta)] \frac{\mathbf{P}}{P} \quad (5.5)$$

The total intrinsic AM of the beam is preserved:  $J_z = S_z + L_z = \sigma + l$ , so that the eq.5.5 can be interpreted as if a part of SAM was transferred to the OAM. This is another fundamental manifestation of the SOI: the spin-orbital AM conversion. Part of the orbital AM becomes helicity dependent, i.e., a helicity-dependent vortex should appear even in beams with  $l = 0$ .

The spin-orbit effect considered above is called intrinsic SOI, which originates from fundamental properties of the Maxwell equations and is not related to specific media. Another class of SOI effect can be induced by particular properties and symmetries of the medium[127][128][129]. These "extrinsic" effects emerge in anisotropic media and artificial structures including metamaterials[130]. Let us consider light transmission through a planar anisotropic element. For simplicity, we assume a transparent retarder providing a phase  $\delta$  with the anisotropy axis oriented at an angle  $\alpha$  in the  $(x, y)$ -plane. In the coordinates attached to the anisotropy axis, the evolution of light is described by the transmission Jones matrix  $T = \text{diag}(e^{i\delta/2}, e^{-i\delta/2})$ . Performing a rotation by the angle  $\alpha$  to the laboratory coordinate frame and also writing this matrix in the helicity basis of the right-hand and left-hand circular polarizations, the Jones-matrix transformation of the wave polarization becomes:

$$\mathbf{E}' = \begin{bmatrix} \cos(\frac{\delta}{2}) & i \sin(\frac{\delta}{2})e^{-2i\alpha} \\ i \sin(\frac{\delta}{2})e^{2i\alpha} & \cos(\frac{\delta}{2}) \end{bmatrix} \mathbf{E} \quad (5.6)$$

Here the off-diagonal element with phase factors  $\exp(\pm 2i\alpha)$  originates from geometric phases induced by the rotation of coordinates. For the half-wave retardation  $\delta = \pi$ , the matrix eq.5.6 becomes off-diagonal and describes the transformation for  $\sigma = \pm 1$  circularly-polarized light into the opposite polarization  $\sigma' = \mp 1$ , with geometric phase difference  $\Phi_G = -2\sigma\alpha$ .

Let the orientation of the anisotropy axis change linearly with one of the coordinates:  $\alpha = \alpha_0 + qx$ . In this case, for half-wave retardation, the  $\sigma$ -polarized light is converted into light of opposite helicity and also acquires the helicity-dependent component in the momentum of light  $\mathbf{P}'_x = -2\sigma q$ . Thus, the x-variant anisotropic structure deflects the right-hand and left-hand polarized beam in opposite x-directions. This can be considered as the anisotropy-induced spin-Hall effect of the light. While in the intrinsic spin-Hall effect the coordinate shift is caused by the wavevector gradient of the geometric phase, here the momentum shift is generated by the coordinate gradient of the geometric phase. The extrinsic spin-Hall effect generated by the space-variant anisotropic element allows complete spatial separation of the two spin-states of light: a linearly-polarized light with  $\sigma = 0$  is transformed into two well-separated  $\sigma' = \pm 1$  beams propagating in different directions.

## 5.2 Spin momentum in evanescent wave

The quantum nature of light introduces the quantity of spin that can be associated with the variation of the helicity of the light beam. Spin defines an angular momentum (SAM) and a  $\mathbf{p}_s$  momentum, which, however, is a virtual quantity that cannot be observed experimentally. Instead, spin in terms of angular momentum can be observed in optics through the spin-orbit coupling (SOI) effect. In the previous chapter, SOI was shown using various techniques that also allow for its practical uses (e.g., the construction of metasurfaces that modulate the

polarization of the electric field). However, SOI can also be observed in phenomena that induce evanescent waves such as surface plasmons. Plasmonics SOI coupling shows unique characteristics compared to other types of SOI given the nature of evanescent waves[120]. Let us consider the electric evanescent-wave field:

$$\mathbf{E} = \frac{A}{\sqrt{1+|m|^2}} \left( \bar{\mathbf{x}} + m \frac{k}{k_z} \bar{\mathbf{y}} - i \frac{\kappa}{k_z} \bar{\mathbf{z}} \right) \exp(ik_z z - \kappa x) \quad (5.7)$$

where  $\kappa$  is the decay rate of the evanescent wave. Substituting the electric and magnetic field (eq.5.7) into eqs.5.2, we calculate the canonical momentum, spin momentum, and spin AM density in an evanescent wave:

$$\begin{aligned} \mathbf{p}^O &= \frac{w}{\omega} k_z \bar{\mathbf{z}} \\ \mathbf{s} &= \frac{w}{\omega} \left( \sigma \frac{k}{k_z} \bar{\mathbf{z}} + \frac{\kappa}{k_z} \bar{\mathbf{y}} \right) \\ \mathbf{p}^s &= \frac{w}{\omega} \left( -\frac{\kappa^2}{k_z} \bar{\mathbf{z}} + \sigma \frac{\kappa k}{k_z} \bar{\mathbf{y}} \right) \end{aligned} \quad (5.8)$$

where  $w$  is the spatially-inhomogeneous energy density (see eq.2.16). Given this equation, we observe some characteristics in sharp contrast with the propagative wave. In particular, the transverse y-component of the momentum and spin in the wave propagating solely within the  $(x, z)$  plane. In addition, the momentum  $p_y^s \propto \sigma$  is helicity dependent, while the spin is helicity independent. This property is due to the features of the evanescent field:

the first one is the imaginary longitudinal component of the field polarization  $-i \frac{\kappa}{k_z} \bar{\mathbf{z}}$ . This induces a rotation of the fields in the propagation plane and generates the spin  $s_y$  independently of  $\sigma$ . The second feature is the evanescent energy density  $w$  starting with eq.2.16 with the assumption of the field eq.5.7 became:

$$w = \frac{1}{8\pi} |A|^2 e^{-2\kappa x} \quad (5.9)$$

This inhomogeneity destroys the cancellation of the spin momentum in  $(x, y)$ -plane which results from a non-zero transverse Belinfante's spin momentum  $p_y^s \neq 0$ . The direction of the transverse spin momentum becomes uniquely locked [131] with the direction of propagation of the evanescent wave. Oppositely, propagating waves with  $k_z > 0$  and  $k_z < 0$  carry opposite transverse spins  $p_y^s > 0$  and  $p_y^s < 0$  respectively. In evanescent waves, given the properties that distinguish the transverse moment,  $\mathbf{p}^s$  is not a virtual quantity as in the propagative case, and therefore measurements can be made to be able to reveal its intensity.

In particular, illuminating a prism with a laser beam generates an evanescent wave by internal reflection. If a nano-cantilever is placed on the prism, it undergoes a force caused by the  $\mathbf{p}^s$  moment and begins to oscillate transversely to the propagating wave[132]. Based on the oscillation of the cantilever, the effect of  $\mathbf{p}^s$  induced by the evanescent waves can be measured. Similarly, it is possible to perform the same measurement using SPPs in a prism in a Kreshmann

configuration, obtaining very intense transverse forces given the field amplification properties typical of surface plasmons. The  $\mathbf{p}_s$  moment was also detected in LSPs. In particular, a system consisting of a circularly polarized incident wave impinging on a gold nanoparticle was evaluated[133]. It is shown that under resonant conditions the orbital momentum has a greater intensity than the Poynting vector (see eqs.5.1-5.2) since the plasmonic  $\kappa$  is greater than  $k_z$ . Furthermore, the spin couples with the moment of the evanescent wave but in a manner independent of the helicity of the incident wave, due to spin-momentum locking. A  $\mathbf{p}^s$  momentum is generated in a different direction than the orbital  $\mathbf{p}_O$  momentum. However, given the characteristics of LSPs, that is, the amplified field is strongly localized around the surface of the sphere, and the spin momentum and spin-orbit coupling remain localized around the surface of the sphere tending to decrease with increasing distance[55]. In the case where a test particle is located in the vicinity of a nanosphere under resonant conditions, it experiences a very intense transverse force, in addition to radiation pressure, due to the spin-orbit coupling of the evanescent field[134]. The direction of the transverse force, however, is dependent on the incident helicity and presents a direction reversal when the helicity goes from 1 to -1. The phenomenon can be observed, albeit to a lesser extent even when the nanosphere is outside the plasmonic resonance since the evanescent wave is equally generated along the surface of the nanosphere. Moreover, the phenomenon does not require an incident helicity to be generated; if the gold nanosphere is polarized along y and with an incident electric field directed along z and under resonant conditions, a transverse momentum (along the x direction) is induced by the spin-orbit effect creating a different trajectory in the test particle.

### 5.3 Polarization-Addressable Optical Force on Plasmonic Nanoparticles and Hot-Spot Spin Vortices

Previously we observed that the evanescent wave forms a transverse spin momentum in addition to the usual orbital momentum. In this section, we analyze the consequences of the spin induced by the LSP resonance of a gold nanoparticle. Unlike the literature case [134] where we observed the dynamics of a probe particle near a resonant gold particle; here we show the dynamics of the resonant gold nanoparticle considering the effects that the generated spin induces on the particle itself. Starting with a 10 nm radius sphere of gold immersed in an air substrate; the particle is irradiated by a linearly polarized plane wave with a wavelength of 530nm. Specifically, the COMSOL Multiphysics model features a gold sphere of radius 10nm immersed in an air sphere of radius 400nm concentrically. PML domains are placed around the air sphere to avoid backscattering and multiple reflection effects of the incident field. The physics used is in the "Electromagnetic wave frequency domain" module, which is very similar to the "wave optics" used in Chapter 4 but with the possibility of observing the far

field domain of the system as well as the near field (needed to evaluate radiation pressure behavior). The incident wave is a parameterized background field and can be easily varied to modulate its amplitude and polarization. The mesh, in addition to a domain quadrilateral subdivision for the PML, has two different tetrahedra sizes for the physical domain subdivision. The outer sphere is subdivided by tetrahedra with a maximum size equal to  $\lambda/8$  and a minimum size equal to  $\lambda/125$ . In the golden sphere instead, the tetrahedra have a maximum size equal to  $\lambda/50$  and a minimum size equal to  $\lambda/6000$ . This subdivision is necessary to maximize the accuracy in calculating the electric field around the sphere surface. In fig.5.1 the incidence radiation is directed along  $z$  and polarized along  $x$ ; in fig.5.1(a) we observe the calculation, of the spin moment  $\mathbf{s}$  and the Electric field amplitude on the surface of the gold sphere using eq.5.2. In resonance, the electric field is distributed such that the area of maximum amplitude is the  $yz$  plane. From eq.5.2 it is known that the spin depends on the electric field components, for this reason, the spin is most widely distributed along the same surface of the electric field maximum i.e. the  $yz$  plane.  $\mathbf{s}$  is also distributed such that the direction is tangent to the plane under consideration. If we change the direction of polarization, for example, using an incident beam polarized along  $y$ , the electric field changes its distribution and the maximum shift to the  $xz$  plane. For the eq.5.2 relationship, the spin also becomes distributed, tangent to the surface, along the  $xz$  plane. It is therefore possible to assume that given a beam with a linear electric field polarization direction, the spin always distributes tangent to the plane orthogonal to the polarization direction. In Fig.5.1(a) and particularly in Fig.5.1(b) where the distribution of spin over the entire spherical surface is represented; it is shown that the spin distribution is symmetrical to the  $x$ -axis; we observe that the  $yz$  plane at  $x > 0$  exhibits an anti-clockwise distribution while the corresponding one at  $x < 0$  exhibits a clockwise distribution, moreover there is a transition zone between the two planes where the spin is discontinuous. The axial symmetry of the spin is in agreement with the geometry of the structure. In Fig.5.1(c) we observe the plot of the spin momentum intensity (the Belinfante [121] component) as compared to the Poynting vector, according to eq.5.1, as a function of wavelength. It is shown that the spin moment exhibits a resonant peak for values around 540/550nm where it reaches a value of 0.5; it follows that the spin moment becomes an important component of the Poynting vector with consequences in force analysis. If, on the other hand, we analyze the graph away from the resonance peak, the spin moment becomes negligible compared to the orbital moment in the evaluation of the Poynting vector and the radiation pressure remains the dominant force on the system. The plot is compared to the Absorption Plot (ACS); ACS indicates the absorption coefficient of the gold sphere and is indicative of the plasmonic resonance of the gold nanosphere as specified in [55]. The result implies that the maximum spin value is reached when occurring a plasmonic resonance, following [120], where the relationship between the Belinfante moment and the evanescent waves is specified. Once we had studied the behavior of the Belinfante moment intensity, we evaluated in Fig.5.1(d) the behavior of the direction of the spin momentum on the surface of the sphere. In

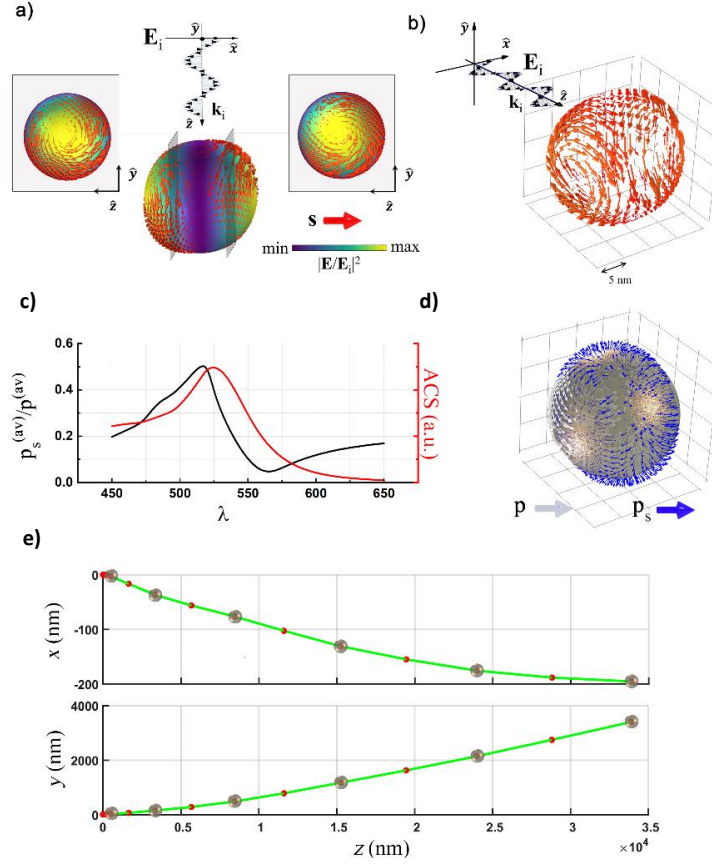


Figure 5.1: a)x-polarized electric field distribution in a resonant fold nanosphere and the spin distribution along the surface. b) 3D vision of the sphere surface with spin distribution in resonant condition. c) ACS plot (red line) and the ratio  $p_s/p_{tot}$  in the function of the wavelength. d) 3D vision of the nanosphere with distribution of  $\mathbf{p}_s$  and  $\mathbf{p}$  along the surface. e) trajectory of a resonant gold nanoparticle with an x-polarized electric field.

agreement with eq.5.2 we observe that, given an incident beam polarized along x, the spin moment is transverse to  $\mathbf{s}$  so it is radial to the yz plane. Even tuning linear polarization, for example considering a polarization along y, the spin moment tends to form along the plane orthogonal to the polarization direction (in this case the xz plane) directed radially. The direction of  $\mathbf{p}^s$  varies in the two hemispheres; as in the case of  $\mathbf{s}$ , we will have two different directions depending on whether we are positioned at  $x > 0$  or  $x < 0$ . Once we have studied the behavior of the spin moment, we use the force equation (eq.A.21) to evaluate the effect of the spin moment on the dynamics of the gold particle. Fig.5.1(e) shows the dynamic of the gold nanoparticle for an incident wave polarized along x.

The nanoparticle dynamics are obtained using the same *LiveLink<sup>TM</sup>* method seen in chapter 4. These results are obtained when we evaluate the force using

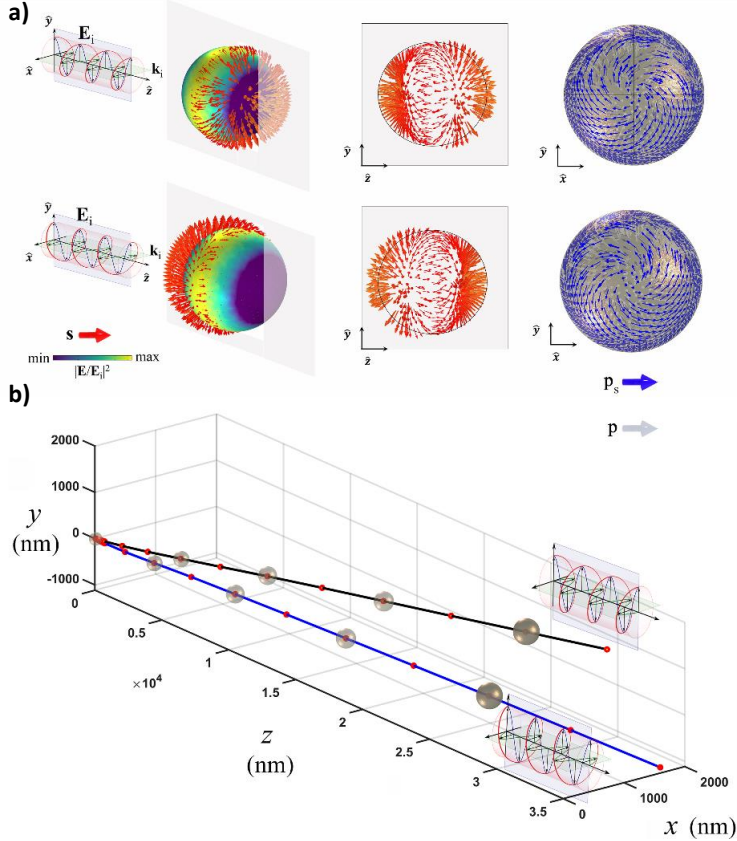


Figure 5.2: a) on the upper side, electric field, spin distribution, and momentum distribution along the sphere surface of a gold nanosphere LCP polarized; on the lower side, electric field, spin distribution, and momentum distribution along the sphere surface of a gold nanosphere RCP polarized. b) trajectory of the gold nanoparticle for LCP polarization and RCP polarization.

the Maxwell Tensor, see eq.A.21 and derived the dynamic parameters using the equation of motion. As a consequence of  $\mathbf{p}^s$  distribution, the gold nanoparticle has a displacement along the  $y$ -axis in addition to the expected movement along the  $z$ -axis induced by the radiation pressure of the incident beam. The observed displacement exhibits a polarization dependence; since we have already observed that the distribution of  $\mathbf{p}^s$  depends on the direction of incidence of the beam, this phenomenon also manifests in the dynamics that is orthogonal to the direction of polarization; in fact if, for example, we consider a beam polarized along  $y$  instead of along  $x$ , the gold nanosphere undergoes a displacement along the

x-axis. Once we have observed the behavior of linear polarization in Fig.5.1 we go on to analyze the results in the case of circular polarization. In Fig.5.2(a) we observe the spin vector ( $\mathbf{s}$ ) and associated moment ( $\mathbf{p}_s$ ) defined by the eq.5.2 on the surface of the gold nanoparticle illuminated by a beam of light circularly polarized. Given a polarized LCP beam, we can observe in Fig.5.2(a) top left, the electric field distribution with associated  $\mathbf{s}$  distribution on the surface of the gold sphere. In particular, we can see that the spin, unlike linear polarization, is distributed along the electric field minimum and directed radially to the plane. As in the linear case, the distribution reverses its direction along one axis of the sphere, as we can see in Fig.5.2(a) in the upper center; however, unlike the linear case, the distribution presents an asymmetry in intensity given that the spin is present more intensely in one hemisphere than the other. In Fig.5.2(a) on the upper right we observe the behavior of  $\mathbf{p}^s$  along the surface of the sphere, we can see that, following eq. 5.2,  $\mathbf{p}^s$  is tangent to the surface of the sphere and keeps the characteristics observed previously for  $\mathbf{s}$ . Considering instead a polarized RCP light beam, as we can observe in the lower part of Fig.5.2(a), the behavior of  $\mathbf{s}$  and  $\mathbf{p}_s$  is the same respect a beam LCP-polarized, but we also noted that the two trends are symmetrical to an axis of the sphere. Thus, from the results of the simulations, a helicity-dependent behavior is obtained for circular polarizations such that the spin and its associated momentum are distributed more in an area of the spherical surface that changes as the helicity changes. The behavior of the spin moment is reflected in the dynamics of the gold nanoparticle observed in Fig.5.2(b). Remember that the Poynting momentum, when the gold particle is near the plasmon resonance, has a relevant Belinfante term, as seen in Fig.5.1(c). The force and dynamics induced by the spin distribution, present some differences compared to that induced only for the radiation pressure. We observe in Fig.5.2(b) a displacement from the radiation pressure trajectory along the xy plane, in agreement with the Belinfante momentum distribution (Fig5.2(a)). In particular, for an LCP polarization, the nanosphere will have a deviation along the  $y < 0$  axis and  $x < 0$  axis while in RCP polarization the nanosphere has a deviation along the  $y < 0$  axis and  $x > 0$  axis. This result involves that the nanoparticle's path in circular polarization is helicity dependent; in particular, we observe a symmetry for the y-axis of the trajectory when the helicity of the beam changes.

### 5.3.1 Spin Momentum in Plasmonic Dimer

Once we have studied the behavior of SAM on a gold monomer and observed the dynamic variation of the particle, we turn to the study of a gold dimer; in particular, given the particular dimer field configuration, the spin moment takes on a nontrivial topological conformation. This new distribution depends on the polarization of the incident beam, as was the case for SAM in the monomer, but also the gap size between the two particles. In Fig.5.3 a dimer formed by two gold particles of radius 10nm positioned parallel to the x-axis and separated by a gap of size 1nm. The incident light is directed along the z-axis and polarized along the x-axis with a wavelength of 530nm. The FEM model of a plasmonic

dimer has the same features as the previous case but we design two gold spheres of radius 10nm separated by a gap of 1nm centered at the origin. The physics and mesh are the same as in the previous case, except that a dense subdivision in the sphere domain results in a refined mesh in the gap. We use a refined mesh for an accurate momentum distribution in the gap dimer. In Fig.5.3(a),

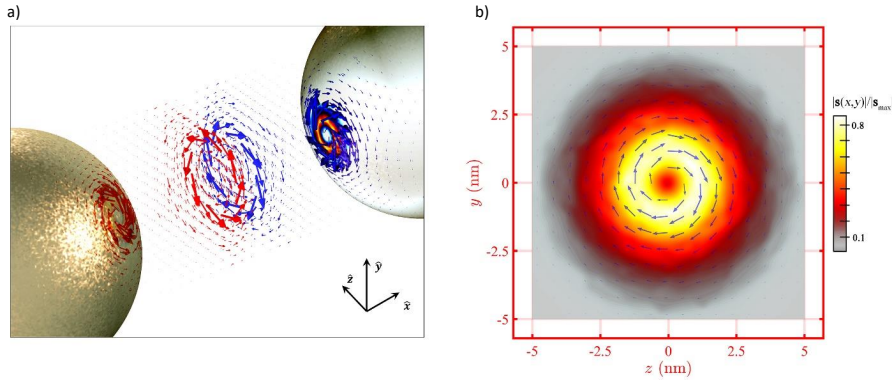


Figure 5.3: a) 3D spin distribution in the dimer gap. b) 2D spin distribution and spin amplitude along the sphere surface in a gold dimer.

the distribution of the spin momentum within the gap of the structure is shown; In this case, the spin moment tends to form a counterclockwise vortex nearby the left nanoparticle and clockwise nearby the right particle. The two vortices tend to intersect in the center of the gap where they collapse, generating a discontinuity. Fig.5.3(b) shows a section along the yz plane of the spin within the dimer gap. The spin is directed tangentially to the plane, evaluating its intensity as a function of its maximum value, it is observed that it is most concentrated at the center of the gap by decreasing its intensity radially. The phenomenon is explained by considering the behaviors of plasmonic structures observed in the literature[134]. the eq.5.2 defines a relationship between the spin components with the electromagnetic field components; a consequence is a direct relationship between the electric field amplitude and the intensity of the spin vector. For this reason, from fig.5.3 it was shown that in the dimer plasmonic hotspot, there is a more intense spin distribution. In agreement with what we have already seen in the single-particle case, the direction of the spin in a plasmonic dimer is tangent to the maximum field distribution. Since the dimer exposes the opposite surface in the gap between the structures we expect the directions of the two vortices to be opposite. The formation of the spin discontinuity can be explained by considering an overlapping phenomenon between the two spin vortices at the

center gap between the two structures. As in the case of the gold monomer, the spin distribution in the dimer is polarization-dependent. In particular, if we illuminate the structure with a y-polarized beam, i.e., transverse to the gap direction, the electric field is generated orthogonally to the gap. For the eq.5.2, the spin vortex is orthogonal to the gap and not inside the dimer. If we use the circularly polarized incident beam, like Fig.5.2, the spin distribution of the plasmonic monomer is asymmetric to the axis of rotation of the sphere. In a dimer, using circular polarization, spin distribution forms a vortex within the gap between the two surfaces. However, since the asymmetry along the rotation axis of the nanosphere, the spin distribution within the gap is asymmetric, unlike the linear case. In Fig.5.4, we analyze the behavior of spin intensity, considering

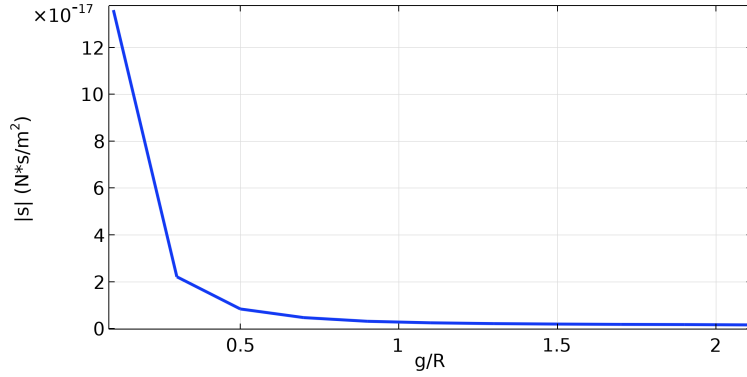


Figure 5.4: spin amplitude in function of the ratio  $g/R$  in a x-polarized gap dimer

an x-polarized beam, as the distance between the two nanoparticles varies. In particular, we observe the maximum amplitude of  $\mathbf{s}$  (calculated within the gap between the two particles), relate to the factor  $g/R$ , where  $R$  is the radius of the nanosphere. The maximum spin value tends to decay as the  $g/R$  factor changes. In particular, you can make a fit of the type  $y = Ax^b$  on the plot obtained and we get that  $A = 3.22 * 10^{-18}$  and  $b = -1.66$ , so the maximum spin value shows this trend:

$$s_{max} \simeq \frac{1}{g^2}$$

In conclusion, manipulation of the trajectory of a nanoparticle by evanescent waves led to the analysis of the spin-orbit effect. Specifically, the coupling between photon spin and angular momentum in the presence of an evanescent wave leads to the generation of a momentum transverse to the direction of the incident wave. By analyzing the phenomenon of gold nanospheres in plasmon resonance, we observed that we can induce polarized-dependent trajectory shifts. In addition, the formation of plasmonic dimer results in the formation

of a spin vortex such that at the center of the gap the distribution exhibits discontinuities. The presence of these phenomena in the evaluation of nanoparticle trajectories opens up new scenarios in the definition of the propulsion system. In particular, the detection of the plasmonic spin momentum would allow control over the direction of the nanoparticle exit velocity by ensuring directionality in a plasmonic thruster.



## Chapter 6

# Fabrication and Characterization

The optimized device, which was analyzed in the previous chapter using the FEM method, promises to provide usable performance in real applications compared to other plasmon thrusters; in fact, the parameters and the estimates obtained from simulations are optimal for secondary propulsion in a nanosatellite. Therefore, the final part of our research activity is finalized to fabricate a prototypal device and to obtain experimental results in agreement with what is predicted by the numerical analysis. In this chapter, we discuss the fabrication method of the designed and simulated trapezoidal device; then some measurements to characterize its effectiveness are carried out and reported.

### 6.1 Technological process for device fabrication

The technological process used to fabricate our plasmonic nanodevices is based on standard steps for the microelectronic industry. The peculiar aspects of the process flow are to be found in the electron beam lithography, necessary to guarantee the resolutions required by the design, and in the lift-off phase for the physical definition of the devices. In general, this fabrication process is used for creating a structure of a target material on the surface of a substrate using a sacrificial layer. It is an additive technique and the structure size can vary from the nanoscale to the centimeter scale. The whole process can be summarized (see fig.6.1) in the following point:

- 1) the substrate is prepared;
- 2) sacrificial layer is deposited, and an inverse pattern is created (ex. photoresist is exposed and developed). Depending on the resist, different methods can be used such as Extreme UltraViolet Lithography (EUVL) or Electron Beam Lithography (EBL). The photoresist is removed in the

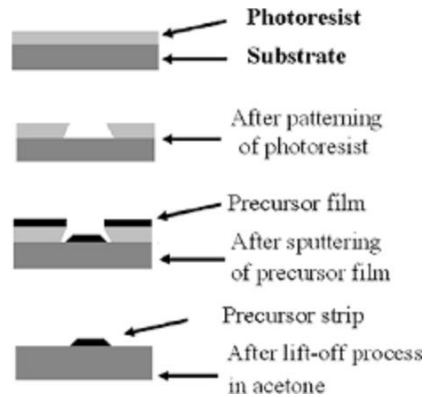


Figure 6.1: Summaries of the process based on lift-off etching

areas where the target material is to be located, creating an inverse pattern.;

- 3) target material (usually a thin metal layer) is deposited on the whole surface of the wafer). This layer covers the remaining resist as well as part of the wafer that was cleaned of the resist in the previous developing steps;
- 4) the rest of the sacrificial material is washed out together with parts of the target material covering it, only the material that was in the "holes" having direct contact with the underlying layer (substrate/wafer) stays.

Usually, this flowchart is utilized when a direct etching of structural material would have undesirable effects on the layer below. However, this useful technique presents some issues:

- 1) retention: unwanted parts of the metal layer may remain on the substrate. The reason can be different: the resist below the parts that should have lifted off not dissolved properly. Also, the metal may have adherent so well to parts that should remain that it prevents lift-off;
- 2) ears: when the metal is deposited, and it covers the sidewall of the resist, "ears" can be formed. These are made of metal along the sidewall which will be standing upwards from the surface. Also, these ears may fall over the surface, causing an unwanted shape of the substrate;
- 3) re-deposition: during the lift-off process particles of metal may become reattached to the surface, at a random location.

In this chapter, we will explain in detail all phases listed previously. We will also give a brief introduction of the machines used, specifying the process recipes used for the construction of the samples that we will analyze and evaluate.

## Plasma-enhanced chemical vapor deposition (PECVD)

First of all, we need a proper substrate for the plasmonic system. In general, the substrate for a plasmonic system must be much thicker than the thickness of the metal on which the interaction phenomenon occurs. Therefore, a microscope slide of 1mm thickness is typically used as the basis for plasmonic devices. However, standard glass slides have excessive surface roughness which causes problems throughout the manufacturing process and is a source of unwanted scattering of optical radiation. For this reason, it is necessary to deposit on this slide, a buffer layer of  $SiO_2$  using a technique known as Plasma Enhanced Chemical Vapor Deposition (PECVD). The  $SiO_2$  layer deposited through PECVD turns out to be smooth and free of imperfections reducing errors in the manufacturing process. Thickness of this layer must be in the order of 100/150nm.

The PECVD (fig.6.2(a)) is a vacuum deposition method used to produce high-quality and high-performance solid materials. The process is usually used to produce thin films. In typical CVD (Chemical Vapor Deposition), the substrate is exposed to one or more volatile precursors, which react and/or decompose on the substrate surface to produce the desired deposit. Frequently, volatile products are also obtained which are removed by the gas flow through the reaction chamber. However, in PECVD the plasma enhances the chemical reaction rates of the precursor. A plasma is any gas in which a significant percentage of the atoms or molecules are ionized. Processing plasmas are typically operated at pressures of a few millitorrs to a few torrs.

Plasmas are of great interest for material processing because electrons are so light, compared to atoms and molecules, that energy exchange between the electrons and neutral gas is very inefficient. Therefore, the electrons can be maintained at a very high equivalent temperature while neutral atoms remain at ambient temperature. These energetic electrons can induce many processes that would otherwise be very improbable at low temperatures, such as the dissociation of precursor molecules and the creation of large quantities of free radicals. The second benefit of the PECVD is in the mobility of the electrons. Since the electrons are more mobile respect to the ions, the plasma is normally positive respect to the other elements in the CVD otherwise a large flux of electrons flows from the plasma. The presence of the electron's flow generates a potential difference between the plasma and the reagent in a thin region of the CVD. Ionized atoms or molecules that diffuse to this region feel an electrostatic force and are accelerated toward the neighboring surfaces. Thus, all surfaces exposed to the plasma receive energetic ion bombardment. The potential in the thin region is typically only 10 – 20V but a much higher potential amplitude is achievable with a variety of geometry and configuration. The ion bombardment can increase the density of the film, help to remove contaminants, and improves the film's electrical and mechanical properties. When a high-density plasma is used, the larger ion density induces the sputtering of the deposited film. This sputtering can be employed to planarize the film and fill trenches or holes.

The PECVD[135] apparatus used is an Oxford PlasmaLab System 100 fig.6.2(b). The system, used for deposition of  $SiO_2$ , consists of a load-lock and a reactor

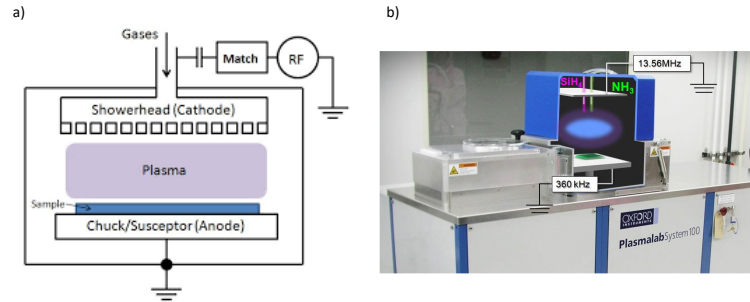


Figure 6.2: a) sketch of the PECVD working principle b) Image of Oxford Plasmalab 100 used for the sample. Image reproduced by [135]

chamber. The former can be easily vented or pressurized at room temperature and is used for sample loading. The latter can be kept at low pressure and heated to a temperature up to 400°C. Through a sealed venting port the sample can be transferred between the load lock and the reactor chamber without any contamination. Mass flow controller (MFC) valves, interfacing the reaction chamber with specific cylinders in the technical room of the clean room, allow the injection of the precursor gasses (silane  $SiH_4$ , ammonia  $NH_3$  and oxygen  $O_2$ ) with a controlled ratio. Such a reaction can be enhanced by the mean of an RF field created by a plasma of precursor gases between a top electrode and the bottom grounded sample plate. Temperature and gases-ratio can be used to control the deposition rate of the film and therefore the final thickness.

### Reactive Ion Etching (RIE)

After using PECVD we obtain a glass substrate with a surface free of imperfections and impurities. The next step is to coat the substrate with a resist, in our specific case PMMA. However, the glass surface, due to the low reactivity of the material, does not bond with PMMA, consequently, the PMMA layer does not adhere to the glass substrate. Therefore, to achieve perfect adhesion between the resist and substrate, the glass surface must be chemically "activated"; this process is carried out using Reactive-Ion Etching (RIE).

RIE technology used in microfabrication is a type of dry etching and uses chemically reactive plasma to remove material deposited on substrates. RIE generates the plasma under low pressure (vacuum) by an electromagnetic field. High-energy ions from the plasma attack the wafer surface and react with it.

A typical RIE[135][136] (as can be seen in fig.6.3) consists of a cylindrical vacuum chamber, with a wafer platter situated in the bottom portion of the chamber. The wafer platter is electrically isolated from the rest of the chamber.

Gas enters through small inlets in the top of the chamber, and exits to the vacuum pump system through the bottom. The types and amount of gas used depend on the process. The method of operation is the following: Plasma

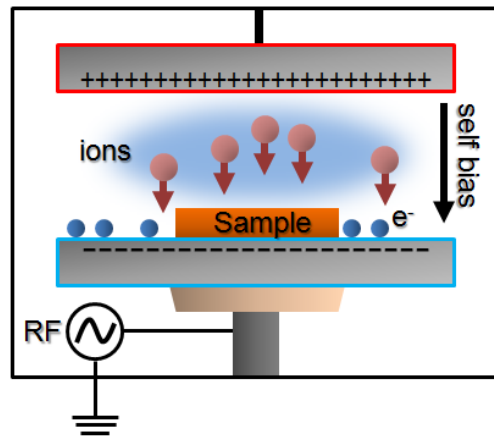


Figure 6.3: sketch of RIE system

is induced in the system by applying a strong RF electromagnetic field to the wafer platter. The oscillating electric field ionizes the gas molecules by stripping them of electrons, creating a plasma. In each cycle of the field, the electrons are accelerated up and down in the chamber striking both the upper wall of the chamber and the wafer platter. At the same time, the ions move in response to the RF electric field. When the chamber's wall absorbs the electrons, they are fed out to the ground and do not alter the electronic state of the system. However, electrons deposited on the wafer platter cause the platter to build up charge due to its DC isolation. The charge develops a large negative voltage on the platter, typically around a few hundred volts. The plasma itself develops a slightly positive charge due to the higher concentration of positive ions compared to free electrons. Because of a large voltage difference, the positive ions tend to drift toward the wafer platter, where they collide with the samples to be etched. The ions react chemically with the materials on the surface of the samples and knock off (sputter) some materials with their kinetic energy. Due to the vertical delivery of reactive ions, the RIE produces a very anisotropic etch profile.

### Spinning of resist layer

Once the RIE has activated the substrate, we can deposit on it the layer of PMMA, that is the sacrificial layer in the lift-off process. The PMMA layer must be enough thin to pattern it with the geometry of the designed device through the lithography process. Therefore, a solution containing PMMA is

spun at a speed of 4000 rpm on the substrate in liquid form to completely cover the surface; finally, the PMMA film is heated with a heating plate to a temperature of about 100°C to make the solvent evaporate and to bring the polymeric layer to the solid state. Once this process is completed, we obtain a substrate covered by an electron sensitive polymeric film that can be patterned with the geometry of the plasmonic device.

### E-beam lithography (EBL)

The substrate plus PMMA layer must finally be patterned, that is we must define the geometry of our sample. PMMA is exposed and then removed in some areas by defining the shape of the desired structures through a process using an electron beam called Electron Beam Lithography (EBL). Since our sample has very thin features, it is necessary to use high-resolution lithography like EBL because its higher precision. EBL[135][137] consists in the scanning of a focused beam of electrons to draw custom shapes on a surface covered with an electron-sensitive film called a resist (exposition). The electron beam changes the solubility of the resist, enabling selective removal of either the exposed or non-exposed regions of the resist by immersing it in a proper solvent (development). The purpose is to create very small structures in the resist that can subsequently be transferred to the substrate material, often by etching. The primary advantage of electron-beam lithography is that it can draw custom patterns with sub-10nm resolution. This form of maskless lithography has high resolution but low throughput and low volume of production. The EBL system

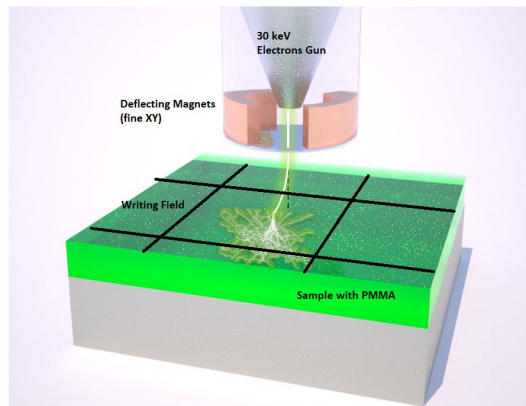


Figure 6.4: sketch of Electron Beam Lithography working principle. Image adapted by [135]

consists (fig.(6.4)) of a motorized  $x - y - z$  stage, a  $30keV$  electron gun inside a scanning electron microscope (SEM) column, a movable beam deflector and blacker, and a pattern generator that allows for the high-resolution control of

the relative position between sample and electron beam. The electron source emits electrons with thermionic or field electrons emission effect. The position accuracy is controlled within  $1nm$  using laser interferometric techniques. The pattern is drawn by the electron beam into the e-beam sensitive resist following the coordinates of a series of geometrical shapes that can be specified in dedicated software. The software allows the control also the electron dose of the emitter. In particular, the minimum time to expose a given area for a given dose depends on the following formula:

$$D \cdot A = t \cdot I \quad (6.1)$$

where  $t$  is the time to expose the object (can be divided into exposure time/space size),  $I$  is the beam current,  $D$  is the dose and  $A$  is the area exposed. The software is used to input  $t, I, A$  and define the output for the electron source. An initial manual alignment is necessary to regulate the sample orientation, the aperture, the stigmation and the focus of the beam, and the write-field mismatch. The write field is an imaginary square of  $100 \times 100\mu m^2$  and is the smallest unit of discretization in the raw movement of the electron beam. While proceeding with the automatic patterning, the stage moves from the center of one writing field to another. Within each write field, a stitching error  $< 50nm$  may occur. The SEM detectors can also be used to perform mix-and-match exposures on a substrate already patterned with alignment marks. When the electron beam hits the resist surface an inelastic scattering or collision occurs. The momentum transfer from the incident electron is capable of breaking the atom's bond in the resist. In general for a molecule  $AB$ :



The electrons obtained from the atoms bound generate an electron cascade and have a significant contribution to the evaluation of energy deposition. The secondary electrons induced by the incident beam and the forward scattering of the primary electrons (incident electrons make multiple scattering with the substrate) generate a proximity effect. The proximity effect increases the electron dose and exposure area of the resist, effectively enlarging the image and reducing the contrast. The proximity effect can be addressed by evaluating an inverse problem and calculating the exposure function  $E(x, y)$  that leads to a dose distribution as close as possible to the desired dose  $D(x, y)$ . Thus, in our case, initially using CAD software, the geometries for the samples, named  $Pr_01$  and  $Pr_02$ , were defined. Once the geometries are imported into the software, the minimum dose and current fed into the EBL are defined to obtain the pattern with the least possible error. The ideal dose, in our case, is between 800 and  $1400 \mu C/cm^2$  with current ranging from 1nA to 2nA. Once the lithography process is completed, the sample is developed i.e., the PMMA weakened by the electron beam is removed using a proper solvent.

### Metal evaporation and etching (lift-off)

After the development process, our system consists of a substrate with a PMMA layer on top that has "holes" with the shape of the designed sample geometry. The specimen is then ready for the following step of the process, that is the metal layer deposition. The metals used for the fabrication of our sample are titanium and gold, 2nm and 30nm thick respectively. The titanium is only intended to act as an adhesion layer between the gold and the  $SiO_2$  substrate so that (as analyzed in Chapter 4) it does not excessively alter the field response. Evaporation is a common method for thin metal film deposition. The source material is evaporated in a vacuum chamber. The vacuum allows vapor particles to travel directly to the target object (substrate), where they condense back to a solid state. The evaporator[138][135] is an electron-beam type machine where

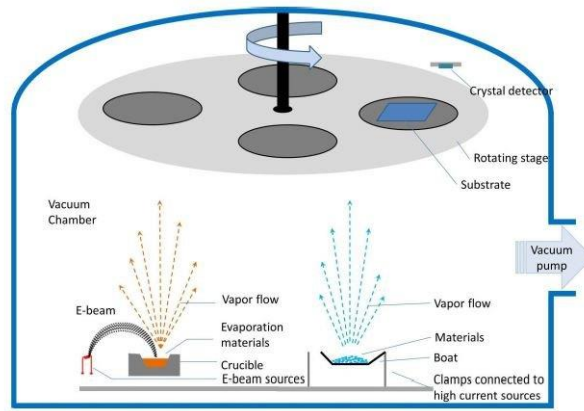


Figure 6.5: sketch of metal evaporator working principle

the metals are loaded in crucibles that can be selectively rotated and heated up to very high temperatures by an electron beam with energy up to  $15keV$ . Once the metal starts to evaporate, a shutter is opened allowing the migration of its atoms towards the surface of the sample mounted inside the main vacuum chamber at  $\simeq 10^{-7}mbar$ . The evaporated metal particle can travel directly to the deposition target without colliding with the background gas, thanks to the high vacuum made in the chamber. The deposition rate, and therefore the final thickness, is monitored using a piezoelectric sensor which resonance frequency depends on the thickness of material deposited on the crystal.

However, evaporated atoms may collide with other gas molecules which are present in the chamber and react to them. This reduces the amount of matter that reaches the substrate and so the thickness becomes difficult to control. In addition, if the substrate has a rough surface, the evaporated atoms deposition is non-uniform. Because the evaporated material attacks the substrate mostly from one direction, the surface's grooves block the evaporated atoms in some areas. This phenomenon is called "shadowing" or "step coverage". The metal

condensed then on the entire wafer forming a thin metallic layer with controlled thickness. Once the evaporation process is concluded, the metal coats the entire surface of the substrate. Finally, through a bath in an acetone-based solution, the PMMA film is chemically removed together with the metal layer deposited on it. On the other hand, only the metal regions deposited in correspondence with the areas exposed during the EBL lithography and in which the PMMA had already been removed before the evaporation, remain present on the sample. This last phase of the process is more properly called lift-off. The obtained samples, named Pr-01 and Pr-02, will be then characterized by microscopy techniques to verify the accuracy of the technological process.

## 6.2 Fabrication Result

Once the lift-off process was terminated, we have fabricated two samples named Pr-01 and Pr-02. The samples have a  $5mm \times 5mm$  area in which a series of trapezoidal structures ready for the characterization step was written. Specifically, sample Pr-01 is composed of trapezoidal structures of gold and titanium (30nm and 2nm thick respectively) with constant gaps in two different configurations:

- 1) linear array configuration,  $3\mu m$  long and composed of about 15 elementary cells;
- 2) circular array configuration, with two different radii,  $5\mu m$  and  $10\mu m$ .

The linear array configuration is replicated several with different geometric parameter values (major base, height, gap, spacing along y) so that the results of the simulations can be verified as the geometric parameters change (section 4.5.3). Instead, the circular configuration has a geometry optimized for resonance at the wavelength of 810nm, which is the wavelength of the laser source available in our laboratory. The Pr-02 sample, on the other hand, is composed of similar trapezoidal titanium and gold structures, but with alternating or linearly variable gap, organized in the following configurations:

- 1) linear array of alternating gap structures, with length of  $6\mu m$ , composed of 15 elementary cells;
- 2) linear array of linearly variable gap structures with length of  $6\mu m$ , composed of 15 elementary cells;
- 3) circular arrays of alternating gap structures, with radius  $5\mu m$  and  $10\mu m$  respectively;
- 4) circular arrays of linearly varying gap structures, with radius  $5\mu m$  and  $10\mu m$  respectively.

As in the case of sample Pr-01, the linear arrays in the Pr-02 sample are replicated several times with different geometrical parameters. The circular arrays

in the Pr-02 sample are designed to have resonance at 810nm, but they were replicated with different spacings between the elementary cells for solving some fabrication process issues that will be exposed latter in this section. Each array in the two samples is separated by about  $0.5\mu\text{m}$  to avoid interference effects between one structure and the next. The Pr-01 sample was designed to test the technological process developed and used, while Pr-02 is the sample designed for characterization. In this chapter, we report the results obtained from the morphological characterization of the fabricated devices using the Atomic Force Microscope (AFM) and the Scanning Electron Microscope (SEM), which have a sub-wavelength resolution, given the geometrical features we expect to evaluate.

### Atomic Force Microscopy

Once the fabrication process is terminated, the PR-01 sample is tested with Atomic Force Microscopy (AFM). AFM is a very-high-resolution type of scanning probe microscopy, with a resolution of a nanometer's fraction ( $0.1\text{nm}$ ), more than 1000 times better than the optical diffraction limit. The AFM sys-

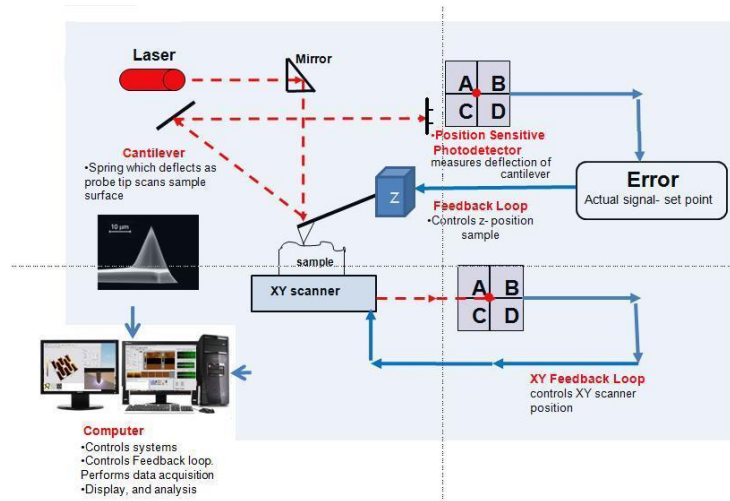


Figure 6.6: Sketch of AFM working principle

tem is sketched in (fig.6.6)[139]. A small spring-like cantilever ( $l = 110\mu\text{m}$ ,  $w = 35\mu\text{m}$ ) is carried by the support, a piezoelectric element (made of ceramic material) oscillates the cantilever, a sharp tip (curvature radius  $10\text{nm}$ ) is fixed to the free end of the cantilever, a laser is focalized on the cantilever and a four-sector photodetector records the deflection of the laser, deriving the motion of the cantilever. The photodetector converts the deflection of the cantilever into an electric signal; the intensity of the signal is proportional to the displacement of the cantilever. The sample is mounted on a stage and an x-y-z drive allows its displacement in a controlled way. A z-feedback loop controls the z-position

of the cantilever, and it verifies the position error of the tip and evaluates the z-topography.

The AFM systems have two main operating modes, according to the nature of the tip motion: contact mode and non-contact mode.

In contact mode[140], after defining a signal intensity like a "set point", the tip is placed across the surface of the sample. The atomic force, in virtue of the Lennard-Jones potential, is repulsive; thus, the tip suffers a force that displaces it, so altering its position respect to the laser focalized on it. The variation of the laser spot position is monitored with a four-sector photodetector and its changes modify the produced electrical signal intensity. The z-electronic feedback loop is employed to keep the probe sample force constant during scanning. Thus, the difference between the new signal intensity and the "set point" is an input to the z-feedback loop, and its output controls the distance along the z-axis. When the feedback modifies the distance, the signal returns to the "set point" intensity. The repetition of this cycle for each point  $(x, y)$  during a raster scan of the sample allows us to obtain the topography its surface.

In non-contact mode[140], the tip of the cantilever does not contact the sample surface. The cantilever instead oscillates at its resonance frequency ( $320Hz$  in our microscope). The van der Waals forces are strongest in the range from  $1nm$  to  $10nm$  above the surface than any other long-range force. This force extends above the surface decreasing the resonance frequency of the cantilever. The shift of the resonance frequency, combined with the feedback loop system, maintains a constant oscillation frequency by adjusting the tip-to-sample distance. Measuring the tip-to-sample distance at each  $(x, y)$  data point allows the scanning software to reconstruct a topographic image of the sample surface.

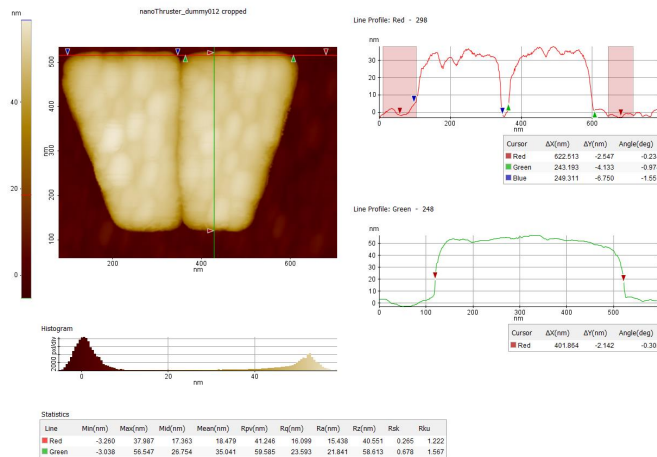


Figure 6.7: AFM imaging of sample Pr-01

Fig.6.7 shows the results of the *Pr – 01* sample analysis carried out with the AFM in contact mode. Through AFM measurements, we observed some elementary cells present in the linear and circular arrays, focusing on the dimensions of the geometric parameters of the trapezoid, namely major base, minor base, height, gap, and spacing between the elementary cells. The data obtained from the AFM analysis are compared with the design parameters of the Pr-01 sample; it was noticed that the dimensions of the major base, minor base, and height are increased in the fabricated structures by 20nm compared to the design data, while the spacing between the elementary cells is reduced by 15nm. From the AFM analysis, we are not able to obtain information about the size of the gap; because the AFM tip has a larger dimension (radius of curvature) than the gap between the two structures. For this reason, AFM can not reconstruct the correct topology of the gap and then we decided to analyze this specific feature of the Pr-01 sample through a scanning electron microscope (SEM).

### 6.2.1 Scanning Electron Microscope (SEM)

The results of the AFM analysis report partial indications on sample Pr-01. The reason is that the low resolution due to the tip size being larger than the gap size of trapezoidal devices. To overcome this limit, switching from probe microscopy to electron scanning microscopy (SEM) is required (fig.6.8). Electron scanning microscopy[141][142] has a higher resolution and thus allows gap analysis, together with other geometric parameters that are "invisible" to AFM analysis. An SEM is a type of microscope that produce images of a sample by scanning its

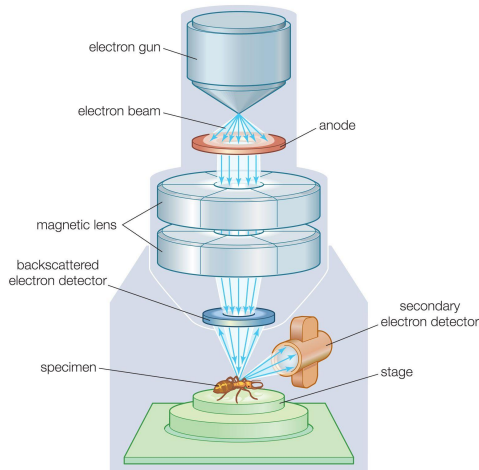


Figure 6.8: Sketch of SEM system

surface with a focused beam of electrons. The electrons interact with atoms of

the sample, producing various signals that contain information about its topography. The electron beam is scanned in a raster pattern, and the intensity of the detected signal is correlated with the position of the beam to produce an image. The signals used in a SEM to produce an image result from interactions of the electron beam with atoms at various depths within the sample. Various types of signals come from secondary electrons (SE), back-scattered electrons (BSE), characteristic X-rays, and cathodoluminescence (CL). Secondary electrons (SE) have very low energy, on the order of  $50\text{eV}$ , which limits their mean free path in solid matter. SE can only escape from the top few nanometers of the sample surface. The signal from secondary electrons tends to be highly localized at the point of impact of the primary electron beam, making it possible to collect images of the sample with a resolution of  $1\text{nm}$  and below. Back-scattered electrons (BSE) are beam electrons that are reflected from the sample by elastic scattering. Since they have much energy than SE, Back-scattered electrons emerge from deeper locations within the specimen; consequently, the resolution of BSE images is lower than SE images. BSE images, thanks to the characteristic X-ray spectra, can provide information about the distribution but not the identity of a different element of the sample. Due to the very narrow electron beam, SEM micrographs have a large depth of field yielding a characteristic three-dimensional appearance useful for understanding the surface structure of the sample. In a typical SEM, an electron beam is emitted from an electron gun fitted with a tungsten filament cathode or with a field emission source (Schottky emitter or tungsten tip). Tungsten is normally used in electron guns because it has the highest melting point and lowest vapor pressure of all metals, thereby allowing it to be electrically heated for electron emission. The electron beam has an energy ranging from few hundreds of eV up to several tens of keV and is focused by one or two condenser lenses to a spot from about  $0.5\text{nm}$  up to  $5\text{nm}$  in diameter. The beam passes through pairs of scanning coils in the electron column, typically the final lenses, which deflect the beam in the x and y axis and scan in a raster way a rectangular area of the sample surface. When the primary electron beam interacts with the sample, the electrons lose energy by repeated random scattering and by absorption within a part of the volume, which extends from less than  $100\text{nm}$  to approximately  $5\mu\text{m}$  into the surface. The energy exchange between the electron beam and the sample results in the reflection of high-energy electrons by elastic scattering, the emission of secondary electrons by inelastic scattering, and the emission of electromagnetic radiation, each of which can be detected by specialized detectors. The beam current absorbed by the specimen can also be detected and used to create images of the distribution of the specimen current. Electronic amplifiers of various types are used to amplify the signal, which is displayed as a variation in brightness on a computer monitor. Each pixel of computer video memory is synchronized with the position of the beam on the specimen in the microscope, and the resulting image is, therefore, a distribution map of the intensity of the signal being emitted from the scanned area of the specimen. The sample Pr-01 was visualized with the SEM microscope (see fig.6.9; in particular, some elementary cells of different linear and circular arrays were analyzed focusing on the size of the geometric

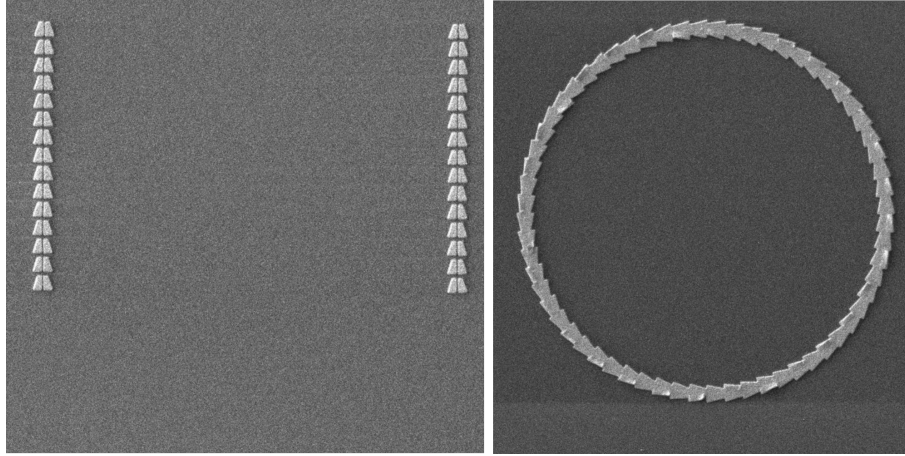


Figure 6.9: SEM imaging of sample Pr-01

parameters of each elementary cell, as in the case of analysis by AFM. The SEM data are in agreement with those of AFM about the dimensions of the major base, minor base, heights, and spacing between elementary cells. Given the resolution of the SEM microscope, it was possible to visualize the size of the gap between the two trapezoids. From SEM images, it is evident that the gap between the trapezoids decreases by about 15nm compared with that predicted from the design data of sample Pr-01. However, as observed in fig.6.9, a problem arises at the time when the elementary cells in the end-to-end configuration are analyzed. In particular, it can be seen from the figure that the gap of the elementary cells in an end-to-end matrix tends to close around the fifth or sixth trapezoidal structure along the array; this event can be observed for both linear and circular array structures. The phenomenon can be explained by considering a manufacturing defect that occurs during the patterning of the sample caused by the proximity error typical of the EBL technique (see paragraph 6.1.3). In the Pr-02 sample, to avoid the formation of structures with closed gaps, we preferred to design the array configurations with the constant presence of an offset in the spacing between the elementary cells. The Pr-02 sample, fabricated with these corrections, can then be analyzed under an optical microscope to verify the plasmonic resonance predicted by the numerical simulations discussed in the previous chapters.

### 6.3 Characterization of the sample

Once the results of the fabrication process are completely analyzed, the Pr-02 sample is tested in some experiments to characterize the electric field response of the surface plasmon and its resonance wavelength.

An initial experimental analysis was carried out using an optical microscope

in transmission mode. For the experiment, we use a Leica DM 6000M micro-



Figure 6.10: Microscope Leica DM6000M in laboratory

scope, shown in fig.6.3, with a white light lamp source and collection objectives with magnification up to 100x, needed for visualizing plasmonic structures. In our setup, we focus the white light through the microscope onto the sample, and then we collect the transmitted light on the opposite side, in the so-called transmission mode. A polarizer oriented along  $x$  (see fig.6.11) is applied to the incident light beam, while a polarizer orthogonal to the input one is placed in front of the collection objective. In this way, we get a better view of the response field of the plasmonic structure by cutting off the incident field. The results are shown in Fig.6.11. In particular, the figure illustrates that the circular structures exhibit a response field only in some areas of the ring (highlighted in green) This conformation is repeated symmetrically over the entire circumference. The result is in agreement with the characteristics of our plasmonic device. Specifically, when incident light passes through the polarizing filter, becoming  $x$ -polarized, and illuminates the circular structure, a resonance is generated in devices with transverse gap at the light polarization. The resonance is manifested, in far-field analysis by the formation of a shadow cone in the area of



Figure 6.11: Result of the transmission analysis in circular plasmonic device with x-polarized incident field and a y-polarized filter on the collector; highlighted in green the excitation zones of the plasmonic device

interest. If the polarized light along x passes through a filter that orthogonally polarizes the beam, the incident wave is darkened. This implies that the area where the circular device is not excited, i.e., where the polarization is parallel to the gap, is darkened. Finally, we consider the plasmonic response of the circular device that is partially excited by the incident beam (green circle of fig.6.11), i.e., the structures in which the polarization of the incident light is neither parallel nor transverse to the gap and therefore the device reacts to the incident field partially. In the area highlighted in green in Fig.6.11, only the transverse gap component of the incident polarization excites the structures while the component parallel to the gap passes undisturbed through the system. Since the component that excites the system is not transmitted, only the incident field component parallel to the gap of the structures in green in fig.6.11 arrives on the collector. Since a polarizer has been placed on the collector along y (according to the reference system in fig.6.11) and the component parallel to the gap is a superposition of  $E_x$  and  $E_y$  it follows that only part of the field is absorbed by the polarization filter and for this reason, the area highlighted in green remains illuminated.

The results obtained from fig.6.11 show the resonant behavior of the plas-

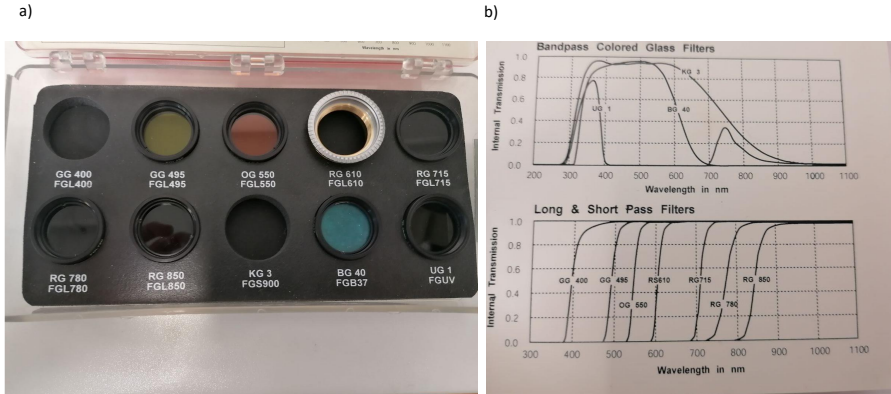


Figure 6.12: a) the high-pass laboratory filter for the infrared transmission analysis b) transmittance as a function of the wavelength in each filter

monic device. However, with this type of setup, we are unable to confirm that the plasmonic resonance is at the wavelength predicted by the simulations with the geometrical parameters used for the fabrication of the  $Pr - 02$  sample (810nm). Therefore, it is necessary to reduce the spectrum of wavelengths emitted by the light source. For this reason, we place high-pass filters on the incident beam (fig.6.12(a)); the filters can cut the wavelengths of the incident beam according to the curves observed in fig.6.12(b). With this type of setup, we observed circular devices with two different polarizations. Initially, in fig.6.13 the circular devices with spacings along the elementary cells are shown with the same polarization as in fig.6.11 and for different filters. We note how as the wavelength increases, the filter cuts the intensity of the transmitted field in the area around the green circle up to 850nm, where the transmitted field is not visible. The decrease in intensity can be explained if we look at the transmittance spectrum of an elementary cell of the plasmonic device reported in fig.4.26; in particular, it is evident from the graph that in the area around the plasmon resonance the transmittance decreases rapidly compared to what happens in other spectral ranges. Therefore, the more the filter tends to eliminate light radiation close to the plasmon resonance, the lower the amount of transmitted light we receive from the plasmonic device. When the transmitted radiation is no longer visible, the system does not admit resonance in the filter spectrum, as all the transmitted beam is absorbed by the filter placed on the microscope collector. The same phenomenon occurs in fig.6.14 where we analyze in transmission some circular devices in an end-to-end configuration in which the incident beam is polarized as indicated in the upper left figure and along the collector we have a

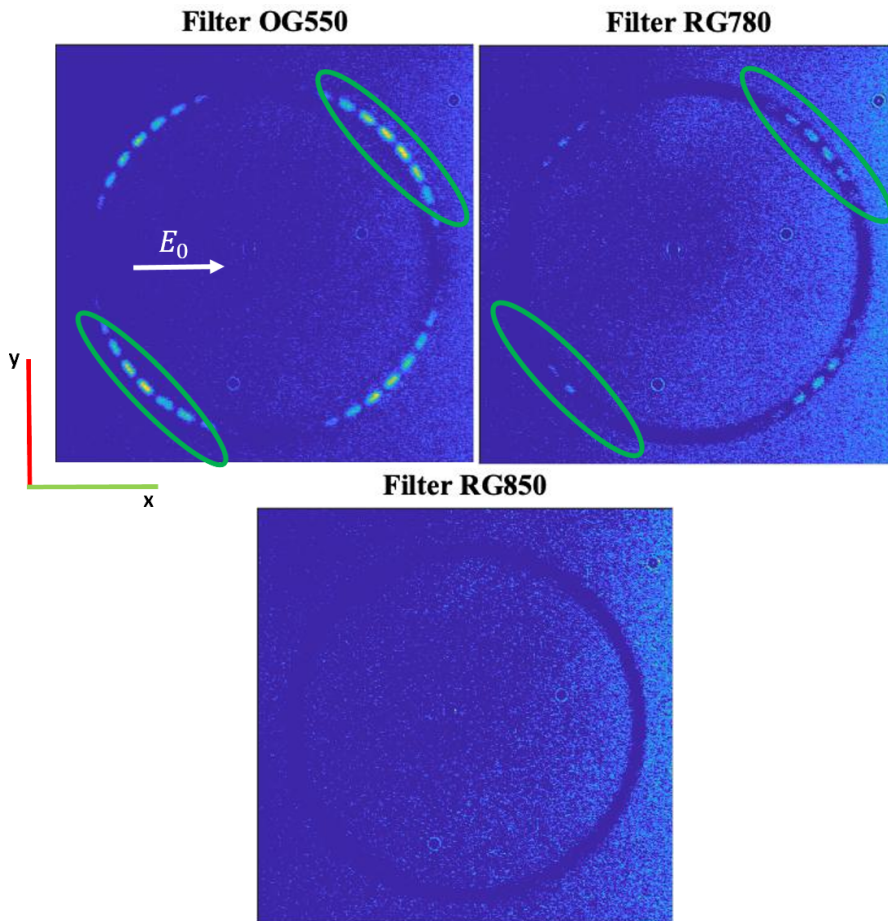


Figure 6.13: Transmitted beam in circular plasmon device with spacing in the elementary cell. The incident field is polarized along x and the analyzer is polarized along y; highlighted in green the excitation area of the plasmonic device. The incident wavelength is cut with different high-pass filters seen in fig.6.12(a)

polarizer filter transverse to the incident field. Since the polarization is different from that in fig.6.13, the area illuminated by the transmitted beam shifts around the x and y-axis (as indicated by the green circle), which repeats symmetrically throughout the circumference. Again, passing through filters with longer cut-off wavelengths results in a reduction in the intensity of the transmitted beam until 850nm, following what is predicted by the calculated transmission spectrum. Measurements produced with this setup appear to identify a wavelength spectrum in which the plasmonic structure can resonate and in agreement with what is predicted by the calculated transmission spectrum appears to be be-

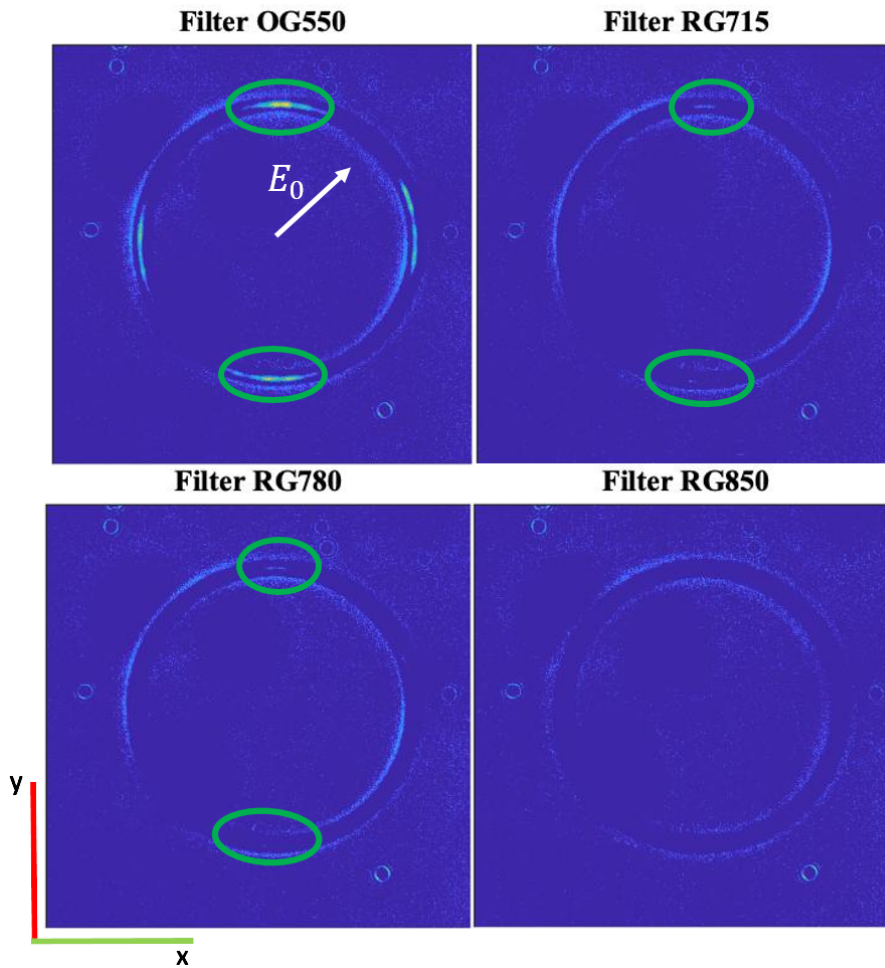


Figure 6.14: Transmitted beam in circular plasmon device. The incident electric field is polarized as indicated in the upper left figure and the collector has a filter with transverse polarization with respect to the incident field; highlighted in green an excitation zone of the plasmonic device. The incident wavelength is cut with different high-pass filters seen in fig.6.12(a)

tween 780nm and 850nm. However, the CCD that collects the transmitted light by the device has a higher efficiency in the visible than in the infrared range, so the reduction in intensity can also be induced by the loss of efficiency of the CCD. A final analysis of the plasmonic structure characteristics was performed by replacing the white light lamp with a laser beam with a wavelength of 805 nm. (See fig.6.15) In this case, we use the same polarizer and the same analyzer of the fig.6.14.



Figure 6.15: Transmission Microscope Leica DM6000M with a source laser of 805nm of wavelength (red circle).

The results obtained are reported in fig.6.16 where a behavior similar to fig.6.14 is observed. In fact, the partial resonance is found around (the green circle) repeated with symmetry along the entire circumference. In fig.6.16 we also observe the ray transmitted by a linear array. The measurement performed confirms the presence of a resonance in a wavelength spectrum of approximately 100nm around the value of  $\lambda = 805$  originating from the laser source.

Finally, an analysis of the scattered field was also carried out, which unlike the transmission analysis allows to obtain the confirmation of the electric field induced by the surface plasmon. Specifically, the sample was analyzed using a

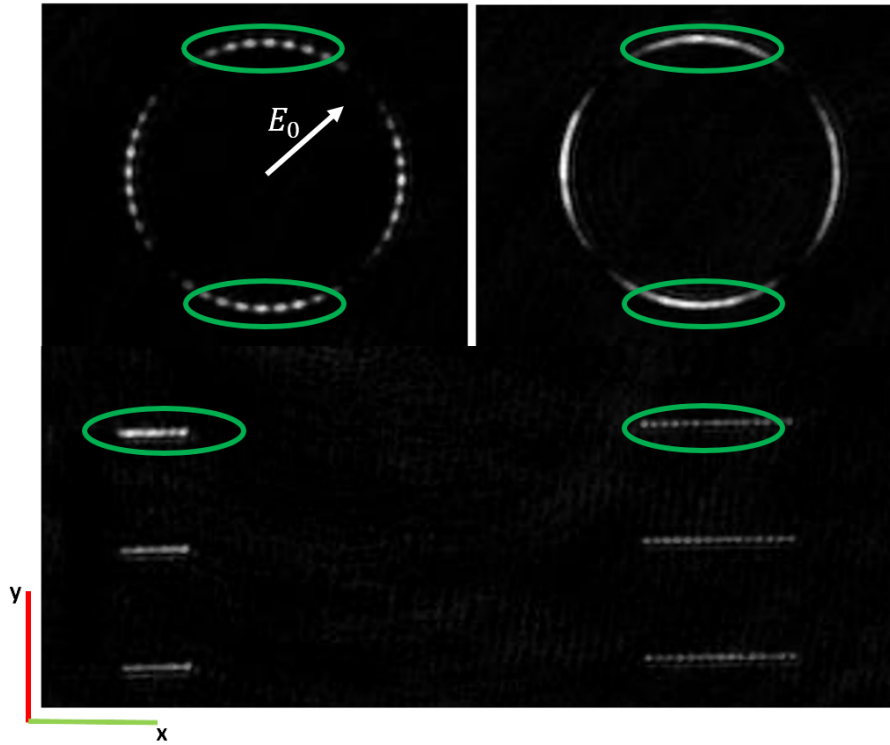


Figure 6.16: Transmission spectrum of circular device (upper left with spacing between elementary cell and upper right end-to-end configuration) and linear device (lower left end-to-end configuration and lower-right with spacing between elementary cell) in which the incident field (laser beam with wavelength 805nm) is polarized as indicated by the upper left figure; along the collector we use a polarizer filter transverse to the incidence polarization. Highlighted in green an excitation area of the plasmonic device

WiTec alpha300R SNOM (fig.6.17) that is capable to visualize the electric field distribution through the scattered field analysis. The analysis of the scattered field (s-SNOM) allows us to collect only the field diffused by the sample excluding the transmitted beam so as to be able to visualize the areas in which the field re-emitted by the plasmon structure tends to maximize. Fig.6.18 shows the results of scattered field analysis; in particular, the incident field comes from a supercontinuum laser, i.e., Super K with a maximum power of 4W and wavelengths ranging from visible to infrared [450 – 2500nm]. We observe that the structure exhibits amplification in the plasmonic device placed along the x-axis, in agreement with when observed in transmission analysis, as shown in Fig.6.1. Analysis of the wavelength spectrum showed that the system tends to be in resonance at around 750nm. This result is in fair agreement with what



Figure 6.17: The WiTec alpha300R microscope

was observed in the simulations in which the structures were found to have resonance at about 810 nm; however uncontrolled spacings between the various elementary cells in the fabricated device result in a blue shift of the resonance length. Furthermore, to overcome the manufacturing defects found in the AFM and SEM analyses, it was necessary to design the sample structures with a lower height than the simulated one; this may have led to a further blue shift of the wavelength.

Summarizing what was presented in this chapter, given the good outcome of the FEM simulations, we first moved on to the phase of realizing the designed devices and then to their morphological and functional characterization. The technological process used consists of the following steps:

- 1) starting from a 1mm-thick glass slide, 150nm of  $SiO_2$  were deposited to reduce substrate imperfections;
- 2) after surface activation by RIE, the substrate was coated with a thin layer of PMMA;
- 3) the PMMA was patterned with the geometry of the plasmonic device using EBL;
- 4) the patterned PMMA was developed with a solvent and then titanium (2nm) and gold (30nm) layers were deposited on the substrate;
- 5) the substrate, except for the patterned area, is cleaned of excess metal and PMMA with a bath in acetone solution (lift-off step).

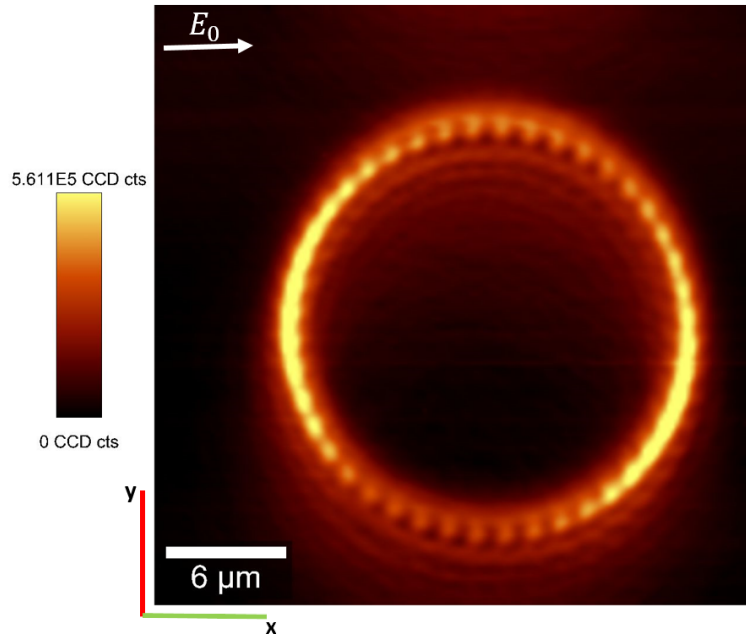


Figure 6.18: Scattered field microscopy of the circular plasmonic device

Two samples Pr-01 and Pr-02 were obtained by this process. Pr-01 is the sample used to verify the goodness of the fabrication method. After AFM and SEM analyses, some imperfections were observed in the dimensions of the various geometric parameters and in the gap between the structures. Sample Pr-02, taking into account the corrections obtained from the Pr-01 characterization, was fabricated and then used for the first analysis of plasmonic resonances. The analysis was performed using two different methods: a transmission microscope and a scattered near-field scanning optical microscope (s-SNOM). In both cases, the system showed resonance in the range between 700nm and 850nm, in agreement with what was predicted by FEM simulations on the same structures. The results obtained are decidedly encouraging and can be the starting point for further experimental verifications, in particular for the characterization of the dynamics induced by these systems on nanospheres.



# Conclusion

The new frontier of satellite design for intra- and extra-orbital missions has led to the development of the nanosatellite concept. However, to optimize the performance and payload capacity of nanosatellites, it is necessary to adopt a propulsion system, that is extremely compact and lightweight, maintaining performance for the satellite control. The required characteristics have led to the development of several remote propulsion techniques, in which thrust is induced through the activation of various physical phenomena by a source of energy placed at a certain distance from the body on which the propulsion acts.

In this thesis, we discussed one of these approaches, i.e., the propulsion induced by the emission of nanoparticles from a propulsion system inside the nanosatellite appropriately activated by a remote source. The need to manipulate nano- and microscopic objects with remote techniques has implied the development of devices capable of locally amplifying and concentrating the electromagnetic field of a remote source, intensifying the electromagnetic force acting on the nanoparticles and inducing their ejection and propulsion. One of the most interesting techniques is based on the use of surface plasmonic phenomena that can amplify and model the electromagnetic field in small areas.

In this thesis work, we have reported the results of the activity of study, analysis, and numerical simulation of the operation of a plasmonic nanostructure optimized to generate an appropriate spatial distribution of EM field. The research activity carried out has led to the definition of an optimized geometry that allows to overcome the limitations of similar structures presented in the recent scientific literature, thus making their performance of real application interest. The proposed nanostructure consists of two trapezoidal scalene prisms of gold deposited on a glass substrate; when the device is illuminated with polarized light, a plasmonic phenomenon is excited, i.e., a coupling between LSP (Localized Surface Plasmon) and SPP (Surface Plasmon Polaritons), which generates a strongly asymmetric and amplified electromagnetic field distribution that induces kinetics on a nanoparticle. A numerical technique called Finite Element Method (FEM) implemented in the commercial software COMSOL Multiphysics, coupled with Matlab software, was used to simulate the operation of the structure and evaluate its performance. In the first step, we derived the electric field distribution and the optical force in the plasmonic structure when it is excited with light radiation with the correct wavelength and polarization. Results were compared with those of other similar devices proposed in

literature, obtaining better performance in terms of induced force. For the elementary cell, we next evaluated the effects of varying geometrical parameters on the characteristics of the plasmonic phenomenon, such as resonance wavelength and electric field distribution, and consequently on the force generated. From the simulation results, we define the guidelines for the design of an optimized structure at the wavelength of a specific illumination source. The spatial replication of the proposed nanostructure was designed to analyze the behavior of linear or circular arrays of such elementary cells. This is a useful approach to periodically replicate and thus amplify the contribution of the generated force, and increase the final velocity of the ejected nanoparticles. Among the two configurations analyzed, the circular one achieves the same performance as the linear array, but with a spatially more compact structure eliminating the dependence of the final velocity on the number of elementary cells composing the array. However, due to inevitable manufacturing imperfections, the trajectory of the uniformly accelerated particle in a circular array may not be easily predictable, as well as its ejection point. A spiral configuration could be adopted to overcome this limitation.

The estimated results (induced force between 30-450 pN/W, final velocity with an incident electric field  $E_0 = 1(V/m)$  of about 0.01-0.15  $\mu\text{m/s}$  for an elementary cell, depending on the size of the nanoparticle considered) are interesting because the proposed structure, without the need of a power source on board the nanosatellite, and at the same time, characterized by small size and weight, has performance comparable to other secondary optical thrusters. In addition, we analyzed the difference between the two configurations (circular and linear) observing that the circular configuration with the same size is more efficient than the linear array.

A required property for a secondary propulsion system is the control of the nanosatellite displacement to improve the accuracy of the orbit corrections. Thus, the second step of the work performed is directed toward finding a solution for controlling the trajectory of the ejected propellant. For this reason, we studied a technique for the direct control of ejected nanoparticles that exploits the coupling effect between the wave intensity with the direction of field polarization. This effect arises from the quantum nature of the light that associates the electromagnetic wave with a particle (photon) with a spin of its own and is known as the spin-orbit effect. The spin-orbit effect in evanescent waves defines a transverse momentum that changes the trajectories of particles affected by it. Based on this information, we studied the phenomenon of a gold nanoparticle generating an LSP resonance and derived the following characteristics:

- 1) in the case of a single particle, the spin is distributed tangentially to the plane orthogonal to the polarization direction of the incident field and exhibits vortex and anti-vortex, given the symmetry of the system;
- 2) the dynamics of the resonant nanoparticle undergo deflections induced by the spin transverse momentum. This deflection depends on the incident polarizations;

- 3) in a plasmonic dimer, a vortex and an anti-vortex are formed within the gap for only a few polarizations, with varying intensities depending on the size of the gap and the polarization used; these two vortices collapse at the center, forming a discontinuous spin zone.

It is possible to modulate the direction of a nanoparticle exiting a plasmonic thruster by applying an appropriate polarization to the incident field. In addition, the plasmonic spin-orbit effect also has significant consequences on plasmonic dimers, leading to the generation of spin vortices and topological charging of the system. Spin control in surface plasmons may also have other future applications besides those related to propulsion, particularly in the development of spintronics, or the creation of electronics controlled by the spin of an electromagnetic wave.

Finally, given the encouraging results obtained from the FEM analysis of the structure, the design of the optimized structure led to the fabrication of a family of prototype devices at a nanofabrication foundry, where a technological process based on the use of electron beam lithography and subsequent lift-off step was developed and employed. The devices fabricated, in both linear and circular array configurations, were characterized morphologically and from the optical point of view for the evaluation of resonance wavelengths and the generated EM field distribution. From initial analyses, the experimental results appear to be in excellent agreement with the simulative ones. Shortly, we will try to improve the performance of the structure; the first goal is to overcome the main limitation of plasmonic devices, namely the strong decay of electric field amplification when moving away from the metal structure supporting the plasmon itself. In particular, we observed that nanoparticles located higher than the gap where LSPs and SPPs are generated, that is, in the region of exponential decay of the plasmonic wave, have lower force parameters. To overcome the lower force amplification, one can exploit a structure with a similar electric field distribution, but characterized by a lower reduction in the amplification induced by plasmonic damping; one example sees the excitation of plasmonic phenomena in semiconducting materials instead of metals. In the literature, it is known that semiconductors are capable of exciting surface plasmonic effects, but the material induces a plasmonic electric field with less spatial damping. The derived optical force does not reduce its intensity by moving away from the structure, and the velocity of even distant nanoparticles could be significant. In addition, the thermal stability of a semiconductor structure reduces the thermal effects related to heating-induced deformation in the trapezoidal device, and the dynamics induced on the nanoparticle turn out to be more stable.

In conclusion, a plasmonic propulsion system would take the use of CubeSats to the next level. The remote use of nanosatellites, controlled through the plasmonic propulsion system, would ensure easier maneuverability of the CubeSat with the ability to acquire data and images most efficiently. However, a propulsion system with this size and phenomenology can have other applications besides the aerospace sector. In particular, in the medical-biological field, a recurring theme is the displacement of genetic and molecular material.

Thus, such a plasmonic locomotion system, suitably tuned for biological systems, would ensure the movement of the genetic material of various types with efficiency and stability. Given these premises, plasmonic propulsion turns out to be a topic with higher prospects, the improvement of which would bring incredible development in many areas of research.

# Appendix A

## Electromagnetism in vacuum

### A.1 Vacuum Relation of $E$ and $B$

In this first part, we will look in detail at the equations describing light in a material focusing on how to derive mechanical quantities (force and energy) from electromagnetic waves. In 1893 Maxwell demonstrated the electromagnetic nature of light i.e., that light rays are the result of a combination of two vectors  $\mathbf{E}$  and  $\mathbf{B}$  electric field and magnetic induction field, respectively. Electromagnetic waves are defined through relationships between the electric field and the magnetic induction field, namely Maxwell's equations, which can be schematized as follows[54]:

$$\nabla \times \mathbf{B} = \frac{1}{c} \dot{\mathbf{E}} \quad (\text{A.1a})$$

$$\nabla \times \mathbf{E} = -\frac{1}{c} \dot{\mathbf{B}} \quad (\text{A.1b})$$

$$\nabla \cdot \mathbf{E} = 0 \quad (\text{A.1c})$$

$$\nabla \cdot \mathbf{B} = 0 \quad (\text{A.1d})$$

To describe the effect of the fields on a material object it is necessary to introduce a second set of vectors: the electric current density  $\mathbf{J}$ , the electric displacement  $\mathbf{D}$ , and the magnetic field  $\mathbf{H}$ . The presence of a continuous medium changes Maxwell's equations eq.A.1a-A.1d which will be defined as[54]:

$$\nabla \times \mathbf{H} - \frac{1}{c} \dot{\mathbf{D}} = \frac{4\pi}{c} \mathbf{J} \quad (\text{A.2a})$$

$$\nabla \times \mathbf{E} - \frac{1}{c} \dot{\mathbf{B}} = 0 \quad (\text{A.2b})$$

$$\nabla \cdot \mathbf{D} = 4\pi\rho \quad (\text{A.2c})$$

$$\nabla \cdot \mathbf{B} = 0 \quad (\text{A.2d})$$

where  $\rho$  is a known scaled quantity representing the charge density within the continuous medium;  $\rho$  is related to  $\mathbf{J}$  by the following equation[54]:

$$\dot{\rho} + \nabla \cdot \mathbf{J} = 0 \quad (\text{A.3})$$

the eq.A.3 is called the equation of continuity. It represents the charge conservation in the neighborhood of any point.

The Maxwell equations connect the five basic quantities  $\mathbf{E}$ ,  $\mathbf{H}$ ,  $\mathbf{B}$ ,  $\mathbf{D}$  and  $\mathbf{J}$ . The result is a unique determination of the field vectors from a given distribution of currents and charge; however, these equations must be supplemented by relations that describe the behavior of substances under the influence of the field. These relations are known as constitutive relations. They take the following form[54]:

$$\mathbf{J} = \sigma \mathbf{E} \quad (\text{A.4a})$$

$$\mathbf{D} = \epsilon \mathbf{E} \quad (\text{A.4b})$$

$$\mathbf{B} = \mu \mathbf{H} \quad (\text{A.4c})$$

Where  $\sigma$  is called specific conductivity,  $\epsilon$  is known as dielectric constant and  $\mu$  is called magnetic permeability. Eq.A.4a is the differential form of Ohm's law. Substances with  $\sigma \neq 0$  are called conductors. Substances with  $\sigma$  negligible are called dielectrics. Their electric and magnetic properties are determined from the value of  $\epsilon$  and  $\mu$ . In general, most substances have  $\mu \simeq 1$ ; however in the case in which  $\mu \neq 1$  appreciably, the material is defined as magnetic. Maxwell's equation is only applicable to regions of space in which the physical properties of the medium are continuous. In optics, it is easy to find situations in which the properties of the medium change abruptly across one or more surfaces. The vectors  $\mathbf{E}$ ,  $\mathbf{H}$ ,  $\mathbf{B}$ ,  $\mathbf{D}$  become discontinuous and  $\rho$  and  $\mathbf{J}$  degenerate into corresponding surface quantities. Thus, it is possible to determine the behavior of the electric and magnetic field components when moving from one continuous medium to another[143][144]. It is shown that the normal component of the magnetic induction is continuous across the surface of discontinuity:

$$\mathbf{n}_{12} \cdot (\mathbf{B}^{(2)} - \mathbf{B}^{(1)}) = 0 \quad (\text{A.5})$$

where  $n_{12}$  is the norm across the discontinuity surface. The normal component of the electric field displacement change across the surface:

$$n_{12} \cdot (\mathbf{D}^{(2)} - \mathbf{D}^{(1)}) = 4\pi\tilde{\rho} \quad (\text{A.6})$$

where  $\tilde{\rho}$  is the charge density along the discontinuity surface.

Instead, The tangential component of the electric field is demonstrated that is continuous across the surface:

$$n_{12} \times (\mathbf{E}^{(2)} - \mathbf{E}^{(1)}) = 0 \quad (\text{A.7})$$

While the tangential component of the magnetic vector changes abruptly as:

$$n_{12} \times (\mathbf{H}^{(2)} - \mathbf{H}^{(1)}) = \frac{4\pi}{c} \tilde{\mathbf{J}} \quad (\text{A.8})$$

where  $\tilde{\mathbf{J}}$  is the charge surface current density.

Maxwell's equations define the relationships between electric and magnetic fields, however, it is possible to relate the intensity of electromagnetic fields to mechanical properties such as energy flows and transferred moments. Recalling Maxwell's equations (eq.A.2a-A.2d) it follows that[54][144]:

$$\mathbf{E} \cdot \nabla \times \mathbf{H} - \mathbf{H} \cdot \nabla \times \mathbf{E} = \frac{4\pi}{c} \mathbf{J} \cdot \mathbf{E} + \frac{1}{c} \mathbf{E} \cdot \dot{\mathbf{D}} + \frac{1}{c} \mathbf{H} \cdot \dot{\mathbf{B}} \quad (\text{A.9})$$

By a known vector identity, i.e.  $a \cdot (b \times c) = b \cdot (a \times c) = c \cdot (a \times b)$ , the left term may be expressed as the divergence of the vector product of  $\mathbf{H}$  and  $\mathbf{E}$  and obtain:

$$\frac{1}{c} (\mathbf{E} \cdot \dot{\mathbf{D}} + \mathbf{H} \cdot \dot{\mathbf{B}}) + \frac{4\pi}{c} \mathbf{J} \cdot \mathbf{E} + \nabla \cdot (\mathbf{E} \times \mathbf{H}) \quad (\text{A.10})$$

After we make the product between this equation and the factor  $\frac{c}{4\pi}$  and integrate throughout an arbitrary volume and apply Gauss's theorem, obtain:

$$\frac{1}{4\pi} \int (\mathbf{E} \cdot \dot{\mathbf{D}} + \mathbf{H} \cdot \dot{\mathbf{B}}) dV + \int \mathbf{J} \cdot \mathbf{E} dV + \frac{c}{4\pi} \int (\mathbf{E} \times \mathbf{H}) \cdot \mathbf{n} dS = 0 \quad (\text{A.11})$$

where the last integration is taken over the boundary of volume and  $\mathbf{n}$  is the normal unit outward. Considering the presence of a continuous medium, the constitutive relations (eq.A.4a-A.4c) are valid, and the eq.A.11 can be rewritten as follows:

$$\frac{1}{4\pi} \int \left( \frac{\partial}{\partial t} \epsilon \mathbf{E}^2 + \frac{\partial}{\partial t} \mu \mathbf{H}^2 \right) dV + \int \mathbf{J} \cdot \mathbf{E} dV + \frac{c}{4\pi} \int (\mathbf{E} \times \mathbf{H}) \cdot \mathbf{n} dS = 0 \quad (\text{A.12})$$

we can define  $w_e = \frac{1}{8\pi} \epsilon \mathbf{E}^2$ ,  $w_m = \frac{1}{8\pi} \mu \mathbf{H}^2$  and  $W = w_e + w_m$ . It is possible to demonstrate that  $W$  represents the total energy contained within the volume so that  $w_e$  is the electric density within the volume and  $w_m$  is the magnetic density within the volume. For an isolated system, the increase of  $W$  per unit of time is associated with the work done on the system during this time. We can define  $Q = \mathbf{J} \cdot \mathbf{E}$ ; this term represents the resistive dissipation of energy (called Joule's heat) in a conductor. Another term appears if the field extends to the boundary surface. In particular, we define  $S = \mathbf{E} \times \mathbf{H}$  as a Poynting vector and represent the amount of energy which crossed per second a unit of area normal to the direction of  $\mathbf{E}$  and  $\mathbf{H}$ .

The electromagnetic field, since it generates energy and work on a body, consequently also defines dynamic and thus electromagnetic field-induced moments. The forces defined by the electric field are called Lorentz Forces and are defined as follows[56]:

$$\mathbf{F} = q(\mathbf{E} + \mathbf{v} \times \mathbf{B}) = \int \rho(\mathbf{E} + \mathbf{v} \times \mathbf{B}) dV \quad (\text{A.13})$$

where  $q$  is the charge of the body,  $\rho$  is the volume charge density and  $v$  the velocity of the body. we can define  $f = \rho\mathbf{E} + \mathbf{J} \times \mathbf{B}$  as the electromagnetic force per unit volume. Given Maxwell's equations (A.2a-A.2d), we replace  $\rho$  and  $\mathbf{J}$  in terms of the electric and magnetic fields respectively and obtain:

$$\mathbf{f} = \epsilon_0(\nabla \cdot \mathbf{E})\mathbf{E} + \frac{1}{\mu_0}(\nabla \times \mathbf{B}) \times \mathbf{B} - \epsilon_0 \frac{\partial \mathbf{E}}{\partial t} \times \mathbf{B} \quad (\text{A.14})$$

The part of the equation with the time derivative can be rewritten in terms of the Poynting vector using a combination of Leibniz's rule and Maxwell's equations (A.2a-A.2d) in the following way:

$$\frac{\partial \mathbf{E}}{\partial t} \times \mathbf{B} = \frac{\partial(\mathbf{E} \times \mathbf{B})}{\partial t} + \nabla \times (\nabla \times \mathbf{E}) \quad (\text{A.15})$$

Substituting into  $f$  and separating the terms in E and B we get the following result:

$$\mathbf{f} = \epsilon_0[(\nabla \cdot \mathbf{E})\mathbf{E} + \nabla \times (\nabla \times \mathbf{E})] + \frac{1}{\mu_0}[(\nabla \cdot \mathbf{B})\mathbf{B} - \nabla \times (\nabla \times \mathbf{B})] - \epsilon_0 \frac{\partial(\mathbf{E} \times \mathbf{B})}{\partial t} \quad (\text{A.16})$$

The term  $(\nabla \cdot \mathbf{B})\mathbf{B}$  was added by considering equation A.2d to keep the symmetry of the relation. We also use the vector identity  $\frac{1}{2}\nabla(a \cdot a) = a \times (\nabla \times a) + (a \cdot \nabla)a$  to eliminate curl from the formula of  $f$  (eq.A.16) and obtain:

$$\begin{aligned} \mathbf{f} = \epsilon_0[(\nabla \cdot \mathbf{E})\mathbf{E} + (\mathbf{E} \cdot \nabla)\mathbf{E}] + \frac{1}{\mu_0}[(\nabla \cdot \mathbf{B})\mathbf{B} + (\mathbf{B} \cdot \nabla)\mathbf{B}] + \\ - \frac{1}{2}\nabla(\epsilon_0\mathbf{E}^2 + \frac{1}{\mu_0}\mathbf{B}^2) - \epsilon_0 \frac{\partial}{\partial t}(\mathbf{E} \times \mathbf{B}) \end{aligned} \quad (\text{A.17})$$

This expression contains every aspect of electromagnetism and momentum and is relatively easy to compute. It can be written more compactly by introducing the Maxwell stress tensor[56]:

$$T_{ij} = \epsilon_0(E_i E_j - \delta_{ij}|E|^2) + \frac{1}{\mu_0}(B_i B_j - \delta_{ij}|B|^2) \quad (\text{A.18})$$

Such that the overall moment induced by the electromagnetic field is thus defined as:

$$\nabla \cdot \mathbf{T} = \mathbf{f} + \epsilon_0 \mu_0 \frac{\partial \mathbf{S}}{\partial t} \quad (\text{A.19})$$

So Maxwell's tensor includes all the dynamics of objects induced by the electromagnetic field. If integrate the eq.A.19 over an arbitrary volume  $V$  which contain all sources  $\rho$  and  $\mathbf{J}$  we obtain[94]:

$$\int_V \nabla \cdot \mathbf{T} dV = \frac{d}{dt} \frac{1}{c^2} \int_V [(E \times H)dV + \int_V \rho\mathbf{E} + \mathbf{J} \times \mathbf{B}dV$$

remember that  $f = \rho\mathbf{E} + \mathbf{J} \times \mathbf{B}$ . The volume integral can be transformed into a surface integral using Gauss's integration law

$$\int_V \nabla \cdot \mathbf{T} = \int_{\partial V} \mathbf{T} \cdot \mathbf{n} da$$

$\partial V$  denotes the surface of  $V$ ,  $\mathbf{n}$  the unit vector perpendicular to the surface, and  $da$  an infinitesimal surface element. We then finally arrive at the conservation law for linear momentum:

$$\int_{\partial V} \mathbf{T}(\mathbf{r}, t) \cdot \mathbf{n} da = \frac{d}{dt} [G_{field} + G_{mech}] \quad (\text{A.20})$$

Here,  $G_{field}$  and  $G_{mech}$  denote the mechanical momentum, i.e.  $F = \frac{d}{dt} G_{mech}$  and the field momentum ( $G_{field} = \int_V \frac{1}{c^2} [E \times H] dV$ ). If we consider the time average of the force the field term disappears thus the average mechanical force is:

$$\langle F \rangle = \int_{\partial V} \langle \mathbf{T}(\mathbf{r}, t) \rangle \cdot \mathbf{n}(\mathbf{r}) da \quad (\text{A.21})$$

this equation is of general validity. It allows the mechanical force acting on an arbitrary body within the closed surface  $\partial V$  to be calculated. The force is entirely determined by the electric and magnetic field on the surface  $\partial V$ .

## A.2 Electromagnetic wave and optical phenomena

Maxwell's equations relate the field vectors using simultaneous differential equations. For the evaluation of the electric and magnetic field distribution, we need an equation system where the fields are decoupled. Starting with the eq.A.2b, using a curl operator on each term of the equation and substituting the  $\mathbf{B}$  term using the eq.A.2a remember that  $H = \frac{\mathbf{B}}{\mu}$  as can be seen in the eq.A.4c, this became[56][54]:

$$\nabla \times \left( \frac{1}{\mu} \nabla \times \mathbf{E} \right) + \frac{\epsilon}{c^2} \ddot{\mathbf{E}} = 0 \quad (\text{A.22})$$

using the identity vector for the curl elimination and considering the homogeneous media we obtain:

$$\nabla^2 \mathbf{E} - \frac{\epsilon\mu}{c^2} \ddot{\mathbf{E}} = 0 \quad (\text{A.23a})$$

$$\nabla^2 \mathbf{H} - \frac{\epsilon\mu}{c^2} \ddot{\mathbf{H}} = 0 \quad (\text{A.23b})$$

The eq.A.23b is obtained when we make the same process substituting  $\mathbf{E}$  instead of  $\mathbf{B}$ . The equations just obtained recall the form of differential equations known as wave equations for this reason they are defined, the coupling of Maxwell's equations is also referred to as "electromagnetic waves". The term  $\frac{c}{\epsilon\mu}$  is then the propagation speed of the wave with  $c = 3 \times 10^8$  which is defined as the speed of light in a vacuum. The characterization of the wave equation allows a formal evaluation of light phenomena.

Before analyzing the characteristics of the main light-induced phenomena, it is necessary to introduce the concept of polarization[54][143]. Let us consider a harmonic wave plane, i.e., when each Cartesian Component of  $\mathbf{E}$  and  $\mathbf{H}$  have the following form:

$$\mathbf{E}, \mathbf{H} = a \cos(\omega t - \mathbf{k} \cdot \mathbf{r} + \delta) \quad (\text{A.24})$$

where  $\omega$  is the frequency of the wave and  $\mathbf{k}$  is the propagation length of the wave and  $\delta$  is the phase shift of the wave. In the eq.A.24 we have chosen the z-axis-like propagation direction; it can be demonstrated that  $\mathbf{E}, \mathbf{H}$  and the propagation direction formed an orthogonal triad of vectors. The field component is only in the x and y directions obtained:

$$E_x = a_1 \cos(\omega t - \mathbf{k} \cdot \mathbf{r} + \delta_1) \quad E_y = a_2 \cos(\omega t - \mathbf{k} \cdot \mathbf{r} + \delta_2) \quad (\text{A.25})$$

These two terms can be manipulated and rewritten in the following way:

$$\left(\frac{E_x}{a_1}\right)^2 + \left(\frac{E_y}{a_2}\right)^2 - 2\frac{E_x E_y}{a_1 a_2} \cos \delta = \sin^2 \delta \quad (\text{A.26})$$

where  $\delta = \delta_2 - \delta_1$ . This is a conic equation; in particular, this is the ellipse equation since the associate determinant is not negative. The electric field is defined as elliptical polarized; it can be demonstrated that also the magnetic field is elliptically polarized. it is possible to define the polarization parameters instead of on the Cartesian axes, on the axes of the ellipse by redefining the field components on a new  $O\xi\eta$  reference system and obtain:

$$E_\xi = a \cos(\omega t + \mathbf{k} \cdot \mathbf{r} + \delta_0) \quad E_\eta = \pm b \cos(\omega t + \mathbf{k} \cdot \mathbf{r} + \delta_0) \quad (\text{A.27})$$

where  $a$  and  $b$  are the axes of the ellipse; The two reference systems are related in the following way:

$$a_1^2 + a_2^2 = a^2 + b^2 \quad (\text{A.28a})$$

$$\tan \psi = (\tan(2\alpha)) \cos \delta \quad (\text{A.28b})$$

$$\sin 2\chi = (\sin 2\alpha) \sin \delta \quad (\text{A.28c})$$

where  $\alpha = \tan \frac{a_2}{a_1}$ ,  $\psi$  is the angle between the new reference system  $O\xi\eta$  and the Cartesian system and  $\chi$  is an auxiliary angle that defines the shape and orientation of vibrational ellipse. From the ellipse parameter, it is possible to distinguish two particular cases of polarization. One is the linear polarization and is generated when  $\chi = 0 \rightarrow \delta = 0$  and the shape of the ellipse degenerate in a linear shape. The circular polarization instead is according to the sense in which the endpoint of the electric vector describes the ellipse. For this reason, we can define a right-handed polarization when an observer looking in the direction where the light is coming and the ellipse is described in a clockwise sense; otherwise, we have a left-handed polarization. Concerning the ellipse parameter, we have that  $\delta > 0$  or for the eq.  $0 < \chi \leq \pi/4$  for the right-handed and  $\delta < 0$  and  $-\pi/4 \leq \chi < 0$  for the left-handed. We have observed that to characterize the polarization ellipse three independent quantities are necessary: the amplitudes  $a_1, a_2$ , and the phase difference  $\delta$  or in the ellipse reference system the axis  $a$  and  $b$  and the angle  $\chi$  which specifies the orientation of the ellipse.

For practical purposes, it is convenient to characterize the state polarization by certain parameters that have all the same physical dimensions, introduced by Stokes[54]. The Stokes parameters of a plane monochromatic wave are four quantities:

$$s_0 = a_1^2 + a_2^2 \quad (\text{A.29a})$$

$$s_1 = a_1^2 - a_2^2 \quad (\text{A.29b})$$

$$s_2 = 2a_1a_2 \cos \delta \quad (\text{A.29c})$$

$$s_3 = 2a_1a_2 \sin \delta \quad (\text{A.29d})$$

three of them are independent and they are related by the following identity:

$$s_0^2 = s_1^2 + s_2^2 + s_3^2 \quad (\text{A.30})$$

the value  $s_1, s_2, s_3$  may be regarded as a point P on a sphere  $\sigma$  of radius  $s_0$ . This implies that every possible state of polarization of a plane monochromatic wave of a given intensity ( $s_0 = \text{const}$ ), corresponds at one point on  $\sigma$  and vice-versa. The relation of  $\sin \delta$  and  $s_3$  imply that the left-handed polarization is represented by the point in  $\Sigma$  below the equatorial plane and the right-handed polarization is the point in  $\sigma$  above the equatorial plane; the linear polarization instead is the point in the equatorial plane. The sphere  $\Sigma$  is called the Poincaré sphere.



## Appendix B

# Mathematical Tools of Finite Element Method

### B.1 Linear Triangular Discretization

Let us consider the differential equation,[145] in  $\Omega$ :

$$\left\{ \begin{array}{l} \text{find } u \text{ in } H^1(\Omega), \text{ such that} \\ u = g_0 \text{ on } \Gamma_D \\ \int_{\Omega} \nabla u \cdot \nabla v + c \int_{\Omega} uv = \int_{\Omega} fv + \int_{\Gamma_N} g_1 v \quad \forall v \in H_{\Gamma_D}^1(\Omega) \end{array} \right. \quad (\text{B.1})$$

Now, we want to discretize this differential equation and the physical domain to obtain an approximate value of  $u$ . Let us take an arbitrary, non-degenerate triangle  $K$ , a vertices  $p$  is uniquely determined by the value of points  $(x_1, x_2)$  for the following equation:

$$p = a_0 + a_1x_1 + a_2x_2 \quad a_0, a_1, a_2 \in \mathbb{R} \quad (\text{B.2})$$

The set of the vertices  $p$  that follows this equation is called  $\mathbb{P}_1$ . In other words, an edge is determined only from the adjacent vertices, this point is called the local grade of freedom.

Starting from the eq.B.2, we can generate the domain partition into a triangle. A triangulation of  $\Omega$  is a subdivision of this domain into triangles that must cover all  $\Omega$  with the followings rules:

- 1) if two triangles have some intersection, it is either on a common vertex or a common full edge and two different triangles do not overlap;
- 2) the triangulation must respect the partition into Dirichlet and Neumann boundaries. This means that an edge of a triangle that lies of  $\Gamma$  cannot be part Dirichlet and part Neumann, there must be a transition from the boundaries.

The set of triangles that the domain has been divided is called  $T_h$  with  $h$  as the length of the longest side among all the triangles. Focalize now to the function defined in the whole polygon  $\Omega$  that has been triangulated. Given the space  $T_h$  that contains all triangles, we take two triangles  $K$  and  $K'$  who have a common edge. In this case, we can define four functions  $u_h \in \mathbb{P}_1$  of the edge of two triangles. Since any function of  $\mathbb{P}_1$  depends only on the vertices adjacent to the edge under consideration, all the functions  $u_h$  are unique and globally continuous. If we consider the functions  $u_h$  for all vertices of all triangles we obtain a space  $V_h$  defined:

$$V_h = \left( u_h \in C(\bar{\Omega}) | u_h|_K \in \mathbb{P}_1, \quad \forall K \in T_h \right) \quad (\text{B.3})$$

If we fix a node and associate value one to the node and zero to all other elements, exists a unique function  $\phi_i \in V_h$  such that:

$$\phi_i(p_j) = \delta_{ij} \quad (\text{B.4})$$

where  $\delta_{ij}$  is the Kronecker delta respect to  $i$ -vertex. The function  $\phi_j$  represents the union of triangles that have  $p_j$  as a vertex. Take  $u_h \in V_h$  we can show that:

$$u_h = \sum_{j=1}^N u_h(p_j) \phi_j \quad (\text{B.5})$$

For a complete partition of domain  $\Omega$  it is necessary to define the partition of the boundary edge.

First of all, we define two different boundary edges: the Dirichlet boundary  $\Gamma_D$  and Neumann boundary  $\Gamma_N$  that is associated with the boundary condition of the differential equation. The defined boundaries define two different discrete entities: the Dirichlet node and Neumann edges. Remind that the function  $v$  is defined as  $v = 0$  in  $\Gamma_D$  so it belongs to the space  $H_{\Gamma_D}^1(\Omega)$ . When we perform a triangulation in  $\Omega$  the condition on  $v$  becomes a condition on a function  $v_h$  associated with the triangle set  $T_h$  such that  $v_h$  is in the space  $V_h^{\Gamma_D}$  defined as:

$$V_h^{\Gamma_D} = V_h \cap H_{\Gamma_D}^1 = (v_h \in V_h | v_h = 0 \text{ on } \Gamma_D) \quad (\text{B.6})$$

For this condition,  $v_h$  vanished on  $\Gamma_D$  if and only if vanished in all Dirichlet nodes. As in the domain  $\Omega$ , it is possible to write  $v_h$  with a linear combination of elements in the nodal basis that is:

$$v_h = \sum_{j=1}^N v_h(p_j) \phi_j \quad (\text{B.7})$$

Consider the system of equation defined in eq.B.7, the finite element method consists of the following discrete version of the previously weak formulation:

$$\left| \begin{array}{l} \text{find } u_h \in V_h, \text{ such that} \\ u_h(p) = g_0(p) \text{ for all Dirichlet node } p \\ \int_{\Omega} \nabla u_h \cdot \nabla v_h + c \int_{\Omega} u_h v_h = \int_{\Omega} f v_h + \int_{\Gamma_N} g_1 v_h \quad \forall v_h \in V_h^{\Gamma_D} \end{array} \right. \quad (\text{B.8})$$

In this formulation, we have reduced the problem in eq.B.1 to the solution of  $u_h$  in the vertices of the triangulation, and the number of unknowns is finite; in addition, the Dirichlet condition is fixing for the Dirichlet nodes and reduces the number of unknown only at the free nodes. Without loss of generality, we take  $v_h = \phi_i \in V_h^{\Gamma_D}$  and the method is equivalent in a set of  $N$  equations whose unknown is the function  $u_h$ :

$$\int_{\Omega} \nabla u_h \cdot \nabla \phi_i + c \int_{\Omega} u_h \phi_i = \int_{\Omega} f \phi_i + \int_{\Gamma_N} g_1 \phi_i \quad \forall i \in \mathbf{Ind} \quad (\text{B.9})$$

where  $\mathbf{Ind}$  is the set of indices that indicates the number of Dirichlet nodes. To obtain a linear system, we write  $u_h$  in terms of nodal basis function (see eq.B.1) with  $j \in \mathbf{Nod}$ , where  $\mathbf{Nod}$  is the set of indices that indicates the number of nodes in  $\Omega$ . The set  $\mathbf{Nod}$  can be separated into two subsets: one is  $\mathbf{Ind}$ , i.e. the number of free nodes and the other is  $\mathbf{Dir}$ , i.e. the number of the Dirichlet nodes. This implies that  $u_h$  can be written as:

$$u_h = \sum_{j \in \mathbf{Ind}} u_h \phi_j + \sum_{j \in \mathbf{Dir}} u_j \phi_j \quad (\text{B.10})$$

Then we substitute the discrete Dirichlet condition in this expression:

$$u_h = \sum_{j \in \mathbf{Ind}} u_h \phi_j + \sum_{j \in \mathbf{Dir}} g_0(p_j) \phi_j$$

Finally, we apply this expression in the discrete variation equation (eq.B.8) linearly, and we note that:

$$\nabla u_h = \sum_{j \in \mathbf{Ind}} u_j \nabla \phi_j + \sum_{j \in \mathbf{Dir}} g_0(p_j) \nabla \phi_j$$

and the discrete variational equation became:

$$\begin{aligned} \sum_{j \in \mathbf{Ind}} \left( \int_{\Omega} \nabla \phi_j \cdot \nabla \phi_i + c \int_{\Omega} \phi_i \phi_j \right) u_j &= \int_{\Omega} f \phi_i + \int_{\Gamma_N} g_1 \phi_i + \\ &- \sum_{j \in \mathbf{Dir}} \left( \int_{\Omega} \nabla \phi_i \cdot \nabla \phi_j + c \int_{\Omega} \phi_i \phi_j \right) g_0(p_j) \end{aligned} \quad (\text{B.11})$$

This is a linear system in which the nodal values of  $u_h$  on the free vertices (non-Dirichlet) of the triangulation are unknown. After solving the linear system, the formula for  $u_h$  recovers the function everywhere, not only on the nodes. It is possible to define two matrices from eq.B.12. The first is called the Stiffness matrix such that:

$$W_{ij} = \int_{\Omega} \nabla \phi_j \cdot \nabla \phi_i \quad (\text{B.12})$$

and the second one is called mass matrix:

$$M_{ij} = \int_{\Omega} \phi_i \phi_j \quad (\text{B.13})$$

both matrices are symmetric and the mass matrix is positive definite, instead, the stiffness matrix is semidefinite positive. The eq.B.11 can be rewritten in a simpler form:

$$\sum_{j \in \text{Ind}} (W_{ij} + cM_{ij})u_j = b_i - \sum_{j \in \text{Dir}} (W_{ij} + cM_{ij})g_0(p_j) \quad \forall i \in \text{Ind} \quad (\text{B.14})$$

where  $b_i = \int_{\Omega} f\phi_i + \int_{\Gamma_N} g_1\phi_i$  is called source term.

## B.2 Assembly

Starting with the value of stiffness ( $W_{ij}$ ) and mass ( $M_{ij}$ ) matrices. The  $\Omega$  integration domain can be decomposed as a sum of integrals over different triangles[146]:

$$W_{ij} = \int_{\Omega} \nabla\phi_j \cdot \nabla\phi_i = \sum_K \int_K \nabla\phi_j \cdot \nabla\phi_i = \sum_K w_{ij}^K \quad (\text{B.15})$$

On each triangle, we define three local nodal basis functions. Since the vertices of a triangle  $K$ :  $p_1^K$ ,  $p_2^K$  and  $p_3^K$  consider the function  $N_{\alpha}^K$  with  $\alpha = 1, 2, 3$  such that:

$$N_{\alpha}^K(p_{\beta}^K) = \delta_{\alpha\beta} \quad \alpha, \beta = 1, 2, 3 \quad (\text{B.16})$$

The nodal basis function  $\phi_i$  restricted to the triangle  $K$  is either zero when  $p_i$  is not one of the three vertices of  $K$  or one of the  $N_{\alpha}^K$  functions. More precisely, let  $n_{\alpha}$  be the global number of the local node with the number  $\alpha$  in the triangle  $K$ . This means that  $N_{\alpha}^K = \phi_{n_{\alpha}}$  on the triangle  $K$ ; we now compute the matrix  $k_{\alpha\beta}$ :

$$k_{\alpha\beta}^K = \int_K \nabla N_{\beta}^K \cdot \nabla N_{\alpha}^K \quad \alpha, \beta = 1, 2, 3$$

and we associate the local matrix  $k$  with the global matrix  $w^K$  consider that  $k_{\alpha\beta}^K = w_{n_{\alpha}n_{\beta}}^K$ . For the assembly process, we can compute the local matrices for the stiffness and the mass matrix and obtain a local definition of the discrete equation system:

$$\int_K \nabla N_{\beta}^K \cdot \nabla N_{\alpha}^K + c \int_K N_{\beta}^K N_{\alpha}^K \quad \alpha, \beta = 1, 2, 3 \quad (\text{B.17})$$

For the linear computation of the elements, we need an effective way to evaluate the functions  $N_{\alpha}^K$  and their gradients and a closed form for the resulting integrals. Both possibilities are usually obtained by moving to the so-called reference element. The reference triangle (usually indicated by  $\hat{K}$ ) is design by the following point:  $\hat{p}_1 = (0, 0)$ ,  $\hat{p}_2 = (1, 0)$  and  $\hat{p}_3 = (0, 1)$ . In math literature, it is indicated as  $(\xi, \eta)$  the variables in the reference triangle and  $(x, y)$  the variables

in the physical system. The local nodal functions in the reference triangles satisfy the same condition of the local function in the physical system (eq.B.17), but the variables are fixed and the local nodal function has the following form:

$$\hat{N}_1 = 1 - \xi - \eta \quad \hat{N}_2 = \xi \quad \hat{N}_3 = \eta \quad (\text{B.18})$$

Let us now take three vertices of a triangle  $K$ :

$$p_1^K = (x_1, y_1) \quad p_2^K = (x_2, y_2) \quad p_3^K = (x_3, y_3)$$

It is possible to define an affine transformation:

$$(x, y) = B_K \times (\xi, \eta) + (x_1, y_1) \quad (\text{B.19})$$

where  $B_K$  is the affine matrix transformation. This transformation called  $F_K$  maps the reference triangle  $\hat{K}$  into  $K$  such that:

$$F_K(\hat{p}_\alpha) = p_\alpha^K \quad \alpha = 1, 2, 3$$

Using this equation we can write the nodal function in the physical system in terms of the nodal function in the reference system:

$$N_\alpha^K(x, y) = \hat{N}_\alpha^K(F_K^{-1}(x, y)) \quad (\text{B.20})$$

this formula gives a simple way to evaluate the functions  $N_\alpha^K$ . To evaluate the gradient of  $N_\alpha^K$  we have to apply the chain rule:

$$B_K^T(\nabla\phi \circ F_k) = \hat{\nabla}(\phi \circ F_K)$$

where  $B_K^T$  is the transposed of the matrix of the linear transformation  $F_K$  and  $\phi$  is a general function. Taking  $\phi = N_\alpha^K$  in this expression we obtain a formula for the gradient of the local basis functions:

$$\nabla N_\alpha^K = B_K^{-T}((\hat{\nabla}\hat{N}_\alpha) \circ F_K^{-1}) \quad (\text{B.21})$$

The formula shows that if we want the value of the gradient of  $N_\alpha^K$  in a point  $(x, y) \in K$ , we first compute the transformed point  $(\xi, \eta) = F_K^{-1}(x, y)$  in the reference triangle, evaluate the gradient of  $\hat{N}_\alpha$  in this point and then multiply it by the matrix  $B_K^{-T}$ , which is the transposed of the inverse of  $B_K$ .

Now the values of the local nodal functions have been uniquely evaluated, it is necessary to find a method for solving the integrals in the physical system. The general resolution of the integrals is possible in the reference system, so we make a change of coordinates. For the mass matrix, the change of variables gives:

$$\int_K N_\beta^K N_\alpha^K = |\det B_K| \int_{\hat{K}} \hat{N}_\beta \hat{N}_\alpha \quad (\text{B.22})$$

The evaluation of the integral in the reference system is defined and the result is the matrix  $\hat{K}_0$ , we obtain the following result:

$$M_{ij}^K = |\det B_k| \hat{K}_0$$

$$K_0 = \frac{1}{24} \begin{bmatrix} 2 & 1 & 1 \\ 1 & 2 & 1 \\ 1 & 1 & 2 \end{bmatrix} \quad (\text{B.23})$$

For derivatives the result is more complex:

$$\begin{aligned}
\int_K \nabla N_\beta^K \cdot \nabla N_\alpha^K &= |\det B_K| \int_{\hat{K}} (\nabla N_\beta^K \circ F_K) \cdot (\nabla N_\alpha^K \circ F_K) \\
&= |\det B_K| \int_{\hat{K}} (B_K^{-T} \hat{\nabla} \hat{N}_\beta) \cdot (B_K^{-T} \hat{\nabla} \hat{N}_\alpha) \\
&= |\det B_K| \int_{\hat{K}} C_K \hat{\nabla} \hat{N}_\beta \cdot \hat{\nabla} \hat{N}_\alpha
\end{aligned}$$

where  $C_K = B_K^{-1} B_K^{-T}$  is asymmetric 2x2 matrix that depends only on the triangle considered. If we compute the following matrices in the reference element:

$$\begin{aligned}
\hat{K}_{\xi\xi} &= \int_{\hat{K}} \partial_\xi \hat{N}_\beta \partial_\xi \hat{N}_\alpha = \frac{1}{2} \begin{bmatrix} 1 & -1 & 0 \\ -1 & 1 & 0 \\ 0 & 0 & 0 \end{bmatrix} \\
\hat{K}_{\eta\eta} &= \int_{\hat{K}} \partial_\eta \hat{N}_\beta \partial_\eta \hat{N}_\alpha = \frac{1}{2} \begin{bmatrix} 1 & 0 & -1 \\ 0 & 0 & 0 \\ -1 & 0 & 1 \end{bmatrix} \\
\hat{K}_{\xi\eta} &= \int_{\hat{K}} \partial_\xi \hat{N}_\beta \partial_\eta \hat{N}_\alpha = \frac{1}{2} \begin{bmatrix} 1 & 0 & -1 \\ -1 & 0 & 1 \\ 0 & 0 & 0 \end{bmatrix}
\end{aligned}$$

The final result for the stiffness matrix is the following:

$$W_{ij}^K = |\det B_K| (C_{11}^K \hat{K}_{\xi\xi} + C_{22}^K \hat{K}_{\eta\eta} + C_{12}^K (\hat{K}_{\eta\xi} + \hat{K}_{\eta\xi}^T)) \quad (\text{B.24})$$

Where  $C_{ij}^K$  are the element of the matrix  $C^K$ .

After the evaluation of the stiffness and mass matrices, we apply the same process at the source term. The source term is composed of two vectors:

$$b_i = \int_\Omega f \phi_i + \int_{\Gamma_N} g_1 \phi_i$$

this is applied for the free nodes, but it is possible to compute them for all nodes and discard the element to Dirichlet nodes. the first term of the equation can be treated in a similar way to the stiffness and mass matrix:

$$\int_\Omega f \phi_i = \sum_K \int_K f \phi_i$$

and for each  $K$  triangle we can compute the vector in the function of the local nodal function:

$$\int_K f N_\alpha^K \quad \alpha = 1, 2, 3$$

This process can be done at the same time as the matrix assembly since it makes

triangle by triangle.

$$\begin{aligned}
\int_K f N_\alpha^K &\simeq \frac{1}{3} \sum_{\beta=1}^3 f(p_\beta^K) \int_K N_\alpha^K \\
&\simeq \frac{|\det B_K|}{3} \sum_{\beta=1}^3 f(p_\beta^K) \int_{\hat{K}} \hat{N}_\alpha^K \\
&\simeq \frac{\det B_K}{18} \sum_{\beta=1}^3 f(p_\beta^K)
\end{aligned} \tag{B.25}$$

For the  $\mathbb{P}_1$  elements the three integrals to the element  $K$  are approximated by the same number. The function  $f$  is approximated by a function constant over each triangle: the constant value is the average of the values on its vertices.

The Neumann boundary conditions impose the computation of the second part of the source term integral. The process is different from the computation of eq.B.25. First of all, we have to decompose the Neumann boundary in the set of edges that lie on it:

$$\int_{\Gamma_N} g_1 \phi_i = \sum_L \int_L g_1 \phi_i$$

Next, for each edge consider the two vertices that delimit it:  $p_1^L$  and  $p_2^L$ . Like as the triangular element, we define a nodal basis function for the local point of the Neumann edge, and considering the parameterization of the segment  $L$  the following function:

$$\psi_1 = 1 - t \quad \psi_2 = t$$

define the nodal basis function for the reference element  $[0, 1]$  for the space of a linear polynomial in one dimension. It is simple to see that:

$$\phi_i \circ \phi_L(t) = \begin{cases} \psi_1(t), & \text{if } p_i = p_1^L \\ \psi_2(t), & \text{if } p_i = p_2^L \\ 0, & \text{otherwise} \end{cases}$$

The integrals to be computer are:

$$\int_L g_1 \phi_{n_\alpha} = l_L \int_0^1 (g_1 \circ \phi_L)(t) \psi_\alpha(t) \quad \alpha = 1, 2$$

as before  $n_\alpha$  denotes the global index for the local nodes  $\alpha$  and  $l_L$  is the length if the segment  $L$ . We can approximate this result and obtain:

$$\int_L g_1 \phi_{n_\alpha} \simeq \frac{1}{2} (g_1(p_1^L) + g_1(p_2^L)) \int_L \phi_i = \frac{l_L}{4} (g_1(p_1^L) + g_1(p_2^L)) \quad \alpha = 1, 2 \tag{B.26}$$

### B.3 Isoparametric Element

Let us consider  $\hat{K}$  to be the reference triangle and  $K^0$  a triangle with the vertices  $p_\alpha^K = (x_\alpha, y_\alpha)$  with  $\alpha = 1, 2, 3$  and with this point, we construct the linear map  $F_k^0 : \hat{K} \rightarrow K^0$ . Let us take a point called  $\hat{p}_4^K$  that is the midpoint of the segment that joins  $\hat{p}_2$  and  $\hat{p}_3$  and using the function  $F_K^0$ , take the transformed point in the physical space  $p_4^K = (x_4, y_4)$  and compute its deviation from the midpoint of  $p_2^K$  and  $p_3^K$  [145]:

$$\begin{aligned}\delta_x &= x_4 - \frac{x_2 + x_3}{2} \\ \delta_y &= y_4 - \frac{y_2 + y_3}{2}\end{aligned}$$

Finally take the transformation  $F_K : \hat{K} \rightarrow \mathbb{R}^2$  given by:

$$F_K(\xi, \eta) = F_k^0(\xi, \eta) + 4\xi\eta\boldsymbol{\delta} \quad (\text{B.27})$$

where  $\boldsymbol{\delta} = [\delta_x, \delta_y]$ . Note that is a linear transformation plus a correction term. The transformation satisfied the following properties[145]:

- 1) It sends the chosen points in the reference domain to the ones in the physical space:

$$F_K(\hat{p}_\alpha) = p_\alpha^K \quad \alpha = 1, \dots, 4$$

- 2) If  $\xi = 0$  then  $F_K(0, t) = F_K^0(0, t)$ . This means that the image of the vertical edge in reference coordinates is the segment joining  $p_1^K$  and  $p_3^K$ , covered at a constant velocity as if we were using the linear transformation. The same happens to the horizontal side of  $\hat{K}$ .
- 3) If  $p_4^K$  is aligned with  $p_2^K$  and  $p_3^K$ , then the image of the edge that joins  $\hat{p}_2$  and  $\hat{p}_3$  is the segment that joins  $p_2^K$  and  $p_3^K$ . However, this segment is parameterized at a constant velocity only when  $p_4^K$  is the midpoint of  $p_2^K$  and  $p_3^K$  (in that case  $\delta_x = \delta_y = 0$  and we have only linear term in  $F_K$ ).
- 4) The Jacobian Matrix of  $F_K$  is not constant:

$$B_K = DF(\xi, \eta) = B_K^0 + 4\boldsymbol{\alpha} \cdot \boldsymbol{\delta} \quad (\text{B.28})$$

where  $\boldsymbol{\alpha} = [\eta, \xi]$  vector. When  $p_4^K$  is not too far from the midpoint of  $p_2^K$  and  $p_3^K$ , that is when the deviation  $(\delta_x, \delta_y)$  is not large, it is possible to prove that the image of  $\hat{K}$  under this transformation  $K = F_K(\hat{K})$  is mapped bijectively from the reference element and there we can construct an inverse transformation.

Now we have the physical element,  $K$  which is defined as the image of  $\hat{K}$  by the transformation  $F_K$ . So we define the local space transforming the triangulation method  $\mathbb{P}_2$  on reference variables using the following transformation:

$$\mathbb{P}_2(K) = (p : K \rightarrow \mathbb{R} | p \circ F_K \in \mathbb{P}_2)$$

The degrees of freedom are placed in six nodes: the three vertices, the midpoints of the two straight sides, and the point  $p_4^K$ . Following the same method,  $\hat{N}_\alpha^K$  are the nodal basis function of the  $\mathbb{P}_2$  reference element, and we can define:

$$N_\alpha^K = \hat{N}_\alpha \circ F_K^{-1} \quad (\text{B.29})$$

form a basis of  $\mathbb{P}_2(K)$ . The following properties are considered[145]:

- 1) A function in  $\mathbb{P}_2(K)$  is uniquely determined by the values on the six nodes on  $K$ .
- 2) Restricted to any of the two straight sides of  $K$ , a function of  $\mathbb{P}_2(K)$  is a polynomial of degree two in one variable (that is, the form of function does not depend on the geometry of the element) and is uniquely determined by its values on the three nodes that lie on the side.
- 3) The value of a function in  $\mathbb{P}_2(K)$  on the curved edge of  $K$  is uniquely determined by its value on the three nodes that lie on that edge.

Using these properties we can design an approximate triangulation of a curved domain following the rules:

- 1) Intersection of two different triangles can only happen in a common vertex or edge.
- 2) There must be a vertex placed on each transition point from Dirichlet to Neumann boundaries.
- 3) Triangles with an edge on the approximating polygon can have only one edge on this boundary and both vertices have to be on the exact boundary  $\Gamma$ .

The second part of the triangulation process consists of choosing a point on the exact boundary for each boundary edge. This point should be close to the midpoint of the straight edge that approximates the real curved boundary. We use this point to design an isoparametric triangle with the same vertices for each boundary triangle. When we write the equations of the finite element method using the local space, the union of all triangles (curved and straight) is not the original domain  $\Omega$ , but an approximation of it, which we called  $\Omega_h$ . We call Dirichlet nodes the nodes on the Dirichlet boundary, remarking that these nodes are in the correct boundary  $\Gamma$ . The full finite element space is:

$$V_h = \left( u_h \in C(\bar{\Omega}) \Big| u_h|_K \in \mathbb{P}_2(K), \quad \forall K \in T_h \right)$$

and the subspace with homogeneous Dirichlet boundary condition is:

$$V_h^{\Gamma_D} = \left( v_h \in V_h \Big| v_h(p) = 0 \quad \forall p \text{ Dirichlet node} \right)$$

Note that the function of  $V_h^{\Gamma_D}$  is not zero on the Dirichlet boundary  $\Gamma_D$  but on the curved approximation of that boundary. The process of the formation of nodal basis and transformed local nodal function in the Dirichlet boundary is the same for the previous case (eq. B.16). So, the discrete bilinear form is  $a_h : V_h \times V_h \rightarrow \mathbb{R}$ :

$$a_h(u_h, v_h) = \int_{\Omega_h} \nabla u_h \cdot \nabla v_h + \int_{\Omega_h} u_h v_h \quad (\text{B.30})$$

and the linear form is  $l_h : V_h \rightarrow \mathbb{R}$ :

$$l_h(v_h) = \int_{\Omega_h} f v_h + \int_{\Gamma_N^h} g v_h \quad (\text{B.31})$$

with them obtain the Galerkin numerical method:

$$\begin{aligned} & \mathbf{find} \ u_h \in V_h \ \mathbf{such \ that} \\ & u_h(p_i) = g_0(p_i), \quad \forall i \in \mathbf{Dir} \\ & a(u_h, \phi_i) = l_h(\phi_i) \quad \forall i \in \mathbf{Ind} \end{aligned}$$

The triangulation on a curved domain implies the definition of an approximate  $\Omega_h$  domain in which Galerkin's method is developed. When assembling the numerical equations it's important to make some consideration about the differences between the domains  $\Omega$  and  $\Omega_h$ .

The linear functional  $l_h$ , i.e. the term composed by  $f$  the source term and  $g_1$  the Neumann condition, is defined in  $\Omega$  but they may not be defined in the approximate domain  $\Omega_h$ ; therefore in integration, it is necessary to assemble the equations by eliminating the points where the functions are supported. In addition, in the mass and stiffness matrix, the transition from nodal functions from a reference system to a physical system has a non-linear equation system given eq.B.30, so it must be solved by special numerical techniques.

# Bibliography

- [1] Alexander S Shalin and Sergey V Sukhov. “Plasmonic nanostructures as accelerators for nanoparticles: optical nanocannon”. In: *Plasmonics* 8.2 (2013), pp. 625–629.
- [2] Joshua L Rovey, Paul D Friz, Changyu Hu, Matthew S Glascock, and Xiaodong Yang. “Plasmonic force space propulsion”. In: *Journal of Spacecraft and Rockets* 52.4 (2015), pp. 1163–1168.
- [3] Akshay Reddy Tummala and Atri Dutta. “An overview of cube-satellite propulsion technologies and trends”. In: *Aerospace* 4.4 (2017), p. 58.
- [4] Jose C Pascoa, Odelma Teixeira, and Gustavo Filipe. “A review of propulsion systems for cubesats”. In: *ASME International Mechanical Engineering Congress and Exposition*. Vol. 52002. American Society of Mechanical Engineers. 2018, V001T03A039.
- [5] Kristina Lemmer. “Propulsion for cubesats”. In: *Acta Astronautica* 134 (2017), pp. 231–243.
- [6] Bruce Yost, Sasha Weston, Gabriel Benavides, Frederic Krage, John Hines, Stephanie Mauro, Selasi Etchey, Kiara O’Neill, and Barbra Braun. “State-of-the-art small spacecraft technology”. In: (2021).
- [7] Igor Levchenko, Kateryna Bazaka, Yongjie Ding, Yevgeny Raitses, Stéphane Mazouffre, Torsten Henning, Peter J Klar, Shunjiro Shinohara, Jochen Schein, Laurent Garrigues, et al. “Space micropropulsion systems for Cubesats and small satellites: From proximate targets to furthestmost frontiers”. In: *Applied Physics Reviews* 5.1 (2018), p. 011104.
- [8] George P Sutton and Oscar Biblarz. *Rocket propulsion elements*. John Wiley & Sons, 2016.
- [9] Johan Köhler, Johan Bejhed, Henrik Kratz, Fredrik Bruhn, Ulf Lindberg, Klas Hjort, and Lars Stenmark. “A hybrid cold gas microthruster system for spacecraft”. In: *Sensors and Actuators A: Physical* 97 (2002), pp. 587–598.
- [10] Urmas Kvell, Marit Puusepp, Franz Kaminski, Jaan-Eerik Past, Kristofer Palmer, Tor-Arne Grönland, and Mart Noorma. “Nanosatellite orbit control using MEMS cold gas thrusters”. In: *Proceedings of the Estonian Academy of Sciences* 63.2 (2014), p. 279.

- [11] Vigor Yang. “Modeling of supercritical vaporization, mixing, and combustion processes in liquid-fueled propulsion systems”. In: *Proceedings of the Combustion Institute* 28.1 (2000), pp. 925–942.
- [12] Matthew J Casiano, James R Hulka, and Vigor Yang. “Liquid-propellant rocket engine throttling: A comprehensive review”. In: *Journal of propulsion and power* 26.5 (2010), pp. 897–923.
- [13] Wilfried Ley, Klaus Wittmann, and Willi Hallmann. *Handbook of space technology*. John Wiley & Sons, 2009.
- [14] Kartheephan Sathiyathan, Regina Lee, Hugh Chesser, Charles Dubois, Robert Stowe, Rocco Farinaccio, and Sophie Ringuette. “Solid propellant microthruster design for nanosatellite applications”. In: *Journal of Propulsion and Power* 27.6 (2011), pp. 1288–1294.
- [15] B Larangot, V Conedera, P Dubreuil, T Do Conto, and C Rossi. “Solid propellant microthruster: an alternative propulsion device for nanosatellite”. In: *Aerospace Energetic Equipment Conference (Avignon, France)*. 2002.
- [16] KL Zhang, SK Chou, and Simon S Ang. “Development of a solid propellant microthruster with chamber and nozzle etched on a wafer surface”. In: *Journal of Micromechanics and Microengineering* 14.6 (2004), p. 785.
- [17] A Cervone, B Zandbergen, D Cordeiro Guerrieri, M De Athayde Costa e Silva, I Krusharev, and H Van Zeijl. “Green micro-resistojet research at Delft University of Technology: new options for Cubesat propulsion”. In: *CEAS Space Journal* 9 (2017), pp. 111–125.
- [18] Robert H Frisbee. “Advanced space propulsion for the 21st century”. In: *Journal of propulsion and power* 19.6 (2003), pp. 1129–1154.
- [19] Michael Robin, Thomas Brogan, and Eric Cardiff. “An ammonia micro-resistojet (MRJ) for micro satellites”. In: *44th AIAA/ASME/SAE/ASEE Joint Propulsion Conference & Exhibit*. 2008, p. 5288.
- [20] Max Skuhersky, Larissa Balestrero Machado, Markus Wilde, and Christopher Brett. “CERBERUS: Prototype for an Agile Inspection and Servicing Satellite Using Thrust-Vectoring Cold-Gas Propulsion”. In: *AIAA SPACE and Astronautics Forum and Exposition*. 2017, p. 5116.
- [21] John Slough, Samuel Andreason, Timothy Ziemba, and JJ Ewing. “Micro-discharge micro-thruster”. In: *41st AIAA/ASME/SAE/ASEE Joint Propulsion Conference & Exhibit*. 2005, p. 4074.
- [22] Andrew D Ketsdever, Dean C Wadsworth, and EP Muntz. “Gas-surface interaction model influence on predicted performance of microelectromechanical system resistojet”. In: *Journal of Thermophysics and Heat Transfer* 15.3 (2001), pp. 302–307.
- [23] David Fearn. “The future development of gridded ion engines”. In: *39th AIAA/ASME/SAE/ASEE Joint Propulsion Conference and Exhibit*. 2003, p. 4714.

- [24] Paul J Wilbur, Merrill Wilson, Kent Hutchings, and John D Williams. “Emissive membrane ion thruster concept”. In: *Journal of Propulsion and Power* 23.5 (2007), pp. 1049–1054.
- [25] Philippe Knauth and Harry L Tuller. “Solid-state ionics: roots, status, and future prospects”. In: *Journal of the American Ceramic Society* 85.7 (2002), pp. 1654–1680.
- [26] Dan M Goebel and Ira Katz. *Fundamentals of electric propulsion: ion and Hall thrusters*. John Wiley & Sons, 2008.
- [27] G Seikel and E Reshotko. “Hall current ion accelerator”. In: *Bull, Am. Phys. Soc* (1962).
- [28] John Dankanich. “Direct drive for low power Hall thrusters”. In: *41st AIAA/ASME/SAE/ASEE Joint Propulsion Conference & Exhibit*. 2005, p. 4118.
- [29] Edwin H Hall et al. “On a new action of the magnet on electric currents”. In: *American Journal of Mathematics* 2.3 (1879), pp. 287–292.
- [30] Taichiro Tamida, Hiroyuki Osuga, Naoji Yamamoto, Haruki Takegahara, Junichiro Aoyagi, and Kyoichi Kuriki. “Performance improvement of Hall thrusters using a pulse-synchronous driver system”. In: *Journal of Propulsion and Power* 31.3 (2015), pp. 956–961.
- [31] Carl E Pigeon, Nathan G Orr, Benoit P Larouche, Vincent Tarantini, Grant Bonin, and Robert E Zee. “A Low Power Cylindrical Hall Thruster for Next Generation Microsatellites”. In: (2015).
- [32] Enric Grustan-Gutierrez and Manuel Gamero-Castaño. “Microfabricated electrospray thruster array with high hydraulic resistance channels”. In: *Journal of Propulsion and Power* 33.4 (2017), pp. 984–991.
- [33] David Krejci, Fernando Mier-Hicks, Corey Fucetola, Paulo Lozano, Andrea Hsu Schouten, and Francois Martel. “Design and Characterization of a Scalable ion Electrospray Propulsion System”. In: (2015).
- [34] Robert S Legge Jr and Paulo C Lozano. “Electrospray propulsion based on emitters microfabricated in porous metals”. In: *Journal of Propulsion and Power* 27.2 (2011), pp. 485–495.
- [35] Daniel G Courtney, Simon Dandavino, and Herbert Shea. “Comparing direct and indirect thrust measurements from passively fed ionic electrospray thrusters”. In: *Journal of Propulsion and Power* 32.2 (2016), pp. 392–407.
- [36] Wei-dong Song and U Shumlak. “Ultrasonically aided electrospray source for charged particles approaching monodisperse distributions”. In: *Journal of Propulsion and Power* 26.2 (2010), pp. 353–363.
- [37] Kurt A Polzin. “Comprehensive review of planar pulsed inductive plasma thruster research and technology”. In: *Journal of Propulsion and Power* 27.3 (2011), pp. 513–531.

- [38] Michael Keidar, Iain D Boyd, and Isak I Beilis. “Model of particulate interaction with plasma in a Teflon Pulsed Plasma Thruster”. In: *Journal of Propulsion and Power* 17.1 (2001), pp. 125–131.
- [39] Matthew S Glascock, Joshua Rovey, Shae Williams, and Jason Thrasher. “Observation of late-time ablation in electric solid propellant pulsed microthrusters”. In: *52nd AIAA/SAE/ASEE Joint Propulsion Conference*. 2016, p. 4845.
- [40] Rodney L Burton and PJ Turchi. “Pulsed plasma thruster”. In: *Journal of Propulsion and Power* 14.5 (1998), pp. 716–735.
- [41] IW Lee, D Richard, and REH Branam. “Nano-Satellite Gatling-Gun Pulsed Plasma Thruster”. In: *Proceedings of the 49th AIAA Aerospace Sciences Meeting including the New Horizons Forum and Aerospace Exposition, Orlando, FL, USA*. 2011, pp. 4–7.
- [42] Isaac Nason, Jordi Puig-Suari, and Robert Twiggs. “Development of a family of picosatellite deployers based on the CubeSat standard”. In: *Proceedings, IEEE Aerospace Conference*. Vol. 1. IEEE. 2002, pp. 1–1.
- [43] Arash Mehrparvar, D Pignatelli, J Carnahan, R Munakat, W Lan, A Toorian, A Hutputanasin, and S Lee. “Cubesat design specification rev. 13”. In: *The CubeSat Program, Cal Poly San Luis Obispo, US* 1.2 (2014).
- [44] Masud Mansuripur. “Mechanical effects of light on material media: radiation pressure and the linear and angular momenta of photons”. In: *Fifty Years of Optical Sciences at The University of Arizona*. Vol. 9186. SPIE. 2014, pp. 271–276.
- [45] David Murphy, Thomas Murphey, and Paul Gierow. “Scalable solar sail subsystem design considerations”. In: *43rd AIAA/ASME/ASCE/AHS/ASC Structures, Structural Dynamics, and Materials Conference*. 2002, p. 1703.
- [46] Grover A Swartzlander. “Radiation pressure on a diffractive sailcraft”. In: *JOSA B* 34.6 (2017), pp. C25–C30.
- [47] Thierry Botter, Victoria L Coverstone, and Rodney L Burton. “Structural dynamics of spin-stabilized solar sails with applications to UltraSail”. In: *Journal of guidance, control, and dynamics* 31.2 (2008), pp. 402–413.
- [48] S Chad Gibbs IV and Earl H Dowell. “Membrane paradox for solar sails”. In: *AIAA journal* 52.12 (2014), pp. 2904–2907.
- [49] Michael Souder and Matthew West. “Solar Sail Technology for Nanosatellites”. In: *AIAA/AAS Astrodynamics Specialist Conference and Exhibit*. 2008, p. 7078.
- [50] Sandeep Ravi-Kumar, Benjamin Lies, Xiao Zhang, Hao Lyu, and Hantang Qin. “Laser ablation of polymers: A review”. In: *Polymer International* 68.8 (2019), pp. 1391–1401.

- [51] Eric W Davis and Franklin B Mead Jr. “Review of laser lightcraft propulsion system”. In: *AIP Conference Proceedings*. Vol. 997. 1. American Institute of Physics. 2008, pp. 283–294.
- [52] H Horisawa and I Kimura. “Fundamental study on laser plasma accelerator for propulsion applications”. In: *Vacuum* 65.3-4 (2002), pp. 389–396.
- [53] Akihiro Sasoh, Hisashi Tsuruta, Yusuke Katagiri, Osker Dondelowski, and Bin Wang. “CHARACTERISTICS OF ABLATION IMPULSE INDUCED BY REPETITIVE LASER PULSE IRRADIATIONS”. In: *5th European Conference on Space Debris, Furo-cho, Chikusa-ku, Nagoya*. 2009.
- [54] Max Born and Emil Wolf. *Principles of optics: electromagnetic theory of propagation, interference and diffraction of light*. Elsevier, 2013.
- [55] Stefan A Maier et al. *Plasmonics: fundamentals and applications*. Vol. 1. Springer, 2007.
- [56] John David Jackson. *Classical electrodynamics*. 1999.
- [57] Neil W Ashcroft and N David Mermin. *Solid state physics*. Cengage Learning, 2022.
- [58] Yu A Il’inskii and Leonid Veniaminovich Keldysh. *Electromagnetic response of material media*. Springer Science & Business Media, 1994.
- [59] Peter B Johnson and R-WJPrB Christy. “Optical constants of the noble metals”. In: *Physical review B* 6.12 (1972), p. 4370.
- [60] Paul Drude. “Zur elektronentheorie der metalle”. In: *Annalen der physik* 306.3 (1900), pp. 566–613.
- [61] Lev Davidovich Landau, John Stewart Bell, MJ Kearsley, LP Pitaevskii, EM Lifshitz, and JB Sykes. *Electrodynamics of continuous media*. Vol. 8. elsevier, 2013.
- [62] Amnon Yariv. *Optical electronics in modern communications*. Vol. 1. Oxford University Press, USA, 1997.
- [63] Georg Goubau. “Surface waves and their application to transmission lines”. In: *Journal of Applied Physics* 21.11 (1950), pp. 1119–1128.
- [64] Erwin Kretschmann and Heinz Raether. “Radiative decay of non radiative surface plasmons excited by light”. In: *Zeitschrift für Naturforschung A* 23.12 (1968), pp. 2135–2136.
- [65] Andreas Otto. “Excitation of nonradiative surface plasma waves in silver by the method of frustrated total reflection”. In: *Zeitschrift für Physik A Hadrons and nuclei* 216.4 (1968), pp. 398–410.
- [66] Eloise Devaux, Thomas W Ebbesen, Jean-Claude Weeber, and Alain Dereux. “Launching and decoupling surface plasmons via micro-gratings”. In: *Applied physics letters* 83.24 (2003), pp. 4936–4938.

- [67] B Hecht, H Bielefeldt, L Novotny, Y Inouye, and DW Pohl. “Local excitation, scattering, and interference of surface plasmons”. In: *Physical review letters* 77.9 (1996), p. 1889.
- [68] Uwe Kreibig, Michael Vollmer, Uwe Kreibig, and Michael Vollmer. “Theoretical considerations”. In: *Optical properties of metal clusters* (1995), pp. 13–201.
- [69] Craig F Bohren and Donald R Huffman. *Absorption and scattering of light by small particles*. John Wiley & Sons, 2008.
- [70] Gustav Mie. “Beiträge zur Optik trüber Medien, speziell kolloidaler Metallösungen”. In: *Annalen der physik* 330.3 (1908), pp. 377–445.
- [71] Michael Meier and A Wokaun. “Enhanced fields on large metal particles: dynamic depolarization”. In: *Optics letters* 8.11 (1983), pp. 581–583.
- [72] A Wokaun, JP Gordon, and PF Liao. “Radiation damping in surface-enhanced Raman scattering”. In: *Physical Review Letters* 48.14 (1982), p. 957.
- [73] Th Kokkinakis and K Alexopoulos. “Observation of radiative decay of surface plasmons in small silver particles”. In: *Physical Review Letters* 28.25 (1972), p. 1632.
- [74] Stephan Link and Mostafa A El-Sayed. “Shape and size dependence of radiative, non-radiative and photothermal properties of gold nanocrystals”. In: *International reviews in physical chemistry* 19.3 (2000), pp. 409–453.
- [75] Hitoshi Kuwata, Hiroharu Tamaru, Kunio Esumi, and Kenjiro Miyano. “Resonant light scattering from metal nanoparticles: Practical analysis beyond Rayleigh approximation”. In: *Applied physics letters* 83.22 (2003), pp. 4625–4627.
- [76] Stefan A Maier, Pieter G Kik, and Harry A Atwater. “Observation of coupled plasmon-polariton modes in Au nanoparticle chain waveguides of different lengths: Estimation of waveguide loss”. In: *Applied Physics Letters* 81.9 (2002), pp. 1714–1716.
- [77] Erin M Hicks, Shengli Zou, George C Schatz, Kenneth G Spears, Richard P Van Duyne, Linda Gunnarsson, Tomas Rindzevicius, Bengt Kasemo, and Mikael Käll. “Controlling plasmon line shapes through diffractive coupling in linear arrays of cylindrical nanoparticles fabricated by electron beam lithography”. In: *Nano letters* 5.6 (2005), pp. 1065–1070.
- [78] GP Nikishkov. “Introduction to the finite element method”. In: *University of Aizu* (2004), pp. 1–70.
- [79] Francisco-Javier Sayas. “A gentle introduction to the Finite Element Method”. In: *Lecture notes, University of Delaware* (2008).
- [80] Alfio Quarteroni and Silvia Quarteroni. *Numerical models for differential problems*. Vol. 2. Springer, 2009.

- [81] Mark Ainsworth and J Tinsley Oden. “A posteriori error estimation in finite element analysis”. In: *Computer methods in applied mechanics and engineering* 142.1-2 (1997), pp. 1–88.
- [82] Gene H Golub and Charles F Van Loan. *Matrix computations*. JHU press, 2013.
- [83] Edgar Solomonik and James Demmel. “Communication-optimal parallel 2.5 D matrix multiplication and LU factorization algorithms”. In: *Euro-Par 2011 Parallel Processing: 17th International Conference, Euro-Par 2011, Bordeaux, France, August 29-September 2, 2011, Proceedings, Part II 17*. Springer. 2011, pp. 90–109.
- [84] Laura Grigori, James W Demmel, and Hua Xiang. “CALU: a communication optimal LU factorization algorithm”. In: *SIAM Journal on Matrix Analysis and Applications* 32.4 (2011), pp. 1317–1350.
- [85] Boris T Polyak. “Introduction to optimization. optimization software”. In: *Inc., Publications Division, New York* 1 (1987), p. 32.
- [86] R Fletcher and GA Watson. “Numerical analysis dundee 1975”. In: *Lecture notes in Mathematics* 506 (1976), pp. 73–89.
- [87] HA V. der Vorst. “Bi-CGSTAB: a fast and smoothly converging variant of Bi-CG for the solution of nonsymmetric linear systems”. In: *SIAM J. Sci. Statist. Comput.* 13 (1992), p. 631.
- [88] Gerard LG Sleijpen and Diederik R Fokkema. “BiCGstab (ell) for linear equations involving unsymmetric matrices with complex spectrum”. In: *Electronic Transactions on Numerical Analysis*. 1 (1993), pp. 11–32.
- [89] Alexander F Shchepetkin and James C McWilliams. “The regional oceanic modeling system (ROMS): a split-explicit, free-surface, topography-following-coordinate oceanic model”. In: *Ocean modelling* 9.4 (2005), pp. 347–404.
- [90] Stanley C Eisenstat, Howard C Elman, and Martin H Schultz. “Variational iterative methods for nonsymmetric systems of linear equations”. In: *SIAM Journal on Numerical Analysis* 20.2 (1983), pp. 345–357.
- [91] Owe Axelsson. *Iterative solution methods*. Cambridge university press, 1996.
- [92] A Hadjidimos. “Successive overrelaxation (SOR) and related methods”. In: *Journal of Computational and Applied Mathematics* 123.1-2 (2000), pp. 177–199.
- [93] Yousef Saad and Y Saad. “Iterative methods for sparse linear systems, PWS Pub”. In: *Co., Boston* 27 (1996).
- [94] Lukas Novotny and Bert Hecht. *Principles of nano-optics*. Cambridge university press, 2012.
- [95] Sergio Balestrieri, Gianluigi Zito, Giuseppe Coppola, and Mario Iodice. “Plasmonic Nanostructures for optically induced movement”. In: *Frontiers in Nanotechnology* (2022), p. 30.

- [96] Arthur Ashkin. “Optical trapping and manipulation of neutral particles using lasers”. In: *Proceedings of the National Academy of Sciences* 94.10 (1997), pp. 4853–4860.
- [97] ML Juan, M Righini, and R Quidant. *Nat. Photonics* 5 (6), 349 (2011). 2011.
- [98] Mark Daly, Marios Sergides, and Sile Nic Chormaic. “Optical trapping and manipulation of micrometer and submicrometer particles”. In: *Laser & Photonics Reviews* 9.3 (2015), pp. 309–329.
- [99] JA Schuller, ES Barnard, WS Cai, YC Jun, JS White, and ML Brongersma. “Nanoplasmonic Probes of Catalytic Reactions”. In: *Nat. Mater* 9 (2010), pp. 193–204.
- [100] Xiaodong Yang, Yongmin Liu, Rupert F Oulton, Xiaobo Yin, and Xiang Zhang. “Optical forces in hybrid plasmonic waveguides”. In: *nano Letters* 11.2 (2011), pp. 321–328.
- [101] Preston R Huft, Joshua D Kolbow, Jonathan T Thweatt, and Nathan C Lindquist. “Holographic plasmonic nanotweezers for dynamic trapping and manipulation”. In: *Nano Letters* 17.12 (2017), pp. 7920–7925.
- [102] Jiunn-Woei Liaw, Chiao-Wei Chien, Kun-Chi Liu, Yun-Cheng Ku, and Mao-Kuen Kuo. “3D optical vortex trapping of plasmonic nanostructure”. In: *Scientific Reports* 8.1 (2018), p. 12673.
- [103] Kai Wang, Ethan Schonbrun, and Kenneth B Crozier. “Propulsion of gold nanoparticles with surface plasmon polaritons: evidence of enhanced optical force from near-field coupling between gold particle and gold film”. In: *Nano letters* 9.7 (2009), pp. 2623–2629.
- [104] Thomas Søndergaard, Sergey I Bozhevolnyi, Sergey M Novikov, Jonas Beermann, Eloise Devaux, and Thomas W Ebbesen. “Extraordinary optical transmission enhanced by nanofocusing”. In: *Nano letters* 10.8 (2010), pp. 3123–3128.
- [105] Jiao Jiao, En Lin, Gaofeng Liang, and Qing Zhao. “Nano optical propeller based on localized field intensity enhancement of surface plasmons”. In: *Fourth International Symposium on Laser Interaction with Matter*. Vol. 10173. SPIE. 2017, pp. 455–460.
- [106] Jaykob N Maser, Ling Li, Huixu Deng, Xiaodong Yang, and Joshua L Rovey. “Transmission spectrum of asymmetric nanostructures for plasmonic space propulsion”. In: *Journal of Spacecraft and Rockets* 53.5 (2016), pp. 998–1000.
- [107] Leijun Zhang, Jiao Jiao, Jisheng Tong, Chunguang Ma, and Qing Zhao. “Study on the optical field distribution of asymmetric nanostructures based on surface plasmon”. In: *IEEE Photonics Journal* 11.2 (2019), pp. 1–8.
- [108] Joshua L Rovey, Jie Gao, Henry Pernicka, and Xiaodong Yang. *Experimental Demonstration and System Analysis for Plasmonic Force Propulsion*. Tech. rep. 2019.

- [109] AB COMSOL. “Wave Optics Module User’s Guide, COMSOL Multiphysics® v. 5.3 a”. In: *Stockholm, Sweden* (2017), pp. 38–46.
- [110] COMSOL. *COMSOL Multiphysics® v. 6.0., Scatterer on Substrate, Wave-optics Module*. 2022.
- [111] Allen Taflove, Susan C Hagness, and Melinda Piket-May. “Computational electromagnetics: the finite-difference time-domain method”. In: *The Electrical Engineering Handbook 3* (2005), pp. 629–670.
- [112] Steven G Johnson. “Notes on perfectly matched layers (PMLs)”. In: *arXiv preprint arXiv:2108.05348* (2021).
- [113] Anuj Dhawan, Stephen J Norton, Michael D Gerhold, and Tuan Vo-Dinh. “Comparison of FDTD numerical computations and analytical multipole expansion method for plasmonics-active nanosphere dimers”. In: *Optics express* 17.12 (2009), pp. 9688–9703.
- [114] Péter Dombi, Zsuzsanna Pápa, Jan Vogelsang, Sergey V Yalunin, Murat Sivis, Georg Herink, Sascha Schäfer, Petra Groß, Claus Ropers, and Christoph Lienau. “Strong-field nano-optics”. In: *Reviews of Modern Physics* 92.2 (2020), p. 025003.
- [115] AB COMSOL. “COMSOL Multiphysics-LiveLink for Matlab User’s Guide—Version 5”. In: *COMSOL AB: Stockholm, Sweden* (2013).
- [116] Qiwen Zhan. “Cylindrical vector beams: from mathematical concepts to applications”. In: *Advances in Optics and Photonics* 1.1 (2009), pp. 1–57.
- [117] M Khodas, A Shekhter, and AM Finkel’Stein. “Spin polarization of electrons by nonmagnetic heterostructures: The basics of spin optics”. In: *Physical review letters* 92.8 (2004), p. 086602.
- [118] Konstantin Yu Bliokh, Francisco J Rodriguez-Fortuño, Franco Nori, and Anatoly V Zayats. “Spin-orbit interactions of light”. In: *Nature Photonics* 9.12 (2015), pp. 796–808.
- [119] Konstantin Y Bliokh and Franco Nori. “Transverse and longitudinal angular momenta of light”. In: *Physics Reports* 592 (2015), pp. 1–38.
- [120] Konstantin Y Bliokh, Aleksandr Y Bekshaev, and Franco Nori. “Extraordinary momentum and spin in evanescent waves”. In: *Nat. Comm.* 5.1 (2014), pp. 1–8.
- [121] Frederik J Belinfante. “On the current and the density of the electric charge, the energy, the linear momentum and the angular momentum of arbitrary fields”. In: *Physica* 7.5 (1940), pp. 449–474.
- [122] Masaru Onoda, Shuichi Murakami, and Naoto Nagaosa. “Hall effect of light”. In: *Physical review letters* 93.8 (2004), p. 083901.
- [123] Onur Hosten and Paul Kwiat. “Observation of the spin Hall effect of light via weak measurements”. In: *Science* 319.5864 (2008), pp. 787–790.

- [124] Konstantin Y Bliokh, CT Samlan, Chandravati Prajapati, Graciana Puentes, Nirmal K Viswanathan, and Franco Nori. “Spin-Hall effect and circular birefringence of a uniaxial crystal plate”. In: *Optica* 3.10 (2016), pp. 1039–1047.
- [125] Nándor Bokor, Yoshinori Iketaki, Takeshi Watanabe, and Masaaki Fujii. “Investigation of polarization effects for high-numerical-aperture first-order Laguerre-Gaussian beams by 2D scanning with a single fluorescent microbead”. In: *Optics Express* 13.26 (2005), pp. 10440–10447.
- [126] Yiqiong Zhao, J Scott Edgar, Gavin DM Jeffries, David McGloin, and Daniel T Chiu. “Spin-to-orbital angular momentum conversion in a strongly focused optical beam”. In: *Physical Review Letters* 99.7 (2007), p. 073901.
- [127] Chaim Schwartz and Aristide Dogariu. “Conservation of angular momentum of light in single scattering”. In: *Optics express* 14.18 (2006), pp. 8425–8433.
- [128] Alessandro Ciattoni, Gabriella Cincotti, and Claudio Palma. “Angular momentum dynamics of a paraxial beam in a uniaxial crystal”. In: *Physical Review E* 67.3 (2003), p. 036618.
- [129] B Ya Zel’Dovich, ND Kundikova, and LF Rogacheva. “Observation of transverse shift of a focal spot upon a change in the sign of circular polarization”. In: *ZhETF Pisma Redaktsiiu* 59 (1994), p. 737.
- [130] Oleg V Angelsky, Claudia Yu Zenkova, Steen G Hanson, and Jun Zheng. “Extraordinary manifestation of evanescent wave in biomedical application”. In: *Frontiers in Physics* 8 (2020), p. 159.
- [131] Daniel O’connor, Pavel Ginzburg, Francisco J Rodriguez-Fortuño, Greg A Wurtz, and Anatoly V Zayats. “Spin-orbit coupling in surface plasmon scattering by nanostructures”. In: *Nat. Comm.* 5.1 (2014), pp. 1–7.
- [132] Massimo Antognozzi, CR Bermingham, RL Harniman, Stephen Simpson, Jorden Senior, Rosie Hayward, Heinrich Hoerber, MR Dennis, AY Bekshaev, KY Bliokh, et al. “Direct measurements of the extraordinary optical momentum and transverse spin-dependent force using a nanocantilever”. In: *Nat. Phys.* 12.8 (2016), pp. 731–735.
- [133] Francisco J Rodriguez-Fortuño, Nader Engheta, Alejandro Martinez, and Anatoly V Zayats. “Lateral forces on circularly polarizable particles near a surface”. In: *Nature communications* 6.1 (2015), p. 8799.
- [134] Claudia Triolo, Adriano Cacciola, Salvatore Patanè, Rosalba Saija, Salvatore Savasta, and Franco Nori. “Spin-momentum locking in the near field of metal nanoparticles”. In: *ACS Photonics* 4.9 (2017), pp. 2242–2249.
- [135] FM Pagliano. “Dynamic control of the spontaneous emission of single quantum dots in photonic crystal cavities”. In: (2014).
- [136] SJ Yoo, JW Lim, and YE Sung. “Sol. Energy Mater”. In: *Sol. Cells* <https://doi.org/10.1016/j.solmat> 33.90 (2005), p. 477.

- [137] N William Parker, Alan D Brodie, and John H McCoy. “High-throughput NGL electron-beam direct-write lithography system”. In: *Emerging Lithographic Technologies IV*. Vol. 3997. SPIE. 2000, pp. 713–720.
- [138] Richard C Jaeger. “Film Deposition: Introduction to Microelectronic Fabrication”. In: *Upper Saddle Rivers: Prentice Hall* 83 (2002).
- [139] Gerd K Binnig. *Atomic force microscope and method for imaging surfaces with atomic resolution*. US Patent 4,724,318. Feb. 1988.
- [140] Franz J Giessibl. “Advances in atomic force microscopy”. In: *Reviews of modern physics* 75.3 (2003), p. 949.
- [141] G Goldstein, D Newbury, P Echlin, D Joy, A Romig, C Lyman, C Fiori, and E Lifshin. “Scanning Electron Microscopy and X-Ray Microanalysis. New York: Plenum Press”. In: (1981).
- [142] Debbie Stokes. *Principles and practice of variable pressure/environmental scanning electron microscopy (VP-ESEM)*. John Wiley & Sons, 2008.
- [143] Arnold Sommerfeld. *Electrodynamics: lectures on theoretical physics, vol. 3*. Vol. 3. Academic Press, 2013.
- [144] Julius Adams Stratton. *Electromagnetic theory*. Vol. 33. John Wiley & Sons, 2007.
- [145] Dietrich Braess. *Finite elements: Theory, fast solvers, and applications in solid mechanics*. Cambridge University Press, 2007.
- [146] Philippe G Ciarlet. *The finite element method for elliptic problems*. SIAM, 2002.



# Acknowledgements

I would like to thank all the people who have supported me during these three years of my Ph.D. I would like to thank my supervisors Ing. Giuseppe Coppola and Ing. Mario Iodice who allowed me to participate in this challenging and ambitious project and have been my guide and support throughout this period. I would also like to thank Silvia Romano and Gianluigi Zito who took an interest in my Ph.D. project by giving me help and support in the development of the plasmonic device and some sample characterization tests. Sincere thanks also go to all the colleagues we have met over the years in the CNR: Bruno, Federica, Valeria, Sara, Graziano, Bryan, Teresa, and Chiara; even if we worked on different projects, they always tried to make me feel part of the group with their friendliness and cheerfulness. I would also like to thank the rest of the CNR-ISASI staff for how they welcomed me and the support they gave me. Although much of the work was done with the CNR-ISASI group I would also like to thank Professors Enrico Calloni and Luigi Rosa of the University of Naples Federico II, who despite the distance between the two locations always showed themselves available for whatever doubts or curiosities I needed to ask them. The sample fabrication part was carried out in collaboration with a Dutch industry "Nanophab," so I would also like to thank dt. Francesco Pagliano who in my short time in Eindhoven helped me fabricate the sample and guided me in the techniques used in his Clean Room. Finally, I would also like to thank my parents, my sister Serena my grandparents, and all the other members of my family. You have supported me from the beginning of my studies and for that, I will always be grateful. I would also like to thank all my friends: Fabio, Luca, Alberto, Francesco, Giuseppe, Stefano, Angelo, and all the other people who helped me become what I am now. I am grateful to you for your help in difficult times, for always being able to count on your support, and for all the good times shared all these years.